Drug delivery, entry and intracellular trafficking of polymeric nanoparticles

DOCTORAL THESIS

DANIEL HOFMANN

MAX PLANCK INSTITUTE FOR POLYMER RESEARCH, MAINZ

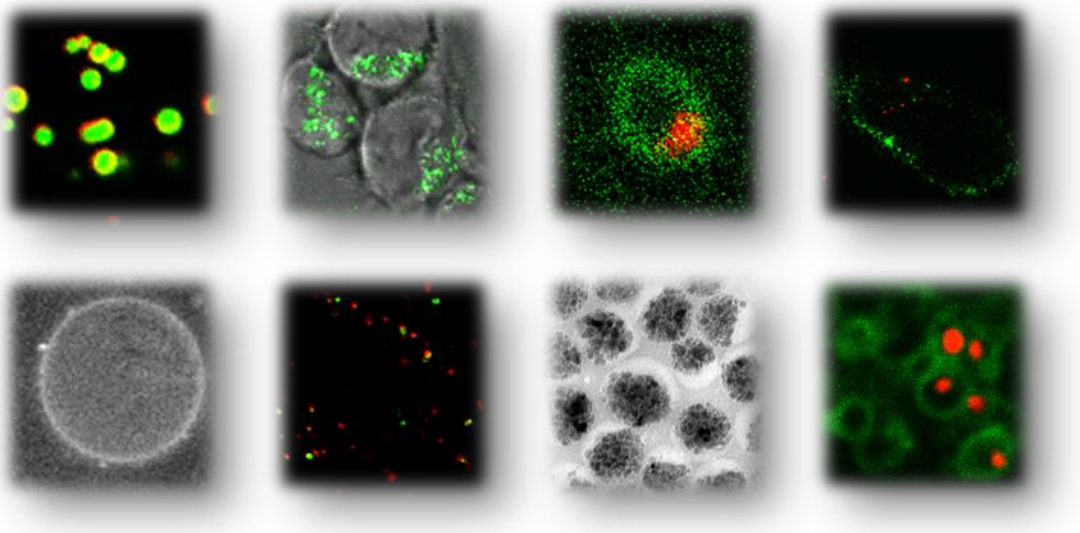

Drug delivery, entry and intracellular trafficking of polymeric nanoparticles

DOCTORAL THESIS

In fulfillment of the requirements for the degree of

Doktor rerum naturalium

(Dr. rer. nat.)

Submitted to

THE FACULTY OF BIOLOGY AT THE

JOHANNES GUTENBERG UNIVERSITÄT, MAINZ

This doctoral thesis has been carried out

AT THE MAX-PLANCK INSTITUTE FOR POLYMER RESEARCH, MAINZ

Daniel Hofmann

M.Sc. Cell and Molecular Biology

Born in [redacted], Germany

Submission: August 2014

JOHANNES GUTENBERG UNIVERSITÄT MAINZ

JG|U

MAX-PLANCK-GESELLSCHAFT

Reviewers of the thesis committee

Supervisor

[redacted]

[redacted]

Second reviewer of the thesis committee

[redacted]

[redacted]

Affidavit

The doctoral thesis was carried out from [redacted] at the Max-Planck Institute for Polymer Research under the supervision of [redacted].

I herewith declare that my doctoral thesis "**Drug delivery, entry and intracellular trafficking of polymeric nanoparticles**" has been written independently with no other sources and aids than quoted in the text. The thesis has never been submitted to other faculties.

Hereby, I accept the examination regulations of the Faculty of Biology (Johannes Gutenberg Universität, Mainz).

_____

Date, Daniel Hofmann

Publications during this thesis

Hofmann, D. & Mailander, V. Pharmacology of nanocarriers on the microscale: importance of uptake mechanisms and intracellular trafficking for efficient drug delivery. *Nanomedicine (Lond) 8, 321-323, doi:10.2217/nnm.13.2 (2013).*

Baumann D., Hofmann D., Nullmeier S., Panther P., Dietze C., Musyanovych A., Ritz S., Landfester K. & Mailänder V. Complex encounters: nanoparticles in whole blood and their uptake into different types of white blood cells. *Nanomedicine (Lond) 8, 699-713, doi:10.2217/nnm.12.111 (2013).*

Hofmann, D., Messerschmidt, C., Bannwarth, M. B., Landfester, K. & Mailander, V. Drug delivery without nanoparticle uptake: delivery by a kiss-and-run mechanism on the cell membrane. *Chemical Communications 50, 1369-1371, doi:10.1039/c3cc48130a (2014).*

Hofmann, D., Tenzer, S., Bannwarth, M. B., Messerschmidt, C., Glaser S-F., Schild H., Landfester, K. & Mailander, V. Mass Spectrometry and Imaging Analysis of Nanoparticle-Containing Vesicles Provide a Mechanistic Insight into Cellular Trafficking, *ACS nano, ASAP, doi: 10.1021/nn502754c*.

Messerschmidt, C, Hofmann D., Kroeger-Brinkmann A., Landfester K., Mailänder V. & Lieberwirth I. Cellular Uptake of Small Nanoparticles: Ultrastructure reveals size dependent membrane morphologies; *Major revision.*

Other publications

Dühren-von Minden M., Übelhart R., Schneider D., Wossning T., Bach M., Buchner M., Hofmann D., Surova E., Follo M., Köhler F., Wardemann H., Zirlik K., Veelken H., Jumaa H. Chronic lymphocytic leukaemia is driven by antigen-independent cell-autonomous signaling. *Nature **489**, 309-312, doi:10.1038/nature1130.*

I. Contents

II. List of Figures

III. List of Tables

IV. Abbreviations

AAV2	**A**deno-**a**ssociated **v**irus **2**
ADRP	**A**dipose **d**ifferentiation-**r**elated **p**rotein
AP-1/AP-2	**A**daptor **p**rotein **1**/ **A**daptor **p**rotein **2**
ARF1	**A**DP-**r**ibosylation **f**actor **1**
BafA1	**Baf**ilomycin **A1**
BSA	**B**ovine **s**erum **a**lbumin
CCP	**C**lathrin **c**oated **p**it
CD	**C**luster of **d**ifferentiation
cdc42	**C**ell **d**ivision **c**ontrol protein **42**
CLIC/GEEC	**C**lathrin-**i**ndependent **c**arriers and **G**PI-**e**nriched **e**ndocytic **c**ompartments
CLSM	**C**onfocal **l**aser **s**canning **m**icroscopy
CME	**C**lathrin-**m**ediated **e**ndocytosis
COP vesicles	**Co**at**p**rotein-coated vesicles
CPP	**C**ell **p**enetrating **p**eptide
CtxB	**C**holera **t**oxin **s**ubunit **B**
DAG	**D**i**a**cyl**g**lycerol
DC-SIGN	**D**endritic **c**ell-**s**pecific **i**ntercellular adhesion molecule-3-**g**rabbing **n**on-integrin
DGAT	**D**i**g**lyceride **a**cyl**t**ransferase
DIC microscopy	**D**ifferential **i**nterference **c**ontrast microscopy
DOPC	1,2-**D**i**o**leoyl-sn-glycero-3-**p**hospho**c**holine
EE	**E**arly **e**ndosome
EEA1	**E**arly **e**ndosome **a**ntigen **1**
EGF	**E**pidermal **g**rowth **f**actor
EPR	**E**nhanced **p**ermeability and **r**etention effect
Eps15	**Eps**in **15**
ESCRT	**E**ndosomal **s**orting **c**omplexes **r**equired for **t**ransport
esiRNA	**E**ndoribonuclease-prepared **siRNA**
FCS	**F**etal **c**alf **s**erum
GAP	**G**TPase **a**ctivating **p**rotein

GAPDH	**G**lycer**a**ldehyde 3-**p**hosphate **d**e**h**ydrogenase
GEF	**G**uanin triphosphate **e**xchange **f**actor
GFP	**G**reen **f**luorescent **p**rotein
GOTERM	**G**ene **o**ntology **term**
GPI	**G**lycosyl**p**hosphatidyl**i**nositol
GRAF1	**G**TPase **r**egulator **a**ssociated with **f**ocal adhesion kinase-**1**
GUV	**G**iant **u**nilamellar **v**esicle
HA	**H**em**a**gglutinin
HCV	**H**epatitis **C** **v**irus
HIV-1	**H**uman **i**mmunodeficiency **v**irus **1**
hMSCs	**H**uman **m**esenchymal **s**tem **c**ell**s**
HOPS	**Ho**motypic fusion and vacuole **p**rotein **s**orting complex
HPV	**H**uman **p**apilloma **v**irus
IL2R	**I**nter**l**eukin-**2**-**r**eceptor
ILV	**I**ntra**l**uminal **v**esicle
INT	**I**ntracellular **n**anoparticle **t**ransport
Lamp	**L**ysosomal-**a**ssociated **m**embrane **p**rotein
LC3	Microtubule-associated protein 1A/1B-**l**ight **c**hain **3**
LD	**L**ipid **d**roplet
LDS	**L**ithium **d**odecyl **s**ulfate
LE	**L**ate **e**ndosome
LNP	**L**ipid **n**ano**p**article
LY	**Ly**sosome
M6PR	**M**annose-**6**-**p**hosphate-**r**eceptor
MACS	**M**agnetic **a**ctivated **c**ell **s**orting
MEP	**M**ini**e**mulsion **p**olymerization
MHC	**M**ajor **h**istocompatibility **c**omplex
MLB	**M**ulti**l**amellar **b**ody
MVB	**M**ulti**v**esicular **b**ody
n. a.	**n**ot **a**vailable
n. d.	**n**ot **d**etermined

n. s.	**n**ot **s**ignificant
nm	**n**ano**m**eter
NP	**N**ano**p**article
NPC	**N**iemann-**P**ick **d**isease, type **C**
NSF	**N**-ethylmaleimide-**s**ensitive **f**actor
NSG	**N**OD **s**cid **g**amma
OA-BSA	**O**leic **a**cid coupled **BSA**
PDMS	**P**oly**d**i**m**ethyl**s**iloxane
PEG	**P**oly**e**thylene **g**lycol
PI3K	**P**hosphatidyl**i**nositide **3**-**k**inases
PKC	**P**rotein **k**inase **C**
PLA	**P**oly**la**ctide
PLC	**P**hospho**l**ipase **C**
PLGA	**P**oly(**l**actic-co-glycolic)
PLLA	**P**oly-**L**-**La**ctide
PM	**P**lasma **m**embrane
PMA	**P**horbol **m**yristate **a**cetate
Pmel17	**P**re**mel**anosome protein **17**
PMT	**P**hoto**m**ul**t**iplier
PNP	**P**olymeric **n**ano**p**articles
ppm	**P**arts **p**er **m**illion
PS	**P**oly**s**tyrene
PTOX	**P**odophyllo**tox**in
PVDF	**P**oly**v**inyli**d**ene **f**luoride
qRT-PCR	**Q**uantitative **r**eal **t**ime **PCR**
Rab	**Ra**s-related in **b**rain
Rac1	**Ra**s-related **C**3 botulinum toxin substrate **1**
RhoA	**R**as **ho**molog family member **A**
RNAi	**RNA i**nterference
RTK	**R**eceptor **t**yrosine **k**inase
SD	**S**tandard **d**eviation

SDS	**S**odium **d**odecyl **s**ulfate
SDS-PAGE	**SDS p**oly**a**crylamide **g**el **e**lectrophoresis
shRNA	**S**mall **h**airpin **RNA**
siRNA	**S**mall **i**nterfering **RNA**
SNAP	**S**oluble **N**SF **a**ttachment **p**rotein
SNARE	**S**oluble **N**-ethylmaleimide-sensitive-factor **a**ttachment **re**ceptor
SPIONs	**S**uperparamagnetic **i**ron **o**xide **n**anoparticle**s**
SPIOPSN	**S**uper**p**aramagnetic **i**ron **o**xide **p**olystyrene **n**anoparticles
SWAP-70	**Sw**itch-**a**ssociated **p**rotein **70**
TEM	**T**ransmission **e**lectron **m**icroscopy
TGN	**T**rans-**G**olgi **n**etwork
TIP47	**T**ail-**i**nteracting **p**rotein **47**
VAMP7	**V**esicle-**a**ssociated **m**embrane **p**rotein **7**
Vps34	**V**acuolar **p**rotein **s**orting **34**
wt	**W**ild **t**ype

V. Acknowledgements

I deeply thank Prof. Dr. Katharina Landfester and PD Dr. Volker Mailänder for their great supervision throughout my thesis. I gratefully acknowledge the members of my thesis committee for their support.

Furthermore, it is a pleasure for me to express my gratitude to all the collaborators who set the basis for a successful thesis. First of all, I would like to thank Dr. Markus B. Bannwarth (MPI-P) for the fruitful discussions and the nanoparticle synthesis. Furthermore, I would like to acknowledge Dr. Stefan Tenzer (Institute of Immunology, Mainz) as a cooperative partner in respect of mass spectrometry. My thanks go to Claudia Messerschmidt and Dr. Ingo Lieberwirth for their great support in the matter of TEM measurements. Last but not least, I am much indebted to the whole (bio) group, especially, Jens-Michael, Susanne, Anita, Mela, Manuel, Marleen, Melanie, Caro, Simone, Steffi, Maria, Patricia, Sandra, Niklas, Birger, Laura, Katta, Biao and Saman for a great time at the institute and in Mainz.

Last but not least, I would like to thank my family, Lisa, friends and musicians for their support and the remarkable moments during the time.

VI. Abstract

Polymeric nanoparticles are small objects that are promising candidates for the delivery of drugs to subcellular compartments. Since nanomaterials contact biological systems in these biomedical applications, it is absolutely necessary to study their interplay with cellular components. The previous research on the nano-bio-interface already revealed a large number of diverse interactions (e. g. nanotoxicity, drug delivery mechanisms). In terms of drug delivery applications it is so far well accepted that a successful cellular delivery of drugs mainly depends on the nanoparticle uptake and a subsequent endosomal release of the cargo. Therefore, we examine (1) the drug delivery mechanism of biodegradable iron-containing poly-L-lactide nanoparticles (PLLA-Fe-PMI) and study (2) the uptake mechanisms and the intracellular trafficking pathways of nondegradable superparamagnetic iron oxide polystyrene nanoparticles (SPIOPSN).

In this study, we identify an unknown and non-invasive drug delivery mechanism. We show that the successful subcellular delivery of nanoparticulate cargo does not necessarily depend on the internalization of nanomedicines. Our findings indicate that the release of nanoparticulate cargo is simply triggered by the physicochemical interaction of hydrophobic poly-L-lactide nanoparticles with a hydrophobic surface. *In vitro*, the membrane-mediated release of nanoparticulate cargo results in its subsequent transport into $TIP47^+$ and $ADRP^+$ lipid droplets. The release mechanism ("kiss-and-run") can be blocked by the covalent attachment of the nanoparticulate cargo molecule to the polymer, highlighting the importance of material properties in drug delivery applications.

Further on, long-term studies reveal that an atypical macropinocytic mechanism mediates the uptake of PLLA-Fe-PMI and SPIOPSN. We characterize this pathway and identify several factors that influence the uptake of SPIOPSN. These include the small GTPases Rac1 and ARF1. Based on the gained knowledge about the portal of entry, we investigate the intracellular trafficking of the nanoparticles in more detail. Therefore, we dissect the intravesicular endolysosomal milieu of magnetically isolated SPIOPSN-containing vesicles by mass spectrometry. Intensive research on this project identifies markers of early endosomes, late endosomes/multivesicular bodies, $Rab11^+$ endosomes, flotillin vesicles, lysosomes and COP vesicles. Finally, we analyze the effect of the lysosomal milieu on the nanoparticulate protein corona. Here, it is shown that the nanoparticulate protein corona is cointernalized with the nanoparticle and subsequently degraded after reaching $Lamp1^+$/$Lamp2^+$ lysosomes.

These findings indicate that one has to reconsider the classical strategy of the invasive nanoparticulate drug delivery. Further on, the data show that polymeric nanoparticles underlie a macropinocytic-like uptake mechanism. This results in an intracellular trafficking of the investigated nanoparticles from macropinosomes via multivesicular bodies to lysosomes. .

VII. Deutsche Zusammenfassung

Polymere Nanopartikel sind kleine Teilchen, die vielseitige Einsatzmöglichkeiten für den Transport von Wirkstoffen bieten. Da Nanomaterialien in diesen biomedizinischen Anwendungen oft mit biologischen Systemen in Berührung kommen, erfordert das eine genaue Untersuchung ihrer gegenseitigen Wechselwirkungen. In diesem speziellen Forschungsgebiet, welches sich auf die Interaktionen von Nanomaterialien mit biologischen Komponenten konzentriert, wurde bereits eine Vielzahl verschiedener Nanopartikel-Zell-Interaktionen (z. B. Nanotoxizität, Wirkstofftransport-mechanismen) analysiert. Bezüglich der Untersuchungen zu nanopartikulären Wirkstofftransport-mechanismen ist es im Allgemeinen akzeptiert, dass ein erfolgreicher zellulärer Transport hauptsächlich von der Aufnahme des Nanotransporters abhängt. Deshalb analysieren wir in dieser Arbeit (1) den Wirkstofftransportmechanismus für biologisch-abbaubare eisenhaltige Poly-L-Milchsäure Nanopartikel (PLLA-Fe-PMI) sowie (2) die Aufnahmemechanismen und die intrazellulären Transportwege von nicht-abbaubaren superparamagnetischen Polystyrolnanopartikeln (SPIOPSN).

In dieser Arbeit identifizieren wir einen bisher unbekannten und nicht-invasiven Wirkstoff-transportmechanismus. Dabei zeigt diese Studie, dass der subzelluläre Transport der nanopartikulärer Fracht nicht unbedingt von einer Aufnahme der Nanotransporter abhängt. Der identifizierte Arzneimitteltransportmechanismus basiert auf einem einfachen physikochemischen Kontakt des hydrophoben Poly-L-Milchsäure-Nanopartikels mit einer hydrophoben Oberfläche, wodurch die Freisetzung der nanopartikulären Fracht ausgelöst wird. In Zellexperimenten führt die membranvermittelte Freisetzung der nanopartikulären Fracht zu ihrem sofortigen Transport in $TIP47^+$- und $ADRP^+$- Lipidtröpfchen. Der Freisetzungsmechanismus („kiss-and-run") kann durch die kovalente Einbindung des Frachtmoleküls in das Polymer des Nanopartikels blockiert werden.

Weiterhin wird in Langzeitversuchen gezeigt, dass die Aufnahme der untersuchten polymeren Nanopartikel von einem Makropinozytose-ähnlichen Mechanismus gesteuert wird. Im Laufe dieser Arbeit werden mehrere Faktoren identifiziert, die in diesem Aufnahmemechanismus eine Rolle spielen. Darunter fallen unter anderem die kleinen GTPasen Rac1 und ARF1, die die Aufnahme von SPIOPSN beeinflussen. Darauffolgend werden die intrazellulären Transportwege der Nanopartikel untersucht. Mit Hilfe eines neuartigen Massenspektrometrieansatzes wird der intrazelluläre Transport von nanopartikelhaltigen endozytotischen Vesikeln rekonstruiert. Intensive Untersuchungen identifizieren Marker von frühen Endosomen, späten Endosomen/ multivesikulären Körpern, $Rab11^+$-Endosomen, Flotillin-Vesikeln, Lysosomen und COP-Vesikeln. Schließlich wird der Einfluss des lysosomalen Milieus auf die Proteinhülle der Nanopartikel untersucht. Hier wird gezeigt, dass die adsorbierte Proteinhülle auf den Nanopartikeln in die Zelle transportiert wird und anschließend im Lysosom abgebaut wird.

Insgesamt verdeutlicht diese Arbeit, dass die klassische Strategie des nanopartikulären und invasiven Wirkstofftransportmechanismuses überdacht werden muss. Weiterhin lässt sich aus den Daten schlussfolgern, dass polymere Nanopartikel einem atypischen Makropinozytose-ähnlichen Aufnahmemechanismus unterliegen. Dies resultiert in einem intrazellulären Transport der Nanopartikel von Makropinosomen über multivesikuläre Körperchen zu Lysosomen.

"Imagination is more important than knowledge."

Albert Einstein

1. Introduction to nanobiotechnology

Nanobiotechnology is a rapidly growing field with a large number of newly synthesized materials that have already been implemented in our daily life. The omnipresence of these nanomaterials raises several issues about nanosafety and the likelihood of interactions with biological systems (1). Especially, their administration in biomedical applications places high demands on the quality and safety of such nanomaterials. Fortunately, there is a way to achieve these high requirements. The improvement of nanoparticles mainly profits from the huge variety of possible synthesis protocols that can be applied to properly adapt nanomaterials for the desired applications. The tremendous number of synthesis routes provides a huge freedom to vary fundamental features such as drug release efficiency, blood circulation half-life or the size of the nanomaterial (1). However, the manifoldness of the diverse materials challenges life scientists to obtain a detailed view about nano-bio-interactions (1). To guarantee safe nanoproducts in the future, it is therefore absolutely necessary to gain knowledge about nano-bio-interactions. These include i. a. nanoparticulate cytotoxicity, cellular uptake mechanisms, their environmental disposition and nanoparticle-membrane interactions.

One of the primary goals in biomedical nanotechnology is to understand these interactions and to exploit them also for the development of novel drug delivery systems. A major hallmark of these systems is that the nanoparticulate matrix serves as a protective carrier for the encapsulated hydrophobic or hydrophilic effector molecules shielding them from environmental degradation (2). The first attempts to design drug delivery systems range back into the 1980s, where scientists already synthesized pH-responsive liposomes for the delivery of drugs (3). Nowadays, these applications are highly customized for *in vivo* studies even applying lipid nanoparticles for a tissue-specific silencing of proteins (4). Besides, also non-lipidic formulations are in the spotlight. At least since the FDA approval of the albumin-based nanocarrier Abraxane® for breast cancer treatment, one has to realize the huge financial interest behind drug delivery systems (5). However, not only the industry but also the scientific community starts to gain deep knowledge about interaction of nanoparticles with cellular systems and even with complete organisms (6). Especially in the field of nanoparticle-membrane interactions and intracellular trafficking mechanisms of nanoparticles, a large progress has been made. The scientific world starts to realize that the understanding of these interactions is a major prerequisite for an efficient design of nanocarriers for future applications. Taking all of this into account, it is realistic to assume that nanocarriers someday might play an indispensable role in biomedical applications.

1.1 Nanomaterials – Synthesis of polymeric nanoparticles

Polymeric nanospheres are frequently defined as colloidal particles in a size range of 10-1000 nm (7, 8). They are subgrouped into two major classes termed as nanocapsules and nanoparticles.

Nanocapsules are hollow-body spheres with a solid material shell that allow the encapsulation of distinct hydrophobic or hydrophilic molecules inside the lumen (9, 10). In contrast, polymeric nanoparticles (PNPs) are solid full-body particles. Distinct desired molecules may be adsorbed to their surface or encapsulated within the polymeric matrix (6). Depending on the synthesized particle, PNPs are either generated from presynthesized polymers or by direct polymerization (8). To obtain particles by direct polymerization, techniques such as miniemulsion or microemulsion are utilized (11). Miniemulsion polymerization (MEP) is a popular technique to synthesize a large number of stable and monodisperse nanospheres (12). MEP provides a broad platform to generate nanospheres with different reaction types (e. g. polyaddition, polycondensation, anionic/cationic polymerization, catalytic polymerization) and empowers to control parameters like size, surface functionalization or cargo loading (11).

Radical miniemulsion polymerization

During the process of radical MEP, a system of at least two immiscible phases is combined (Figure 1A). In oil-and-water (o/w) miniemulsion, the continuous phase consists of demineralized water with a stabilizing ionic or steric surfactant. The dispersed phase contains the monomer or the dissolved polymer, the polymerization initiator and an ultrahydrophobic substance (13). In the first step, mechanical stirring of the two immiscible phases generates a temporary macroemulsion. To create a stable miniemulsion with smaller and homogeneously size-distributed droplets, the dispersion is exposed to high shear forces using ultrasonication. The terminal step of the radical MEP is the polymerization of the monomer. A chain reaction is initiated polymerizing the monomeric core of the nanodroplet. This results in the formation of solid and surfactant-stabilized nanoparticles (11).

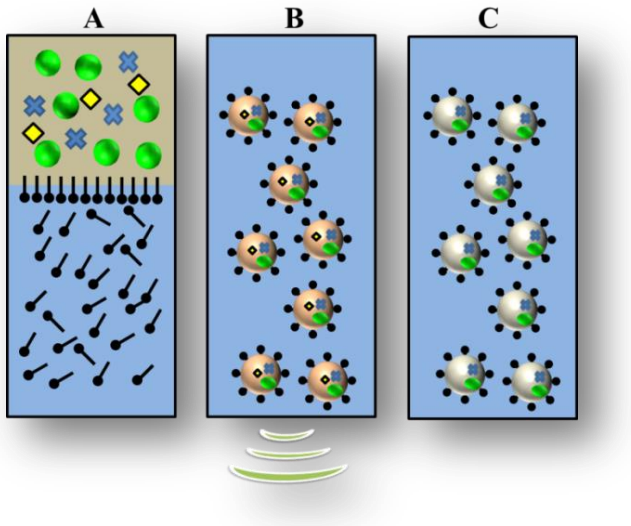

Figure 1: Radical miniemulsion polymerization. (A) Formulation of two immiscible phases. (B) Generation of a stable miniemulsion by mechanical stirring and ultrasound. (C) Radical polymerization of monomers or solvent evaporation for preformed polymers results in the formation of solid nanoparticles. The synthesis of particles inside an emulsion is critical, since particle formation predominantly depends on multiple factors like the surfactant concentration or the applied monomer/polymer.

Other routes of synthesis are performed for nanoparticles consisting of preformed polymers (e. g. PLA nanoparticles) (14). The synthesis of those nanoparticles utilizes the solvent evaporation technique to form particles. In this particular case, the polymer is first dissolved in the dispersed phase. Evaporation of the solvent leads to the precipitation of the polymer inside the droplet. Finally, solid and tenside-stabilized nanoparticles are obtained (11).

1.1.1 Forces inside the nanodroplet

In a nonpolymerized miniemulsion, mechanisms such as Ostwald ripening and coalescence extensively influence the stability of the dispersion (15). Both phenomenon are ascribed to the imbalance between the two major droplet forces – the external LaPlace pressure ($p_{LaPlace}$) and the internal osmotic pressure (p_{osm}) (16). $p_{LaPlace}$ is calculated from the Young-LaPlace equation and describes the pressure difference between the inner and outer interface of the droplet. Here it is to mention that a decrease of the droplet size results in an increased $p_{LaPlace}$ (17). During droplet formation, $p_{LaPlace}$ drives the monomer transdiffusion through the aqueous phase ("Ostwald ripening") (15). Ostwald ripening occurs in polydisperse emulsions and describes a process, where the total surface free energy of an emulsion is decreased owing to the reorganization of monomers from smaller to larger droplets. Notably, the process of Ostwald ripening can be suppressed by the increase of p_{osm}. This is achieved by the incorporation of low-water-soluble monomers (solubility < 10^{-5} g L^{-1}) or by the addition of an ultrahydrophobe (e. g. hexadecane) into the droplets. Nonetheless, not only Ostwald ripening alters the size distribution of nanoparticle dispersions. Also collisions between two encountering droplets ("coalescence") affect the average size distribution of nanoparticle dispersions. Coalescence can be suppressed by surfactants on the surface of the nanodroplet.

1.1.2 Stabilization of nanoparticles in biological fluids

Efficient stabilization of particles is necessary to avoid their aggregation in biological experiments. The colloidal stability of nanoparticles is thereby either obtained by ionic factors or steric stabilizers (18, 19). Steric stabilization can be achieved by the assembly of small particles on larger particles called pickering emulsion (18). Other approaches use long polymer chains that are adsorbed or covalently linked to the particle surface (18). In this particular case, the stability of the particle is mediated by the strong interaction of the chains with the continuous phase. With the proper solvent, the entropy of the polymer chains is reduced due to away-stretching of the chains from the particle by solvent influx into the chain matrix. Thereby, chain movements are restricted to a minimum resulting in a repulsion of the particle from others (20). The higher the density of stabilizing polymer chains is, the higher is the conformational order and the longer is the range of repulsion (21). Though, steric stabilization is not always convertible to all nanoparticle systems. Therefore, it has to be noticed that simple ionic surface charges are frequently applied to stabilize nanoparticles by repulsive forces.

Stability of nanoparticles in biological media

In general, colloidal stability is calculated by the total interaction potential of the sum of the repulsive electrostatic interaction energy (V_E) and the attractive van der Waals energy (V_A) (22). Electrostatic interactions decrease with an increased distance between the encountering nanoparticles while van der Waals forces act proportional to V_E (Figure 2). Consequently, the total interaction energy depicts two minima and a single maximum. The maximum is the energy barrier v_{max} that is needed to prevent coagulation (22). Irreversible aggregation occurs, when the repulsive forces are too weak to preserve v_{max}. Especially i*n vitro* and *in vivo*, the ionic strength of the media has a major effect on the aggregation of nanoparticles. Biological media often have an ionic strength of above 150 mM, which results in the screening of the nanoparticulate repulsive forces. Moreover, the impact of van der Waals forces are diminished (1). It is also worth to mention that the interplay of particles with proteins are crucial for their steric stability inside biological media (23).

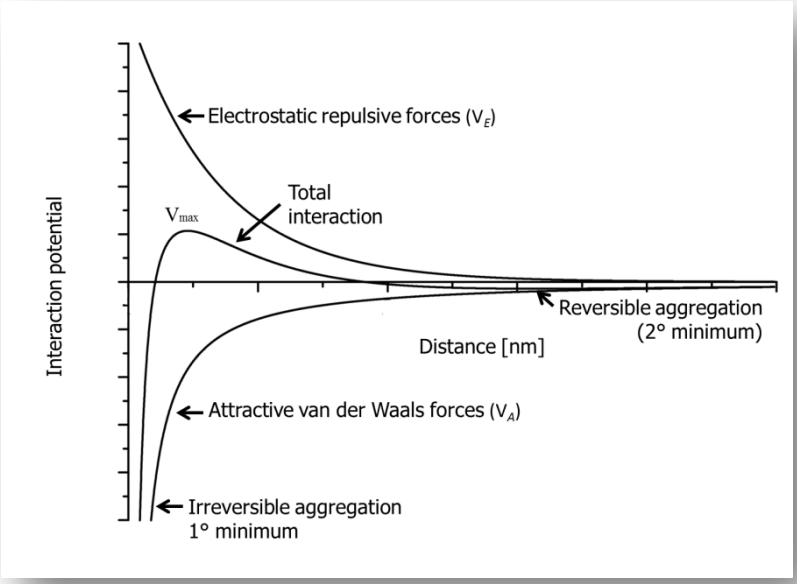

Figure 2: Interaction forces between two encountering nanoparticles over a short distance. The secondary minimum describes the temporarily more powerful van der Waals forces in a long distance range between nanoparticles. In this distance range, the attractive forces between the particles are too weak for a permanent aggregation. The secondary minimum defines the state, where v_{max} was overcome. Irreversible particle aggregation occurs (basic figure obtained from C. Weiß, MPI-P, Mainz).

After the addition of nanoparticles into serum, the nanoparticle surface is covered by over one hundred adsorbed serum proteins (24, 25). Nanoparticulate surface molecules are screened by proteins that massively influence several features in respect of nanoparticulate surface charge, size and colloidal stability (26). However, different studies suggest that adsorbed proteins can also positively act as steric stabilization for nanoparticles preventing their aggregation (23). Technically, the amount of protein adsorption on nanoparticles is well controllable by the application of steric stabilizers on the nanoparticle. Previous studies reveal that the modification by polyethyleneglycol (PEG) is also known

as a promising candidate to suppress the formation of a protein corona (20, 27). In summary, this shows that the stabilization of nanoparticles is an important topic for biomedical applications. Colloidal stability needs to be guaranteed to perform reliable studies *in vitro* and *in vivo* with nonaggregated nanoparticles.

1.1.3 Biodegradable poly-L-lactide nanoparticles

Several investigations demonstrate the synthesis of nanoparticles from preformed polymers like polycyanoacrylate or poly-L-lactide (PLLA) by solvent evaporation (6, 28, 29). Polylactide (PLA) is indispensable in tissue engineering and drug delivery applications owing to their high biocompatibility (30). The ester bonds inside PLLA are hydrolytically cleavable by deesterification (31). Enzymes inside the acidic environment of the endolysosomal system degrade PLLA and generate the non-toxic product lactic acid (31). Subsequently, lactic acid can be easily removed by the organism (e. g. by citric acid cycle). However, it is worth to mention that the efficient degradation of the particles depends on several parameters including the molecular structure of the polymer, environmental conditions, crystallinity, chain orientation or the presence of co-polymers (32). A study of Gonzalez *et al.* showed that degradation of low molecular weight PLA microspheres takes more than eight month under *in vitro* conditions displaying the robust features of PLA (33). In spite of this, the biocompatibility and the high efficiency for cargo loading predestinates PLA nanoparticles as a serious candidate for drug delivery (6). In this work, we use the L enantiomer of the saturated poly-α-hydroxy ester to form iron oxide loaded PLLA-Fe-PMI nanoparticles.

1.1.4 Superparamagnetic iron oxide nanoparticles

For biological applications, superparamagnetic iron oxide nanoparticles (SPIONs) are frequently composed of biocompatible magnetite or its oxidized form maghemite (34). These SPIONs can be embedded in a polystyrene or a poly-L-lactide matrix using a multistep protocol (6, 35, 36). In the first step of synthesis, magnetic nanoparticles are formed in a dispersion of oleic acid (35). In a second miniemulsion process, the stabilized magnetic nanoparticles are used as seeds for the polymeric matrix to form hybrid particles (37). Notably, these nanoparticles behave superparamagnetic (37). When a magnetic field is applied to the nanoparticles, the magnetic moment of all unpaired electrons is oriented in a single direction while the accuracy of orientation increases with the strength of the external magnetic field (38, 39). Owing to their superparamagnetic features, neighboring nanoparticles interact with each other and self-assemble in a single orientation (37). When the magnetic field is removed, the unpaired electrons disorient again, which results in the loss of their magnetic properties. The applications for these SPIONs are diverse. SPIONs can be used for cell separation, sample enrichment (e. g. organelle isolation) or as contrast agents in magnetic resonance imaging (40, 41). Other fields of applications deal with magnetic drug targeting, where ligands or effectors (e. g. viruses,

siRNA, Doxorubicin) are coupled to a particle (42). Nanoparticles are then intravenously applied to the organism. Accumulation of nanoparticles is achieved by placing a magnetic field besides the area of interest (43). However, the fate of such SPIONs is not clarified in detail. Especially, the interaction with membranes after their application remains less investigated.

1.1.5 Nanoparticle-membrane interactions

Cell membranes and artificial membranes either consist of lipids or polymers that self-assemble to ordered structures owing to their amphiphilic nature (44). The structure of a typical lipid can be described as two fatty acid chains that are linked by ester or acyl bonds to distinct backbones. In the case of phospholipids, the hydrophilic head is attracted to the water phase while the hydrophobic tail is repelled by the water (45). After self-assembly, the noncovalent interactions of the hydrophilic parts stabilize the membranes still guaranteeing a fluidic and floating system (46). These dynamics are even more complicated in cell membranes of mammalian cells. The interplay with embedded biomolecules and the large diversity of distinct types of lipids hamper the predictions e. g. of membrane dynamics. Exactly due to this reason, investigations of nano-membrane-interaction are frequently performed with artificial membrane models. Polymersomes or giant unilamellar vesicles represent a minimal system for investigations to study the different potential effects of nanoparticles on membranes (6, 47-50).

Direct interactions of nanoparticles and membranes trigger membrane deformations

In general, nanoparticle-membrane interactions lead to chain stretching of lipids, curvature of membranes and changes in the membranous lipid packing (51-53). This results in a different membrane organization. Especially i*n vitro,* deformation of the bilayer may trigger cytotoxic effects (54). Nanoparticles were shown to increase the porosity of membranes after their intense interaction (55). Membrane thinning or membrane hole formation is induced by several nanoparticles resulting in the disruption of the membrane (55). Here, it is worth to mention that factors like particle size and hydrophobicity of the nanomaterials have an impact on membrane morphology. Hydrophilic nanoparticles smaller than 8 nm are embedded into membranes to reach a thermodynamically more favorable configuration (56). Other silica nanoparticles larger than 22 nm were found to induce an almost complete membrane wrapping around the particle (55). It was also shown that interacting nanoparticles induce the in-curving of the membrane, while noninteracting nanoparticles may be repelled from the surface leading to an out-curving of the membrane (57). Up to now, the imaging of such nanoparticle-membrane interaction is very limited due to technical reasons. However, Welsher and colleagues recently recorded a high resolution movie of a temporary nanoparticles-membrane interaction that can be described as a “kiss-and-run” mechanism (58). This shows that nanoparticles are not necessarily needed to permanently interact with membranes to be taken up. In summary, all of these observations shape a picture of nano-membrane-interactions and pave the way to understand distinct applications (6).

1.1.6 Polymeric nanoparticle based drug delivery

Since the regular application of drugs is commonly systemic, the transport of effectors to the site of action is often less than ideal. The cargo might degrade by hydrolysis, undergo unspecific interactions with healthy tissues or can be excreted via the biliar system (59). As a promising alternative, nanoparticle-based drug delivery could circumvent these issues. The proper design of nanoparticles can protect the cargo from degradation and assists in an efficient drug delivery due to their targeting properties. In these particular applications, micelles, dendrimers, liposomal formulations and a large number of different nanoparticles serve as carriers to deliver e. g. siRNA or anti-cancer drugs to the area of interest (60). Active targeting mechanisms (e. g. "enhanced permeation and retention effect") additionally provide the more effective accumulation of nanospheres inside e. g. solid tumors (61).

1.1.6.1 Passive and active targeting of nanoparticles

A fundamental advantage in the treatment of solid tumors is the defective vascular architecture created by the rapid and uncontrolled growth of blood vessels inside the abnormal tissue (62). Combined with a poor lymphatic drainage, nanomaterials passively accumulate inside the cancer tissue in consequence of the EPR effect (63). In addition, an antigen-dependent targeting can be achieved by the specific binding of nanoparticles to pathological surface proteins. It is worth to mention that cancer cells overexpress particular antigens on their cell membrane. With the selection of the proper binding partner, nanoparticle accumulation can be increased by their specific targeting to the cell of interest (64). This predestines nanoparticles as ideal candidates for the targeting of cancer cells, if the target molecule is not significantly expressed in other parts of the body (65).

In the past, several investigations confirmed the functionality of active targeting concepts. Dinauer *et al.* investigated an antigen-dependent targeting of T cells by anti-CD3-conjugated nanoparticles (66). They could show that these antibody-functionalized nanoparticles specifically bind to the CD3 receptor, which induces an internalization of the nanospheres (66). Other approaches functionalize nanoparticles with DC-SIGN antibodies that bind this receptor on dendritic cells (67). Besides biomolecules, also synthetic molecules can serve for cell specific targeting applications (68). PLGA nanoparticles can be functionalized with prostate-specific-membrane-antigen-targeting aptamers (69). The authors demonstrate an efficient and cell specific delivery of the antitumor agent cisplatin to human prostate cancer cells (69).

However, the design of nanoparticles for active targeting is challenging. The major prerequisites for these applications are that the targeted antigen needs to be well accessible to the nanoparticles and displays a high endocytic internalization rate. Unspecific uptake via bulk endocytosis has to be minimized to prevent unspecific delivery to other types of cells (70). Finally, the interaction of serum proteins with nanoparticles may change their specific binding properties to the target molecule (25). Previous reports suggest that the functionality of transferrin-functionalized nanoparticles is screened

by the protein corona, thereby losing their target-specificity (26, 71). A solution for this could be provided by novel innovative synthesis methods. Here, the targeting molecule is attached via a spacer to the nanoparticle to circumvent the shielding effects of the protein corona (72). This approach could set the basis for a successful targeted delivery.

1.1.6.2 Non-targeted nanoparticle uptake and controlled cargo release

A large number of studies investigate the nonspecific uptake mechanisms of nanoparticles (73, 74). These studies mainly examine nontargeting nanoparticles with an encapsulated cargo to examine the intracellular drug release in cell culture models (75, 76). Notably, these release mechanisms are highly diverse (2). Cargo release either occurs by simple drug leakage from the particle matrix or by a disassembly of the nanomaterial (76). However, after cargo release, the effector molecules are often trapped inside endosomes while the target location is frequently found in the cytoplasm. To deliver the cargo more efficiently to the proper subcellular compartment, an efficient endosomal release mechanism is required.

Endosomal-to-cytoplasmic release either occurs via the membranous diffusion of the payload into the cytosol or by the destruction/deformation of the endosomal membrane. It was demonstrated that the decoration of nanoparticles with cell-penetrating peptides (CPP) results in an endosomal-to-cytoplasmic transfer of the nanocarriers (77). GALA peptides and even other peptides induce a membrane destabilization exclusively inside the acidic environment of the endolysosome (2, 78). In accordance to the approach to exploit endolysosomal pH changes for cargo release, also other applications have been demonstrated (79). Endosomolytic polymers with primary and/or tertiary amines destabilize the endolysosomal milieu by proton-binding (“proton sponge effect”) (80). These amines become protonated at an acidic pH (e. g. in the lysosome), which induce a vesicular influx of protons. Thereby, osmotic swelling and disruption of the endosome occurs (81).

Notably, not only intracellular triggers but also extracellular stimuli are utilized for the controlled nanoparticulate cargo release into the cytosol. Bräuchle and colleagues demonstrate a photochemical rupture of the endosomes. Afterwards, a disulfide-bound dye molecule is activated inside the reducing conditions of the cytoplasm displaying an exposure of the nanoparticulate cargo to the cytosolic milieu (75). Further investigations reveal a near-infrared light-mediated release of photocaged siRNA from silica-coated upconversion nanoparticles into the cytosol (82). Taking all of this into account, a successful passive targeting and cargo release mainly depends on the design of the nanomaterial and the strategy of release. Further on, uptake routes and the intracellular trafficking of cargo can orchestrate the effective delivery of nanoparticle (4, 83, 84).

1.2 Uptake mechanisms of nanoparticulate systems

Cells use endocytosis for a vast number of central processes. Uptake of extracellular nutrients and macromolecules as well as the surface expression of receptors/lipids is orchestrated by the endocytic system. Endocytosis is even indispensable for processes of cell adhesion and signal transduction (85). Moreover, these mechanisms serve as entry portals for pathogens or particles to gain access to the interior of a cell. Thereby, they exploit a large number of different pathways (86) (Figure 3). Here, clathrin-mediated endocytosis (CME) is undoubtedly the best studied mechanism of endocytosis (87). Other clathrin-independent pathways are caveolae-dependent endocytosis, RhoA-mediated endocytosis, Arf6-mediated entry, flotillin-orchestrated uptake as well as the CLIC/GEEC pathway (clathrin-independent carriers and GPI-enriched endocytic compartments) (85, 88-93). The bulk uptake of large volumes of extracellular fluids and particles is mainly mediated by (macro)pinocytic and phagocytic mechanisms (94, 95).

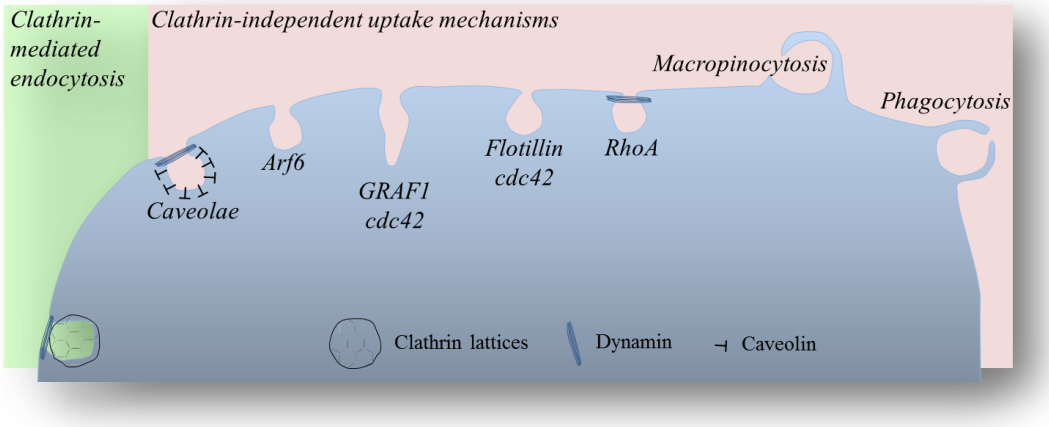

Figure 3: Overview of the major endocytic pathways in mammalian cells. Modified from (85, 93, 96).

1.2.1 Clathrin- and caveolae-mediated endocytosis

Clathrin-mediated endocytosis (CME) is required for the internalization of surface molecules such as transferrin receptors, receptor tyrosine kinases or G-protein coupled receptors (97). Further on, cargoes such as cholera toxin B subunit or nanoparticles have been shown to utilize clathrin-mediated pathways (98, 99). The initial process of CME is accompanied by the assembly of cytoplasmic clathrin at regions of the plasma membrane (PM) called clathrin-coated pits (CCPs) (100). After the invagination of CCPs, the vesicles are pinched off from the PM to form clathrin-coated vesicles (CCVs) (101). The molecular signaling on CCVs is mainly mediated by proteins of the adaptor complex (102). These adaptor proteins interact with a variety of other regulatory proteins (e. g. AP180 and epsin) that influence pit assembly, vesicle budding and cytoskeleton interactions (87, 103).

One regulatory protein that is involved in clathrin lattice rearrangement is epsin 15, which interacts with clathrin via the adaptor protein 2 (104, 105). In general, epsins act as scaffolding proteins that

generate a curved and three dimensional amphiphatic helix for the assembly of clathrin baskets (87). Therefore, it is not surprising that the overexpression of the dominant negative mutant epsin 15 (DIII) suppresses the formation of clathrin-coated pits (104, 106). This shows that the associated regulatory proteins seem to have an important effect on CME. This also affects the regulatory protein AP180 (103). Zhao and colleagues found that the overexpression of AP180 reduces clathrin accumulations on the plasma membrane. This provides information that AP180 is an important organizer in CME (103). Altogether, it is worth to mention that CME is a well understood endocytic pathway. CME as well as caveolae-mediated endocytosis are potential entry pathways of nanoparticles that necessarily have to be studied in detail.

Caveolae-mediated endocytosis

Caveolae are 50 - 80 nm large plasma membrane invaginations that orchestrate a clathrin-independent endocytic pathway (107). On a structural level, caveolae are composed of cholesterol, several sphingolipids, GPI-anchored proteins and the integral membrane proteins caveolin-1 and caveolin-2 (108, 109). Caveolin-1 acts as the major organizing unit into which caveolin-2 is migrating (110, 111). This was shown with two experiments. The first experiment reveals that the stable expression of caveolin-1 in caveolae-deficient K562 cells induces the upregulation and recruitment of caveolin-2. Then, Parolini and colleagues showed a direct binding of both proteins to each other providing information about two necessary markers for the detection of caveolae at the PM (111). Originally, caveolae-mediated endocytosis was described as an entry mechanism of SV40 viruses (112). However, also other small particles with a size of $\leq$ 100 nm have been shown to utilize caveolae-mediated pathways (113, 114). The terminal uptake of such nanoparticles is then conducted by the pinch off of the vesicles from the PM. The scission of vesicles in caveolae- as well as in clathrin-mediated uptake is regulated by dynamin.

1.2.2 Dynamin in clathrin- and caveolae-mediated endocytosis

Dynamin is a GTPase that is recruited to CCPs and caveolae during the endocytic process (115, 116). The protein assists in the scission of vesicles from the plasma membrane after its slow accumulation around the growing pit (117). Originally, the relevance of dynamin for endocytosis was shown in experiments, where the overexpression of dominant negative Dyn2-K44A results in the inhibition of clathrin- and caveolae-mediated endocytosis (118). Morphologically, dynamin inhibition arrests endocytosis at a stage, where vesicles are trapped as tubular structures at the PM (116, 119). This results in an accumulation of non-budded vesicles (116). Altogether, this reveals a clear role for dynamin inside the two best characterized endocytic pathways. However, it is worth to mention that dynamin is also located inside membrane ruffles or podosomes (120, 121). These observations revive the discussions, whether dynamin exclusively acts in CME and caveolae-mediated endocytosis or also plays a role in other endocytic mechanisms (122).

1.2.3 Clathrin and caveolae-independent mechanisms

Nowadays, lively discussions raise issues about the presence of other less characterized endocytic pathways. In this research field, the literature provides a wide range of clathrin- and caveolae-independent mechanisms (85). Though, the strict discrimination between these pathways is sometimes challenging since functional overlaps have partially been observed (88, 90). This rigorous classification is also hampered by the large number of investigated cargoes including viruses, toxins, GPI-linked proteins, interleukin receptors or other cargoes. However, the commonly accepted clathrin-, caveolae- and macropinocytosis-independent pathways are RhoA-mediated uptake, CLIC/GEEC pathways and flotillin-mediated endocytosis.

1.2.3.1 RhoA-mediated uptake

One clathrin-independent but dynamin-dependent pathway is specifically regulated by the small GTPase RhoA (91, 107, 123). This pathway was first discovered in a study that investigated the internalization of the β-chain of the interleukin-2 receptor (IL-2Rβ) (107, 124). It was shown that neither dominant negative epsin 15 nor AP180 overexpression affected the uptake of IL-2Rβ (124). Clathrin-independency was further supported by the criterion that IL-2Rβ uptake is orchestrated by Rac1, PAK1 and PAK2 (123). These factors are not functional in CME. However, observations have shown that the overexpression of constitutively active RhoA can inhibit CME (124). Despite of this, a direct interaction of CME and RhoA is unlikely (85). Altogether, RhoA acts in a clathrin-independent pathway by the modulation of the actin cytoskeleton, thereby probably regulating a large number of other processes (125).

1.2.3.2 CLIC/GEEC pathway

A further clathrin- and caveolae-independent mechanism is represented by the CLIC/GEEC pathway (90). This entry mechanism orchestrates the internalization of glycosylphosphatidylinositol-anchored proteins, extracellular fluids and certain bacterial exotoxins (90). Morphologically, the CLIC/GEEC pathway is characterized by its ~ 40 nm wide tubular invaginations that are decorated with GTPase regulator associated with focal adhesion kinase-1 (GRAF1) and phosphatidylinositol-4,5-bisphosphate 3-kinase (126). These membrane carriers are relatively devoid of caveolin-1 and flotillin-1 but are regulated by cdc42 and ARF1 (90, 95, 126-128). Interestingly, the internalized GPI-linked proteins can bypass conventional $Rab5^+$ endocytic compartments raising questions of novel early endocytic compartments (85). Indeed, GPI-anchored proteins are directly transported to early endocytic vesicles termed as GPI-AP-enriched early endosomal compartment (GEEC). Altogether, these observations provide information about a pathway of fluid phase endocytosis that has to be taken into account, when investigating nanoparticle uptake.

1.2.3.3 Flotillin-mediated endocytosis

Flotillins are membrane proteins with a high homology to caveolin-1 that cluster as organized domains inside the PM (129). In 2006, flotillin-1 was originally described as a protein that mediates the entry of ctxB and the GPI-anchored protein CD59 (88). The authors show that flotillin domains pinch off from the PM in a clathrin-independent manner. After internalization, flotillins are present inside multivesicular bodies and even show a close association to other endosomal processes (130, 131). Flotillins have been suggested to be necessary for the Niemann-Pick-C1-like 1-mediated cholesterol uptake inside endosomes (130). It was shown that the knockdown of flotillins significantly attenuates the internalization of cholesterol and the endocytosis of NPC1L1 (130). These observations could bridge the gap for flotillin in nanoparticle uptake. Indeed, previous studies with polyplexes and silica nanoparticles showed a participation of flotillin in nanoparticle internalization (132, 133). All of these points propose a versatile but important role for flotillin in endocytic processes that have to be considered in the analysis of nanoparticle entry and trafficking.

1.2.4 Macropinocytosis

Classical macropinocytosis is a clathrin-, caveolae- and dynamin-independent process that occurs spontaneously or can be initiated by e. g. a transient activation of receptor tyrosine kinases (Figure 4 and Figure 5) (134). During macropinocytosis, large volumes of fluids and extracellular objects are internalized via macropinosomes (135, 136). Morphologically, macropinocytosis can be characterized by ruffle formation and the internalization of classical fluid phase markers (e. g. HRP, dextran) (137). This process of internalization is orchestrated by several small GTPases such as Ras, Cdc42 and Rac1 (138, 139). The early steps in macropinocytic signaling depend on the Ras/Cdc42/Rac1- or PI3K-mediated activation of different kinases such as p21-activated kinase 1 (PAK1) (136). Active PAK1 induces actin polymerization and lamellipodia formation (137). In the terminal step of macropinocytosis, PAK1 facilitates the closure of the macropinosomes by activating the carboxy-terminal-binding protein-1/brefeldin A-ADP ribosylated substrate (CtBP-1/BARS) (135, 140).

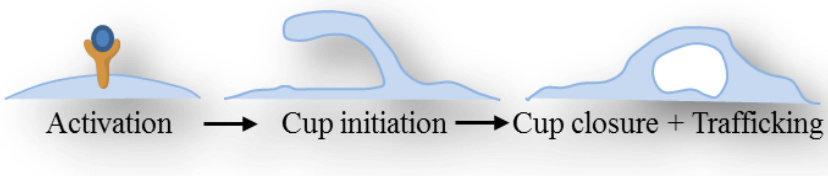

Figure 4: Major stages in receptor-mediated macropinocytosis.

Other factors that influence classical macropinocytosis

Considering the interactions of small GTPases on actin remodeling, it is not surprising that Rah/Rab34 has been associated with macropinosome formation (141). Other studies describe the impact of Rab5 and Rabankyrin-5 on the macropinocytic activity of fibroblasts and epithelial cells (142). While overexpression of Rabankyrin-5 increases the macropinocytic activity of the cells, an RNAi-mediated downregulation of Rabankyrin-5 diminishes the internalization rate of fluid phase markers and lipid nanoparticles (4, 142). The diversity of action mechanisms is also highlighted by the studies that implicate the kinases PLCγ, PKC and Src as factors for membrane ruffling (140, 143, 144). Besides, the ADP-ribosylation factor Arf6 was shown to alter membrane protrusions (145). Altogether, these studies connect a large number of factors to macropinocytic signaling events. With regards to actin rearrangements, small GTPases and several kinases seem to have major impacts on the macropinocytic activity of a cell and are the major targets during the investigations of nanoparticle uptake (Figure 5).

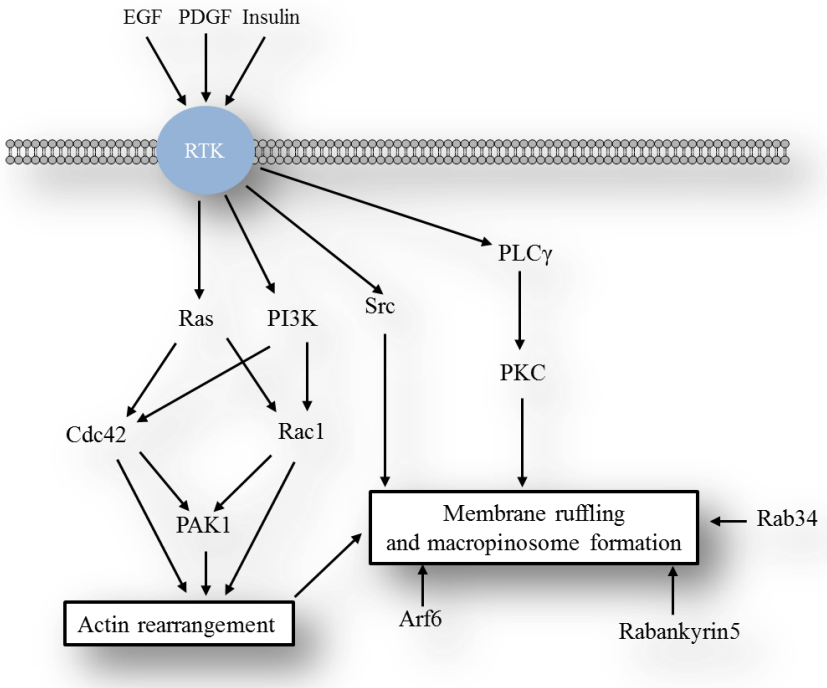

Figure 5: Overview of the general macropinocytic signaling pathways. Macropinocytosis occurs spontaneously or is triggered by a growth factor-mediated activation of receptor tyrosine kinases (RTKs). Several small GTPases and kinases facilitate the signalling cascade resulting in actin modulation. Actin reorganization induces the formation of the macropinocytic cup. Modified from (140, 146).

Macropinocytosis-like mechanisms

Classical macropinocytosis is primarily reliant on the previously described criteria. However, it is worth to mention that also atypical macropinocytic-like mechanisms have been observed in many studies (140, 147, 148). Macropinocytic-like mechanisms depend on parameters that are normally not

considered in fluid phase endocytosis or lack in comparison to classical macropinocytosis (140). In the field of virology, a large number of different atypical macropinocytic types have been well studied (140). Mulherkar *et al.* investigated a dynamin2-dependent macropinocytic entry of Ebola virus glycoprotein. Since dynamin has never been implicated in classical macropinocytosis so far, this mechanism can be considered as a macropinocytic-like pathway (148). Other groups reported an F-actin and cholesterol-dependent, but an atypical pH-independent uptake of human cytomegalovirus into dendritic cells (149). Another case of macropinocytic-like entry was published for human papilloma virus type 16 (150). Entry and infection relies on the major hallmarks of classical macropinocytosis but does not depend on Rho GTPases which are major key players in macropinocytosis. In the field of nanotechnology, macropinocytic-like uptake mechanisms have hardly been investigated. However, a study of Iversen *et al*. focused on several criteria of classical macropinocytosis during quantum dot uptake. They found that ricin-conjugated quantum dots are internalized via a dynamin-dependent macropinocytic-like pathway that was not described before (147). Taken together, atypical macropinocytic-like uptake mechanisms are not only relevant in virology but can also be an issue in the investigation of nanoparticulate entry and intracellular nanoparticle trafficking.

1.3 From early endocytic compartments to lysosomes – intracellular trafficking of nanomaterials

As described in the former chapters, nanoparticles utilize different endocytic mechanisms for their cellular entry (93, 96). After their internalization, nanoparticles are transported along a specific endocytic route (83, 151, 152). The process of intracellular nanoparticle trafficking (INT) is very dynamic in record to the proteomic environment on the endocytic vesicles. During INT, important adaptor and effector proteins are recruited or exchanged on the vesicles´ surface (153). It is important to mention that homotypic/heterotypic fusion of vesicles and vesicular maturation processes can alter the protein composition on a nanoparticle-containing vesicle (153, 154). This already happens in the initial stages of intracellular trafficking. Early endosomes and early macropinosomes merge with each other to form a novel vesicle (140). Moreover, endocytic interactions with recycling endosomes as well as with vesicles of the trans-Golgi network induce the additional exchange of nonendocytic proteins with the endolysosomal system (154). Also the fusion of lysosomes with autophagosomes introduces components of e. g. defective organelles into the endocytic system (155, 156). Figure 6 shows the fusion events and participating vesicles that may be associated with intracellular nanoparticle transport.

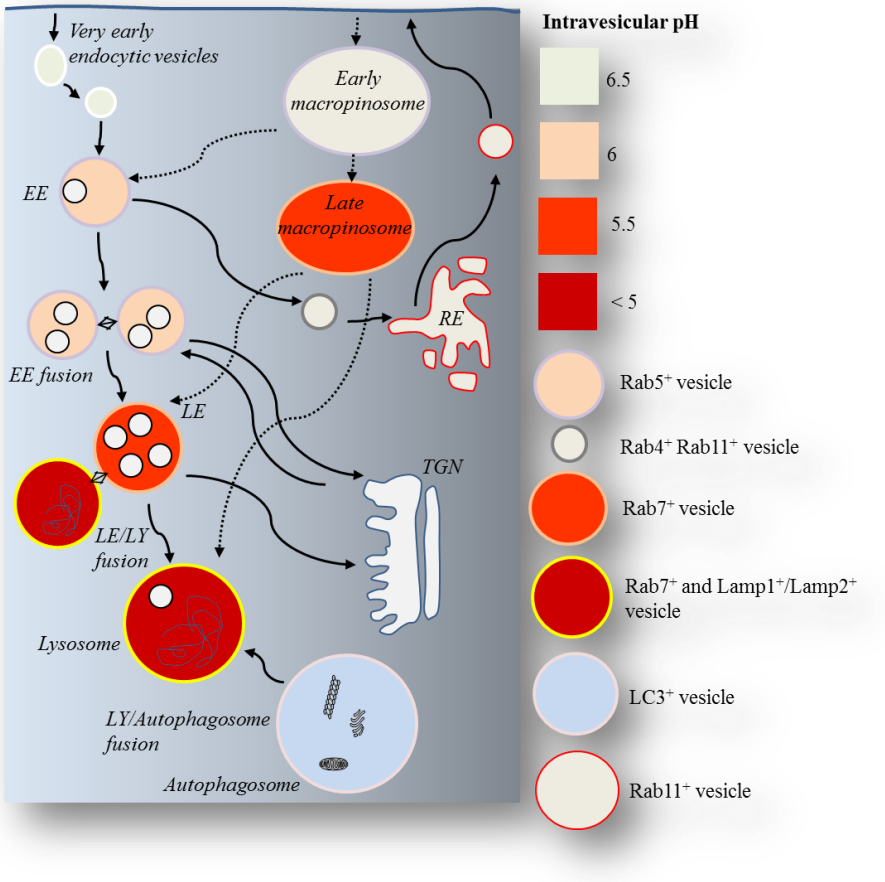

Figure 6: Potential routes of intracellular nanoparticles trafficking. The intravesicular pH values of the endolysosomal vesicles are depicted as distinctly colored vesicles. Abbreviations: EE: Early endosomes; RE: Recycling endosome; LE: Late endosome/multivesicular body; LY: Lysosome; TGN: Trans-Golgi-Network. Arrows indicate endocytic fusion events between the different compartments. Dotted lines indicate the possible macropinocytic interplay with the endocytic system. Adapted from (140, 157, 158).

1.3.1 Early endocytic compartments

Early endocytic vesicles are a heterogeneous class of vesicular carriers during the initial stage of intracellular trafficking (142, 159). Classical early endosomes can be identified by distinct markers such as EEA1 or Rab5 and coexist in different subpopulations (159, 160). A previous report identified at least two distinct classes of EE that display different maturation and mobility kinetics (161). The authors detected a first population of $Rab5^+$ endosomes that rapidly accumulated Rab7 within a short time frame. The second population matures on a much slower time scale without accumulating Rab7 (161). According to these data, the mobility of vesicles on microtubules can be correlated with their maturation state (161). While slowly maturating endosomes move to a less extent, rapidly maturing vesicles show a higher motility rate. If this is connected to the distinct Rab domains on early endosomes is not yet clarified.

However, it is worth to mention that early endosomes contain separated surface patches of Rab4, Rab5 and Rab11 (162). Especially, Rab4 and Rab11 have been shown to control recycling and endosomal fusion (162, 163). According to the study of Sönnichsen *et al*. it was proposed that the different domains on early endosomes promote the pinch off of early endosomal subvesicles that are introduced into the recycling pathway (Figure 6) (162). This shows that early endosomal compartments are closely related precursors of the cellular recycling pathways. However, these classical endosomes seem to be functionally different from early macropinosomes.

Early macropinosomes

Early macropinosomes are budded vesicles that are formed after macropinocytosis and partially bear markers of early endosomes (142). Classical macropinosomes are characterized by the surface markers Rab34, Rab5 and its effector Rabankyrin-5 (141, 142). Other studies highlight the transient association of switch-associated protein 70 (SWAP-70) with macropinosomes in dendritic cells (164). Further well accepted markers of growth factor induced macropinosomes are proteins of the sorting nexin family as well as Rac1 (137, 165). The biogenesis of macropinosomes can be triggered by EGF stimulation or via the overexpression of several sorting nexins such as SNX1 or SNX18 (166). After macropinosomes formation, vesicles can fuse with other endocytic compartments or mature to $Rab7^+$ late macropinosomes (140, 165, 167).

1.3.2 Late endosomes – Multivesicular bodies

Late endosomes are also termed as multivesicular bodies (MVBs) (168). These vesicles frequently originate from $Rab5^+$ early endosomes and are considered to be control centers for different processes such as cell signaling or exocytosis (153, 168). Morphologically, MVBs are 400 – 1000 nm large organelles that contain small intraluminal vesicles (ILVs) in a size range of typically ~ 50 nm (169). When MVBs fuse with the plasma membrane, ILVs are externalized as exosomes in a Rab27b-dependent manner (170, 171). All of these processes are well studied. However, the definite identification of MVBs remains challenging. Unique marker proteins are relatively few since MVB biogenesis mainly occurs transiently (168). Nowadays, characterization of MVBs is therefore performed by the detection of mannose 6-phosphate receptor (M6PR), Lamp1/Lamp2, distinct Rab proteins (Rab5, Rab7, Rab27, Rab35) as well as several tetraspanins (172). Here, it is to mention that the tetraspanins CD82, CD9, CD81 and CD63 are abundant on MVBs (171, 173). Also the intraluminal vesicles can be directly detected by the tetraspanin CD63 (174). In previous reports it was shown that CD63 transports the melanocytic protein Pmel17 on ILVs in an ESCRT (endosomal sorting complexes required for transport)-independent process (174, 175).

Contrary to the sorting of Pmel17 onto ILVs, the biogenesis of MVBs as well as the degradation of proteins inside the endocytic system is mediated by the ESCRT machinery (176). For MVB

biogenesis, Wollert and Hurley showed that the four components of ESCRT (0/I/II/III) induce the formation of intraluminal vesicles inside giant unilamellar vesicles (176). Thereby, they recorded the internalization of fluorescently-labeled ubiquitin. Inside cells, ubiquitinylation is an important modification for the degradation of membrane proteins via ESCRT. Monoubiquitinylated or polyubiquitinylated membrane proteins bind the ubiquitin-binding domain of ESCRT components, which results in the degradation of the proteins (177). Altogether, the functional relevance of functional ESCRTs has been well characterized. This was also shown in biomedical publications. Deregulation of the ESCRT machinery contributes significantly to many human diseases such as cancer or neurological diseases (178).

However, it is worth to mention that not only the late endosomal deregulation of ESCRT can mediate severe diseases. In a particular case, a mutation of Niemann-Pick-disease C1 protein (NPC1) leads to a pathological cholesterol accumulation inside late endosomes (83, 179). Consequently, cholesterol homeostasis and intracellular trafficking pathways are disturbed. In this context, Sahay and colleagues showed that NPC1 deficient cells longer retain nanotransporters inside the endosomal system than healthy cells (83). This implies an important function of NPC1-dependent cholesterol homeostasis in intracellular trafficking pathways of nanoparticles (180).

1.3.3 Lysosomes

Lysosomes are seen as terminal organelles in endocytic and autophagocytic pathways (158). These vesicles are the final destination for a large number of cargos and mediate numerous functions such as the downregulation of surface receptors, inactivation of pathogens or MHC-peptide loading (151, 156). Though, not only the functions of lysosomes are diverse. Electron microscopy reveals that the morphology and size of lysosomes is strikingly heterogeneous (181). They frequently contain electron-dense material and multilamellar membrane whorls (181). This material partially originates from the lysosomal fusion with autophagocytic vesicles resulting in the formation of a multilamellar-body-like structure (182).

Moreover, their acidic interior (pH 4.6-5) is maintained by several vacuolar H^+ ATPases (183). This is especially important for hydrolytic enzymes with an acidic pH optimum (184). Lysosomes supply a protective membrane-shielded lumen for more than 50 different acid hydrolases (e. g. peptidases, proteinases, phosphatases, nucleases, glycosidases, sulphatases, lipases) (156). The transport of these proteins towards prelysosomal vesicles is frequently orchestrated by two independent M6P-receptors that recognize the M6P tag on the potential lysosomal proteins (185). After protein binding, the M6PR-protein-complex is shuttled from the trans-Golgi-network to endosomal vesicles, where the cargo dissociates from M6PRs due to the acidic environment (186). As a consequence, lysosomes can be distinguished from prelysosomal organelles by the lack of M6PR and the presence of Lamp1 and Lamp2 (186).

1.3.4 Fusion events and protein transport inside the endocytic system

In a protein-free system, the fusion of vesicles is mainly based on the interaction of different forces between the two vesicular surfaces (187). Attractive forces like hydrophobicity and van der Waals forces have to overcome several repulsive forces (e. g. electrostatic) for a successful adhesion of the vesicles to each other (188). However, it is believed that the fusion of membranes cannot be induced by simple adhesion, but by factors (e. g. surface charges) that alter the steric configuration of individual lipids (189). The destabilization of single lipid domains facilitates the hydrophobic interplay between lipids on opposing membranes resulting in their fusion (190, 191). In cellular systems, fusion of organelles is additionally supported by two preliminary steps that are mediated by protein complexes. In the first step, a tethering step loosely connects the two merging vesicles to each other. In the subsequent step of docking, an irreversible binding of the vesicles is achieved that results in the terminal fusion of the organelles (181).

The tethering of two early endosomes is mediated by the class C core vacuole/endosome tethering complex (CORVET) while late endosomes and lysosomes are connected via the vacuole protein sorting complex (HOPS) (192). In late endosomes/lysosome fusion processes, Rab7 is utilized as an adaptor protein for the effectors of the HOPS complex (181). Subsequently after formation of the tethering complex, the vesicular fusion is induced by the assembly of a trans-SNARE complex (181). SNARE (soluble N-ethylmaleimide-sensitive factor attachment protein receptor) proteins are characterized by a stretch of 60-70 amino acids that are arranged in heptad repeats (193). When a SNARE protein encounters other SNARE motifs, an alpha-helical structure is formed. In heterotypic late endosome/lysosome fusion, the SNARE complex consists of the R-SNARE VAMP7, Syntaxin-7, Syntaxin-8 and VTI1B (181). In homotypic endosome/endosome fusion, VAMP8 is utilized instead of VAMP7. It is believed that the formation of the SNARE complex finally results in the induction of vesicular fusion (194). Even in macropinosomes/lysosome fusion and in autophagosome/lysosome fusion a participation of SNARE proteins was observed (181). This gives rise to investigate SNARE proteins in intracellular nanoparticle trafficking.

1.3.5 Intracellular trafficking of nanomaterials

The first approaches that studied the intracellular trafficking of nanoparticles have already been made. Via the use of confocal spinning disc microscopy, Sandin *et al.* showed that polystyrene nanoparticles are transported via $Rab7^+$ endosomes to their terminal lysosomal destination (151). Another study revealed similar results with polyplexes that actively moved through the cell inside endolysosomal structures (132). Both of these studies describe less colocalization of nanomaterials with recycling pathways and autophagocytic routes. However, nanoparticles can also exploit several secretory and endocytic pathways. Sahay and colleagues observed a transport of lipid nanoparticles into $Rab11^+$ endosomes implicating that LNPs are trafficked via the recycling pathways of the cell (83). Other

reports detected α-Al_2O_3 nanoparticles inside $LC3^+$ autophagosomes (152). All of these studies used well accepted markers for their investigations. However, these examinations are biased by the present knowledge about the recently known proteins in intracellular trafficking pathways of other objects such as viruses or membrane proteins. Therefore, one primary aim of this thesis is to provide novel information about the intracellular trafficking pathways in an unbiased approach.

1.4 Aims of the study

This study was carried out to analyze the drug delivery abilities, the entry mechanisms and the intracellular trafficking of several polymeric nanoparticles. Thereby, the analysis of nano-bio interactions could reveal novel insights in terms of prospective applications for nanoparticles. In the first part of this study, we wanted to investigate whether biodegradable poly-L-lactide nanoparticles are a suitable candidate for a non-invasive drug delivery system *in vitro*. To analyze this, nanoparticle-membrane interaction were preliminary studied with distinct cellular and cell-free systems. The primary goal was to investigate the release mechanism and the subcellular transport of the nanoparticulate cargo during nanoparticle-membrane interaction.

Secondly, we were interested in the mechanisms by which polymeric nanoparticles enter the cell. In this project, we focused on the interaction of nanoparticles with the macropinocytic system. The internalization of nanoparticles could rely on the classical factors of macropinocytic signaling. Consequently, we intensively studied the influences of small GTPases and kinases on the internalization mechanism of nanoparticles. To validate the functionality of these GTPases in nanoparticle entry, we studied whether constitutively active or dominant negative forms of these effector proteins have an impact on nanoparticle entry. Additionally, a set of small inhibitory molecules and siRNAs was tested to inhibit several pathways of the endocytic system. We investigated, whether this had an effect on nanoparticle entry.

In the third part of this thesis, we examined the intracellular trafficking of nanoparticles (INT). To identify novel proteins of INT, we wanted to establish an innovative and unbiased method that enables us to identify novel proteins in intracellular nanoparticle trafficking. The goal of this approach was to dissect the INT by label free quantitative mass spectrometry. To test the specificity of this method, we investigated promising proteins by confocal live cell imaging and other methods that could influence the nanoparticle trafficking. We finally examined whether the lysosomal milieu had an impact on the degradation of the nanoparticulate protein corona.

2. Materials and Methods

Chapter 2 depicts all the materials and chemicals that were used in this study. Experiments were performed as described in the chapter "Methods". The nanoparticles of this study were synthesized by Dr. Markus B. Bannwarth. The synthesis and characterization procedures are exactly described in his thesis (195).

2.1 Materials

In the following chapter, all relevant materials of this study are depicted.

2.1.1 Nanoparticles

Table 1 contains the abbreviations, properties and characterization parameters of all relevant nanoparticles that were used in this study.

Table 1: Nanoparticles.

Particle	Polymer	Functionalization	Surfactant	Diameter (nm)	Dye	ζ-Potential (mV)
PS-COOH	PS	COOH	SDS	73	PMI (488nm/ 525nm)	n. d.
PS-NH_2-BODIPY	PS	NH_2	CTMA-CL	60	BODIPY II (488nm/ 525nm)	n. d.
PLLA-Fe-PMI	PLLA	OH + magnetite	SDS	126	PMI (488nm/ 525nm)	n. d.
PLLA-PMI	PLLA	OH	SDS	122	PMI (488nm/ 525nm)	-47
SPIOPSN-BODIPY	PS	Sulfonate + magnetite	SDS	126	BODIPY I (504nm/ 527nm)	-62

2.1.2 Chemicals

Chemicals used in this study are listed in Table 2.

Table 2: Chemicals.

Chemical	Supplier
1,2-Dioleoyl-sn-glycero-3-phosphocholine	Avanti Polar Lipids; U. S. A.
2-[4-(2-hydroxyethyl)piperazin-1-yl]ethanesulfonic acid	Sigma Aldrich; U. S. A.
2-Propanol	Sigma Aldrich; U. S. A.
3-[(3-Cholamidopropyl)dimethylammonio]-1-propanesulfonate hydrate	Serva,Germany
4-(2-hydroxyethyl)-1-piperazineethanesulfonic acid	Sigma Aldrich; U. S. A.
Agar	Sigma Aldrich; U. S. A.
Agarose Standard	Roth; Germany
Ampicillin	Sigma Aldrich; U. S. A.
BODIPY I/ BODIPY II	Synthesized as described (196)
Bovine serum albumin	Sigma Aldrich; U. S. A.
Calcium chloride	Sigma Aldrich; U. S. A.
cOmplete protease inhibitor cocktail	Roche; Switzerland
D(+)-Saccharose	Roth; Germany
Dimethylsulfoxid	Sigma Aldrich; U. S. A.
Dipotassium phosphate	Sigma Aldrich; U. S. A.
DL-Dithiothreitol	Sigma Aldrich; U. S. A.
Ethanol	Sigma Aldrich; U. S. A.
Ethylene glycol-bis(2-aminoethylether)- tetraacetic acid	Sigma Aldrich; U. S. A.
Ethylenediaminetetraacetic acid	Roth; Germany
Fetal bovine serum	Invitrogen; U. S. A.
Gentamicin	Invitrogen; U. S. A.
Gluthatione	Sigma Aldrich; U. S. A.
Glycine	Sigma Aldrich; U. S. A.
Immersion oil for microscopy	Leica; Germany
Magnesium chloride	Sigma Aldrich; U. S. A.
Methanol	Fisher Scientific; U. S. A.
***N*-(2,6-diisopropylphenyl)-perylene-3,4-dicarbonacid-imide (PMI)**	BASF; Germany
Nile Red	Sigma Aldrich; U. S. A.
Nuclease-free water	Qiagen; U. S. A.
Oil Red O	Sigma Aldrich; U. S. A.
Paraformaldehyde	Sigma Aldrich; U. S. A.
Penicillin/Streptomycin	Invitrogen; U. S. A.
Peptone	Sigma Aldrich; U. S. A.
Ponceau S	Sigma Aldrich; U. S. A.

Potassium chloride	Sigma Aldrich; U. S. A.
Pyruvate	Life technologies; U. S. A.
Saponin	Sigma Aldrich; U. S. A.
Sodium chloride	Sigma Aldrich; U. S. A.
Sodium hydroxide	Sigma Aldrich; U. S. A.
Thio-Urea	Serva, Germany
Triton X-100	Sigma Aldrich; U. S. A.
Trizma Base	Sigma Aldrich; U. S. A.
Trypan blue solution (0.4%)	Sigma Aldrich; U. S. A.
Tryptone	Sigma Aldrich; U. S. A.
Urea	Serva, Germany
Yeast extract	Sigma Aldrich; U. S. A.

2.1.3 Instruments and Consumables

Table 3 shows the instruments that were used in this work.

Table 3: Instruments.

Instrument	Supplier
4D Nucleofector	Lonza; Switzerland
Automated cell counter TC10	Bio-Rad; U. S. A.
Bacteria incubator UM200	Memmert; Germany
Cell culture flow c-(Max Pro)^3-130	Berner; Germany
Cell culture incubator C200	Labotec; Germany
Centrifuge 5810R and 5430	Eppendorf; Germany
Confocal laser scanning microscope Leica SP5 II with CW-STED	Leica; Germany
Dry blotting system iBlot®	Invitrogen; U. S. A.
Flow cytometer CyFlow ML	Partec; Germany
Fluorescence imager LAS-3000	Fujifilm, Japan
Fluorescence microscope IX81-ZDC	Olympus; Germany
Freezer -20°	Liebherr; Germany
Freezer -80°C Hera Freeze Top	Thermo Scientific; Germany
Hamilton pipette	Hamilton Company; U. S. A.
Incubator Innova 44	New Brunswick Scientific; U. S. A.
Inverted microscope CKX41	Olympus; Germany
Microcentrifuge Minispin plus	Eppendorf; Germany
Microscale AE100	Mettler Toledo; Switzerland
Nitrogen tank LS6000	Taylor-Wharton; Germany
PCR Mastercycler EP Gradient S	Eppendorf; Germany
Pipettes	Eppendorf; Germany

Pipetting aid Accujet Pro	Brand; Germany
Platereader Infinite M1000	Tecan; Germany
Power supply 250-EX	Life technologies; U. S. A.
Real time system CFX96	Bio-Rad; Germany
SDS-PAGE/Western Blot chamber Mini/Maxi	Biometra; Germany
Thermo mixer	HL by Ditabis; Germany
Ultracentrifuge Optima™ MAX	Beckman Coulter; U. S. A.
UV-Vis photospectrometer ND-8000	Thermo Scientific; Germany
Vacuum pump Vacusafe comfort	IBS Integra Bioscience; Germany
Vortexer Reax Control	Heidolph; Germany
Water bath	Memmert; Germany

Table 4 displays the used consumables of this work.

Table 4: Consumables.

Consumables	Supplier
27G needle	BD Biosciences; U. S. A.
Adhesive PCR film	Bio-Rad; Germany
Cell culture flasks	Greiner; Germany
Celltrics sterile filters	Partec, Germany
FACS tubes	Partec; Germany
Falcon tubes (10 ml; 50 ml)	Greiner; Germany
Ibidi itreat µ-dishes	IBIDI; Germany
iBlot® anode stack	Life technologies, U. S. A.
iBlot® cathode stack	Life technologies, U. S. A.
Multiwell plates	Corning Inc.; U. S. A.
Nucleofector cuvettes (100 µl)	Lonza, Switzerland
NuPAGE 10% bis-tris gel	Life technologies; U. S. A.
Parafilm	Pechiney Plastic Packaging, U. S. A.
PCR tubes/PCR plates	Bio-Rad; Germany
Pipette tips	Greiner, Germany
Pipettes (5 ml; 10 ml; 25 ml; 50 ml)	Greiner, Germany
Protran® nitrocellulose membrane	Sigma Aldrich; Germany
PVDF membrane	Millipore, U. S. A.
QIA shredder columns	Qiagen; U. S. A.
Single-use syringes	Henke-Sass-Wolf; Germany
Sterile filter (0.2 µm; 0.45 µm)	Millipore, U. S. A.

2.1.4 Small molecule inhibitors

Table 5 depicts the inhibitors with their known targets/mechanisms that were used for the suppression of different endocytic mechanisms. Inhibitors were dissolved and stored according to manufacturer´s recommendations.

Table 5: Small molecule inhibitors of uptake.

Inhibitor	Supplier
5-(N-Ethyl-N-isopropyl) amiloride (lowering of submembraneous pH)	Sigma Aldrich; U. S. A.
Bafilomycin A1 (Inhibition of v-type ATPases)	Sigma Aldrich; U. S. A.
Blebbistatin (Inhibition of Myosin)	Sigma Aldrich; U. S. A.
Brefeldin A (Inhibition of ARF1)	Sigma Aldrich; U. S. A.
CA-074 methyl ester (Inhibition of cathepsins)	Sigma Aldrich; U. S. A.
Chlorpromazine (Inhibition of CME)	Sigma Aldrich; U. S. A.
Cytochalasin D (Inhibition of F-Actin polymerization)	Sigma Aldrich; U. S. A.
Dynasore® (Inhibition of Dynamin I/II)	Sigma Aldrich; U. S. A.
IPA-3 (Inhibition of PAK1)	Tocris; U. S. A.
Ly294002 (Inhibition of PI3K)	Tocris; U. S. A.
Methyl-β-cyclodextrin (Cholesterol depletion)	Sigma Aldrich; U. S. A.
Nocodazole (Inhibition of microtubule polymerization)	Sigma Aldrich; U. S. A.
Ro 31-8220 (Inhibition of PKC)	Sigma Aldrich; U. S. A.
U18666A (Cholesterol synthesis inhibitor)	Merck; Germany
U73122 (Inhibition of PLC)	Sigma Aldrich; U. S. A.
Wortmannin (Inhibition of PI3K)	Sigma Aldrich; U. S. A.

2.1.5 Cell lines and primary cells

Cell lines used in this study are listed in Table 6.

Table 6: Cell lines.

Name	Cell type	Supplier
Jurkat	Immortalized $CD3^+$ T lymphocytes	DSMZ; Germany
HeLa	Cervical carcinoma	DSMZ; Germany
Multipotent human stroma cells (hMSCs)	Human bone-marrow derived stem $cells^+$ for CD29, CD73, CD44, CD90, CD105, CD146, CD166 and MHC class I; negative for CD1a, CD3, CD14, CD16, CD19, CD34, CD45, CD133, MHC class II and SSEA2	University of Ulm; Germany

2.1.6 Dyes

Dyes used in this work are listed in Table 7. Dyes were used according to manufacturer´s protocol.

Table 7: Dyes.

Dye	Supplier
7-Aminoactinomycin D	Sigma Aldrich; U. S. A.
CellMask™ DeepRed	Invitrogen; U. S. A.
CellMask™ Orange	Invitrogen; U. S. A.
Hoechst 33342	Life technologies; U. S. A.
LysoTracker DND-26	Invitrogen; U. S. A.
Phalloidin	Invitrogen; U. S. A.

2.1.7 Antibodies and proteins

Used primary antibodies, secondary antibodies and fluorescent marker proteins are listed in Table 8. Primary antibodies were titrated for immunofluorescence, flow cytometry and western blotting. Secondary antibodies were used in a dilution of 1:200. Fluorescent tracers were used as stated.

Table 8: Primary, secondary antibodies and fluorescent tracers.

Target	Supplier
Alexa Fluor 488 F(ab´)2 fragment of donkey anti-rabbit IgG	Life technologies; U. S. A.
Alexa Fluor 488 F(ab´)2 fragment of goat anti-mouse IgG	Life technologies; U. S. A.
Alexa Fluor 555 F(ab´)2 fragment of goat anti-mouse IgG	Life technologies; U. S. A.
Alexa Fluor 633 F(ab´)2 fragment of goat anti-guinea pig IgG	Life technologies; U. S. A.
Alexa Fluor 633 F(ab´)2 fragment of goat anti-mouse IgG	Life technologies; U. S. A.
Alexa Fluor 633 F(ab´)2 fragment of goat anti-rabbit IgG	Life technologies; U. S. A.
Guinea pig anti- human TIP47	Progen; Germany
Mouse anti- human ADRP	Fitzgerald; U. S. A.
Mouse anti- human Cathepsin D	BD Biosciences; U. S. A.
Mouse anti- human Caveolin-1	Abcam, England
Mouse anti- human CD63	Biolegend; U. S. A.
Mouse anti- human CD82	ACRIS; Germany
Mouse anti- human CD9	BD Biosciences; U. S. A.
Mouse anti- human Dynamin I	BD Biosciences; U. S. A.
Mouse anti- human GAPDH	Ambion; U. S. A.
Mouse anti- human Lamp1	BD Biosciences; U. S. A.
Mouse anti- human Lamp2	Abcam, England
Mouse anti- human M6PR	BD Biosciences; U. S. A.
Mouse anti- human PMEL17 (NKI/beteb)	Abcam; U. S. A.
Mouse anti- human Rab5	BD Biosciences; U. S. A.

Mouse anti- human Ubiquitin	Biolegend; U. S. A.
Mouse anti-CD81 (5A6)	Santa Cruz Biotechnology; U. S. A.
Mouse anti-human Clathrin heavy chain	BD Biosciences; U. S. A.
Mouse anti-human Flotillin-1	BD Biosciences; U. S. A.
Rabbit anti- human LC3B	Life technologies; U. S. A.
Rabbit anti- human NPC1	Abcam, England
Rabbit anti- human Rab11	Life technologies; U. S. A.
Bovine serum albumin Alexa Fluor 488	Life technologies; U. S. A.
Cholera Toxin Subunit B	Life technologies; U. S. A.
Transferrin-Alexa Fluor 488	Life technologies; U. S. A.

2.1.8 Plasmids

Plasmids obtained from other laboratories/companies are listed in Table 9.

Table 9: Published or purchasable plasmids.

Plasmid	Addgene ID number	Source
Alpha 5 integrin-GFP	15238	Addgene; U. S. A.
Arf4-GFP	39556	Addgene; U. S. A.
EGFP-Dyn2 K44A	n. a.	Dr. Sandra Ritz, MPI-P
GFP-Rab11-wt	12674	Addgene; U. S. A.
GFP-Rab5DN (S34N)	35141	Addgene; U. S. A.
GFP-RhoB	23225	Addgene; U. S. A.
pcDNA3 HA ARF1 DN-T31N	10833	Addgene, U. S. A.
pcDNA3 HA Arf6	10834	Addgene; U. S. A.
pcDNA3 HA Arf6 DN-T27N	10831	Addgene; U. S. A.
pcDNA3-EGFP-Cdc42-Q61L	12600	Addgene; U. S. A.
pcDNA3-EGFP-Cdc42-T17N	12976	Addgene; U. S. A.
pcDNA3-EGFP-RhoA-T19N	12967	Addgene; U. S. A.
pCMV6-AC-GFP-PMEL (NM_006928)	n. a.	Origene; U. S. A.
pCMV6-AC-GFP-SWAP70 (NM_015055)	n. a.	Origene; U. S. A.
pEGFP VAMP7 (1-220)	42316	Addgene; U. S. A.
pEGFP-Rab5A-wt	n. a.	Dr. Sandra Ritz, MPI-P
pEGFP-Tubulin	30487	Addgene; U. S. A.
pEGFP-β-Actin	n. a.	Dr. Sandra Ritz, MPI-P
pmaxGFP™	n. a.	Lonza; Switzerland
pRNAi-H1-green and pRNAi-H1-neo	n. a.	Biosettia; U. S. A.

2.1.9 Self-designed plasmids

shRNA constructs were generated by cloning of DNA oligonucleotides into pRNAi-H1-green and pRNAi-H1-neo vectors. Cloning was conducted according to the manufacturer´s protocol (Biosettia; U. S. A.). shRNA constructs were used to obtain a knockdown of human CD9, CD81, CD82, CD63, flotillin-1, clathrin heavy chain, caveolin-1, NPC1 and dynamin-1. The used oligonucleotides were ordered from Biosettia and are listed in Table 10. Simone-Franziska Glaser performed the cloning of the constructs into pRNAi-H1-green.

Table 10: DNA oligonucleotides cloned in pRNAi-H1-green and pRNAi-H1-neo.

Accession no.	Name	Target sequence	DNA nucleotide sequence
NM_001172895.1	Caveolin-1	GGTCAAGATTGACTTTGAA	AAAAGGTCAAGATTGACTTTGAATTGGATCCAATTCAAAGTCAATCTTGACC
NM_001257389.1	CD63	GCTGCTAACTACACAGATT	AAAAGCTGCTAACTACACAGATTTTGGATCCAAAATCTGTGTAGTTAGCAGC
NM_004356.3	CD81	GGATGTGAAGCAGTTCTAT	AAAAGGATGTGAAGCAGTTCTATTTGGATCCAAATAGAACTGCTTCACATCC
NM_001024844.1	CD82	GCTGGGTCAGCTTCTACAA	AAAAGCTGGGTCAGCTTCTACAATTGGATCCAATTGTAGAAGCTGACCCAGC
NM_001769.3	CD9	GCTTCCTCTTGGTGATATT	AAAAGCTTCCTCTTGGTGATATTTTGGATCCAAAATATCACCAAGAGGAAGC
NM_004859.3	Clathrin heavy chain	GCTTGATGCTCTGAAGAAT	AAAAGCTTGATGCTCTGAAGAATTTGGATCCAAATTCTTCAGAGCATCAAGC
NM_001005336.1	Dynamin-1	GCAACCAGATGAACAAGAA	AAAAGCAACCAGATGAACAAGAATTGGATCCAATTCTTGTTCATCTGGTTGC
NM_005803	Flotillin-1	GGCAGAACAAGGAGATGTT	AAAAGGCAGAACAAGGAGATGTTTTGGATCCAAAACATCTCCTTGTTCTGCC
NM_000271	NPC1	GCCTCTCTGAATGATACAA	AAAAGCCTCTCTGAATGATACAATTGGATCCAATTGTATCATTCAGAGAGGC

2.1.10 siRNA/esiRNA

Table 11 shows the siRNAs/esiRNAs that were used to downregulate the listed target proteins.

Table 11: siRNAs and esiRNAs.

Target	Sequence/Ref. number	Supplier
ATG7-AF555	GGTCAAAGGACGAAGATAATT	Qiagen; U. S. A.
Caveolin-1	GCCGUGUCUAUUCCAUCUATT	Ambion; U. S. A.
CD63	UAUGGUCUGACUCAGGACAAGCUGUTT	MWG, Germany

CD81	UGAUGUUCGUUGGCUUCGUTT	MWG, Germany
CD82	GCCCUCAAGGGUGUGUAUATT	Ambion; U. S. A.
CD9	GGAGUCUAUAUUCUGAUCGTT	Ambion; U. S. A.
Cdc42-esiRNA	EHU117241	Sigma Aldrich; U. S. A.
Clathrin heavy chain	UAAUCCAAUUCGAAGACCAAUTT	MWG, Germany
Dynamin I/II	sc-43736	Santa Cruz Biotechnology; U. S. A.
Flotillin-1	sc-35391	Santa Cruz Biotechnology; U. S. A.
NPC1	s9669	Life technologies; U. S. A.
Rab5A	S11678	Life technologies; U. S. A.
Rabankyrin-5-esiRNA	EHU089471	Sigma Aldrich; U. S. A.
Rac1	S11711	Life technologies; U. S. A.

2.1.11 Primer

All primers for quantitative real time PCR were purchased from Eurofins MWG Operon (Germany) and are listed in Table 12.

Table 12: Primer.

Target	Oligonucleotide sequence
Caveolin-1	5´ GCGACCCTAAACACCTGAAC 3´ 3´ TGTGTGTCAAAAGTGCCGTA 5´
CD63	5´ CGAAAAACAACCACACTGCT 3´ 3´ TTTAGGGAAGGTACAGCTTC 5´
CD81	5´ CTCCAGCACACTGACTGCTT 3´ 3´ TCGTTGGAGAAGTTCCTCCT 5´
CD82	5´ ACTGGACAGACAACGCTGAG 3´ 3´ GTTGTCGGAAAGACACTCCT 5´
CD9	5´ GCATGCTGGGACTGTTCTTT 3´ 3´ TAAGGGTGTTCCTACTCCAC 5´
cdc42	5´ TTGATACTGCAGGGCAAGAG 3´ 3´ ATCTCAGGCACCCACTTTTC 5´
Clathrin heavy chain	5´ GAGCCTCTTGCTGACATCAC 3´ 3´ TTATTAGCGGGTAGACTTCC 5´
DMT1	5´ TGAATGCCACAATACGAAGG 3´ 3´ ATAAAGCCACAGCCGATGA 5´
Dynamin-1	5´ CGATATCGAGCTGGCTTACA 3´ 3´ AGTCCCTTGGTCCTACTCTA 5´
Flotillin-1	5´ GCATTGCCCAGGTAAAAATC 3´ 3´ CTTCTGCCTCCGACTCTAAC 5´
GAPDH	5´ AAGGTGAACGTCGGAGTCAA 3´

	3´ GGTAGTTACTGGGGAAGTAA 5´
NPC1	5´ AAGGGGACGACTTCTTTGTG 3´
	3´ ACACTGGTCCACCAAACGTA 5´
Rac1	5´ CCCGTGAAGAAGAGGAAGAG 3´
	3´ TTGAGCAAAGCGTACAAAGG 5´
β-Actin	5´ TCGTGCGTGACATTAAGGGG 3´
	3´ GTACTTGCGCTCAGGAGGAG 5´

2.1.12 Enzymes

Enzymes for cloning, qPCR and tryptic digest are listed in Table 13.

Table 13: Enzymes.

Enzyme	Supplier
BamHI	NEB; Germany
PacI	NEB; Germany
Reverse transcriptase	Bio-Rad; Germany
T4 ligase	NEB; Germany
Trypsin	Invitrogen; Germany
XhoI	NEB; Germany

2.1.13 Bacteria

One Shot® TOP10 chemically competent *E. coli* (Invitrogen; U. S. A.) were used for the transformation of plasmids and the growth of cultures for plasmid preparations. Bacteria were stored at – 80°C.

2.1.14 Buffers, solutions and markers

Table 14 depicts commercially available buffers, solutions and markers utilized in this study.

Table 14: Buffers, solutions and markers.

Buffer	Supplier
10x Hybridization buffer	Biosettia; U. S. A.
10x Ligation buffer	NEB; Germany
10x Restriction enzyme buffer 3	NEB; Germany
10x T4 Ligase buffer	NEB; Germany
1x Dulbecco´s phosphate buffered saline	Invitrogen; U. S. A.
1x Tris-acetate-EDTA buffer	Sigma Aldrich; U. S. A.
2x LiSD-buffer NuPAGE	Invitrogen; U. S. A.
6x DNA loading buffer	Fermentas; U. S. A.

GeneRuler™ 50 bp/100bp Ladder	Fermentas; U. S. A.
Hypochloride solution for flow systems	Partec; Germany
Novex® AP Chemiluminescent substrate	Invitrogen; U. S. A.
NuPAGE® Reducing agent	Invitrogen; U. S. A.
NuPAGE® SDS Sample buffer	Invitrogen; U. S. A.
SeeBlue® Plus2 prestained standard	Life technologies; U. S. A.
Sheath Fluid for flow systems	Partec; Germany
SYBR® Safe DNA gel stain	Invitrogen; U. S. A.

2.1.15 Media and sera

Table 15 lists the media, supplements and sera for bacterial culture and mammalian cell culture.

Table 15: Media, supplements and sera.

Medium	Supplier
Ciprofloxacin	Sigma Aldrich; U. S. A.
Dulbecco´s Modified Eagle Medium (DMEM)	Invitrogen; U. S. A.
Fetal calf serum (FCS)	Lonza; Switzerland
GlutaMAX™ supplement 100x	Life technologies; U. S. A.
ImMedia™ Amp Agar	Invitrogen; U. S. A.
ImMedia™ Amp Liquid	Invitrogen; U. S. A.
ImMedia™ Kan Liquid	Invitrogen; U. S. A.
ImMedia™ Kan Liquid	Invitrogen; U. S. A.
Non-essential amino acids 100x	PAA; Austria
Penicillin/Streptomycin (Pen/Strep) 100x	Invitrogen; U. S. A.
RPMI-1640	Invitrogen; U. S. A.
S. O. C. medium	Invitrogen; U. S. A.
Self-made nucleofection buffer	According to (197)
α-MEM	Lonza; Switzerland
0.25% Trypsin-EDTA	Life technologies; U. S. A.
2.5% Trypsin	Life technologies; U. S. A.

2.1.16 Commercial kits

Table 16 depicts the used commercial kits.

Table 16: Commercial kits.

Kit	Supplier
Amaxa-SE cell line 4D-nucleofector X Kit L	Lonza; Switzerland
CellTiter-Glo® Luminescent cell viability assay	Promega; U. S. A.
Fugene HD	Promega; U. S. A.

iQ SYBR® Green supermix	Bio-Rad; U. S. A.
iScript™ DNA synthesis kit	Bio-Rad; U. S. A.
Lipofectamin 2000	Invitrogen; U. S. A.
Novex® Western breeze	Invitrogen; U. S. A.
Qiagen plasmid midi kit	Qiagen; U. S. A.
Qiagen plasmid mini kit	Qiagen; U. S. A.
RNeasy mini kit	Qiagen; U. S. A.

2.1.17 Software and bioinformatics

The used software and online tools are depicted in Table 17.

Table 17: Software and bioinformatic tools.

Software	Supplier/Source
Bio-Rad CFX manager	Bio-Rad; Germany
DAVID ontology analysis	http://david.abcc.ncifcrf.gov/
FCS Express V4.0	DeNovo Software; U. S. A.
FlowMax 3	Partec; Germany
Graph Pad Prism 5	Graphpad software inc; U. S. A.
i-control 1.6.19.0	Tecan; Germany
ImageJ (Fiji)	http://rsbweb.nih.gov/ij/
LASAF confocal software	Leica; Germany
ND-8000 V2.0	Thermo Scientific; Germany
Primer3	http://bioinfo.ut.ee/primer3-0.4.0/
shRNA Designer	http://biosettia.com/support/shrna-designer
Velocity	PerkinElmer; U. S. A.

2.2 Methods

In this segment, a description of all used methods is provided.

2.2.1 Preparation of giant unilamellar vesicles

For release studies of nanoparticulate cargo, 1,2-dioleoyl-*sn*-glycero-3-phosphocholine (DOPC) giant vesicles were prepared by electroformation. 10 mM DOPC (Avanti lipids, U. S. A.) were dissolved in chloroform. 25 µl dissolved DOPC was introduced dropwise on indium tin oxide (ITO) coated glass electrodes (5 x 5 cm^2, 20 nm ITO) and dried under vacuum for 2 h. The two electrodes were clamped together and separated by a PDMS spacer. The gap was filled with 400 µl MilliQ water and the electrodes were connected to an AC volt generator (20 MHz programmable function generator, Series 8200, Kontron Messtechnik, Germany) under the following conditions: 1 V at 10 Hz for 2 h. Vesicles were diluted 1:10 in water and release experiments were started with the exposure of GUVs to 150 µg ml^{-1} nanoparticles for 0 to 180 min (198).

2.2.2 Molecular biology and protein biochemistry

In the following section, methods of plasmid cloning and techniques of protein biochemistry are described.

2.2.2.1 Transformation of E. coli

For the amplification of plasmid DNA in bacteria, chemically competent OneShot® TOP10 *E. coli* (Life technologies; U. S. A.) were used. For the transformation, bacteria were thawed on ice for 5 min. 30-300 ng of plasmid was added to the bacteria and incubated on ice for another 15 - 20 min. Heat-shock was performed at 42 °C for 30 sec. After chilling on ice for 2 min, the transformed bacteria were incubated in 1.5 ml S. O. C. medium for 1 h at 37 °C under agitation. The culture was plated on antibiotic LB agar and incubated for 12 - 16 h at 37 °C.

2.2.2.2 Plasmid DNA isolation from E. coli

To amplify plasmid DNA at small or medium scales, a picked *E. coli* colony was cultured in 50 - 100 ml antibiotic LB medium overnight at 37°C. Cells were harvested at 6000 x g for 15 min at 4 °C. Plasmid DNA was isolated with the Qiagen Mini/Midi preparation kits according to manufacturer´s instructions. The DNA pellet was dissolved in an appropriate volume of nuclease-free water and stored at -20 °C.

2.2.2.3 DNA concentration measurements

Concentrations of plasmid DNA and RNA were measured by determining the absorbance (A_{260}) using a NanoDrop 8000 (Thermo Scientific). Protein impurities were routinely checked by determining the A_{260}/A_{280} ratio. Samples with an absorbance ratio A_{260}/A_{280} of 1.8-2.0 were used for further experiments.

2.2.2.4 SDS-PAGE

To separate complex protein mixtures and cell lysates according to their size, a SDS-PAGE was performed. The protein sample was mixed with LDS sample buffer, heated up for 5 min at 95 °C and was then loaded on a 10% NuPAGE bis-tris gel. As a protein marker, the SeeBlue Plus2 prestained marker (Life technologies) was used. Proteins were separated at 100 V for 1.5 h and then forwarded to western blotting or coomassie staining. Coomassie staining was performed after the protocol of Candiano *et al*.(199).

2.2.2.5 Western blotting

Transfer of proteins to PVDF membranes was performed with the iBlot dry-blotting system according to the manufacturer´s protocol (Life technologies). Development of blots was conducted using the western breeze immunodetection kits (Life technologies). The blots were recorded inside a LAS3000 imager (Fujifilm, Japan).

2.2.2.6 RNA isolation and cDNA synthesis

cDNA synthesis was performed after RNA isolation (Qiagen RNeasy kit) from treated or untreated cells utilizing the iScript cDNA synthesis kit (Bio-Rad). cDNA synthesis was performed as stated in the manufacturer´s protocol (Bio-Rad). Concentrations of RNA solutions were determined by Nanodrop measurements. Quality of RNA was investigated on a 3 wt% agarose gel, which was loaded with SYBR green.

2.2.2.7 Quantitative real time polymerase chain reaction

Quantitative real time PCR was used to analyze the expression levels of mRNA after siRNA-mediated mRNA knockdown. Briefly, SYBR green insertion into specifically amplified PCR products was measured. Gene expression was evaluated by the comparative ΔΔCt-method (200). Normalization of data was based on the expression levels of the two reference genes GAPDH and β-actin. Calculations of normalized expression levels were conducted with the software CFX manager (Bio-Rad).

2.2.3 Cell culture

All experiments were aseptically carried out with HeLa, Jurkat and multipotent mesenchymal stroma cells (hMSCs) according to security level S1 safety issues. HeLa cells (DSMZ, Germany) were cultivated in DMEM (Life Technologies) that was supplemented with 10% fetal calf serum (Invitrogen, U.S.A.), 100 units penicillin, 100 µg ml^{-1} streptomycin and 1 mM pyruvate (all Life technologies). Jurkat cells were cultivated in RPMI-1640 supplemented with 10% fetal calf serum (Invitrogen), 100 units penicillin, 100 µg ml^{-1} streptomycin and 1 mM pyruvate. Multipotent mesenchymal stroma cells were cultured in α-MEM with 20% FCS, 100 units penicillin, 100 µg ml^{-1}, 1 mM pyruvate and 2 µg ml^{-1} ciprofloxacin. Cells were passaged until a confluency of ~80% was reached. All cells were incubated in a humidified incubator with 5% CO_2 at 37 °C (Labotec, Germany).

2.2.3.1 Nanoparticle treatment of cells

Nanoparticle studies were performed with the standard concentrations of 75 µg ml^{-1} or 150 µg ml^{-1} (solid content). For this, cells were seeded at a concentration of 15.000 – 20.000 cells per cm^{-2}. Nanoparticles were dispersed in full growth medium, added to cells and incubated for the indicated time. Afterwards, nanoparticles were removed by washing and cells were forwarded to the indicated analysis.

2.2.3.2 Feeding of lipid droplets and nanoparticle cargo release

For nanoparticle cargo release studies, HeLa cells were fed with oleic acid. For this, the complexation of fatty acid free BSA was performed with oleic acid. 100 mM oleic acid was dissolved in 10 ml of 100 mM NaOH at 50 °C. In parallel, 150 mg fatty acid free BSA was dissolved in 1.15 ml PBS under shaking at 50 °C. The molar ratio of OA/BSA was set to 6:1 (pH 7.6). For the feeding of lipid droplets, HeLa cells were incubated with 25 µM OA-BSA overnight. The BSA-carrier served as a control. For cargo release experiments, 150 µl ml^{-1} nanoparticles were added for 30 min and fluorescence images were acquired using an Olympus XI81 fluorescence microscope.

2.2.3.3 Modification of endocytosis and cell signaling by small inhibitor molecules

Inhibition of different endocytosis and signaling pathways was conducted utilizing freely permeable small inhibitor molecules (Table 5). Inhibitors were dissolved according to manufacturer´s recommendations – most frequently in DMSO. Depending on the accepted concentrations in literature and the observed cytotoxic effects, the preincubation of the inhibitors was performed for 30 - 60 min in PBS at the indicated concentrations. For cytochalasin D and the reversible PI3K inhibitor Ly294002, target suppression was performed in full growth medium. After inhibition, nanoparticles

and controls were added to the cells as long as indicated. Quantification of endocytosis was performed by flow cytometry.

2.2.3.4 Nucleofection of siRNA and transfection of plasmid DNA

The transfection of HeLa cells with siRNA was performed by nucleofection. 5 x 10^5 cells were resuspended in 90 µl of SE cell line solution. 30 - 300 pmol of siRNA was added. Nucleofection was carried out in a 100 µl nucleofector cuvette that fitted into the 4D nucleofector (Lonza, Switzerland). A cell line-specific nucleofection program was applied. Nucleofected cells were transferred into 1 ml of full growth medium. After 2 - 3 days of knockdown, mRNA and protein levels were evaluated by qPCR and western blotting, respectively. Transfection of plasmid DNA was performed using Fugene HD (Promega) according to manufacturer´s protocol. Evaluation of protein expression was checked 24 - 48 h after transfection.

2.2.4 Magnetic separation of intracellular vesicles

For the purification of intracellular vesicles from cells, HeLa cells were loaded with SPIOPSN and the magnetic isolation of vesicles was performed. For this, 150 µg ml^{-1} nanoparticles were added to 1.8 x 10^7 HeLa cells growing in the exponential phase (DSMZ, Germany). Cells were exposed to nanoparticles for 20 h at 37 °C and 5% CO_2. Then, cells were thoroughly washed ten times with a total of 1000 ml of PBS (Life technologies) to remove extracellular particles and debris. After the neutralization of trypsin with cell culture medium, further washes were conducted. The last washing fraction was centrifuged (20.000 x g, 30 min) and macroscopically checked for free nanoparticles. Afterwards, cell disruption was performed using a 27 G needle (BD biosciences). Disruption was microscopically monitored after exactly 35 strokes. This step was performed on ice and in 0.5 ml PBS with cOmplete protease inhibitor (Roche). Cell debris was removed by cooled centrifugation (5 min at 453 x g). The supernatant was recentrifuged until no debris was detectable. The brownish cytosolic supernatant was then injected into a custom-made magnetic sorting device with a strong neodymium magnet (Article no. Q-60-30-15-N; Supermagnete; Germany). Magnetic adhesion was conducted over 12 h under cooling and in the presence of protease inhibitors in a strong magnetic field. The small magnetic pellet was carefully washed five times with 3 ml PBS (with protease inhibitor). For quality control, parts of the magnetic pellet were transferred to transmission electron microscopy and checked for non-vesicular impurities. An SDS-PAGE was performed to observe first differences in protein composition of the fractions. For label free quantitative LC-MS, nanoparticle associated proteins were solubilized in 25 µl buffer (7 M urea, 2 M thiourea, 4% CHAPS). After solubilization, nanoparticles were removed for 30 min at 20.000 x g and the supernatant was forwarded to LC-MS analysis. The nonmagnetic fraction was treated comparably.

2.2.5 Mouse experiments and *in vitro* cell sorting

Investigations of the *in vivo* distribution of nanoparticles were performed in the lab of PD Dr. Ralph Meyer at the University medical center in Mainz. For this, 2 mg of SPIOPSN were tail-vein-injected into NSG mice. After 20 h of SPIOPSN exposure, peripheral blood, spleen, liver and kidney were prepared. Single cell suspensions were obtained using a cell strainer. Single cells were magnetically separated by MACS columns and forwarded to confocal microscopy for qualitative analysis.

2.2.6 Immunocytochemistry

The following section describes the methods used for the detection of intracellular proteins and the staining of cell compartments.

2.2.6.1 Immunofluorescence staining

For immunostainings, 15.000 cells cm^{-2} were seeded in Ibidi iTreat µ-dishes. After nanoparticle incubation, cells were fixed with 4% paraformaldehyde and 0.025% glutaraldehyde for 20 min (both Sigma Aldrich). Cell permeabilization was conducted with 0.1% saponin (Sigma Aldrich) for 10 min at RT. Blocking was performed by the incubation of the cells with 3% BSA for 10 min at 37 °C. The primary antibodies were incubated for 60 min in 1% BSA at 37 °C. After washing, the respective secondary antibody was applied for 30 min in 1% BSA at 37 °C. The sample was washed again and then forwarded to confocal microscopy.

2.2.6.2 Filipin staining, CellMask Orange staining and LysoTracker staining

Cholesterol was stained with filipin (83). After washing of the cells with PBS, 50 µg ml^{-1} filipin in PBS was applied to the cells for 15 min. Cells were washed two times with PBS and then analyzed by fluorescence microscopy. Cell Mask Orange and LysoTracker stainings were performed according to manufacturer´s instructions.

2.2.7 Microscopy

In the upcoming section, the used microscopic methods are described.

2.2.7.1 Fluorescence microscopy

An Olympus XI81 fluorescence microscope equipped with a Olympus U-RFL-T-Mercury lamp unit was used for fluorescent microscopy to visualize GUVs and cells. An UPlanFI 100x/1.30 immersion oil objective was used for the experiments. CellSense Dimension software (Olympus) was utilized for image recording.

2.2.7.2 Confocal microscopy

Cells were imaged by confocal laser scanning microscopy using a commercial setup (LSM SP5 STED Leica laser scanning confocal microscope, Leica Microsystems, Germany) consisting of an inverse fluorescence microscope DMI 6000 CS. The microscope was equipped with a laser combination and with five detectors operating in a range of 400 - 800 nm. A HCX PL APO CS 63x/1.4-0.6 oil objective was used. Nanoparticles (pseudocolored red) were excited with an argon laser (20 mW; λ=514 nm) and detected at 530 - 545 nm. Secondary antibodies were excited with a 488 nm HeNe laser (pseudo-colored green) and detected at 510 - 525 nm in a sequential scanning mode. PMI was pseudocolored in green. Image analysis was performed with LAS AF software (Leica, Germany). Recording of z-Stacks was conducted in a stepsize of 300 nm. For live cell imaging, cells were incubated with nanoparticles, washed with DMEM and PBS and analyzed by confocal microscopy using the XYT-mode recording a single image each 3s. Images were evaluated with LAS AF 3000 software (Leica) or Velocity (PerkinElmer).

2.2.7.3 Cryo high pressure freezing electron microscopy

Cryo high pressure freezing electron microscopy experiments were performed by Claudia Messerschmidt as described in the published work (201).

2.2.8 Flow cytometry

Nanoparticle uptake was quantitatively measured by flow cytometry. Cells were seeded at 15 000 cells cm^{-2} and incubated with 75 - 150 µg ml^{-1} nanoparticles for the indicated time. Then, cells were washed with DPBS (Life Technologies), trypsinized and forwarded to flow cytometry. Flow cytometric analysis was performed using a CyFlow ML cytometer (Partec) with a 488 nm laser for the excitation of BODIPY and a 527 nm band pass filter for emission detection. Cytotoxicity was measured staining the cells with 28.6 mg ml^{-1} 7-aminoactinomycin D (7-AAD). Excitation of 7-AAD was conducted at 562 nm and emission was measured at 682 nm. Data analysis was performed using FCS Express V4 software (DeNovo Software, U.S.A.) by selecting the counted cells on a forward/sideward scatter plot, thereby excluding cell debris. These events were further analyzed for uptake. Median intensity was determined in triplicates.

2.2.9 Fluorescence spectroscopy

Fluorescence spectroscopy was performed by using a Tecan Infinite® M1000 PRO (Tecan, Germany). Samples were prepared in a 96-well plate (Greiner). Absorbance or fluorescence measurements were performed with the standardized settings of the software icontrol® (Tecan).

2.2.10 TOP3-based label free quantitative mass spectrometry

Samples were prepared for mass spectrometry as described in section 2.2.4. TOP3-based label free quantitative mass spectrometry measurements were performed by Dr. Stefan Tenzer (Institute of Immunology, University clinics Mainz) (24). Database alignment of the peptide fragments was conducted by Dr. Stefan Tenzer.

2.2.11 DAVID ontology analysis

After the data evaluation of the MS spectra, protein enrichment factors were determined. All proteins that were > 2-fold enriched inside the magnetic fraction in comparison to the nonmagnetic supernatant were forwarded to DAVID protein ontology analysis (http://david.abcc.ncifcrf.gov/). Functional annotation clustering was performed using DAVID ontology analysis with the GOTERM_CC_FAT. High stringency analysis classified proteins in different annotation clusters. P-values and benjamini-values were calculated. Reconstruction of intracellular nanoparticle trafficking is based on the GOTERMs “vesicles” and “lysosome”.

2.2.12 Statistical analysis

Statistical analysis of the data was performed using MS Office Excel 2010 (Microsoft) and GraphPad Prism 5.0 (GraphPad software, U. S. A.). For statistics, mean and standard deviation of the data sets were calculated. For analytical statistics, treated groups were compared and analyzed with GraphPad Prism 5.0. To compare two data sets, a Student´s t-test was performed. Data groups with a p-value less than 0.05 were considered as significantly different.

3. Results

The following chapter provides the major results of this work. The gained observations are subdivided into three parts. The first section is based on the publication "Drug delivery without nanoparticle uptake: delivery by a kiss-and-run mechanism on the cell membrane" describing the interaction of nanoparticles with cell membranes and the non-invasive delivery of hydrophobic molecules to cells (6). The second part reveals the results of the entry mechanisms of superparamagnetic iron oxide polystyrene nanoparticles (2). Finally, the third section presents the findings of the intracellular nanoparticle trafficking (Hofmann *et al.*, major revision).

3.1 Nanoparticles deliver cargo to cells via a "kiss-and-run" mechanism

In the first part of this study, we have investigated the drug delivery potential of biodegradable poly-L-lactide nanoparticles in terms of drug release kinetics, drug release mechanisms and subcellular distribution of the nanoparticulate cargo. The initial idea was to demonstrate a novel and non-invasive strategy for drug delivery, since nearly all concepts of nanoparticulate drug delivery devices rely on intracellular nanoparticle uptake. One major drawback of invasive drug delivery systems is that the nanoparticulate drug stays inside the endosomal lumen, while the target site is frequently located inside the cytoplasm. Release can only be triggered by the disruption of the endosome or by the disassembly of the nanomaterial through fairly unknown endolysosomal components of nanoparticle-containing vesicles. From the site of material science, this strategy also requires a sophisticated synthesis protocol to obtain such nanomaterials (6, 83, 202-204). To bypass complex endocytosis mechanisms and ambitious synthesis routes, a direct way of cargo delivery right on the cell membrane could avoid these hurdles.

One of the most important prerequisites for the demonstration of such a non-invasive drug delivery mechanism is the rapid delivery of the cargo within several minutes. The likelihood of a regular nanoparticulate endocytosis has to be minimized, since cargo release can then occur via the endosomal membrane. After intensive research on this, we have identified a suitable and biodegradable nanoparticulate system that was synthesized of poly-L-lactide (detailed description of nanomaterial properties in Table 1). Additionally, the nanoparticles were loaded with the hydrophobic and fluorescent model cargo *N*-(2,6-diisopropylphenyl)-perylene-3,4-dicarbonacid-imide (PMI, BASF) to monitor cargo release. The magnetite load assisted in the detection of the nanoparticles by transmission electron microscopy (TEM). To examine the nanoparticulate cargo release in more detail, we studied the interaction of nanoparticles with cellular systems.

3.1.1 Hydrophobic nanoparticulate cargo is rapidly delivered into highly diffractive organelles of Jurkat and HeLa cells

To test whether PLLA-Fe-PMI nanoparticles have the potential to rapidly and non-invasively release their cargo molecules, we studied the interactions with the human T lymphocyte cell line Jurkat. Previous studies from our group and others showed that primary T lymphocytes and Jurkat cells lack the uptake of polymeric nanoparticles (66, 205, 206). Therefore, Jurkat cells are a suitable system to demonstrate the non-invasive delivery of the cargo molecules. Experimentally, Jurkat cells were incubated with PLLA-Fe-PMI nanoparticles for 20 min as seen in the representative confocal images in Figure 7. Confocal images were recorded every 2-3 min to track the intracellular cargo delivery. After 5 min of incubation, a perfect colocalization of PMI with highly diffractive organelles was observed (n = 200 cells; colocalization of PMI with highly diffractive organelles = 100%). Similar observations were recorded for the PMI transport into the cervical cancer cell line HeLa (n = 120 cells; 100% colocalization of PMI with highly diffractive organelles).

Over time, the PMI signal accumulated inside the highly diffractive organelles. PMI accumulation was dependent on the PLLA-Fe-PMI concentration as shown by flow cytometry (Figure 7C). Further experiments with hMSCs (n = 10 cells; 100% colocalization with highly diffractive organelles) additionally confirmed the results of a rapid cargo delivery in primary cells (data not shown). Several other tested nanoparticles such as PLLA-PMI and PS-COOH-PMI revealed similar results in concerns to the velocity of PMI delivery into highly diffractive organelles of HeLa cells as also shown in the respective publication (6).

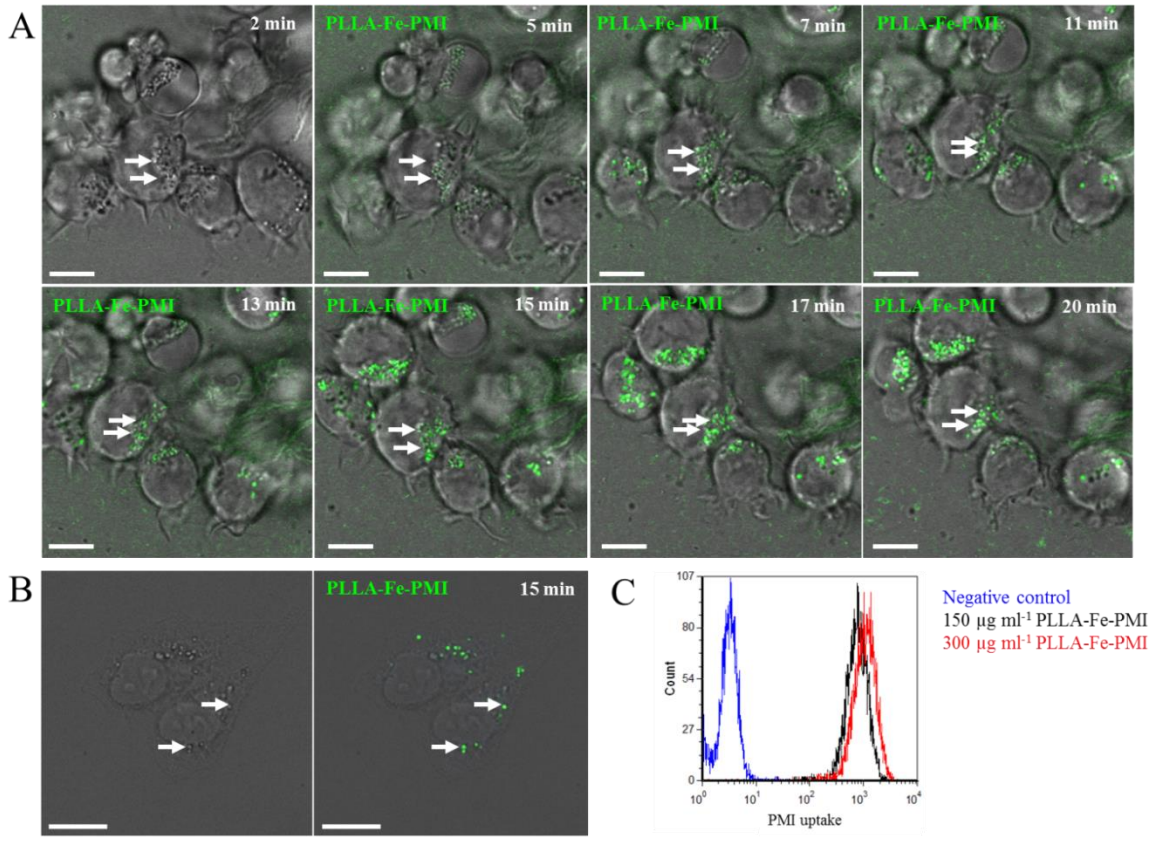

Figure 7: The nanoparticulate cargo PMI is rapidly delivered into a subcellular compartment with a high diffractive index. (A) Jurkat cells were exposed to 150 µg ml^{-1} PLLA-Fe-PMI nanoparticles. PMI accumulation was analyzed by confocal live cell imaging. A low intracellular accumulation of PMI was visible after 5 min of incubation. PMI further accumulated inside organelles that had a high diffractive index in DIC microscopy (white arrows). (B) HeLa cells were exposed to 150 µg ml^{-1} PLLA-Fe-PMI nanoparticles. The accumulation of PMI inside highly diffractive organelles was subsequently recorded by confocal microscopy after 15 min of nanoparticle incubation (white arrows). (C) HeLa cells were exposed to 150 µg ml^{-1} and 300 µg ml^{-1} PLLA-Fe-PMI for 1 h, respectively. PMI delivery was quantified by flow cytometric. Scale bars: 10 µm. Representative images are shown.

To assure that the staining of intracellular compartments originated from the nanoparticle and not from the free dye, we analyzed if non-encapsulated dye molecules are present in our nanoparticulate dispersion. For these experiments, the supernatants of PLLA-Fe-PMI were obtained by the centrifugation of the nanoparticle stock solution. Subsequently, experiments with nanoparticle supernatants were performed. To study the presence of free dye molecules, the same volume of PLLA-Fe-PMI supernatant was added to HeLa cells that was equal to the used volumes in the nanoparticle-containing experiments (Figure 8A). Also a three times higher amount of supernatant did not stain the intracellular compartments. Moreover, we measured the fluorescence of the supernatants by fluorescence spectroscopy (Figure 8B). In summary, the results showed that the nanoparticle supernatants significantly lacked free dye molecules in *in vitro* experiments after two hours of exposure to HeLa cells. Therefore, it was not surprising that only the treatment with PLLA-Fe-PMI nanoparticles induced an accumulation of PMI inside the cells (Figure 8A). The analysis of the supernatants by fluorescence spectroscopy confirmed that the investigated nanoparticle suspension lacked significant amounts of free dye molecules (n = 3; student´s t test; *** indicates $p<0.001$).

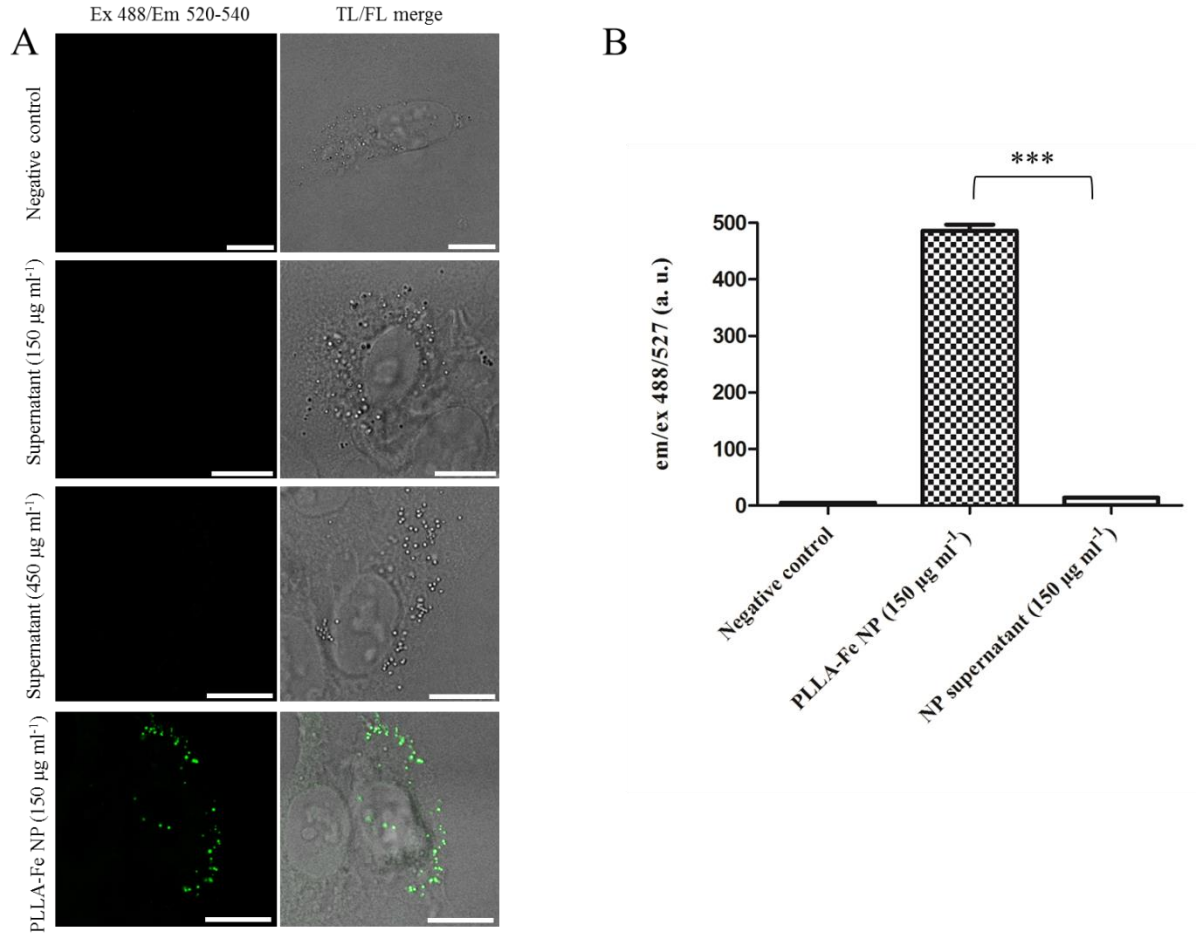

Figure 8: Significant absence of free dye molecules in nanoparticulate supernatants demonstrates that PLLA-Fe-PMI nanoparticles directly deliver PMI to the cells. Supernatants of PLLA-Fe-PMI nanoparticles were tested for the presence of free dye molecules in the continuous phase. (A) PLLA-Fe-PMI supernatants were obtained by the centrifugation of PLLA-Fe-PMI nanoparticles (30 min; 20 000 x g). The appropriate volume of supernatant was added to HeLa cells for 2 h at 37°C that equated to the volumes of the solid contents of 150 µg ml^{-1} and 450 µg ml^{-1}, respectively. Water and pure PLLA-Fe-PMI nanoparticles (150 µg ml^{-1}) served as controls. (B) The fluorescence of PLLA-Fe-PMI supernatants was measured by fluorescence spectroscopy. Water and PLLA-Fe-PMI nanoparticles (150 µg ml^{-1}) served as a control. Values are given as mean + SD. *** indicates $p < 0.001$. Scale bar: 10 µm. TL: Transmission light. FL: Fluorescence light. Representative images are shown.

Taken together, it was shown that PLLA-Fe-PMI nanoparticles directly deliver PMI to Jurkat, HeLa and multipotent human stroma cells in a rapid and efficient manner. In all cells, PMI accumulated inside organelles with a highly diffractive index (Figure 9).

3.1.2 Hydrophobic PMI accumulates inside lipid droplets

By keeping the previous images of DIC microscopy in mind, we suspected that the highly diffractive intracellular compartments could be lipid droplets (LDs) (207). Lipid droplets are intracellular organelles that are present in most of the cells, thereby playing a fundamental role in storing neutral lipids (e. g. triacylglycerols and sterol esters) (208). Lipid droplets are stabilized by a monolayer of amphiphilic phospholipids, whereas integral proteins such as tail-interacting protein 47 (TIP47) or adipose differentiation-related protein (ADRP) are present as important constituents of the LD membrane (209, 210).

To study the subcellular disposition of PMI more precisely, we started to artificially increase the number of lipid droplets by the feeding of HeLa cells with BSA-coupled oleic acid (209). After 18 h of oleic acid treatment, PLLA-Fe-PMI nanoparticles were exposed to the cells (Figure 9). After 5 - 15 min, PMI accumulated again inside these highly diffractive organelles that had increased in number and size due to the oleic acid treatment. These results indicated that the total intracellular accumulation of PMI is dependent on the mass of incorporated fatty acids inside LDs.

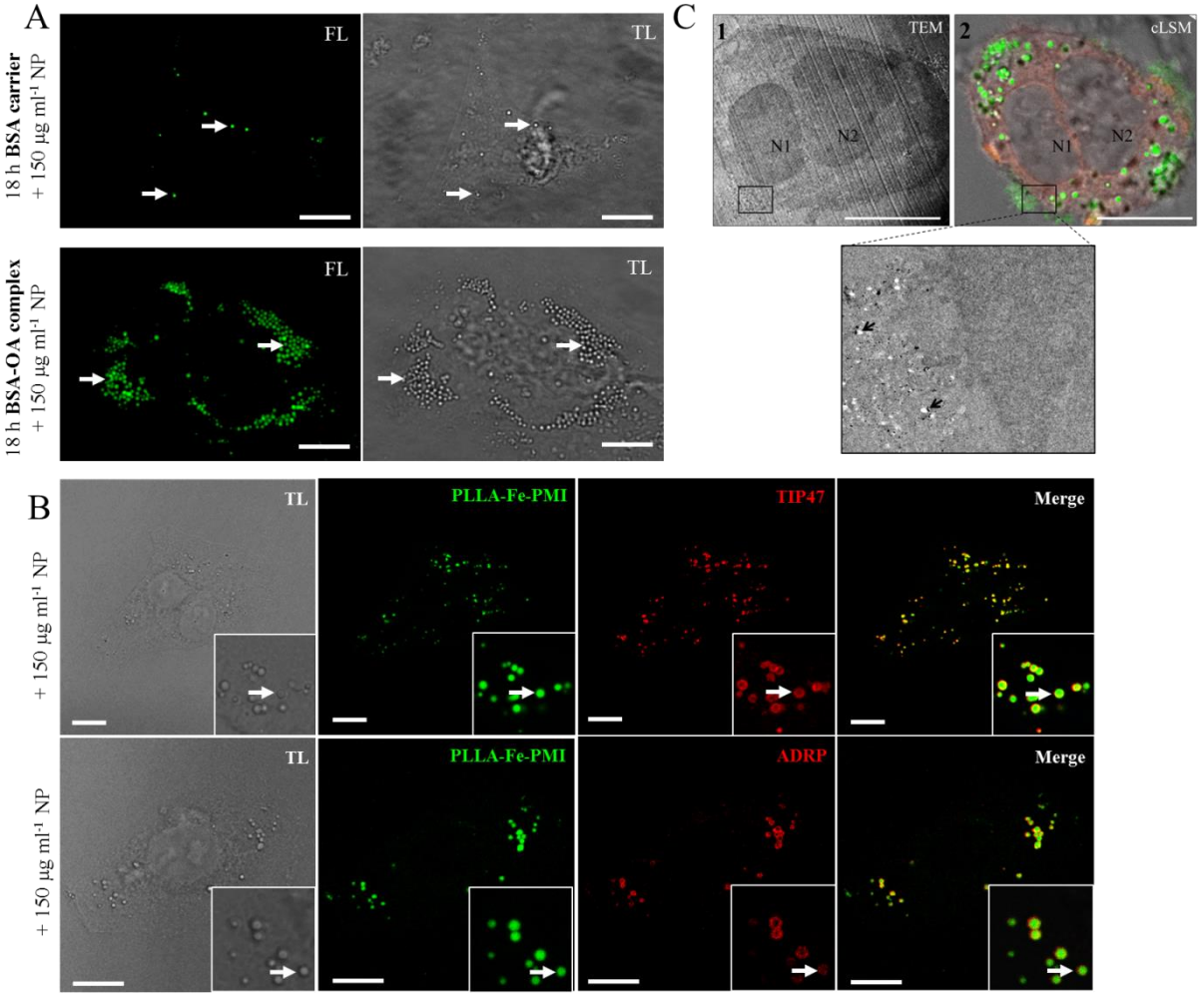

Figure 9: The nanoparticulate cargo PMI accumulates inside hydrophobic lipid droplets. HeLa cells were exposed to PLLA-Fe-PMI nanoparticles. Cells were analyzed for the subcellular disposition of PMI. (A) HeLa cells were fed with pure BSA carrier or with 25 µM BSA-oleic acid complexes for 18 h. Afterwards, cells were exposed to 150 µg ml^{-1} PLLA-Fe-PMI nanoparticles for 15 min. The PMI signal was analyzed by fluorescence microscopy (white arrows). (B) 150 µg ml^{-1} PLLA-Fe-PMI nanoparticles were incubated for 15 min on HeLa cells. After fixation and permeabilization, cells were immunostained for the lipid droplet markers TIP47 and ADRP. Boxes at the bottom right corner show a magnification of the original images. (C) A correlative microscopy approach of a single cell combining transmission electron microscopy (1) and confocal microscopy (2) assisted in the generation of an ultrastructure/fluorescence overlay image to study the disposition of the fluorescent signal and the PLLA-Fe-PMI nanoparticle. Magnification displays PLLA-Fe-PMI nanoparticles (black arrows) in close proximity to the cell membrane. Scale bar: 10 µm. N1/N2: Nucleus 1/ Nucleus 2 (TEM micrographs were recorded by Claudia Messerschmidt). Representative images are shown.

In order to confirm these results further, PMI signals were analyzed for their colocalization with TIP47 and ADRP by immunofluorescence stainings. The PMI signals perfectly colocalized with TIP47 (n = 150 cells; visible ring-like-colocalization: 100%) and ADRP (n = 100 cells; visible ring-like

colocalization: 100%) after nanoparticle exposure. Transmission light analysis identified a high PMI/TIP47/ADRP colocalization with organelles of a high diffractive index. Moreover, a correlative TEM/cLSM approach demonstrated a lack of nanoparticles after 30 min inside cells indicating that PMI delivery is not mediated by an endosomal escape of the dye. Despite of extensive TEM studies, PLLA-Fe-PMI nanoparticles were only detected in the extracellular regions close to the plasma membrane. From these observations one could assume that the interactions between membrane and nanoparticles are not permanent. Indeed, in all live cell imaging experiments, we detected only temporary membrane interactions of PLLA-Fe-PMI nanoparticles that might mediate the delivery of PMI into the cells. Taken together, we could conclude that the encapsulated molecule PMI is released from the nanoparticles into the phospholipid membrane of the cell. This phenomenon was also noticed in release experiments with giant unilamellar vesicles (Figure 10).

3.1.3 Nanoparticulate PMI release is triggered by the contact with hydrophobic media and via the temporary surface interactions with giant unilamellar vesicles

With the previous results, we demonstrated a rapid release and a specific transport of PMI into lipid droplets. In the next experiments, we wanted to gain knowledge about the non-invasive release mechanism of PMI from the PLLA-Fe-PMI nanoparticles. Therefore, we first examined the release of PMI inside different hydrophobic and hydrophilic media (Figure 10A). The release was investigated under permanent contact between the media and nanoparticles for 45 min at 37 °C. Afterwards, we quantified the released dye in the supernatants by fluorescence spectroscopy. We showed that regular growth medium and 1% DMSO failed to trigger the release of hydrophobic cargo into the continuous phase, whereas glyceryl trioleate induced a significant release of PMI into the hydrophobic phase (Figure 10). These results demonstrated that hydrophobic environments can induce the effective release of hydrophobic molecules out of nanoparticles.

Then, we analyzed whether hydrophobic surfaces like artificial cell membranes can potentially trigger the release of PMI. To solve this question, we performed cargo release experiments with giant unilamellar vesicles to simulate a hydrophobic cell membrane a nanoparticle can interact with (Figure 10C). These experiments were performed in pure water and with PLLA-Fe-PMI nanoparticles. The exposure of PLLA-Fe-PMI to DOPC vesicles led to an accumulation of PMI inside the membrane of the GUVs. During this live vesicle experiment, PLLA-Fe-PMI nanoparticles were observed to briefly interact with GUVs for 50 - 100 ms leaving the membrane after a short touching event (Figure 10C; white arrows). We referred to this event as a brief “kiss”, leaving behind some stains on the touched object. After its “kiss”, the particle detached and “runs” away (“kiss-and-run” mechanism). After 15 – 20 min, the DOPC membrane was extensively labeled by PMI.

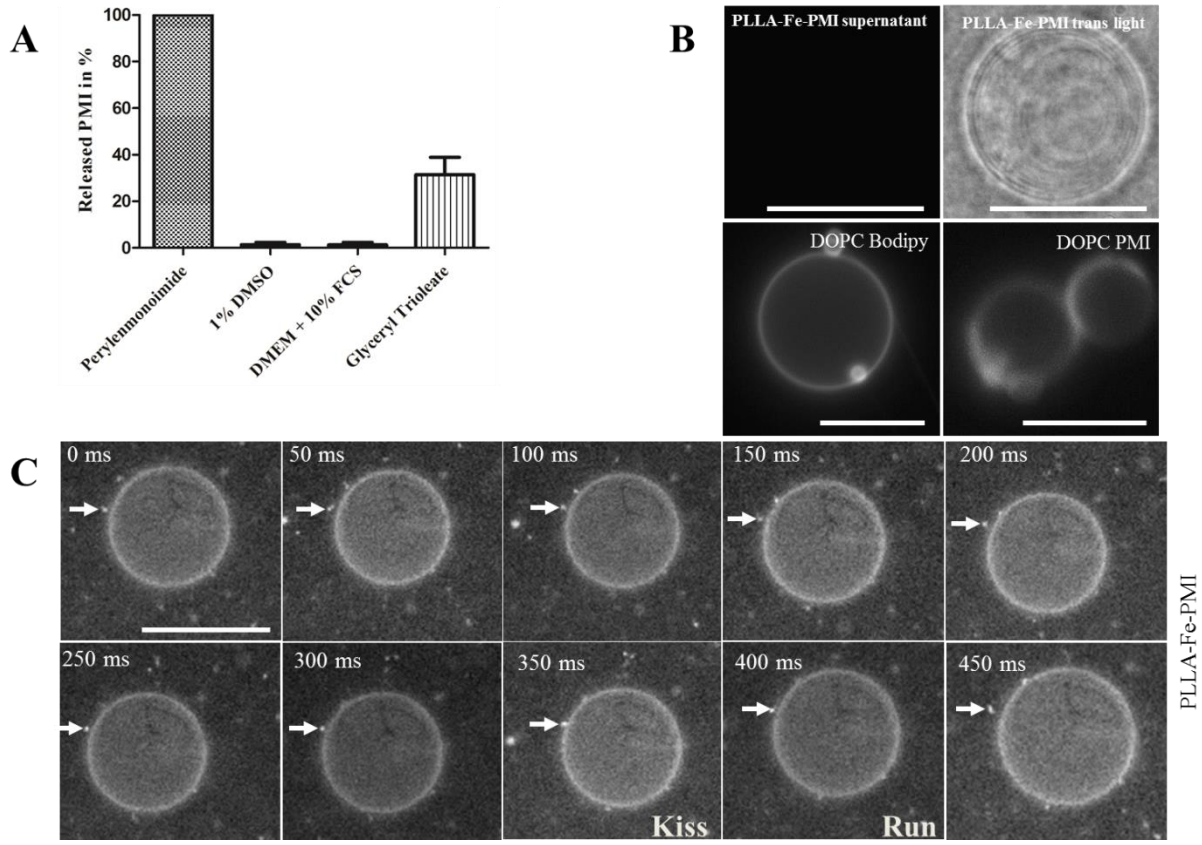

Figure 10: PMI is released from the nanoparticle by hydrophobic interactions with media and surfaces. (A)150 µg ml^{-1} PLLA-Fe-PMI nanoparticles were incubated in 1% DMSO, full growth medium and in glyceryl trioleate solution. The samples were shortly mixed and stored for 45 min at 37°C. After centrifugation, the fluorescence intensity of the supernatant was quantified by fluorescence spectroscopy (measurements were performed by Dr. Markus B. Bannwarth). (B) Giant vesicles made of 1,2-dioleoyl-*sn*-glycero-3-phosphocholine were prepared by electroformation. PLLA-Fe-PMI nanoparticle supernatant, BODIPY and PMI were tested for their features to stain membranes. (C) DOPC vesicles were exposed to 150 µg ml^{-1} PLLA-Fe-PMI nanoparticles for 15 min. PMI accumulation was then recorded by live vesicle imaging to show the "kiss-and-run" mechanism.

Hence, we concluded that the investigated PMI-containing nanoparticles briefly interacted with the phospholipid bilayer of cells and GUVs, thereby releasing the hydrophobic cargo. In cell experiments, PMI diffused through the membrane and accumulated inside the even more hydrophobic surrounding of lipid droplets, while in the case of GUVs only the membrane was stained. In all cases, we observed a "kiss-and-run" mechanism for nanoparticles with noncovalently bound cargo molecules. In contrary, cargo release was suppressed by the covalent bonding of the cargo to the polymeric matrix (Figure 11).

3.1.4 Covalent-bonding of cargo to the polymeric matrix leads to the retention of the cargo molecules inside nanoparticles

In summary, all nanoparticles (with non-covalently bound PMI) that have been tested in this study revealed excellent drug delivery properties. To block the delivery of cargo by "kiss-and-run", polystyrene nanospheres with covalently-bound dyes were synthesized and analyzed by live vesicle and live cell imaging. We identified a polystyrene nanoparticle (PS-NH_2-BODIPY with a covalently-

linked BODIPY dye) that strongly interacted with the giant vesicle. The nanoparticles dashed around on the surface of the vesicle without releasing the dye molecules (Figure 11; white arrows). In contrast, superparamagnetic nanoparticles (SPIOPSN-BODIPY) failed to permanently interact with the surface of the giant vesicle. However, they also revealed a "kiss-and-run"-like mechanism lacking dye release.

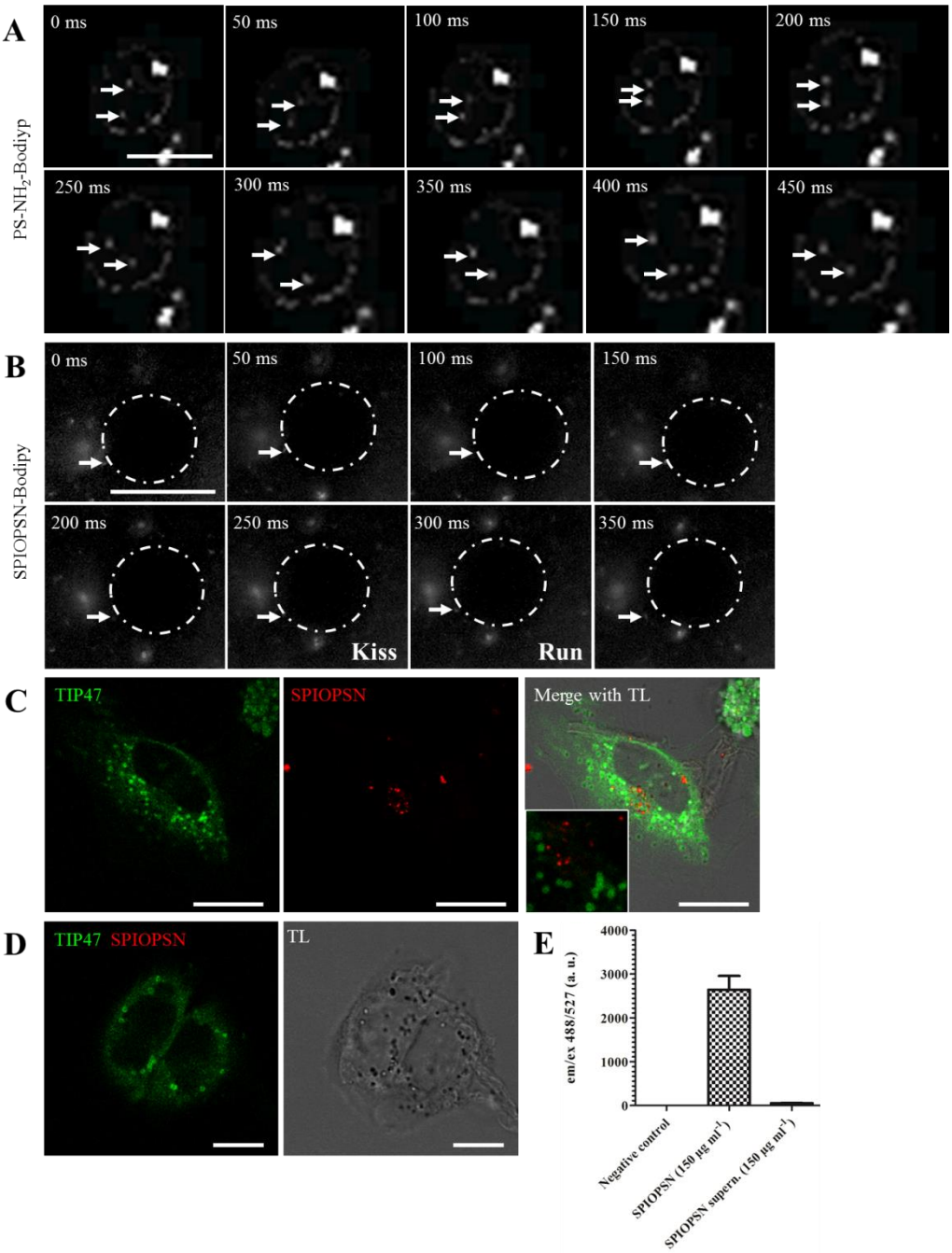

Figure 11: Covalent bonding of cargo molecules to the polymeric matrix inhibits dye release by the "kiss-and-run" mechanism. (A) GUVs (DOPC) were exposed to 150 µg ml^{-1} PS-NH_2-BODIPY nanoparticles for 15 min. Live vesicle imaging was utilized to show "kiss-and-run". (B) 150 µg ml^{-1} SPIOPSN-BODIPY were incubated on GUVs (DOPC) for 15 min. Live vesicle imaging was utilized to show "kiss-and-run". (C) HeLa cells were exposed to 150 µg ml^{-1} SPIOPSN-BODIPY for 20 h. The lipid droplet marker TIP47 was visualized by immunostainings. Representative images are shown. (D) HeLa cells were exposed to SPIOPSN-BODIPY supernatants (volume equaled to the solid content volume of 150 µg ml^{-1}). 20 h later, cells were stained for TIP47 (green). (E) Quantification of free dye molecules was performed by fluorescence spectroscopy.

In cell experiments with SPIOPSN, the nanoparticles also displayed a “kiss-and-run” mechanism in form of a temporary membrane interaction. However, the nanoparticles lacked the colocalization with the lipid droplet marker TIP47 showing that no hydrophobic dye molecules was released from the particles (Figure 11C). Further on, we investigated whether the nanoparticle solution contained free dye molecules. The significant absence of free dye in the supernatant of the nanoparticle dispersion was shown by in vitro measurements and fluorescence spectroscopy (Figure 11D/E).

These observations implied that a covalent bonding between dyes and the polymeric matrix of nanoparticles blocked the dye release by “kiss-and-run”. In this case, SPIOPSN-BODIPY nanoparticles are potentially attractive to study cellular entry mechanisms (see section 3.2).

3.2 SPIOPSN are endocytosed by a macropinocytic-like mechanism

Having investigated the drug delivery properties of several nanoparticles, a well-characterized nanoparticle (SPIOPSN-BODIPY) was identified to analyze the entry mechanisms and intracellular trafficking pathways of polymeric nanoparticles. SPIOPSN-BODIPY are negatively charged superparamagnetic iron oxide polystyrene nanoparticles with an average size of 126 nm that showed less aggregation, only temporarily-interacted with cell membranes and were efficiently taken up into cells. This led us to the analysis of the uptake mechanism, which is utilized by these nanoparticles to enter a cell.

3.2.1 SPIOPSN are cointernalized with dextran-488 and entry is dependent on F-actin

To investigate the entry mechanisms of SPIOPSN, we first analyzed the fluid phase uptake in co-internalization experiments with fluorescently labeled dextran-488. Therefore, HeLa cells were coincubated with SPIOPSN and dextran-488. Colocalization was analyzed after 6 h of incubation by confocal microscopy (Figure 12). Examinations showed that SPIOPSN were transported via dextran-488-filled vesicles. These organelles were also visible by transmission light. Since dextran-488 internalization is generally accepted as a tracer of an F-actin-dependent process called macropinocytosis, we pretreated HeLa cells with cytochalasin D to prevent actin polymerization. After 5 h of SPIOPSN exposure, we detected a significant drop of the internalization rate of nanoparticles in cytochalasin D pretreated cells as compared to untreated cells (decrease to 36.84%, SD 5.17%, $n = 6$, *** indicates $p < 0.001$, Student´s t test). Uptake of dextran-488 was inhibited to a comparable amount (decrease to 52.27%, SD 1.17%, $n = 6$, *** indicates $p < 0.001$, Student´s t test).

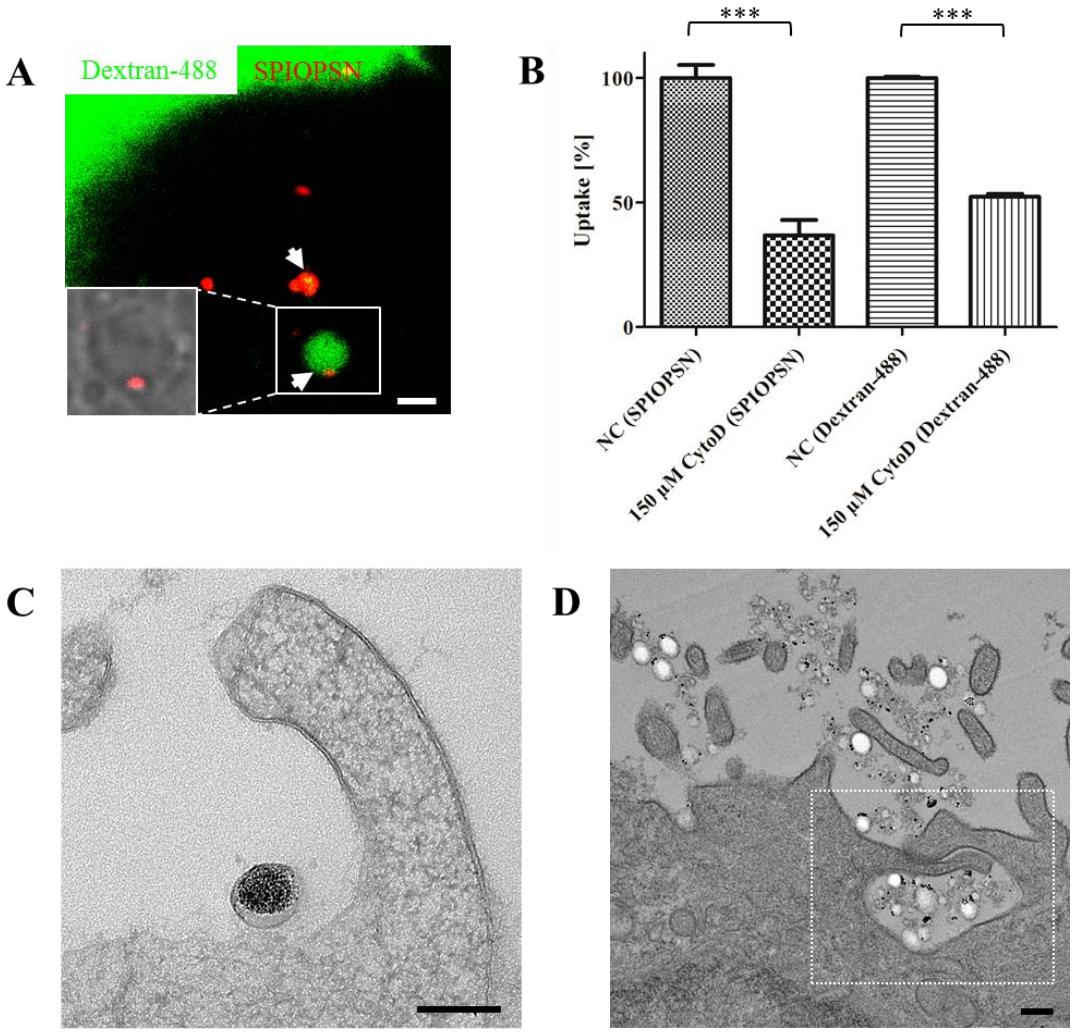

Figure 12: SPIOPSN are cointernalized with the fluid phase marker dextran-488 and entry is dependent on F-actin polymerization. (A) HeLa cells were coincubated with 5 µg ml^{-1} 10 kDa dextran-488 and SPIOPSN for 6 h. Colocalization was then analyzed by confocal microscopy. Scale bar: 1 µm. (B) HeLa cells were preincubated with 150 µM cytochalasin D for 45 min at 37°C. Afterwards, HeLa cells were exposed to 150 µg ml^{-1} SPIOPSN or dextran-488 for 5 h, respectively. Uptake was quantified by flow cytometry. (C) 150 µg ml^{-1} SPIOPSN were incubated on HeLa for 20 h and then analyzed for macropinocytic structures by cryo-transmission electron microscopy. (D) 1200 µg ml^{-1} PLLA-Fe-PMI nanoparticles were incubated for 24 h on HeLa cells and then analyzed for macropinocytic structures (white box) by cryo-transmission electron microscopy (TEM micrographs were taken by C. Messerschmidt). Scale bar: 100 nm. Representative images are shown.

These data pointed towards a macropinocytic uptake mechanism. This hypothesis was supported by transmission electron microscopy, where potential macropinocytic-like structures were identified for SPIOPSN-BODIPY and for PLLA-Fe-PMI nanoparticles. Therefore, we further asked whether small GTPases, which are supposed to be involved in macropinocytosis, mediate the entry of SPIOPSN into HeLa cells (Figure 13).

3.2.2 SPIOPSN entry is accompanied by the small GTPases Rac1 and cdc42 in the initial stages of uptake

The formation of macropinosomes is a complex process that is subdivided into cup initiation, cup extension, cup closure and the separation of macropinosomes (Figure 4). These mechanisms are

tightly regulated by several small GTPases (146). To focus on the early effectors of classical macropinocytosis, we overexpressed constitutively active Rac1 Q61L, cdc42 Q61L and cdc42 T17N as GFP fusion proteins in HeLa cells. 24 h after transfection, SPIOPSN were added to the cells for 6 h. Colocalization of SPIOPSN with Rac1 was analyzed by confocal microscopy. To our knowledge, nanoparticles were found for the first time in roundly shaped Rac1 Q61L^{+} macropinosomes (Figure 13). Nanoparticle tracking analysis revealed that nanoparticles moved inside a defined volume. No direct movements of Rac1 Q61L vesicles were observed. This implied that these vesicles were not budding off from the membrane displaying an early maturation stage of SPIOPSN-containing macropinosomes.

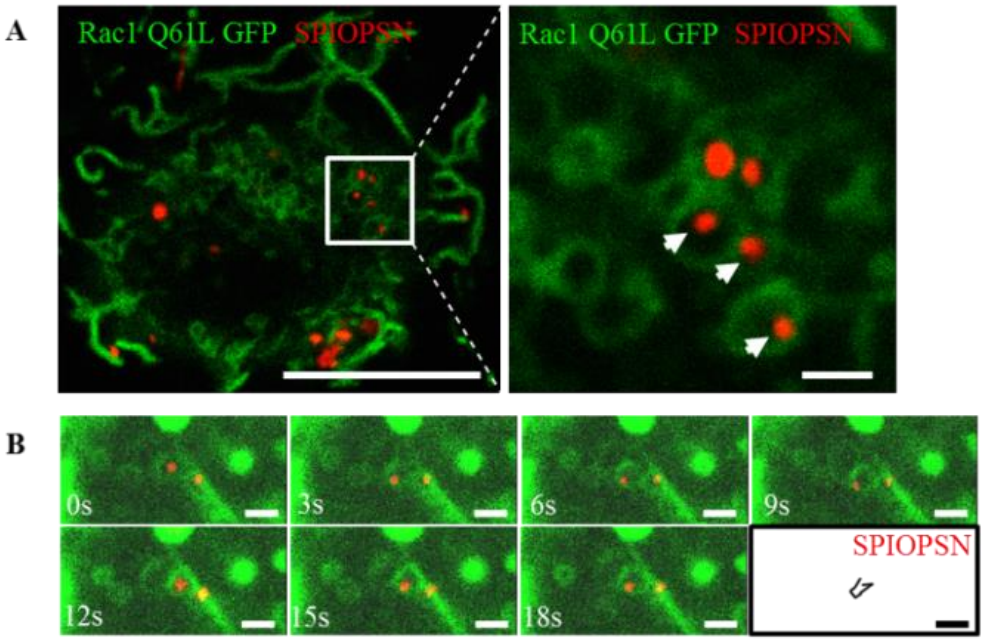

Figure 13: The initial stage of SPIOPSN entry is mediated by the small GTPases Rac1. (A) HeLa cells were transfected with Rac1 Q61L-GFP. 24 h later, cells were exposed to 150 µg ml^{-1} SPIOPSN for 6 h. SPIOPSN entry was analyzed by confocal microscopy. Scale bar (left image): 10 µm. Scale bar (right image): 1 µm. (B) SPIOPSN movement inside Rac1 Q61L-GFP^{+} vesicles was analyzed by live cell imaging generating a motility profile of the nanoparticle on the left site. Scale bar: 1 µm. Representative images are shown.

Similar images were recorded after the overexpression of cdc42 Q61L (Figure 14). After 6 h of incubation, SPIOPSN were located inside roundly shaped premacropinosomes. The morphology of these organelles was similar to the Rac1 Q61L phenotype. In contrary to this, the overexpression of dominant negative cdc42 T17N resulted in a distinct phenotype, also displaying the colocalization with SPIOPSN. Surprisingly, we did not observe a significantly reduced uptake of SPIOPSN in cdc42 T17N^{+} cells (211). Also the downregulation of cdc42 by esiRNA failed to suppress the number of internalized SPIOPSN (Figure 14C). Here, flow cytometric quantification showed no significant changes in SPIOPSN uptake after knockdown. Therefore, we concluded that cdc42 accompanied the internalization of SPIOPSN but had no significant impact to inhibit the uptake.

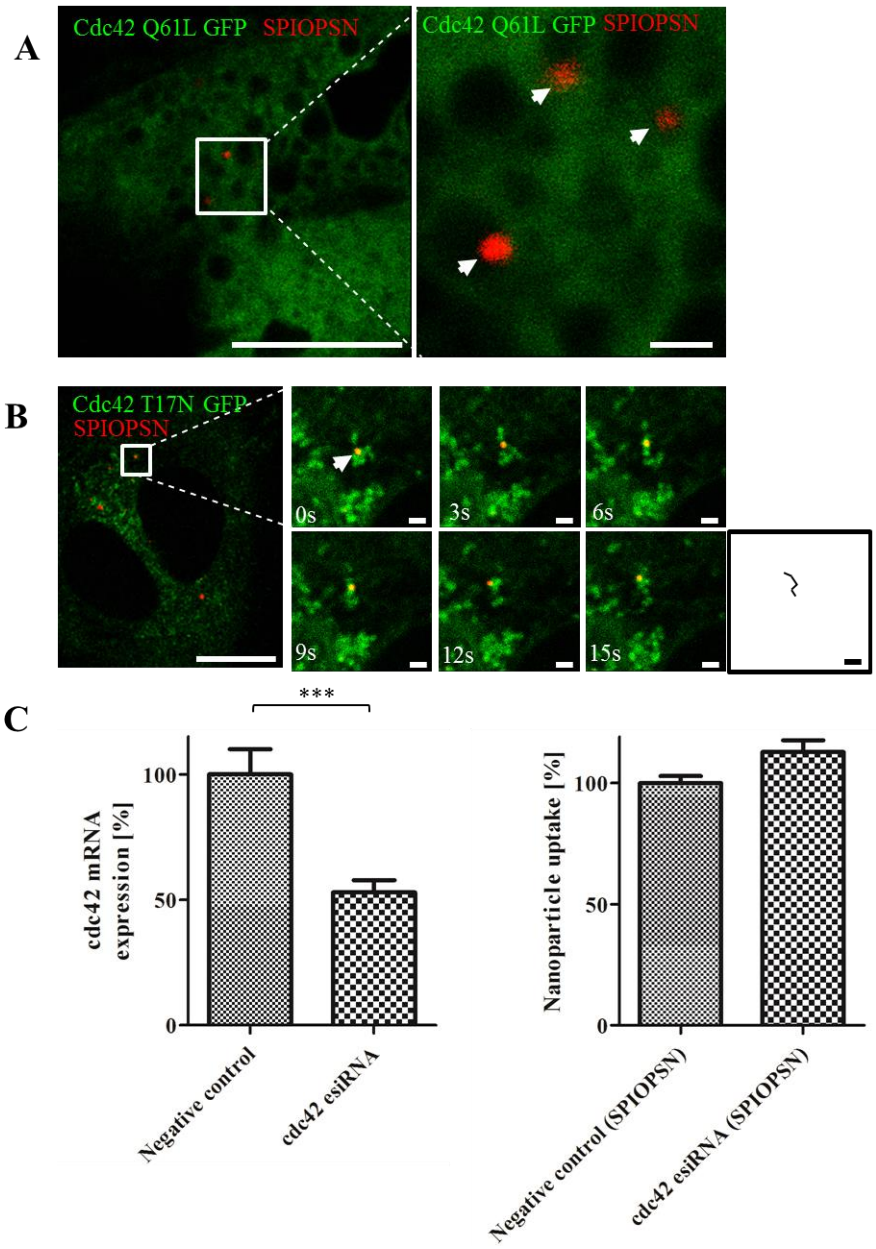

Figure 14: The initial stage of SPIOPSN entry is accompanied by the small GTPases cdc42. (A) HeLa cells were transfected with cdc42 Q61L-GFP for 24 h. Afterwards, cells were exposed to 150 µg ml^{-1} SPIOPSN for 6 h. Colocalization was analyzed by confocal microscopy. (B) HeLa cells were transfected with cdc42 T17N-GFP for 24 h. Subsequently, cells were exposed to 150 µg ml^{-1} SPIOPSN for 6 h. Colocalization was analyzed by confocal microscopy. SPIOPSN movement inside cdc42 $T17N^{+}$ vesicles was recorded by live cell imaging. Representative images are shown. (C) HeLa cells were nucleofected with cdc42 esiRNA. Knockdown efficiency was determined after 3 d by qRT-PCR. HeLa cells were exposed to 150 µg ml^{-1} SPIOPSN. 6 h later, uptake was quantified by flow cytometry.

Taken together, with cdc42 and Rac1, novel proteins have been identified that are associated with the early SPIOPSN-containing macropinosomes. However, we could not show that the overexpression of cdc42 T17N and cdc42 knockdown altered the number of internalized SPIOPSN. These observations pointed towards an atypical macropinocytic-like mechanism. Further on, these investigations raised issues concerning the macropinocytic signaling that might orchestrate SPIOPSN entry (Figure 15).

3.2.3 SPIOPSN entry is dependent on Na^+/H^+ exchangers, phosphoinositide 3-kinase and p21-activated kinase 1 but not on phosphokinase C or phospholipase C

Next, we were interested in the signaling mechanisms, which mediated the endocytosis of SPIOPSN. The previous observations led to the hypothesis that SPIOPSN are internalized by a macropinocytic-like mechanism. To prove this, we preliminary investigated the generally accepted factors that influence viral macropinocytosis (212). Therefore, we tested whether Na^+/H^+ exchangers controlled SPIOPSN entry (94). Other factors that were shown to regulate viral macropinocytosis are kinases. Two of the most important kinases are p21-activated kinase (PAK1) and phosphoinositide 3-kinase (PI3K) (136). Further regulatory kinases such as the protein kinase C (PKC) and phospholipase C have been implicated to be necessary for a classical macropinocytosis (144, 213).

To analyze whether ethylisopropylamiloride (EIPA; inhibitor of Na^+/H^+ exchangers) had an inhibitory effect on SPIOPSN entry, we pretreated HeLa cells with a high, but nontoxic concentration of EIPA. After 5 h of SPIOPSN incubation, uptake decreased to 75.50% (SD 0.23%; n = 4; *** indicates $p < 0.001$; Student´s t test) (Figure 15). The uptake of fluid-phase marker dextran-488 was reduced to 83.66% (n = 3; *** indicates $p < 0.001$, student´s t test) in comparison to nontreated cells.

Furthermore, we observed a suppressed uptake of SPIOPSN after PI3K inhibition in wortmannin-pretreated HeLa cells (n = 6; *** indicates $p < 0.001$, student´t t test; 73.27% uptake in comparison to non-treated cells; SD 2.01). Similar results were obtained after the pretreatment of cells with the PI3K inhibitor Ly294002 (n = 6; *** indicates $p < 0.001$, student´t t test; reduction of uptake down to 61.24%; SD 2%). Inhibition of PAK1 by IPA3 diminished SPIOPSN uptake to 75.51% in comparison to nontreated cells (n = 3; *** indicates $p < 0.001$, student´t t test; SD 1.23%). The control experiment showed that PAK1 inhibition significantly suppressed the internalization rate of the fluid-phase marker dextran-488 (n = 2; *** indicates $p < 0.001$, student´s t test; reduction to 83.33%) (Figure 15C).

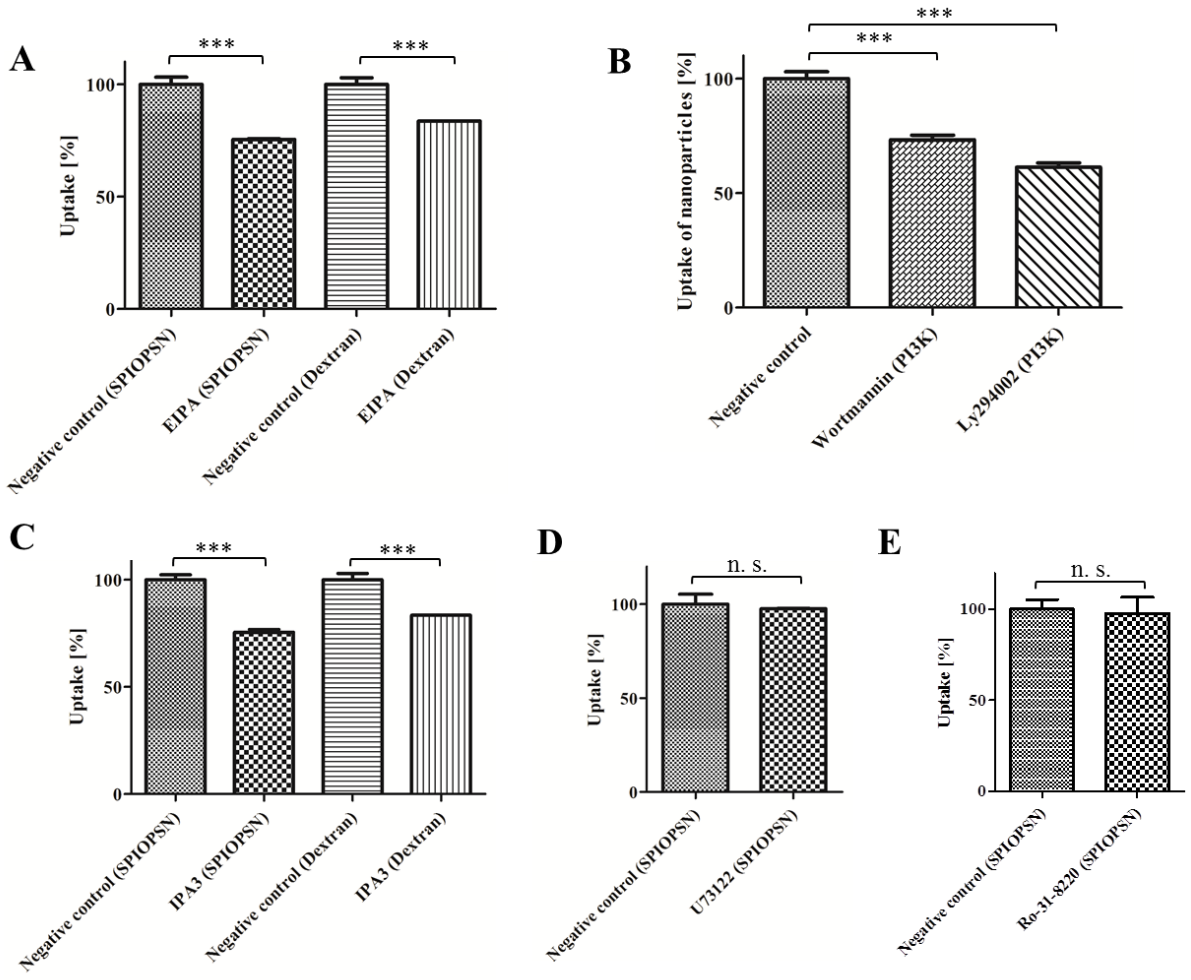

Figure 15: Na^+/H^+ exchangers, PI3K and PAK1 control the uptake of SPIOPSN. Flow cytometric quantification of SPIOPSN uptake in HeLa cells. Cells were pretreated (30 - 45 min) with several inhibitors for Na^+/H^+ exchangers (EIPA), PI3K (Wortmannin and Ly294002), PAK1 (IPA3), protein kinase C (Ro-31-8220) and phospholipase C (U73122). The applied concentrations showed no morphological toxicity. After pretreatment, HeLa cells were exposed to 150 µg ml^{-1} SPIOPSN for 5 h. Subsequently, the uptake of SPIOPSN was quantified by flow cytometry. Reversible inhibitors were coincubated with nanoparticles. DMSO served as a negative control. Dextran served as a control for fluid-phase endocytosis. (A) Pretreatment of HeLa cells with 100 µM EIPA (n = 3 independent experiments; *** indicates $p < 0.001$, student´s t test). (B) Pretreatment with 25 nM Wortmannin and with 50 µM of Ly294002 (n = 3 independent experiments; *** indicates $p < 0.001$, student´s t test), respectively. (C) Pretreatment with 25 µM IPA3 (n = 3 independent experiments; *** indicates $p < 0.001$, student´s t test). (D) Pretreatment with 7 mM Ro-31-8220 (n = 2 independent experiments). (E) Pretreatment with 10 µM U73122 (n = 2 independent experiments).

Then, we investigated the effects of phospholipase C (Inhibitor U73122) and phosphokinase C (Inhibitor Ro-31-8220) on the internalization rate of SPIOPSN. Cells were exposed to high but non-toxic concentrations of both inhibitors. Taken together, no significant changes in the uptake of SPIOPSN were observed. This showed that PLC and PKC did not play are role during the entry of SPIOPSN. Other factors that were tested included nocodazole. Inhibition of microtubule polymerization by nocodazole reduced SPIOPSN internalization to 75.50% (n = 2; SD 3.55%; data not shown). Though, this was not surprising since nocodazole inhibits a large number of distinct mechanisms. Exactly due to this reason, we focused on a more specific mechanism and investigated the effect of dynamin II on the entry rate of SPIOPSN. We found that the internalization of SPIOPSN is dependent on dynamin II (Figure 16).

3.2.4 The macropinocytic-like uptake of SPIOPSN is dependent on dynamin II

After demonstrating that several kinases affected the endocytosis of SPIOPSN, we focused on the GTPase dynamin II. Dynamin II has been extensively studied in CME and caveolae-dependent endocytosis. However, the participation of dynamin II in macropinocytic processes has been controversially discussed (214). In spite of this, we investigated the role of dynamin II during the entry of SPIOPSN. Our experiments showed that the overexpression of dominant negative dynamin 2 K44A-GFP resulted in a significant reduction of SPIOPSN uptake in comparison to non-transfected cells (white circles in Figure 16A). This was confirmed by the dynasore-mediated inhibition of dynamin II (uptake in comparison the non-treated control: 68.68%, n = 3; *** indicates $p < 0.001$; SD 2.06%). Altogether, these data indicated that dynamin II played an important role during the entry of SPIOPSN.

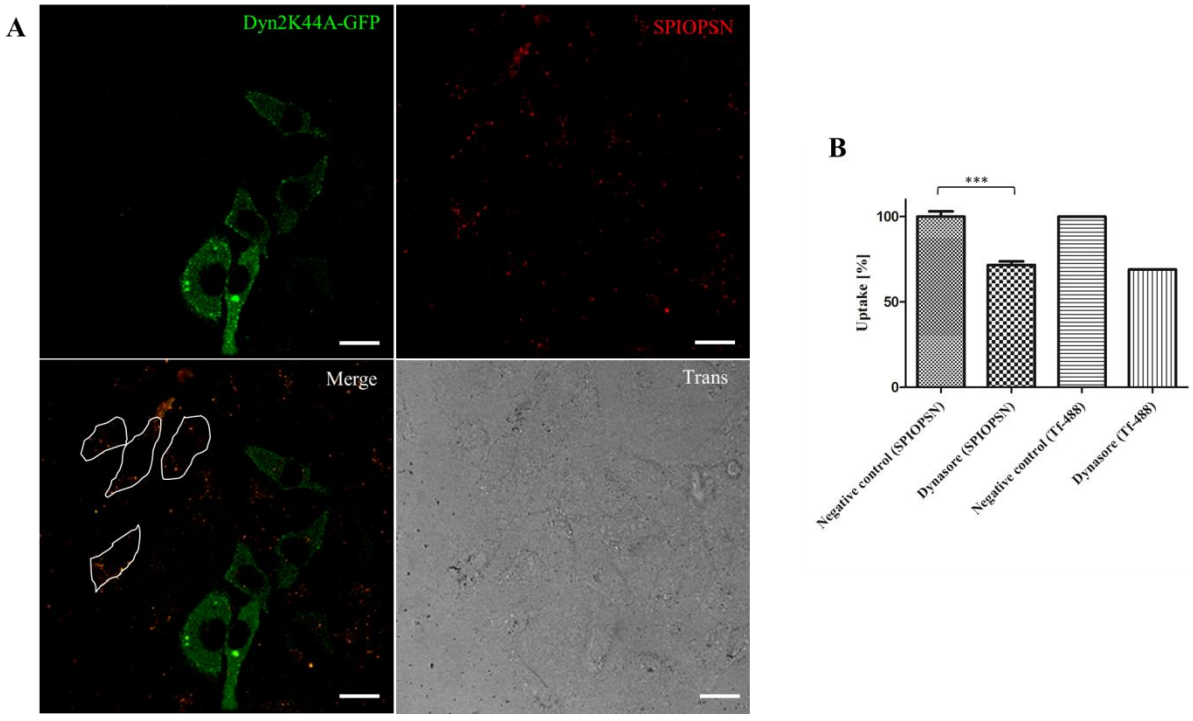

Figure 16: Dynamin II is required for the internalization of SPIOPSN. A qualitative and quantitative analysis of SPIOPSN uptake in dependence on dynamin II manipulations was performed. (A) 24 h after transfection of Dyn2K44A-GFP, HeLa cells were exposed to 150 µg ml^{-1} SPIOPSN for 6 h. The uptake of SPIOPSN was qualitatively analyzed by confocal microscopy. White borders indicate GFP-negative cells. Representative images are shown. (B) HeLa cells were pretreated with 100 µM Dynasore for 40 min. Dynasore-treated and nontreated cells were exposed to 150 µg ml^{-1} SPIOPSN for 5 h. 40 µg ml^{-1} Alexa Fluor-488 coupled transferrin served as a control. Uptake was quantified by flow cytometry ($p < 0.001$; n =3 independent experiments). In all samples, uptake was quantified as the median of the cellular fluorescence intensity.

This chapter and the previous sections showed that several inhibitors were tested to explore the factors that mediated SPIOPSN uptake. Contrary to the inhibitor experiments, we investigated whether several stimulatory effects have an impact on the uptake of SPIOPSN. Surprisingly, the data revealed that the stimulation of macropinocytosis via DAG and EGF resulted in a reduced uptake of SPIOPSN (Figure 17).

3.2.5 Stimulation of classical macropinocytic pathways inhibits the uptake of SPIOPSN

Phorbol-12-myristate-13-acetate is a phorbol ester that is known to activate phosphokinase C. Thus, downstream pathways such as macropinocytosis and others can be triggered (215). Further on, growth factor mediated macropinocytosis can be induced by epidermal growth factor (EGF) stimulation (134, 216).

To approach the question, if classical stimulators of macropinocytosis can boost the uptake of SPIOPSN, we pretreated HeLa cells with PMA or EGF for 45 min. Subsequently, we removed the supernatant and incubated SPIOPSN for 5 h. The incubation with dextran-488 served as a control of fluid-phase endocytosis. After incubation, SPIOPSN uptake was quantified by flow cytometry. Upon PMA stimulation, SPIOPSN uptake decreased to 75.5%; (SD 1.6%; n = 6; *** indicates $p < 0.001$; student´s t test), whereas dextran uptake was stimulated to ~190%; (SD 0.8%; n = 4; *** indicates $p < 0.001$, student´s t test) in comparison to the untreated control (Figure 17). Moreover, the stimulation of HeLa cells with EGF decreased the uptake of SPIOPSNs, too. This was also qualitatively confirmed by the imaging of EGF-stimulated and nonstimulated HeLa cells. Dextran uptake was not affected by the EGF stimulation (Figure 17B).

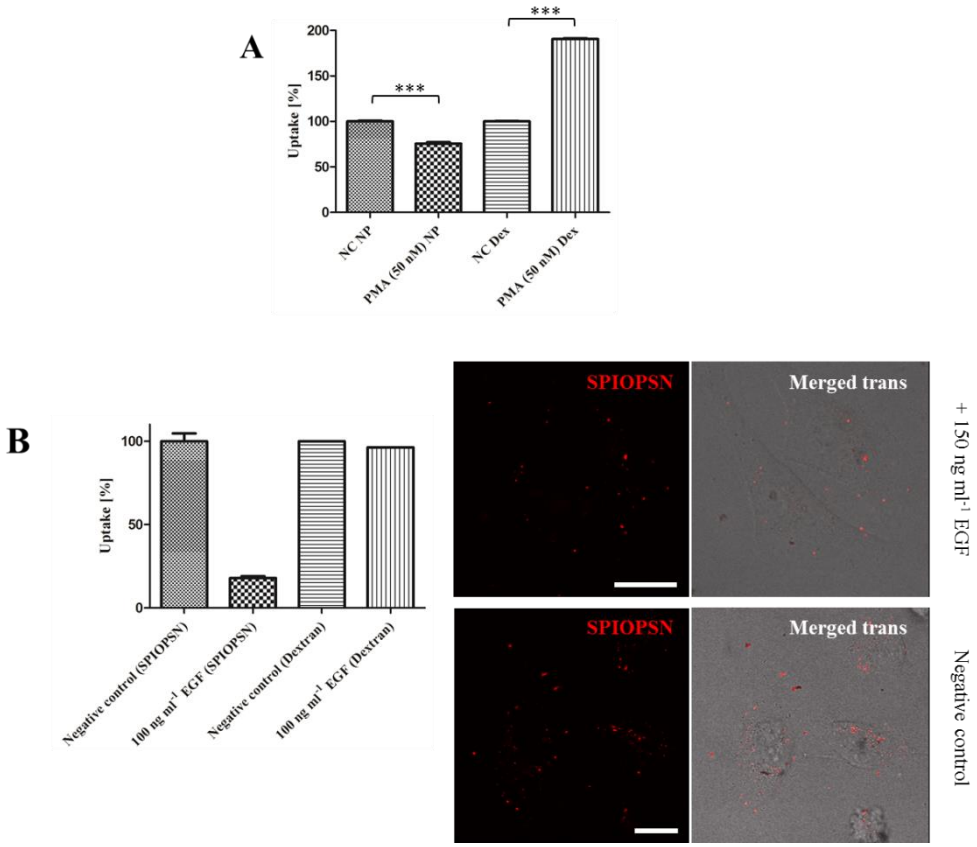

Figure 17: Stimulation of classical macropinocytic pathways suppress SPIOPSN uptake. (A) To stimulate macropinocytosis, HeLa cells were treated with 50 nM phorbol-12-myristate-13-acetate (PMA) for 45 min. Stimulated and non-stimulated cells were exposed to 150 µg ml^{-1} SPIOPSN or 2.5 µg ml^{-1} dextran-488 (10 kDa) for 5 h, respectively. Uptake was quantified by flow cytometry. (n = 6; $p < 0.001$; student´s t test). (B) HeLa cells were stimulated with 150 ng ml^{-1} epidermal growth factor (EGF) for 45 min. Cells were exposed to 150 µg ml^{-1} SPIOPSN or 2.5 µg ml^{-1} Dextran-488 (10 kDa) for 5 h, respectively. Uptake was quantified by flow cytometry. Qualitative analysis of SPIOPSN uptake (A+B) was performed by confocal microscopy. Scale bar: 10 µm. Values are given as median + SD. *** indicates $p < 0.001$. Representative images are shown.

Altogether, these experiments confirmed that SPIOPSN uptake is mediated by an atypical pathway of macropinocytosis. To exclude the participation of other endocytic pathways, we investigated the role of caveolin-1 and clathrin during SPIOPSN entry (Figure 18 and Figure 19).

3.2.6 SPIOPSN are not taken up by a clathrin- and caveolae-dependent mechanisms

After the validation that SPIOPSN are taken up by an atypical macropinocytic mechanism, we wanted to exclude any participation of other pathways that could orchestrate SPIOPSN endocytosis. To approach this, we pretreated HeLa cells with chlorpromazine to block clathrin-mediated endocytosis (Figure 17). Furthermore, we silenced clathrin heavy chain by siRNAs and overexpressed epsin 15 DIII to block clathrin lattice assembly (106). siRNA-mediated silencing of clathrin heavy chain led to a downregulation of clathrin HC down to ~40%. Qualitatively as well as quantitatively no significant changes in SPIOPSN uptake were observed (Figure 18). This was confirmed by the chlorpromazine-

mediated inhibition of CME, where also no significant changes in the uptake of SPIOPSN were observed.

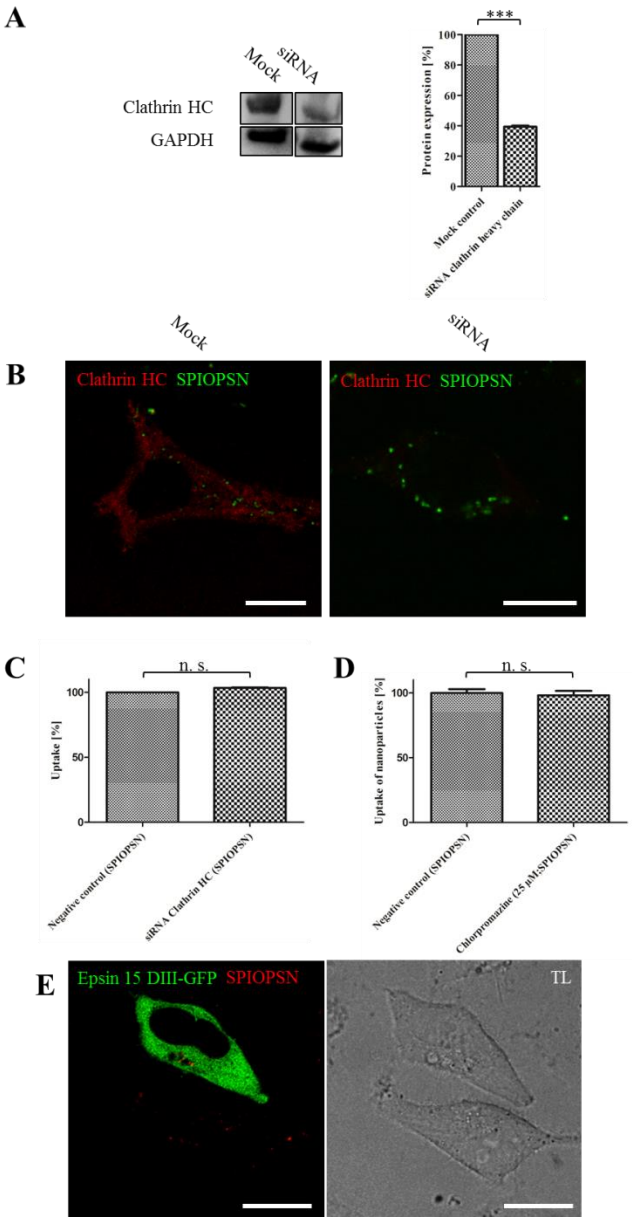

Figure 18: SPIOPSN are not internalized via a clathrin-mediated endocytic mechanism. HeLa cells were transfected with siRNA to silence the clathrin heavy chains. Additionally, CME was inhibited by chlorpromazine treatment and via the overexpression of epsin 15 DIII-GFP. Subsequently, SPIOPSN uptake was qualitatively and quantitatively analyzed. (A) Three days after the nucleofection of siRNA, downregulation of clathrin heavy chain was quantified by western blotting. (B) Mock treated and siRNA treated HeLa cells were exposed to 150 µg ml^{-1} SPIOPSN for 6 h. Immunofluorescence stainings for clathrin heavy chains were performed. Uptake was qualitatively examined by confocal imaging. (C) Uptake of SPIOPSN in siRNA- and mock-treated cells was quantified by flow cytometry (n = 4). (D) HeLa cells were pretreated with 25 µM chlorpromazine and then exposed to 150 µg ml^{-1} SPIOPSN for 5 h. Quantification of uptake was performed via flow cytometric analysis (n = 4). (E) HeLa cells were transfected with epsin 15-DIII-GFP. 24 h after transfection, cells were exposed to 150 µg ml^{-1} SPIOPSN for 6 h. Uptake was qualitatively studied by confocal microscopy. Scale bars: 10 µm. Representative images are shown.

Moreover, also the overexpression of dominant-negative epsin 15 (DIII) did not display any impact on the internalization rate of SPIOPSN. Taking all of this into account, we concluded that CME is not significantly utilized during the entry of SPIOPSN.

Next, we investigated the impact of caveolae-mediated endocytosis on the uptake rate of SPIOPSN. Three days after nucleofection, siRNA-mediated silencing suppressed the levels of caveolin-1 to ~ 32% (Figure 19A). Qualitatively and quantitatively, no differences in SPIOPSN uptake were observed. As expected, overexpression of caveolin-1 did not significantly alter the amount of SPIOPSN that were internalized (Figure 19D). Therefore, we concluded that SPIOPSN are not internalized by a caveolin-1 dependent mechanism.

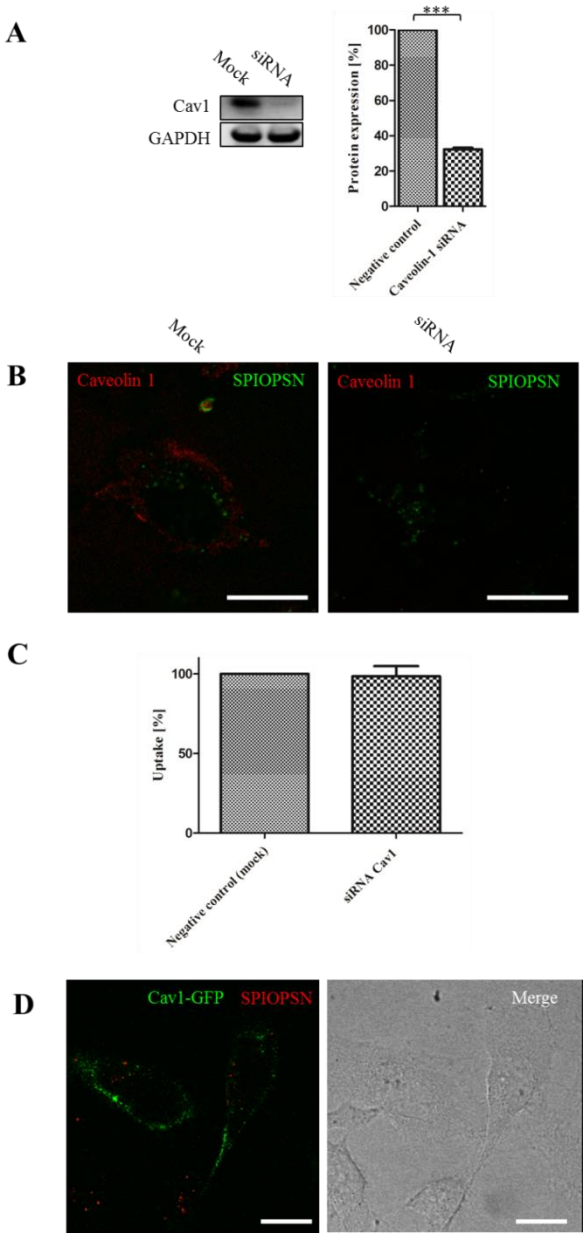

Figure 19: Caveolin-1 is not significantly required during the internalization process of SPIOPSN. HeLa cells were transfected with siRNA to silence caveolin-1. Caveolae-mediated endocytosis was disturbed by the overexpression of caveolin-1-GFP. The uptake of SPIOPSN was qualitatively and quantitatively analyzed. (A) Three days after nucleofection, downregulation of caveolin-1 was quantified by western blotting (B) Immunofluorescence stainings were performed for caveolin-1. Uptake was qualitatively determined by confocal imaging. (C) Mock- and siRNA treated cells were exposed to 150 µg ml^{-1} SPIOPSN for 6 h. Uptake was quantified by flow cytometry. (D) HeLa cells were transfected with caveolin-1-GFP. 24 h after transfection, cells were exposed to 150 µg ml^{-1} SPIOPSN for 6 h. Uptake was qualitatively studied by confocal microscopy. Scale bars: 10 µm. Representative images are shown.

Other pathways that might have an impact on the internalization rate of SPIOPSN were also investigated. Among others, we focused on the CLIC/GEEC-mediated endocytosis. To investigate whether this pathway mediates the uptake of SPIOPSN, we performed cointernalization experiments with the CLIC/GEEC marker cholera toxin subunit B to analyze the colocalization with SPIOPSN (data not shown). In this particular case, no colocalization of SPIOPSN with ctxB was observed. Therefore, we concluded that SPIOPSN are not taken up via the CLIC/GEEC pathway. This was confirmed by TEM studies were no tubular CLIC/GEEC-like invaginations were observed.

Further on, we checked whether the small GTPase RhoA had an impact on the uptake of SPIOPSN (data not shown). The overexpression of the dominant negative RhoA had no effect on the internalization rate of SPIOPSN. Therefore, we concluded that SPIOPSN did not exploit a RhoA-mediated endocytosis.

3.2.7 Other factors that orchestrate SPIOPSN entry: RNAi screening identifies flotillin-1 and the tetraspanin CD81 as important factors during the uptake process of SPIOPSN

As shown in the previous sections, the uptake of SPIOPSN is partially dependent on factors of a macropinocytic-like mechanism. Still, it is equally important to mention that uptake seemed not to be affected by CME; caveolae-mediated endocytosis, RhoA-mediated endocytosis or the CLIC/GEEC pathway. Also the ADP-ribosylation factor Arf6 does not seem to play a role in the uptake of SPIOPSN (Figure 25). However, the literature also provides several proteins that have been described to act independently from the commonly accepted endocytic pathways (88, 217). Therefore, we investigated the influences of some proteins that were assumed to interact with SPIOPSN.

Since tetraspanins and flotillin-1 were earlier described as part of the plasma membrane, of intracellular vesicles and as proteins that control the endocytotic machinery, we focused on these factors. We studied the internalization rates of SPIOPSNs after RNAi-mediated silencing of flotillin-1 and the tetraspanins CD82, CD81, CD63 and CD9. The reason for the selection of these distinct proteins is based on an experiment, where we magnetically isolated SPIOPSN-containing vesicles (shown in Figure 35). The previously mentioned vesicular proteins were present inside this fraction as detected by peptide mass spectrometry. These data implicated that SPIOPSN-containing vesicles contained significant amounts of flotillin-1 and the previously mentioned tetraspanins.

Knockdown was verified by the quantitative evaluation of the western blots except for the expression levels of CD82. The expression levels of CD82 knockdown was validated by qRT-PCR. We observed a silencing rate of ~15% (remaining CD82 mRNA; data not shown). Subsequently after gene silencing, the uptake rates of SPIOPSN were quantified. Flow cytometric analysis revealed a significant reduction of uptake in cells that were silenced for flotillin-1 ($n = 4$; $p < 0.01$, student´s t

test) and CD81 (n = 4; p < 0.001, student´s t test). The knockdown of the tetraspanins CD82, CD63 and CD9 did not impair SPIOPSN uptake (Figure 20).

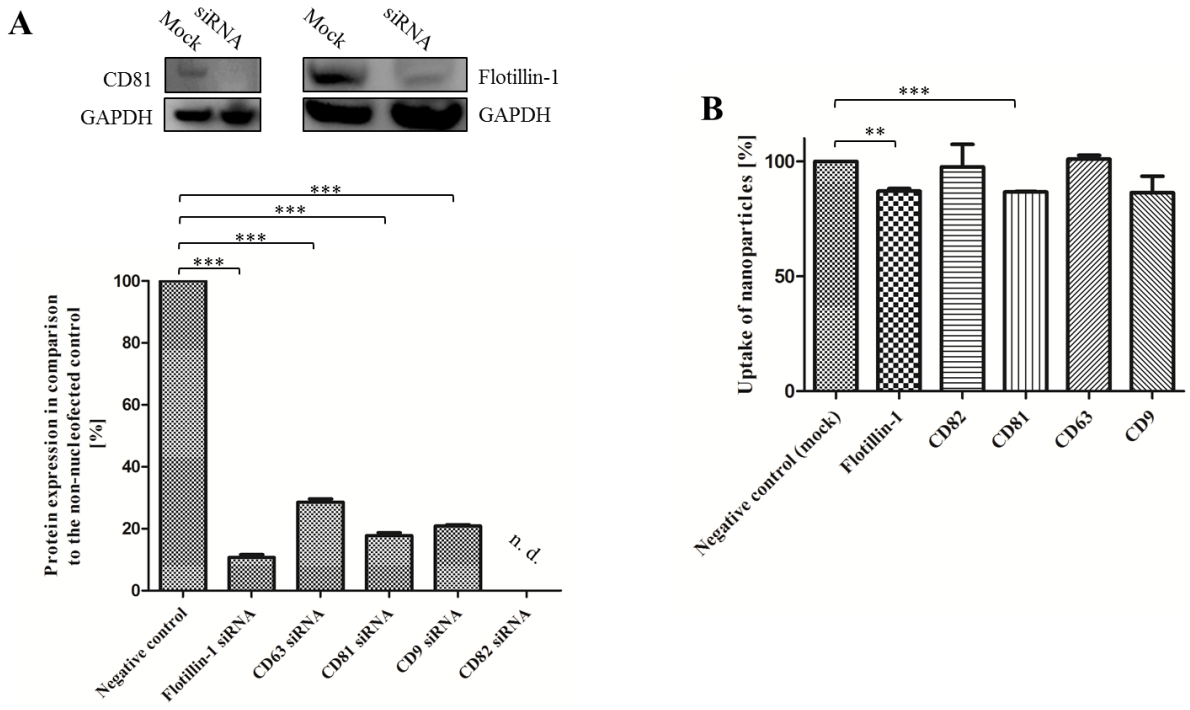

Figure 20: Flotillin-1 and CD81 partially control the internalization of SPIOPSN. To silence flotillin-1 and CD81, HeLa cells were nucleofected with 60 pmol of target-specific siRNA. (A) 3 d after nucleofection, protein expression levels were determined by western blotting (all samples: n = 3; p < 0.001; student´s t test). Knockdown of CD82 was quantified by q-RT-PCR (mRNA silencing down to ~15%; data not shown). (B) 3 d after nucleofection, HeLa cells were exposed to 150 µg ml^{-1} SPIOPSN for 6 h. The uptake of nanoparticles was quantified by flow cytometry. Significant changes in uptake were observed in flotillin-1 and CD81 silenced samples in comparison to the mock control. No significant changes in SPIOPSN uptake were detected in the samples that were silenced for CD82, CD63 and CD9.

Altogether, it was shown that CD81 and flotillin-1 had an impact on the internalization mechanisms of the nanoparticles. Since the membrane organization of CD81 and flotillin-1 was previously shown to depend on cholesterol, we investigated the impact of cholesterol depletion on the uptake of SPIOPSN (Figure 21) (131, 218). Moreover, it is worth to mention that cholesterol was also suggested to have a major impact on macropinocytic events.

3.2.8 Changes in cholesterol levels influence the endocytosis of SPIOPSN

Since the depletion of cholesterol often deregulates macropinocytic processes, we tested whether changes in cholesterol homeostasis have an impact on the internalization rate of SPIOPSNs. Therefore, we depleted the membranous cholesterol by the treatment of methyl-β-cyclodextrin (Figure 21). After cholesterol depletion and nanoparticle exposure, we observed a significant drop of the amount of internalized nanoparticles to 75.24% (n = 6; ** indicates p < 0.01; SD 2.57%). We further disturbed the intracellular cholesterol homeostasis by the cholesterol synthesis inhibitor U18666A. This inhibitor induced a Niemann-Pick-disease-like phenotype (Figure 21B). These NPC-like HeLa

cells were exposed to nanoparticles. The uptake of SPIOPSN was quantified by flow cytometry. Dextran served as a control. We observed a concentration-dependent drop of SPIOPSN and dextran in U18666A-deregulated cells (n = 6; *** indicates $p < 0.001$).

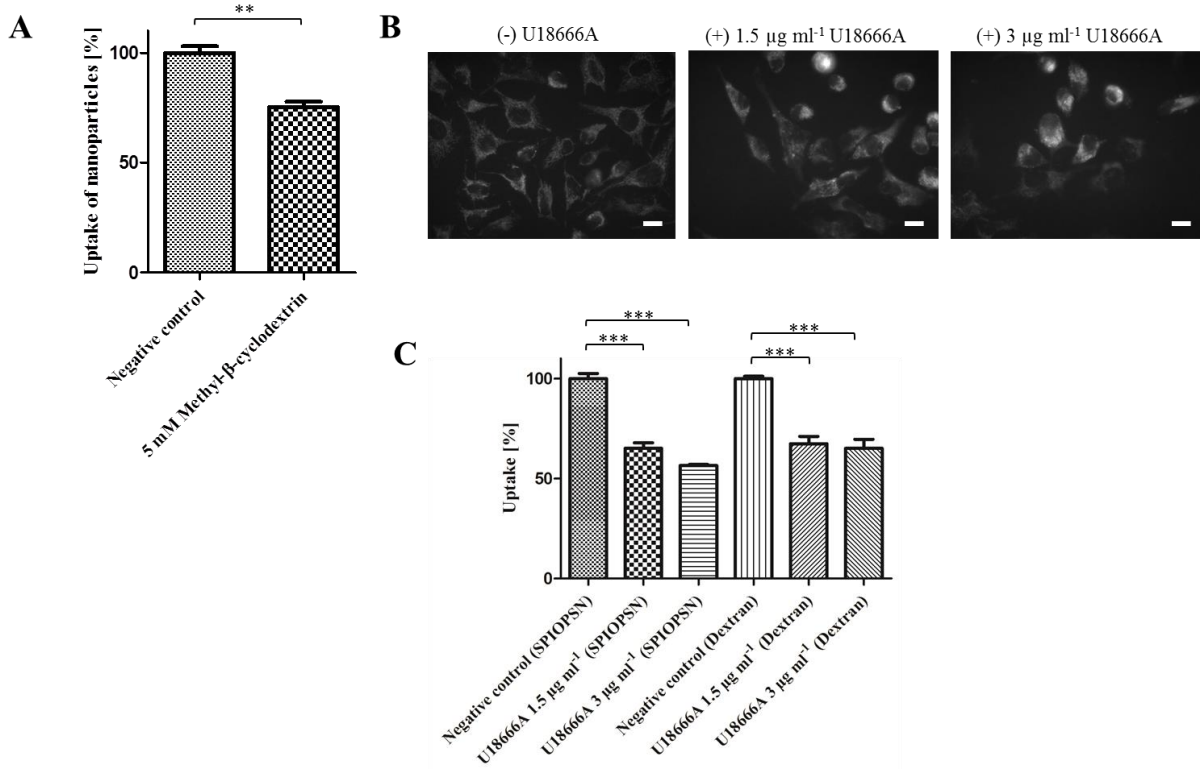

Figure 21: Deregulation of the cholesterol homeostasis decreases SPIOPSN uptake. (A) HeLa cells were pretreated with 5 mM methyl-β-cyclodextrin for 45 min. Subsequently, cells were exposed to 150 µg ml^{-1} SPIOPSN for 5 h. The uptake was quantitatively measured by flow cytometry (n = 6; ** indicates $p < 0.05$; student´s t test). (B) To achieve an endolysosomal accumulation of cholesterol, HeLa cells were treated with 1.5 µg ml^{-1} and 3 µg ml^{-1} U18666A for 24 h, respectively. The accumulation of cholesterol was detected by filipin stainings. Scale bar: 10 µm. (C) After 24 h of U18666A treatment, cells were exposed to 150 µg ml^{-1} SPIOPSN and 2.5 µg ml^{-1} dextran-488, respectively. After 5 h of incubation, uptake was quantified by flow cytometry. Values are given as mean + SD (n = 6; *** indicates $p < 0.001$, student´t t test).

These data implied that the deregulation of the cellular cholesterol homeostasis resulted in a decreased amount of internalized nanoparticles. Since we have shown that an NPC-like phenotype can reduce the internalization rate of nanoparticles we focused on the cholesterol transporter NPC1. NPC1 and NPC2 were identified by mass spectrometry and seemed to directly interact with SPIOPSN (Figure 34). Therefore, we silenced NPC1 by RNAi. The assumption was that the downregulation of NPC1 (remaining protein ~ 27%, data not shown) induces a deregulation of the intracellular cholesterol homeostasis and a decrease of the internalization rate of nanoparticles. However, no reduction of the uptake rate of SPIOPSN was observed (data not shown). Therefore, we tested other factors that were identified by mass spectrometry (Figure 22).

3.2.9 ARF1 is an important factor in SPIOPSN uptake

ADP-ribosylation factor 1 (ARF1) is a small GTP-binding protein that has a crucial function during the process of COP vesicle formation (219). Furthermore, it was also shown that ARF1 regulates macropinocytic events (220). Experimentally, ARF1 can be inhibited by brefeldin A or by the overexpression of dominant negative mutants (221).

To investigate the role of ARF1 during the uptake of SPIOPSN, we firstly blocked ARF1 by a pharmacological treatment of HeLa cells with brefeldin A. Subsequently, the pretreated cells were exposed to nanoparticles and nanoparticulate uptake was quantified (Figure 22). Brefeldin A treated cells showed a significantly decreased internalization rate of SPIOPSN (71.7%; n = 6; * indicates $p < 0.05$; SD 10,6%). Dextran uptake was not affected by the brefeldin A treatment. Owing to this result, we now asked whether SPIOPSN are directly associated with ARF1. Since we have identified ARF1 as a SPIOPSN-associated protein by mass spectrometry, we overexpressed a dominant negative mutant of ARF1 in HeLa cells and measured the colocalization with SPIOPSN. Here, rare events of colocalization were observed. This low rate of colocalization was also linked to the observation that less nanoparticles were taken up from ARF1 $T31N^+$ cells. Refering to this we concluded that the nonfunctional ARF1 had a massive effect on the uptake of SPIOPSN. Therefore, we quantified the number of endocytic vesicles of ARF1 T31N transfected and nontransfected cells by analyzing the confocal z-stacks. By comparing GFP^+ and GFP^- cells, it was shown that the number of endocytosed SPIOPSN was significantly decreased in the ARF1 $T31N^+$ fraction (n = 31; *** indicates $p < 0.001$) (Figure 22).

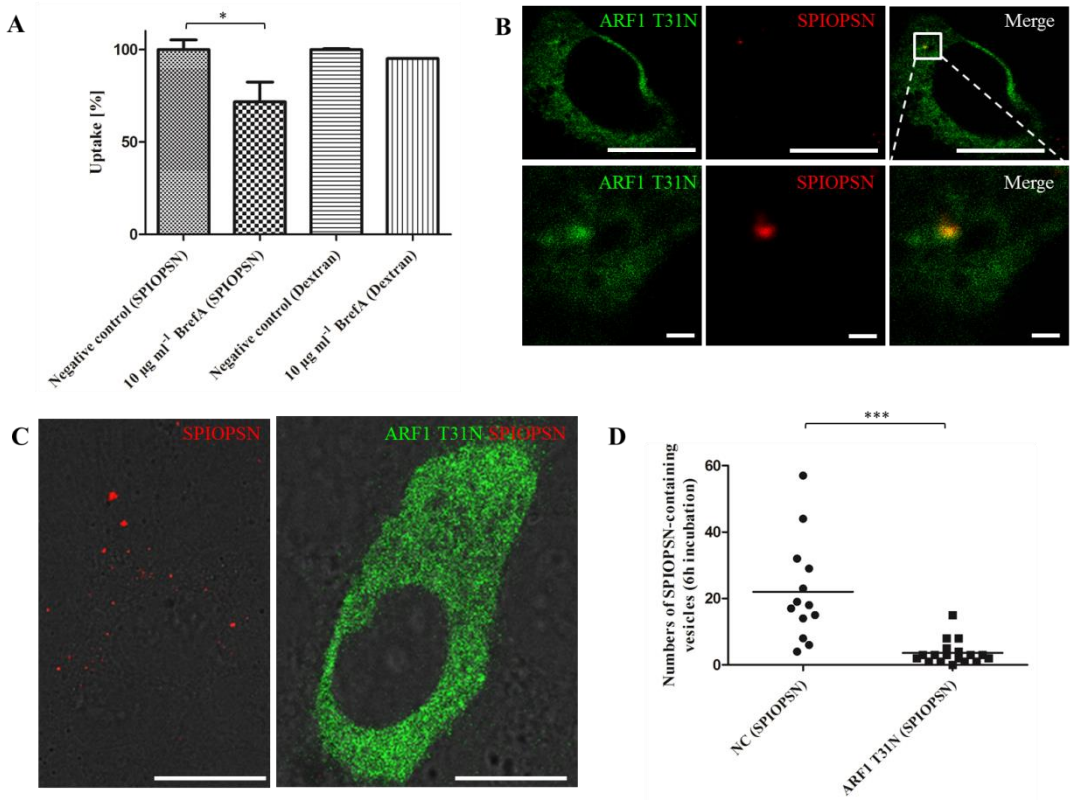

Figure 22: ARF1 has a crucial function during the uptake of SPIOPSN. SPIOPSN uptake was investigated upon ARF1 inhibition. (A) HeLa cells were pretreated with 10 µg ml^{-1} brefeldin A to inhibit ARF1. Pretreated and nontreated HeLa cells were exposed to 150 µg ml^{-1} SPIOPSN for 6 h. Uptake of SPIOPSN was quantified by flow cytometry (n = 6; * indicates $p < 0.05$, student´s t test). (B) Colocalization studies with the dominant negative mutant ARF1 T31N-GFP revealed rare colocalization events with SPIOPSN after 6 h of nanoparticle exposure. Scale bar: 10 µm. ROI: Scale bar: 1 µm. (C) HeLa cells were transfected with ARF1 T31N-GFP. 24 h later, cells were exposed to 150 µg ml^{-1} SPIOPSN for 6 h. Qualitative confocal images revealed a massively reduced amount of internalized nanoparticles in ARF1 T31N-GFP^+ cells. (D) z-stacks of ARF1 T31N-GFP^+ and GFP^- cells were recorded to manually quantify the number of SPIOPSN-containing vesicles after 6 h of nanoparticle exposure. A significant reduction of SPIOPSN-containing vesicles in ARF1 T31N-GFP^+ cells was observed ($p < 0.001$; student´s t test). Representative images are shown.

Altogether, it was shown that ARF1 is a crucial factor during the uptake of SPIOPSN. Whether ARF1 is also deregulated after the deacidification of the endocytic system is unknown. However, this is not the major question we wanted to solve. In the next section, we showed that the deacidification of the endocytic system resulted in a drop of the nanoparticulate uptake rate (Figure 23).

3.2.10 Deacidification of the endolysosomal vesicles affects uptake of SPIOPSN

The acidification of the endolysosomal system is facilitated by the endolysosomal v-type ATPase H^+ pumps. To approach the question, if deacidification of the endolysosomal system affects the uptake of SPIOPSN, v-type ATPase H^+ pumps were inhibited by bafilomycin A1. The efficiency of inhibition was confirmed by LysoTracker staining (Figure 23). If our hypothesis holds true, HeLa cells should reduce their ability to internalize SPIOPSN. Therefore, we pretreated HeLa cells with bafilomycin A1 for 45 min and then exposed them to SPIOPSN or dextran. Deacidification of the endolysosomal system significantly reduced the internalization of SPIOPSN and dextran. The analysis showed that

the pretreatment of HeLa cells with bafilomycin A1 reduced SPIOPSN uptake to 59% (SD 4.9%; n = 6; *** indicates $p < 0.001$). Dextran uptake was reduced to 25% (SD 3.26%; n =6; *** indicates $p < 0.001$).

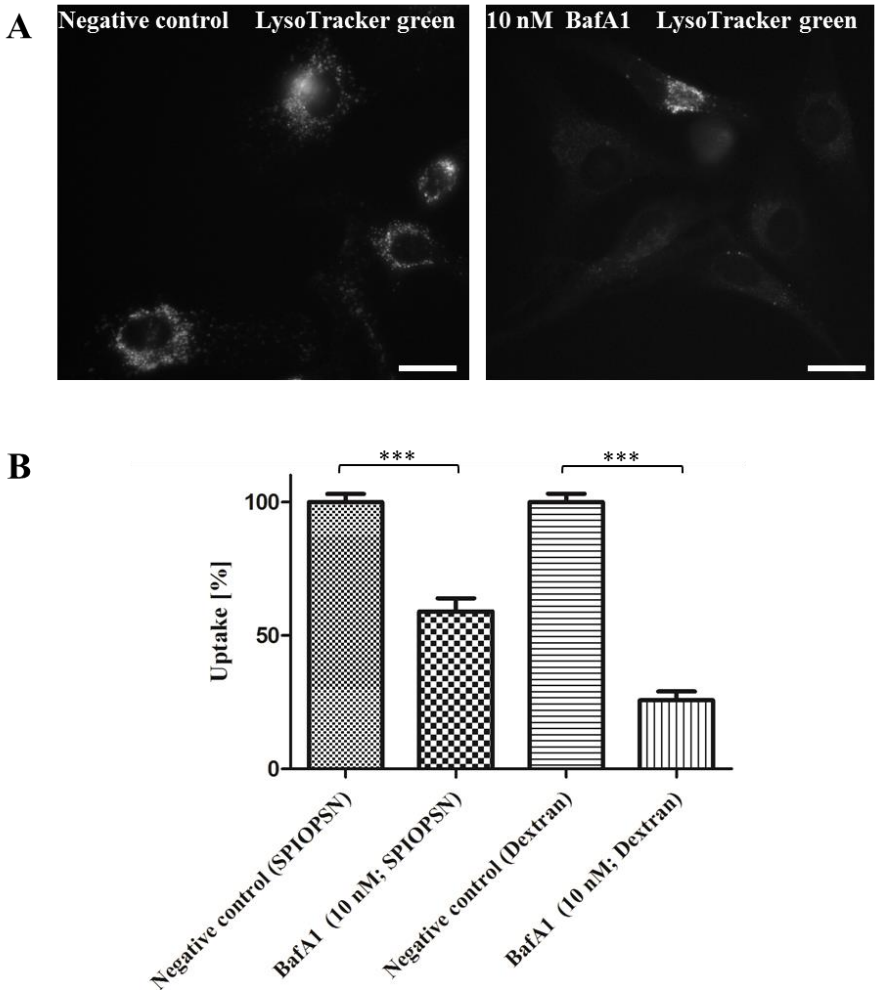

Figure 23: Deacidification of the endolysosomal system inhibits the uptake of SPIOPSN. The acidification of the endolysosomal system was blocked by bafilomycin A1, an inhibitor of vacuolar-type H^+ ATPase. (A) HeLa cells were pretreated with 10 nM Bafilomycin A1 for 45 min. Acidification/deacidification was visualized by the staining with LysoTracker green DND-26. Scale bar: 10 µm. (B) Pretreated HeLa cells were incubated for 5 h with 150 µg ml^{-1} SPIOPSN or 2.5 µg ml^{-1} AF-Dextran-488. Uptake was quantitatively analyzed by flow cytometry. Values are given as median + SD (n = 6;*** indicates $p < 0.001$).

To summarize the results of chapter 3.2, we found that SPIOPSN were internalized by a macropinocytic-like mechanism. This mechanism depends on several classical factors of macropinocytosis but also showed some unexpected features. With this information, the work was continued. It was assumed that the primary nanoparticulate portal of entry was a macropinosome-like organelle. The pinch off of this organelle results in an intracellular trafficking of nanoparticles that we have investigated in the next section.

3.3 Reconstruction of intracellular nanoparticle trafficking

The previous chapters showed that SPIOPSN have been internalized via a macropinocytic-like mechanism. The identified mechanism is dependent on several factors that have never been associated with nanoparticulate entry. This newly gained knowledge raised interesting issues that primarily focused on the fate of the nanoparticles after their entry. Indeed, the intracellular nanoparticle trafficking after macropinocytic-like entry is less investigated. Therefore, we asked how SPIOPSN traffic through the cell when the primary compartment is a macropinosome-like organelle.

3.3.1 SPIOPSN are primarily transported via macropinosome-like organelles

Preliminary, we analyzed several classical markers of early endosomes in the initial stage of endocytosis. Therefore, we focused on the Ras-related protein 5A (Rab5A), which is known to be present on classical macropinosomes and early endosomes (142, 222). In colocalization experiments with overexpressed Rab5A wt, only low amounts of colocalization with nanoparticles was observed. However, we found some SPIOPSN inside $Rab5A^+$ vesicles after 6 h of exposure (Figure 24A/B). These $Rab5A^+$ vesicles were visible under transmission light and resembled fluid-filled vesicles (Figure 24B). Since Rab5 was described as an important protein in the biogenesis of endosomes and macropinosomes, we analyzed whether the downregulation of Rab5A had an impact on the internalization rate of SPIOPSN. Surprisingly, no reduction in the endocytosis rate of SPIOPSN was observed (Figure 24D). Other proteins that have been described as markers of early endosomes are early endosome antigen 1 (EEA1). In this case, no colocalization of EEA1 with SPIOPSN was found in immunofluorescence staining. This was confirmed by the MS data, where EEA1 was not enriched (data not shown).

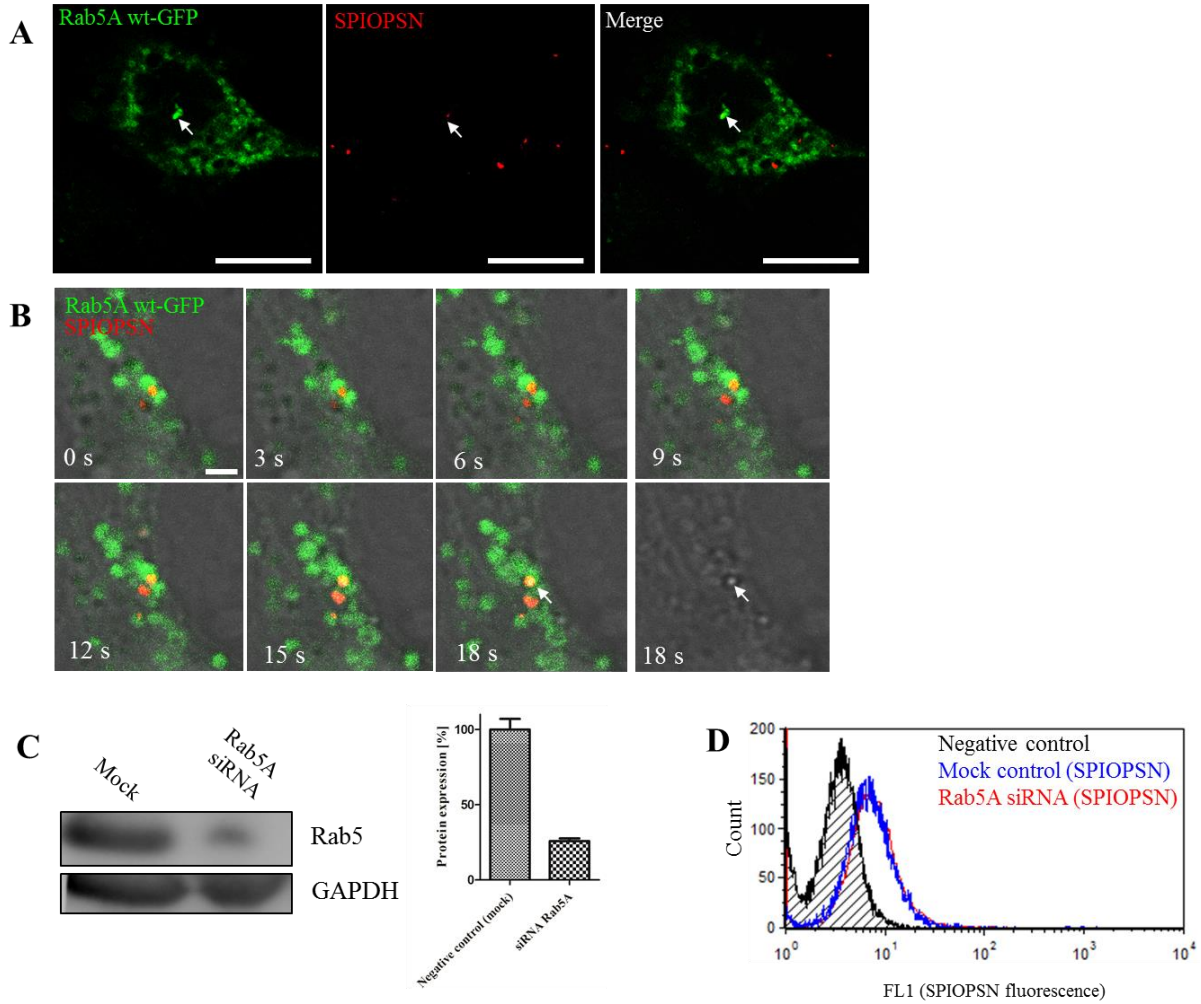

Figure 24: SPIOPSN colocalize with Rab5A in the early stage of nanoparticle trafficking. (A) HeLa cells were transfected with Rab5A wt-GFP. 24 h after transfection, cells were exposed to 150 µg ml^{-1} SPIOPSN for 6 h. Colocalization of SPIOPSN was analyzed with Rab5A by confocal live cell imaging. Less colocalization was found with the early endosomal marker Rab5A. Scale bar: 10 µm. (B) Live cell imaging displayed SPIOPSN that moved inside $Rab5A^+$ vesicles, which were visible in transmission light (last panel). Scale bar: 1 µm (C) To investigate the effect of Rab5A depletion on the uptake of SPIOPSN, Rab5A was silenced by RNAi. Knockdown efficiency was determined by western blotting. (D) Rab5A-siRNA sample and mock control were incubated with 150 µg ml^{-1} SPIOPSN for 6 h. Uptake of SPIOPSN was quantitatively determined by flow cytometry. Representative images are shown.

We further focused on the interaction of SPIOPSN-containing vesicles with typical proteins that were previously associated with macropinosomes. In earlier studies, it was shown that SWAP-70 is a component of macropinosomes (164). To study the participation of SWAP-70 in SPIOPSN trafficking in more detail, we overexpressed SWAP-70-GFP and analyzed its colocalization with SPIOPSN. Despite of extensive studies, we failed to show a colocalization with SWAP-70 (Figure 25). Therefore, the studies were continued with the focus on the small GTPase RhoB. RhoB was previously described as a factor that was involved in macropinocytosis of viral particles (223). Since we have identified the small GTPase RhoB as an SPIOPSN-associated protein by mass spectrometry, colocalization experiments with RhoB wt-GFP were performed. SPIOPSN colocalized with RhoB in regions close to the membrane and in endosome-like structures. Further observations revealed that $RhoB/SPIOPSN^+$ endosomes were visible in transmission light that resembled fluid-phase filled macropinosomes.

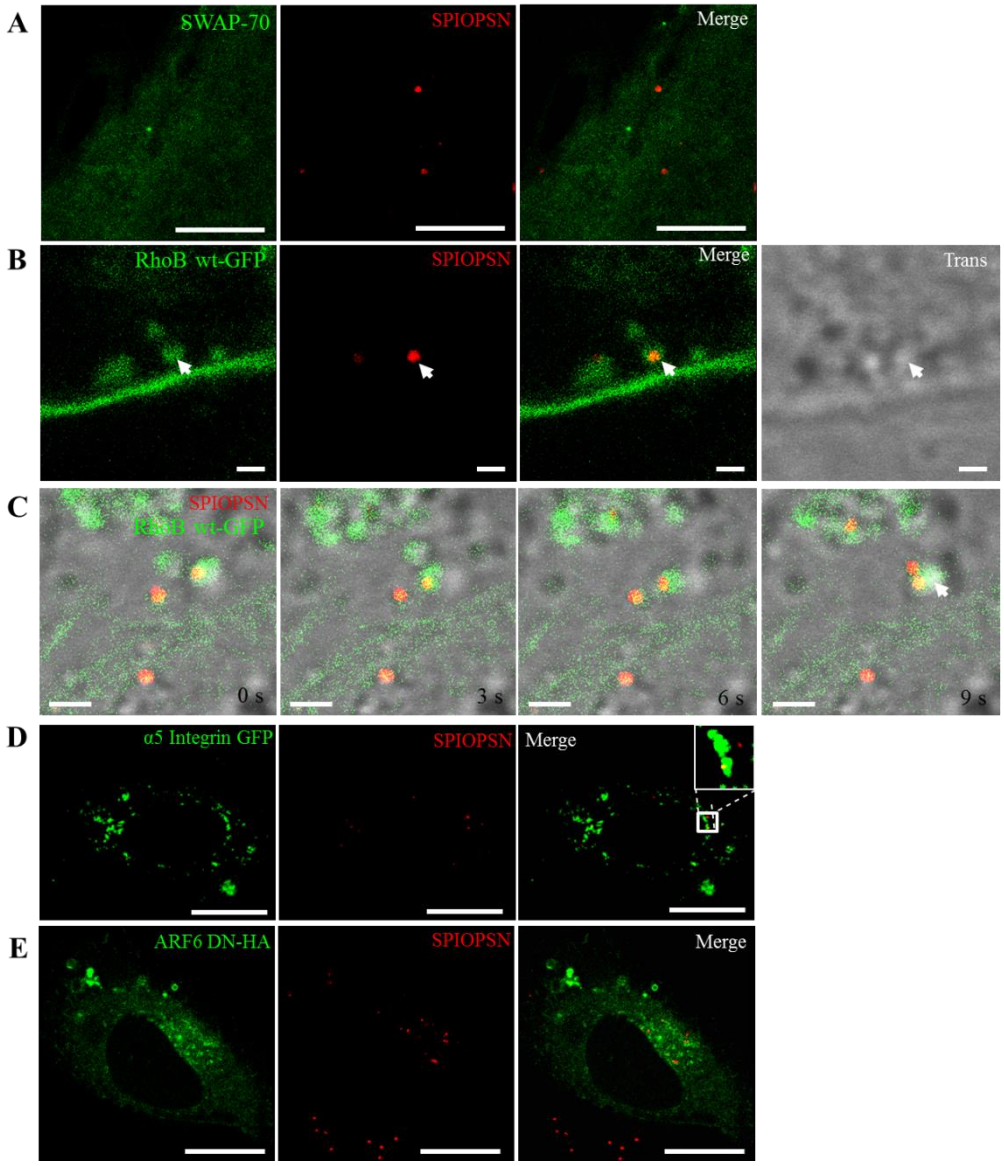

Figure 25: RhoB is associated with SPIOPSN-containing macropinosomes. To investigate specific markers of macropinosomes, several proteins were overexpressed. SWAP-70 is a protein that was shown to be transiently present on macropinosomes. RhoB is a small GTPase that was associated with macropinocytosis. ARF6-GFP is a small GTPase that is known to transiently mediate classical macropinocytosis. After 24 h of transfection, HeLa cells were exposed to 150 µg ml^{-1} SPIOPSN for 6 h. Subsequently, colocalization was analyzed by confocal live cell imaging. (A) SWAP-70 displayed no colocalization with SPIOPSN. (B) Colocalization of SPIOPSN with RhoB was found in close proximity to the cell membrane (B) and in the perinuclear regions of the cell. (C) Live cell imaging showed that SPIOPSN moved within fluid-phase filled $RhoB^{+}$ vesicles through the cell. (D) Less colocalization was observed with α5-Integrin-GFP (E) No colocalization was found with ARF6 DN-HA. Detection of ARF6 DN-HA was performed by immunofluorescence. Qualitatively, the expression of dominant negative ARF6 did not alter the internalization rate of SPIOPSN in comparison to nontransfected cells. Representative images are shown.

Next, overexpression of α5-Integrin-GFP resulted in rare colocalization events with SPIOPSN. α5-Integrins were previously identified as important proteins during the early macropinocytic stages of adenoviruses (224). Moreover, we investigated the influences of ARF6 on SPIOPSN trafficking. ADP-ribosylation factor 6 is a GTP-binding protein that was identified as a modulator of Rac-GTPases. Previous work showed that ARF6 can control the actin structure and colocalized with an early phagosomal mechanisms (92). To get a closer insight if ARF6 has an impact on SPIOPSN uptake, we overexpressed the dominant negative form ARF6 T27N-HA. Afterwards, cells were

exposed to SPIOPSN and cells were immunostained for ARF6-HA. Neither colocalization nor a reduction of SPIOPSN internalization was observed. Therefore, we concluded that ARF6 did not affect the macropinocytic structures of SPIOPSN-containing vesicles. This was also confirmed by mass spectrometry, where no association of SPIOPSN with ARF6 was observed. Taken together, we found that SPIOPSN are internalized via a fluid-filled macropinocytic organelle. Up next, we wanted to know whether the SPIOPSN traffic a regular route via late endosomes (Figure 26).

3.3.2 SPIOPSN traffic along Rab7$^+$ and Rab9$^+$ late endosomes

The colocalization of SPIOPSN with markers of early endosomes/early macropinosomes gave rise to the assumption that SPIOPSN trafficked along the endolysosomal system. Therefore, colocalization studies with the late endosomal marker Rab7 and Rab9 were performed. Rab7 was previously identified as a protein that replaced Rab5 in later stages of intracellular trafficking (153). Rab9 is a GTPase that is present on late endosomes and plays a role in the endosome-to-trans-Golgi-network transport (225). Indeed, after the overexpression of Rab7 and Rab9, SPIOPSN colocalized with both markers (Figure 26). Live cell imaging revealed that SPIOPSN were actively transported through the cell. The presence of Rab7 and Rab9 was confirmed by mass spectrometry, where both markers were identified in the magnetically enriched fraction.

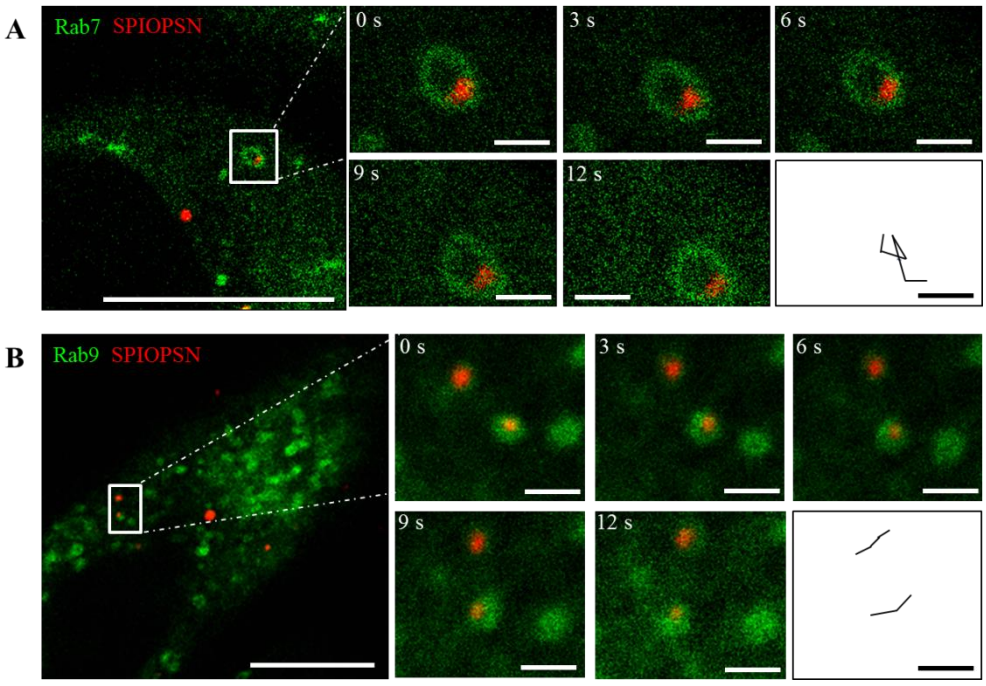

Figure 26: SPIOPSN are transported along Rab7 and Rab9$^+$ late endosomes. HeLa cells were transfected with Rab7 wt-GFP (A; Scale bar: 10 µm; magnification: 1 µm) and Rab9 wt-GFP (B; Scale bar: 5 µm; magnification: 1 µm) to detect late endosomes. 24 h after transfection, cells were exposed to 150 µg ml^{-1} SPIOPSN for 6 h. Colocalization with Rab-proteins was investigated by confocal live cell imaging. Motion profiles of nanoparticles were generated to track the movements of SPIOPSN inside vesicles. Representative images are shown.

3.3.3 The R-SNARE protein VAMP7 is present on SPIOPSN-containing vesicles

After the detection of SPIOPSN inside Rab7$^+$ and Rab9$^+$ vesicles it was assumed that SPIOPSN were transported via late endosomes. To investigate whether these late endosomes fuse with lysosomes, we investigated the colocalization of SPIOPSN with the vesicle-associated membrane protein 7 (VAMP7). VAMP7 is a membrane protein of the SNARE family that mediates the heterotypic fusion of late endosomes and lysosomes (191). To investigate the participation of VAMP7 in SPIOPSN trafficking, full-length VAMP7-GFP was overexpressed and SPIOPSN trafficking was investigated by confocal live cell imaging. A colocalization of SPIOPSN with VAMP7 was observed. The tracked nanoparticles were actively transported inside VAMP7$^+$ vesicles through the cell (Figure 27). An association of VAMP7 with SPIOPSN was also shown by mass spectrometry. Here, we identified VAMP7 as an enriched protein of the magnetic vesicular fraction.

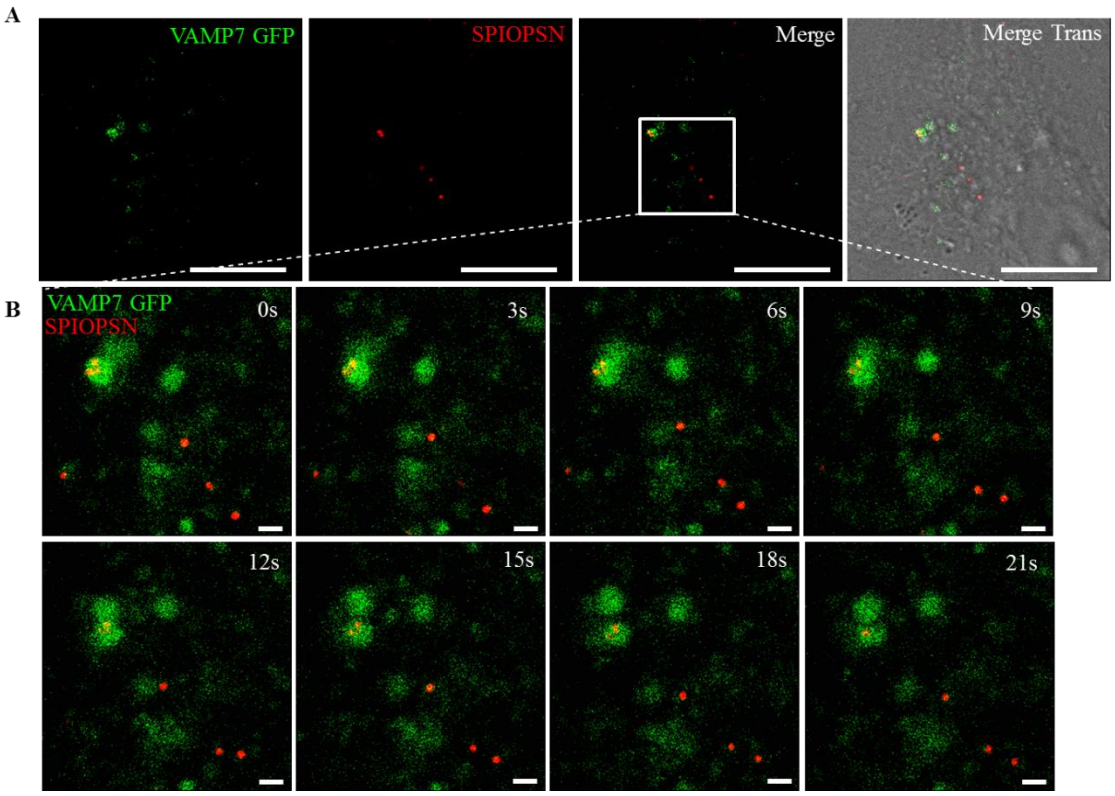

Figure 27: VAMP7 is associated with SPIOPSN-containing vesicles. To investigate the presence of VAMP7 on SPIOPSN-containing vesicles, we overexpressed VAMP7-GFP. (A) HeLa cells were transfected with VAMP7-GFP. 24 h later, cells were exposed to 150 µg ml^{-1} SPIOPSN for 6 h. Subsequently, colocalization of SPIOPSN with VAMP7 was analyzed by confocal live cell imaging (Scale bar: 10 µm). (B) Confocal live cell imaging displayed an active transport of SPIOPSN inside VAMP7$^+$ vesicles. Representative images are shown.

3.3.4 SPIOPSN are transported inside vesicles that are positive for markers of intraluminal vesicles

Early and late endosomes accumulate intraluminal vesicles (ILVs) during the processes of vesicular maturation (171). ILVs have been shown to carry several markers such as the melanocytic protein Pmel17. In previous reports it was demonstrated that Pmel17 is sorted via an ubiquitin-/ ESCRT-independent mechanism into ILVs of MVBs (174, 226). Furthermore, it was shown that the tetraspanin CD63 decorates the ILVs (227). Therefore, Pmel17 and CD63 were used to investigate the association of SPIOPSN with multivesicular bodies. As expected, we have identified no native Pmel17 in HeLa cells (Figure 28B). Therefore, we overexpressed Pmel17 in HeLa cells. 24 h after transfection, cells were exposed to SPIOPSN. The detection of Pmel17 was performed by immunofluorescence. Notably, a clear colocalization of Pmel17 with nanoparticles was observed. Next, we incubated HeLa cells with SPIOPSN and detected CD63 by immunofluorescence staining. Nanoparticles displayed a high rate of colocalization with CD63 (Figure 28).

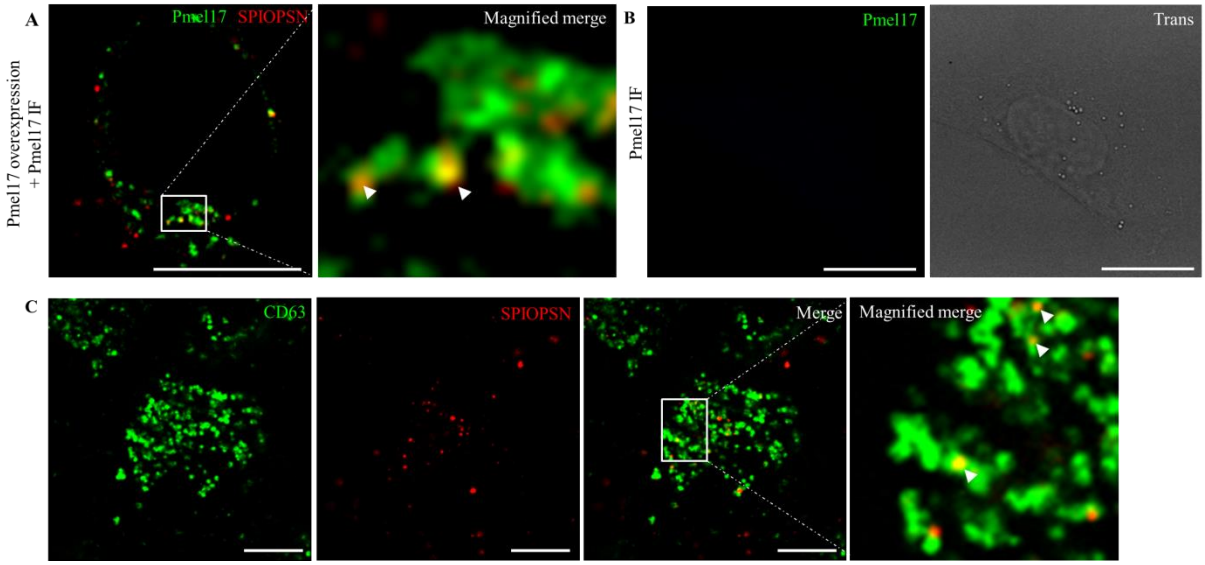

Figure 28: SPIOPSN are transported inside vesicles that are positive for the intraluminal vesicle marker Pmel17 and CD63. (A) HeLa cells were transfected with Pmel17. 24 h later, cells were exposed to 150 µg ml^{-1} SPIOPSN for 6 h. Pmel17 was detected by immunostaining. Colocalization was analyzed by confocal microscopy. Scale bar: 10 µm. (B) Staining of nontransfected HeLa cells with NKI/Beteb antibodies showed that HeLa cells lack the expression of Pmel17. Scale bar 10 µm. (C) HeLa cells were incubated with 150 µg ml^{-1} SPIOPSN for 20 h and then stained for CD63. Scale bar: 10 µm. Spots of colocalization were marked with white arrows (n = 5; representative images are shown).

Since previous reports suggested that Pmel17 is sorted via an ESCRT-independent mechanism into MVBs, we hypothesized that SPIOPSN-containing vesicles contained a low amount of ubiquitin. Indeed, we were not able to detect ubiquitin by immunofluorescence in any SPIOPSN-containing vesicle (data not shown). In spite of this, the morphology of SPIOPSN-containing vesicles revealed that the nanoparticles are transported via classical MVBs (Figure 29).

3.3.5 SPIOPSN are transported via multivesicular bodies to multilamellar lysosomes

The data of the previous sections showed that SPIOPSN were transported via early endocytic vesicles to multivesicular bodies. To confirm this on an ultrastructural level, cryo-freezed sections of nanoparticle-exposed HeLa cells were prepared. After recording the TEM micrographs, SPIOPSN-containing-vesicles were subclassified owing to distinct morphological criteria. Vesicles that lacked intraluminal vesicles were classified as early endocytic vesicles. Vesicles, which contained ILVs were categorized as multivesicular bodies. Multilamellar lysosomes are vesicles that stored membrane whorls of an onion-like structure. Further on, we recorded hybrid structures of multivesicular bodies and multilamellar lysosomes/multilamellar bodies (MLL or MLB). These vesicles contained intraluminal vesicles and membrane whorls.

The analysis of the TEM micrographs confirmed the previous experiments of confocal imaging. SPIOPSN were transported along early endocytic vesicles, multivesicular bodies, MVB-MLL-hybrid organelles and multilamellar lysosomes (Figure 29). To analyze the distribution of SPIOPSN inside the distinct types of vesicles more precisely, a semiquantitative classification was performed. The morphological subcategorization of the vesicles was based on the formerly described criteria. Quantification was performed with the data of four independent experiments, counting the identified SPIOPSN-containing vesicles on the prepared slices inside more than 25 cells. Taken together, most of the SPIOPSN were found inside MVB/MLL-hybrid organelles and in multilamellar lysosomes after 20 h of nanoparticle exposure.

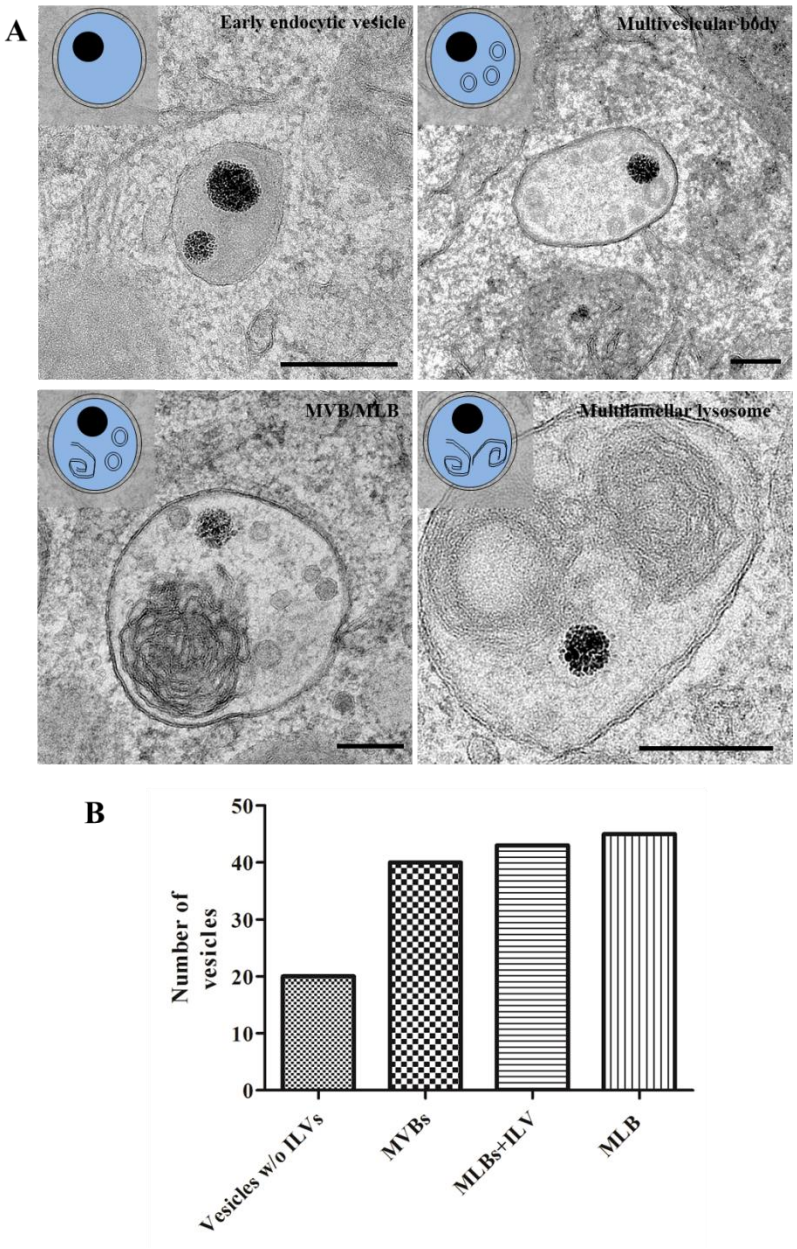

Figure 29: SPIOPSN are transported inside morphologically distinct vesicles along the endolysosomal pathway (HeLa). Cryo-TEM micrographs revealed the different types of vesicles that contained electron dense SPIOPSN (dark areas). Scale bar: 200 nm. (A) HeLa cells were exposed to 150 µg ml^{-1} SPIOPSN for 20 h. Cells were cryo-freezed and prepared for TEM. SPIOPSN were found in vesicles with a size range of 0.5 – 1 µm in diameter. Vesicles without ILVs were identified (early endocytic vesicles). Multivesicular bodies contained SPIOPSN and intraluminal vesicles (size ~ 50 nm). Multilamellar lysosomes were identified. MVB/MLB-hybrid organelles were found. (B) Semiquantitative analysis of TEM micrographs revealed that SPIOPSN were mainly present inside multilamellar bodies after 20 h of incubation (n = 4 independent experiments). Vesicles were categorized due to their morphological appearance as shown in the scheme in (A). (Sample preparation and TEM micrographs were prepared by C. Messerschmidt).

To assure that MLBs are the final organelle in SPIOPSN trafficking, HeLa cells were pulsed for 6 h with SPIOPSN. This procedure was followed by a postincubation of 14 h without nanoparticles in the growth medium. Notably, almost all of the SPIOPSN accumulated inside MLB-like-structures (data not shown).

Similar experiments were performed with primary human mesenchymal stroma cells. Here, we were able to confirm the former data. Early endocytic vesicles, as well as multivesicular bodies and multilamellar lysosomes participated in the transport of SPIOPSN. After 20 h of SPIOPSN exposure, most of the nanoparticles were found in Cathepsin D^+ lysosomal compartments (Figure 30).

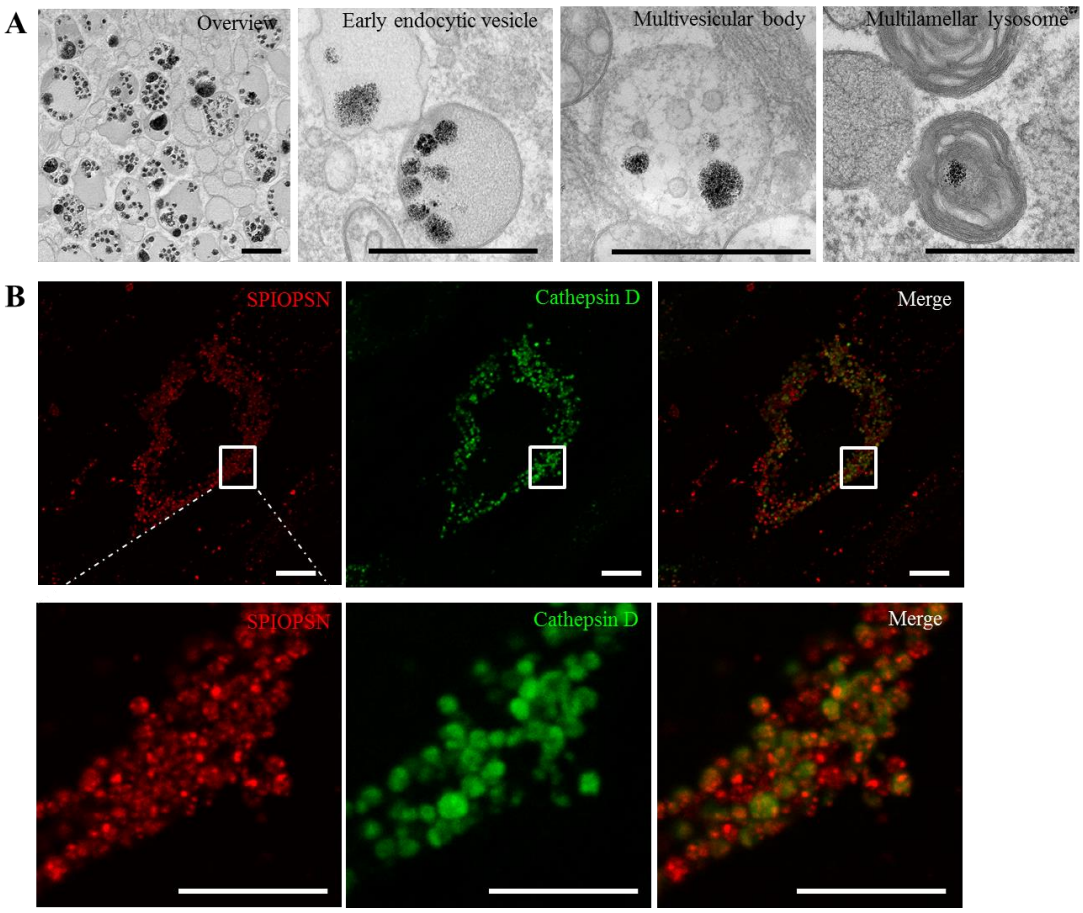

Figure 30: SPIOPSN are transported inside morphologically distinct vesicles along the endolysosomal pathway (hMSCs). (A) hMSCs were exposed to 150 µg ml^{-1} SPIOPSN for 20 h and prepared for TEM. Micrographs showed SPIOPSN densly packed inside early endosomes, multivesicular bodies and multilamellar lysosomes. Scale bar: 1 µm. (TEM micrographs were taken by C. Messerschmidt). (B) After 20 h, most of the SPIOPSN were found in Cathepsin D^+ vesicles. Scale bar of upper image: 10 µm. Scale bar of magnification: 1 µm. (n = 3; representative images are shown).

Notably, the observation that SPIOPSN were stored inside lysosomes was also recorded for HeLa cells. After 20 h of nanoparticle exposure, most of the SPIOPSN accumulated inside vesicles that bore the lysosomal markers Lamp1/Lamp2 and Cathepsin D (Figure 31).

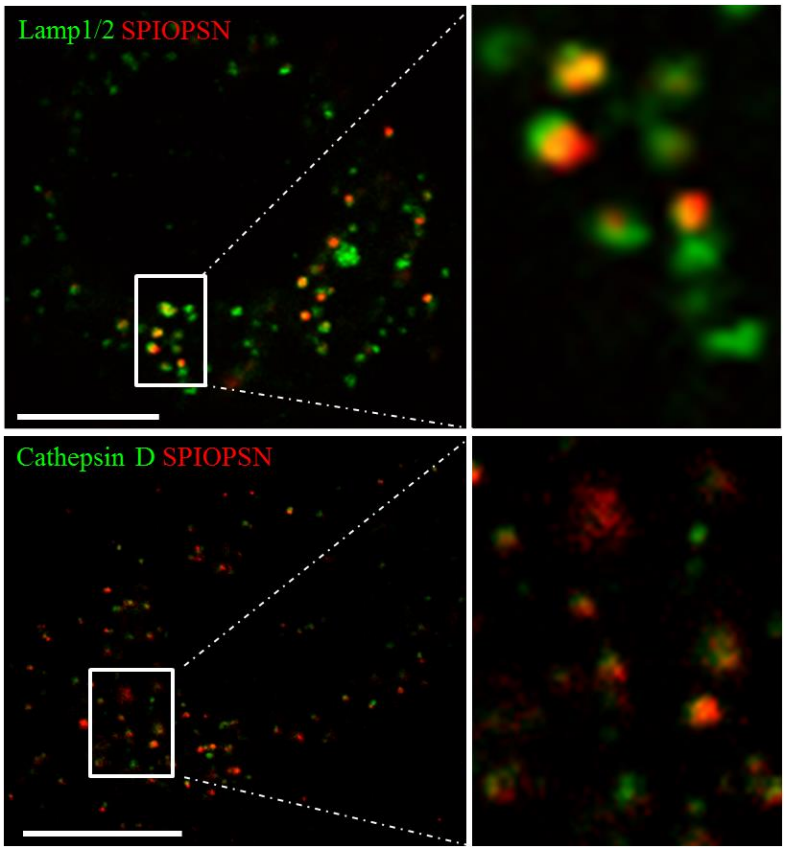

Figure 31: SPIOPSN are finally stored inside Lamp1/2$^+$ and Cathepsin D$^+$ lysosomes. HeLa cells were exposed to 150 µg ml^{-1} SPIOPSN for 20 h, fixed, permeabilized and double-stained for the lysosomal markers Lamp1/Lamp2. Another sample was stained for the lysosomal marker cathepsin D. SPIOPSN showed colocalization with both markers (n = 8). Representative images are shown

3.3.6 SPIOPSN are neither exocytosed nor transported by autophagosomes

Next, we analyzed whether intracellular nanoparticle trafficking interfered with recycling pathways or autophagosomal trafficking. Since we have identified Rab11A and Rab11B by mass spectrometry, we asked the question whether SPIOPSN are generally exocytosed by recycling endosomes. To quantify this process, HeLa cells were pulsed for 4 h with SPIOPSN and postincubated without nanoparticles for another 16 h. The mean fluorescence intensity of the cells was measured over time. Notably, no significant drop of the fluorescent nanoparticle signal was observed (Figure 32A). We concluded that SPIOPSN were not exocytosed by the cell. This observation was confirmed by the following set of experiments. Intensive research on this project confirmed that SPIOPSN did not colocalize with Rab11 wt-GFP and Rab11 that was visualized by immunofluorescence stainings (Figure 32B). Consequently, we suggested that SPIOPSN were not significantly externalized by the recycling pathways.

To investigate the interplay with autophagosomes, HeLa cells were incubated with SPIOPSN and immunostained for the autophagosomal marker LC3. Also here, SPIOPSN did not colocalize with the LC3. This indicated that SPIOPSN trafficking was not directly linked to the autophagosomal system.

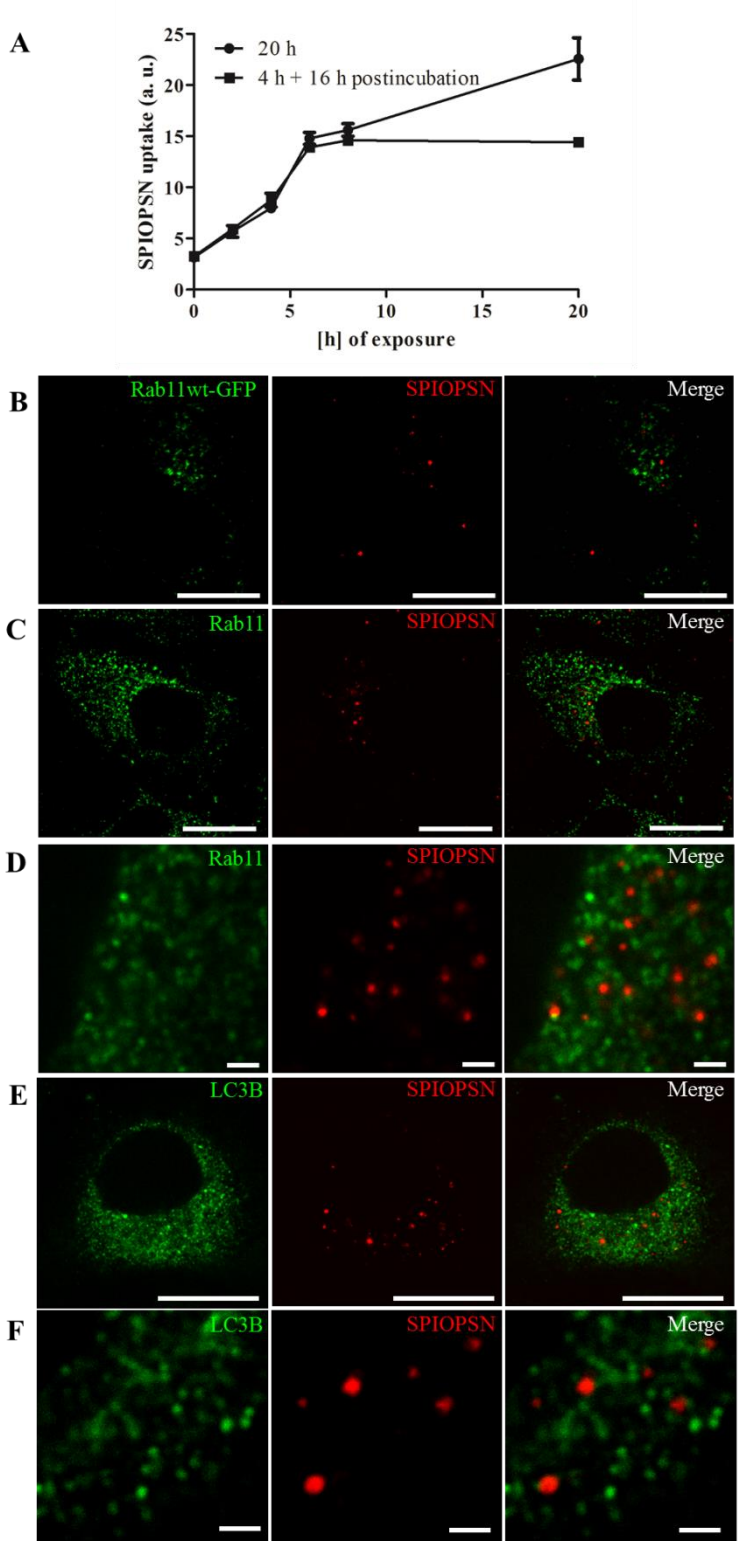

Figure 32: SPIOPSN are neither exocytosed by Rab11$^+$ recycling endosomes nor transported via LC3B$^+$ autophagosomes. (A) To test whether SPIOPSN are exocytosed, we pulsed HeLa cells for 4 h with 150 µg ml^{-1} SPIOPSN. After a washing step, we postincubated the cells without nanoparticles for another 16 h. The mean fluorescence intensity of the nanoparticles was recorded over time. Full-time exposed cells served as a control. No significant exocytosis of SPIOPSN was observed after 20 h of total exposure. (B) HeLa cells were transfected with Rab11 wt-GFP. 24 h later, cells were exposed to 150 µg ml^{-1} SPIOPSN for 20 h. Live cell imaging displayed no clear colocalization of Rab11 with SPIOPSN. (C/Magnification: D) HeLa cells were exposed to 150 µg ml^{-1} SPIOPSN and then immunostained for Rab11 after 20 h of nanoparticle exposure. SPIOPSN displayed very low amounts of colocalization with Rab11$^+$ endosomes. (E) To study the crosstalk of SPIOPSN trafficking with the autophagosomal pathway, we incubated HeLa cells with 150 µg ml^{-1} SPIOPSN. 20 h later, autophagosomes were immunostained for LC3. Cells were examined by confocal imaging. No clear colocalization of SPIOPSN with LC3 was observed. (B/C/E): Scale bar: 10 µm. (D/F): Scale bar: 1 µm. Representative images are shown.

3.3.7 *In vivo* distribution of SPIOPSN in mice

The former chapters described the intracellular trafficking routes of nanoparticles. In the upcoming sections, we exploited the formerly gained knowledge and the superparamagnetic features of the nanoparticles to further investigate the intracellular trafficking pathways and the biodistribution of nanoparticles.

To study whether superparamagnetic nanoparticles were an appropriate tool to analyze the biodistribution in mice, we tail-vain injected SPIOPSN into NSG mice. 24 h later, peripheral blood, bladder fluid, spleen, liver and kidney were isolated. Single cell suspensions were obtained from spleen, liver and kidney. SPIOPSN-containing cells were magnetically isolated and examined via confocal microscopy. In summary, a magnetic enrichment of cells from the peripheral blood failed. Therefore, we concluded that nanoparticles were efficiently cleared from the blood stream without the uptake by the phagocytic system of the blood. In this context, it is worth to mention that NSG mice are immunodeficient mice with less or no phagocytic cells (228).

Also kidney cells and the bladder fluids lacked SPIOPSN. In contrary, massive amounts of SPIOPSN accumulated inside liver and spleen. Most of the SPIOPSN displayed endocytic structures that resembled the previously identified intracellular vesicles (Figure 33).

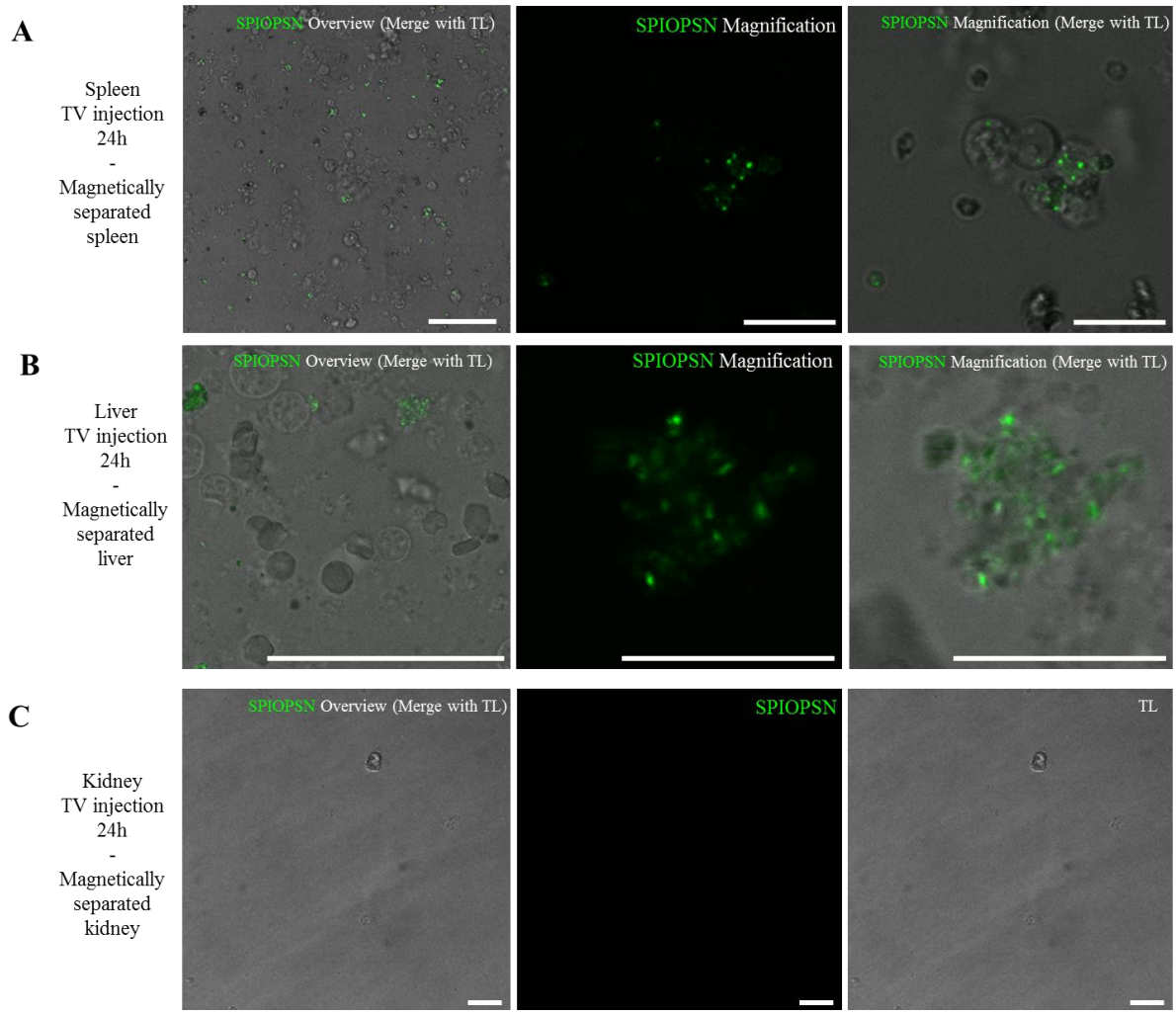

Figure 33: *In vivo* distribution of SPIOPSN. 2 mg of SPIOPSN were tail-vain injected into NSG mice (n = 4). 24 h later, spleen, liver, kidney, peripheral blood and bladder were isolated. Single-cell suspensions were generated. Tissue fractions were magnetically sorted by MACS. Uptake was qualitatively analyzed by confocal microscopy. (A) Splenic cells internalized SPIOPSN via endocytic structures. The left image shows a randomly recorded overview about the isolated fraction. The right image displays a randomly chosen magnification of SPIOPSN-containing cells (B) Liver cells internalized SPIOPSN via endocytic-like vesicles. The left image presents an overview about the isolated fraction. The right image displays a randomly chosen magnification of SPIOPSN-containing cells. (C) No SPIOPSN were detected inside the magnetically enriched fraction of the kidney. Scale bar: 10 µm. Tail-vain injection and animal preparation was performed by Patricia Okwieka, University Medical Center, Mainz.

Taking all of the results into account, we resumed that SPIOPSN are applicable to study their biodistribution (*in vivo*) after magnetic cell separation. We could show that SPIOPSN are taken up into endocytic-like vesicles *in vivo*. These vesicles resembled the identified structures *in vitro*. Therefore, we thought about an approach to exploit the magnetic features of the SPIOPSN on a subcellular level. The aim of the next project was the magnetic isolation of intracellular SPIOPSN-containing vesicles. With this application, we wanted to dissect the intracellular nanoparticle trafficking on a proteomic level (Figure 34).

3.3.8 Shaping a picture of endocytosis: Reconstruction of intracellular nanoparticle trafficking

As stated in the previous chapters, we found that SPIOPSN are trafficked from macropinosomes via multivesicular bodies to multilamellar lysosomes. Therefore, we asked whether we could characterize the SPIOPSN-containing vesicles in more detail.

To obtain a proteomic snapshot of SPIOPSN-containing vesicles, HeLa cells were incubated with SPIOPSN for 20 h (Figure 34). Subsequently, noninternalized SPIOPSN were removed by extensive washing. Cells were mechanically disrupted and cell debris was removed by multistep centrifugation. SPIOPSN-containing vesicles were magnetically separated in a magnetic field for 12 h under cooling and with the addition of protease inhibitors. The magnetic fraction was carefully washed with PBS and then solubilized inside urea buffer. The nonmagnetic fraction was also solubilized with urea buffer. Quality controls were performed by the analysis of the magnetic/nonmagnetic fraction by TEM and SDS-PAGE. Subsequently, the fractions were forwarded to Dr. Stefan Tenzer, who performed the mass spectrometry measurements (Institute for Immunology, University Medical Center, Mainz).

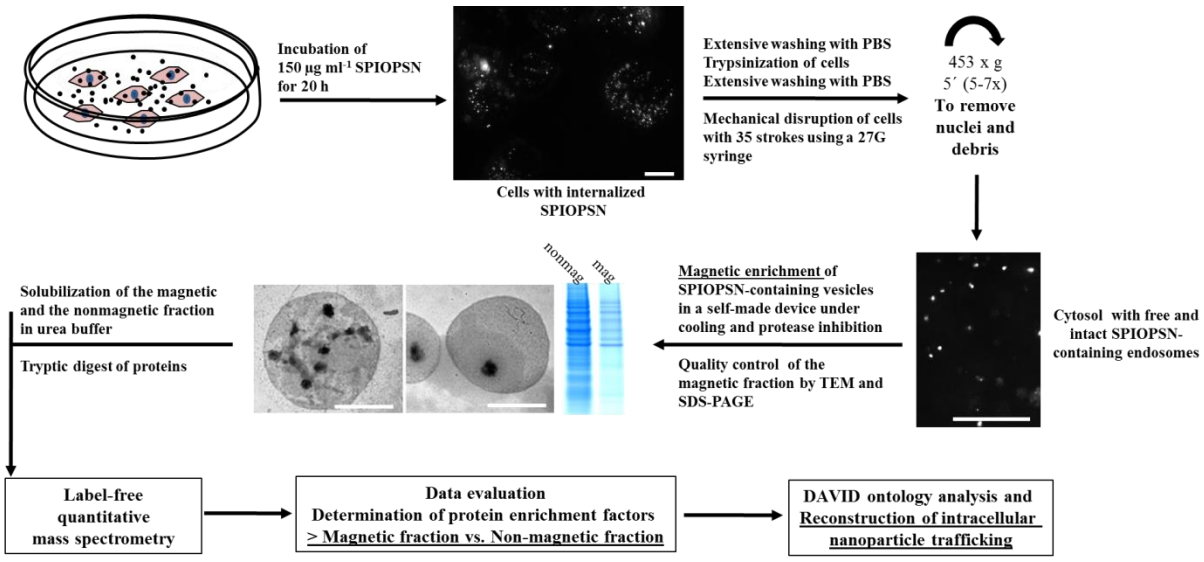

Figure 34: Scheme for the isolation of intracellular magnetic vesicles and their analysis by quantitative peptide mass spectrometry. 1.8 x 10^7 HeLa cells were exposed to 150 µg ml^{-1} SPIOPSN for 20 h. After incubation, non-internalized SPIOPSN were extensively removed by washing. Cells were trypsinized, centrifuged and extensively washed with PBS. The terminal washing fraction was centrifuged at 20 000 x g for 30 min. No free SPIOPSN were detected. To obtain the cytosol with SPIOPSN-containing vesicles, cells were mechanically disrupted. Intact cells and debris were removed by centrifugation. This step was repeated until no pellet was visible anymore. The cytosolic supernatant with the magnetic endosomes were injected into a custom-made magnetic device. Magnetic separation of SPIOPSN-containing vesicles was performed for 12 h under cooling and the inhibition of proteases. The magnetic pellet was carefully washed with PBS. Proteins of the magnetic and the nonmagnetic fraction were solubilized in urea buffer. Peptides were generated by a tryptic digest. Samples were quantitatively measured by a TOP3-dependent MS approach and peptide fragments were identified by a database-related search. Enrichment factors are based on the determined ppm values and were calculated comparing the magnetic vs. the nonmagnetic fraction. Enriched proteins were forwarded to DAVID ontology analysis and classified by their subcellular localization. Intracellular nanoparticle trafficking was reconstructed based on the results of DAVID protein ontology analysis.

After mass spectrometry measurements and data evaluation, the amount of proteins between the magnetic and the nonmagnetic fraction was compared. Based on the averaged ppm values of the quantified proteins, protein enrichment factors were calculated (example in Table 18).

Table 18: Calculation of the protein enrichment factors (example). Ppm values of the proteins in the magnetic fraction were compared with the ppm values of the proteins of the supernatant. Based on the averaged ppm values, enrichment factors were calculated for each protein. The calculation of the enrichment factor of the protein Rab5C is shown as an example. Quantification of proteins was performed in triplicates. Averaged ppm values were calculated.

Uniprot ID	Magnetic pellet (ppm value)	Supernatant (ppm value)	Enrichment factor
RAB5C_HUMAN	34285	6339	5,41

3.3.9 DAVID protein ontology analysis of the vesicular fraction reveals an association of endolysosomal proteins with SPIOPSN-containing vesicles

Overall, we were able to identify and quantify 1492 proteins in the magnetically enriched fraction, whereas 884 were significantly enriched by a factor of at least 2 in comparison to the nonmagnetic fraction. We then applied the online tool "DAVID protein ontology" to analyze the intracellular nanoparticle trafficking (INT) *in silico* (229). Proteins were grouped into annotation clusters owing to their known subcellular localization in literature (Table 19).

Table 19: DAVID protein ontology analysis (GOTERM: GOTERM_CC_FAT). Proteins that were magnetically enriched > 2-fold in comparison to the nonmagnetic supernatant have been considered in DAVID ontology analysis. The ontology analysis clustered the different proteins owing to their known subcellular localization. The enrichment scores for the distinct subgroups are based on the EASE score. In the presented table, the starting five annotation clusters are shown with enrichment scores larger than 9. The full analysis is provided in the supplementary information of this thesis. Counts show the proteins that are classified into the individual terms. We mainly identified proteins of the endolysosomal system and from mitochondria. P-value: modified fisher exact p-value. The smaller the p-value, the higher enriched the proteins inside the respective class. The proteins of the red-marked GOTERMs are listed in the supplementary information of this work.

Annotation Cluster	Enrichment Score/ Term	Protein count	p-value
Annotation Cluster 1	Enrichment Score: 42.07		
	envelope	145	3.6E-45
	organelle envelope	144	1.2E-44
	mitochondrial envelope	115	7.1E-43
	mitochondrial membrane	111	1.6E-42
	mitochondrial inner membrane	96	5.3E-41
	organelle inner membrane	99	1.5E-40
Annotation Cluster 2	Enrichment Score: 29.76		
	lysosome	69	1.3E-30
	lytic vacuole	69	1.3E-30
	vacuole	75	2.9E-30

Annotation Cluster 3	Enrichment Score: 16.73		
	vesicle	105	3.8E-18
	membrane-bounded vesicle	93	2.5E-17
	cytoplasmic membrane-bounded vesicle	91	2.9E-17
	cytoplasmic vesicle	100	4.2E-17
Annotation Cluster 4	Enrichment Score: 9.24		
	membrane fraction	99	2.9E-10
	insoluble fraction	101	4.7E-10
	cell fraction	120	1.4E-9

3.3.10 Reconstruction of intracellular nanoparticle trafficking

The dissection of intracellular nanoparticle trafficking is based on the identified proteins that were categorized into the GOTERMs lysosome and vesicle (Table 19, for a detailed protein list, see supplementary information). We used the simplest endocytic model for the reconstruction of INT (Figure 35). In our approach, we identified several enriched endolysosomal proteins in the magnetic fraction. Early endosomes can be recognized by the markers RAB5A and RAB5C (230). Further adaptor proteins such as proteins from the AP-1/AP-2 family (e. g. AP1A1, AP1B1, AP2B2) have been described as key players in endocytic trafficking (231, 232). Proteins such as RhoB and ARF1 have been associated with the (macro)pinocytic machinery (90, 233).

RAB7A and RAB9 are important markers of multivesicular bodies (234). MVBs have been associated with several tetraspanins (e. g. CD9, CD63, CD81, CD82) and HLA molecules (e. g. HLA MHC class I antigen A*68) (173, 174, 235-237). Further proteins that are present on MVBs are Niemann Pick disease C1 (NPC1) and Niemann Pick disease C2 (NPC2) (238). Flotillin 1 (FLOT1) and flotillin 2 (FLOT2) was also identified by MS. Proteins such as LAMP1 and LAMP2, Mannose-6-P-receptor-CD (MPRD) and Mannose-6-P-receptor-CI (MPRI) have been shown to associate with the endolysosomal pathway (239, 240). LTOR1, LTOR2, LTOR3 are present on lysosomes and mediate several events of intracellular trafficking (241). We were also able to identify several v-type proton ATPase pumps that obtain the lysosomal pH (e. g. VATG1, VATC1). In case of recycling endosomes, RAB11A and RAB11B were identified. RAB11 is mainly associated with recycling endosomes, but also fulfills different tasks inside the cell, for instance on MVBs (162, 242). Additionally, we identified proteins that were previously shown to be with COP vesicles (e. g. SC23A, SAR1A, COPE) (243).

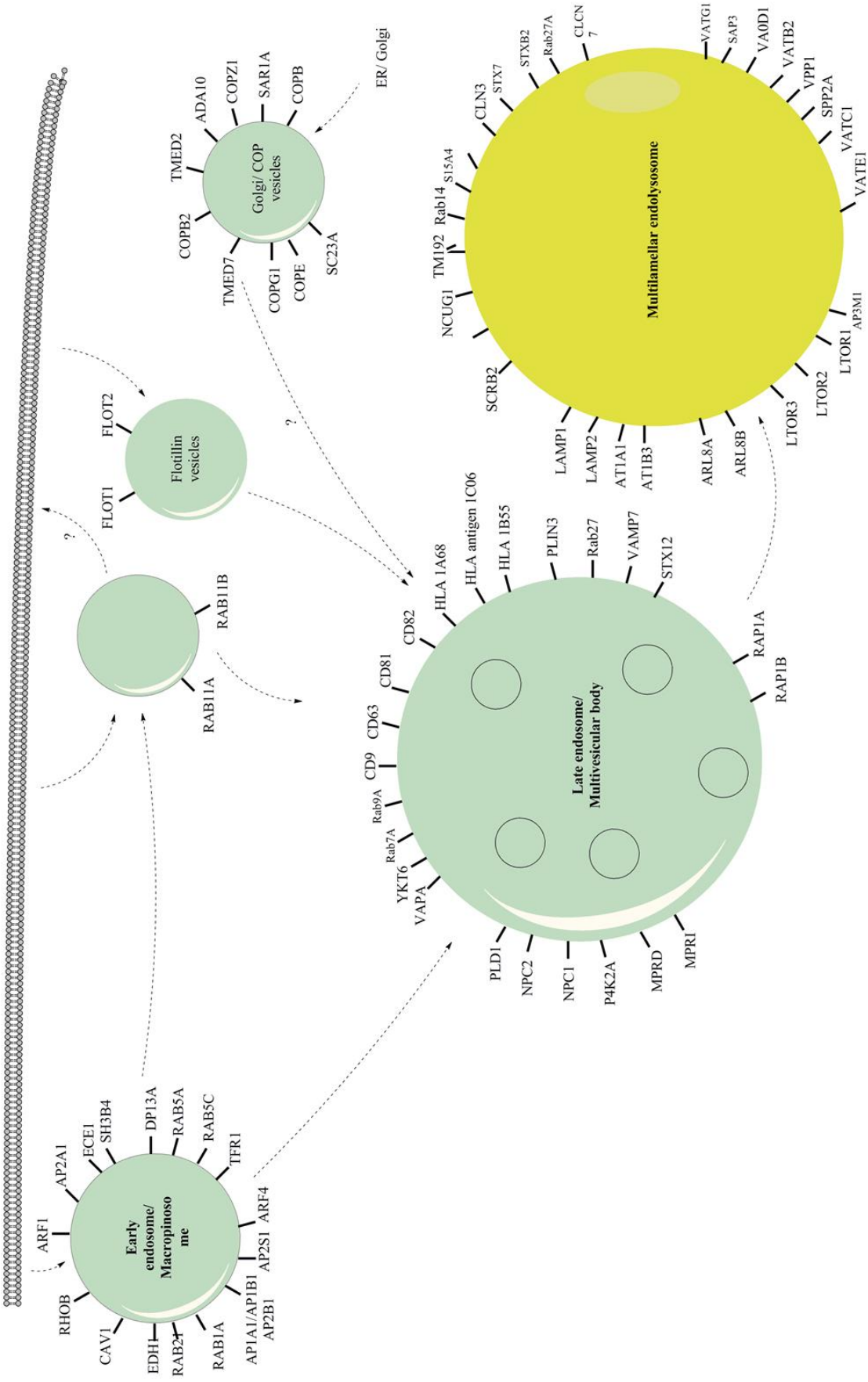

Figure 35: Reconstruction of intracellular SPIOPSN trafficking. Intracellular nanoparticle trafficking was dissected. INT is based on the GOTERMs vesicle and lysosome (see red marked terms in Table 19). Protein names are depicted by their Uniprot_IDs. The full names are provided by the supplementary part.

Altogether, we have identified a large number of novel marker proteins that were associated with SPIOPSN-containing vesicles. These proteins enable us to create a snapshot of the participating vesicles during nanoparticle trafficking after 20 h of exposure. Since we have detected the majority of nanoparticles inside lysosome-like organelles after 20 h, it was not surprising that we have identified a large number of enriched lysosomal matrix proteins. Therefore, we reconstructed the intravesicular milieu of a nanoparticle in more detail (Figure 36).

3.3.11 Reconstruction of the intravesicular lysosomal matrix

The hydrolases and cofactors of the lysosomal matrix have been extensively studied in the proteomic field (156). Many of the previous investigations performed density gradient fractionation or affinity chromatography to obtain the vesicles of interest. Our approach utilized the magnetic isolation of SPIOPSN-containing vesicles.

In our study, we have identified acetylgalactosamine-6-sulphatase *N* (GALNS) and N-acetylglucosamine-6-sulphatase (GNS) as hydrolases for the degradation of chondroitin sulphate and keratin sulphate. Acid ceramidase (ASAH1) is known to hydrolyze ceramide into sphingosine and free fatty acids. Arylsulphatase A (ARSA) and arylsulphatase B (ARSB) hydrolyzes cerebroside sulphates. Cathepsin B/D/Z/L1/C are enzymes for unspecific proteolysis. The CLN5 protein was also identified as a lysosomal matrix protein. Other identified proteins are hexosaminidase A (HEXA) and hexosaminidase B (HEXB). These proteins have the potential to degrade GM2 gangliosides. β-mannosidase (MANBA) cleaves mannosyl residues. Palmitoyl-protein thioesterase 1 and palmitoyl-protein thioesterase 2 removes thioester-linked fatty acyl groups from proteins and peptides. Proteins that are not mentioned in the text are listed as Uniprot IDs in Figure 36.

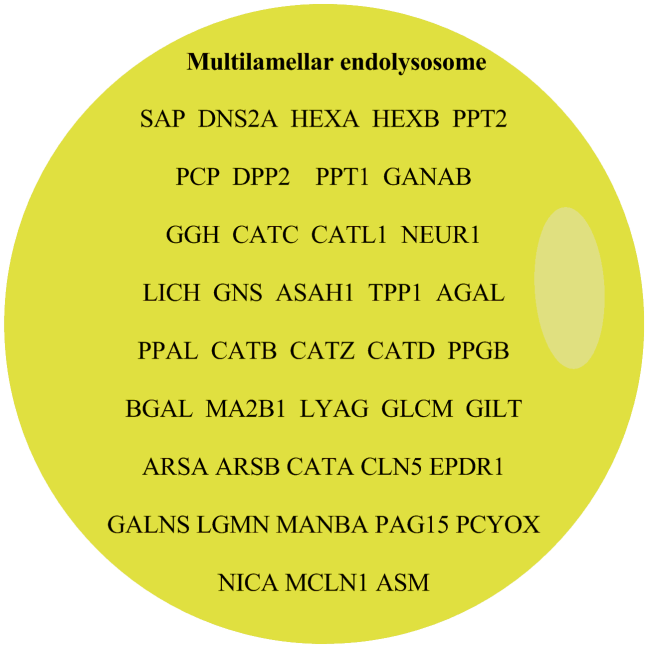

Figure 36: The proteomic dissection of a nanoparticle-containing lysosome. The data of mass spectrometry revealed that several lysosomal proteins were enriched inside the magnetic fraction. Protein abbreviations are given as Uniprot_ID. Full names are provided by the supplementary information.

The reconstruction of the lysosomal milieu of nanoparticles becomes especially important for the design of biodegradable nanocarriers. Frequently, the nanoparticle synthesis is often not tailormade for the endolysosomal system. Consequently, the intravesicular degradation of the nanocarriers fails. Since we used a non-biodegradable nanoparticle, we were not able to show the degradation of the particle itself. However, we tested whether the components of the lysosome can degrade the nanoparticulate protein corona (Figure 37 and Figure 38).

3.3.12 The nanoparticle protein corona is degraded inside Lamp1^{+}/Lamp2^{+} lysosomes

Based on the gained knowledge about the reconstructed lysosomal matrix, we next asked the question whether the enzymes of the lysosomal matrix have the potential to degrade the protein corona of SPIOPSN. The nanoparticulate protein corona is formed, when nanoparticles enter a biological fluid with proteins (244). To investigate whether the protein corona is degraded inside the lysosome, SPIOPSN were incubated with Alexa Fluor 647 labelled bovine serum albumin to adsorb a fluorescently labeled protein on the surface of the nanoparticles.

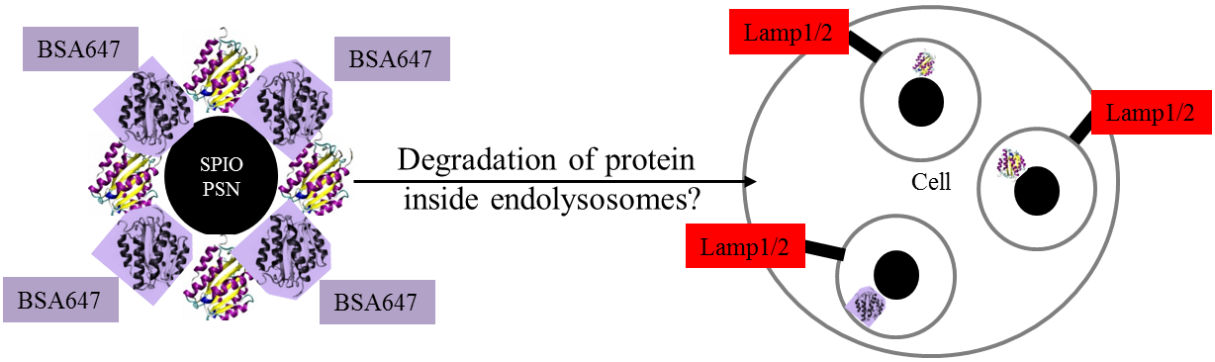

Figure 37: Schematic illustration of the system that was used to study the degradation of the protein corona inside the lysosomes. Nanoparticles were preincubated in pure BSA647 for 60 min. Afterwards, nanoparticles were diluted with media and then added to the cells. After incubation, cells were immunostained for Lamp1/2. SPIOPSN and BSA647 were analyzed for colocalization with the lysosomal markers by confocal microscopy.

The coincubation of SPIOPSN with BSA647 (without preincubation) led to the internalization of both cargos into different vesicles only showing a minor rate of colocalization (Figure 38). This shows that BSA-AF647 was not significantly adsorbed on the surface of nanoparticles, which were already covered with proteins. Furthermore, we concluded that SPIOPSN and BSA647 exploited distinct internalization pathways. Taking this into account for the following experiments, we resumed that we only could detect preadsorbed proteins on the nanoparticles. Indeed, the incubation of BSA647-preincubated SPIOPSN revealed strong signals of colocalization between SPIOPSN and BSA647. Therefore, it was concluded that the protein corona is cointernalized with the nanoparticle into endocytic vesicles. Next, we investigated, whether BSA647 is still present inside lysosomes. Interestingly, no BSA647 was observed inside Lamp1/Lamp2$^+$ vesicles. In contrary, vesicles negative for Lamp1/2 still contained BSA647. Our interpretation for this was that BSA647 is degraded inside Lamp1/Lamp2$^+$ organelles. The investigation of BSA647-coated SPIOPSN revealed that the nanoparticles inside Lamp1/Lamp2$^+$ vesicles lack BSA647 after 20 h of incubation (Figure 38). Owing to this, we concluded that parts of the protein corona were degraded by the environment of the lysosomes.

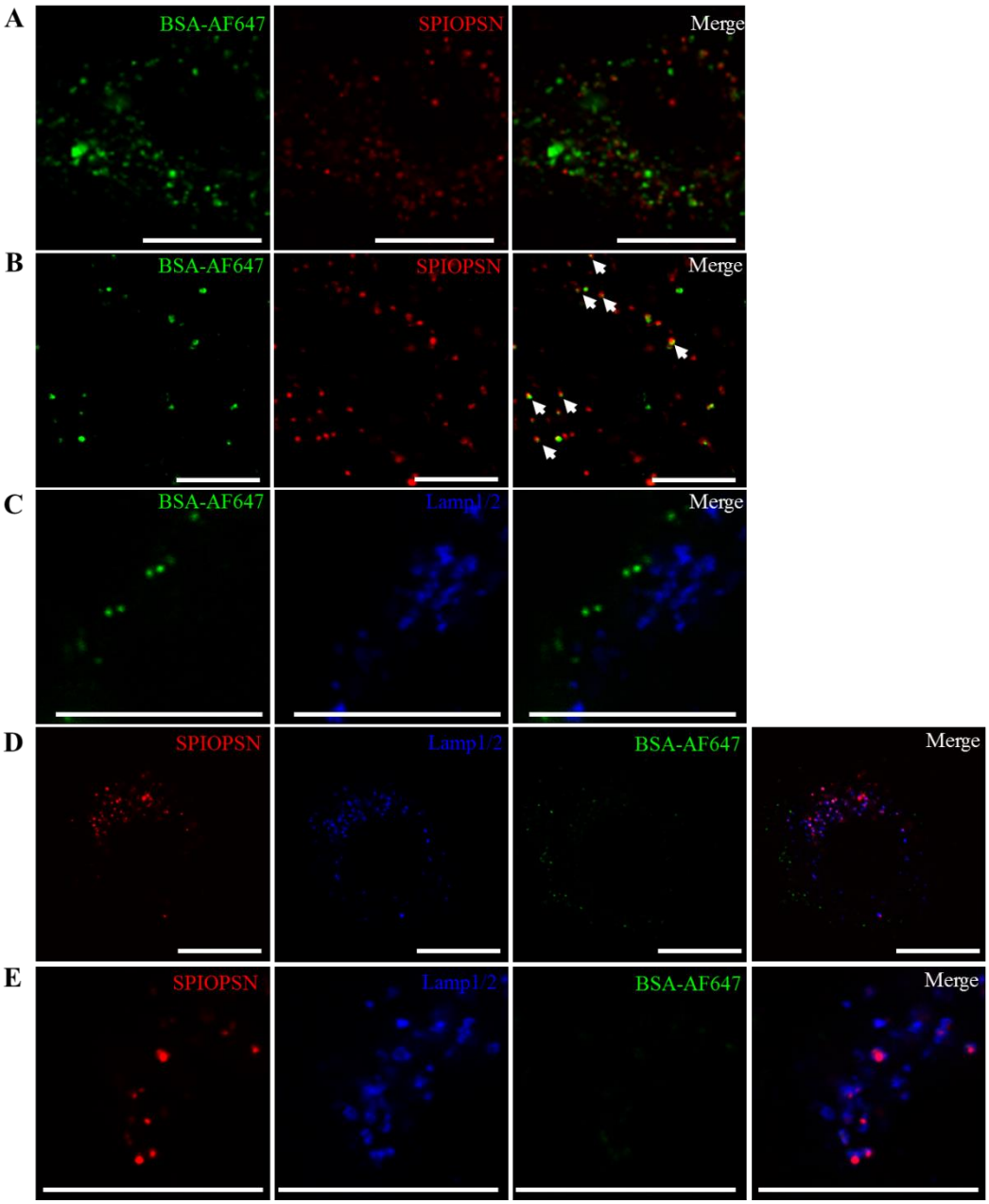

Figure 38: The protein corona is cointernalized with nanoparticles and then degraded inside the lysosome. (A) HeLa cells were coexposed to 150 µg ml^{-1} SPIOPSN and 0.5 mg ml^{-1} BSA647 for 8 h. Almost no colocalization was observed. (B) 150 µg ml^{-1} SPIOPSN were preincubated in 0.5 mg ml^{-1} BSA647 for 60 min and then added for 6 h to HeLa cells. A large number of colocalization spots were observed (white arrows). (C) HeLa cells were incubated with BSA647 for 20 h. BSA647 was not detectable in Lamp1/2^{+} lysosomes. (D) Cells were exposed to BSA647-preincubated SPIOPSN (150 µg ml^{-1}) for 20 h. No BSA647 was present on SPIOPSN. Minor amounts of excess BSA647 accumulated inside Lamp1/Lamp2^{-} cells after 20 h of incubation. (E) Magnification of Lamp1/2^{+} lysosomes containing SPIOPSN. Less to no BSA647 was detected inside lysosomes that harbored BSA647-precoated SPIOPSN.

4. Discussion

This study aimed to elucidate the interaction of polymeric nanoparticles with biological systems in terms of drug delivery, entry and intracellular trafficking pathways of nanomaterials. In summary, we could show that biodegradable PLLA nanoparticles are potentially suitable for a rapid and effective delivery of drugs by a novel mechanism we referred to as "kiss-and-run". For the first time, we provide evidence for a non-invasive mechanism transporting nanoparticulate cargo over the cell membrane into lipid droplets. The nanoparticulate cargo release occurs during several milliseconds owing to a physicochemical interaction between the nanoparticle and the plasma membrane.

We further show that these polymeric nanoparticles are taken up by cells after their long-term exposure. Therefore, issues about the uptake mechanisms and intracellular trafficking pathways of polymeric nanoparticles were raised. For this project, we changed the polymer of the nanoparticle to polystyrene. We show that ~ 126 nm large SPIOPSN are internalized by a macropinocytic-like entry mechanism. In a series of experiments we demonstrate that their entry mainly depends on distinct small GTPases, kinases and on cholesterol.

Further on, we established a novel method for the unbiased dissection of intracellular nanoparticle trafficking. This method is based on the identification of proteins, which are located on nanoparticle-containing vesicles. Under native conditions, nanoparticles are transported from early endocytic vesicles via multivesicular bodies into the terminal multilamellar lysosomes. This dissection of INT may serve as a novel fundament to describe nanoparticle trafficking in more detail. Taking all of these data together, we propose a novel drug delivery mechanism for polymeric nanoparticles and investigated a so far unknown mechanism of the entry and trafficking of polymeric nanoparticles.

4.1 Interaction of polymeric nanoparticles with biological systems can trigger a release of different nanoparticulate components

Polymeric nanoparticles are a versatile tool to shield drugs from environmental influences (2, 6). The primary goal of these drug delivery vehicles is the transport of the loaded cargo to the location of interest (43, 245). However, less is known about the release of nanoparticulate components that coexist inside the nanoparticle and should primarily not be delivered. These factors include polymers, stabilizing surfactants or dye molecules (246). Notably, the circumstance that these factors sometimes are released is no disadvantage. Moreover, this observation was utilized to study the mechanism of nanoparticulate drug delivery in more detail. To track the interaction of nanoparticles with cells, we chose a nanoparticulate model system with a noncovalently-bound dye. This enabled us to fluorescently track the cargo release during the interplay with different cell types.

The release kinetics of PMI during the exposure of HeLa cells or other cell types to PLLA-Fe-PMI nanoparticles reproducibly revealed a fast accumulation of the model dye into lipid droplets (Figure 7, Figure 8 and Figure 9). To our knowledge, no comparable study exists that could show an uptake of nanoparticles within the first five minutes of exposure. Such fast rates of internalization are only known for biomacromolecules (e. g. EGF) or for freely diffusing small molecules (247, 248). Therefore, we assumed and also demonstrated that the encapsulated dye molecules were independently transported from the polymeric matrix into the cells (Figure 9). Interestingly, this phenomenon was afterwards also recognized for other nanoparticles (e. g. PLLA-PMI or PS-COOH) (6). Tomcin and colleagues used these observations and demonstrated that also other components of nanoparticles (e. g. surfactants) are released during nano-bio-interactions (249). They microscopically showed a release of block-co-polymers from nanoparticles before the nanoparticle itself enters the cell.

Another interesting observation was made during the investigation of the interaction of cells with SPIOPSN. Here an undesired delivery of a nanoparticulate component was observed. After nanoparticle exposure, it was obvious that the number of intracellular $TIP47^+$ lipid droplets had more than doubled (data not shown). It seemed that this effect is triggered by a surfactant-like component of the nanoparticle. During miniemulsion polymerization, SPIOs are generated inside oleic acid droplets that are probably not completely removed from the nanoparticle after their magnetic purification (35, 37). In biological experiments it is likely that oleic acid molecules are released from the particle and are subsequently stored inside lipid droplets. *In vitro*, this is artifically achieved by the feeding of cells with a BSA carrier, which is complexed with oleic acid (209). In the context of lipid droplets and nanoparticles, it is worth to mention that other studies also observed a increase of LDs after nanoparticle exposure (250, 251). Here the authors assumed that the increase of LDs is triggered by the quantum dot-mediated induction of reactive oxygen species. After the exposure of PC12 cell to CdTe nanoparticles, the amount of ROS was significantly increased in the culture (250). We also considered this and measured ROS levels and the mRNA levels of hypoxia-inducible transcription factor-1α (data not shown). However, no significant elevation of these factors was observed (data not shown). Therefore, it was concluded that the increased number of LDs is based on the import and the incorporation of nanoparticulate oleic acid into LDs.

Taken together, the observation of a membrane-nanoparticle-interaction-triggered release of nanoparticulate components is exciting. Though, this newly gained knowledge also raises issues about the relevance of these data for other studies. Here it should be noted that a large number of distinct nanoparticles are synthesized and tested for their interaction with biological systems (252). Thereby, a variety of studies already used noncovalently bound fluorescent tracers in nanoparticles that might be released during biological experiments (253). Most notably in uptake studies of nanoparticles, the release of such fluorescent dyes or the presence of nonencapsulated dye molecules can result in the false positive interpretation of the data (254, 255). This thesis should motivate nanoscientists to

recognize that the deep characterization of the nanomaterial is a major prerequisite for their application in biological studies (256). Furthermore, the scientific community has to raise issues about the fate of such distinct hydrophobic molecules (e. g. dyes or drugs) that are released from nanoparticles and partially accumulate inside lipid droplets (208). Since the biology of LDs is so far less understood, one can only hardly predict the biological consequences after the disposition of distinct hydrophobic drugs. Especially, the question whether the hydrophobic molecule can be released after LD disassembly is a point that needs to be clarified in the future.

Prospective applications that could utilize the non-invasive "kiss-and-run" mechanism

In general, non-invasive nanoparticle-based drug delivery mechanisms can be utilized to gain access to cells with a low rate of endocytosis. In the human body, several cells are predestined for a rapid and high uptake of extracellular material due to their high phagocytic potential (257). Conversely, other cell types such as lymphocytes naturally lack high endocytic rates (206). These cells are hardly accessible via invasive drug delivery mechanisms (205). However, in several cases an intracellular delivery of drugs is mandatory. For such applications, one can exploit the "kiss-and-run" mechanism.

Moreover, the accumulation of hydrophobic substances inside lipid droplets bears the potential to develop novel applications. One example could be the treatment of dyslipidemic patients (258). So far, the metabolism of LDs is less understood, but it is known that the fatty acid synthesis depends on the enzymes DGAT1 and DGAT2 (259). In dyslipidemic patients, an excess of lipid storage is observed (260). To counteract this, the nanoparticulate delivery of a niacin-conjugate to LDs seems to be promising for a therapeutic approach (258). Others reported the importance of LDs in the life cycle of hepatitis C viruses (HCV) (261). It was shown that the replication of HCV depends on LDs. Someday this could give the motivation to establish a nanoparticle-based drug delivery approach for the targeting of LDs to inhibit the life cycle of HCV.

4.2 PLLA and polystyrene nanoparticles release hydrophobic cargo on hydrophobic surfaces by "kiss-and-run"

Before PMI accumulates inside lipid droplets, PMI is released by a "kiss-and-run" mechanism (Figure 10). This mechanism can be described as a physico-chemical and temporary interaction of the nanoparticle with a hydrophobic membrane (Figure 39). But what are the parameters that drive the release of PMI out of the polymeric matrix? Probably one of the most crucial factors is the partition coefficient of the hydrophobic substance (262). This coefficient describes the ratio of distribution of a compound in two imminiscible phases (263, 264). In pharmacokinetics of nanoparticulate systems it is desirable that the compound is hydrophobic enough to stay in the nanoparticle. However, the cargo should also be able to pass the plasma membrane without getting stuck. After the diffusion through the

cell membrane, the cargo should further have the ability to cross the hydrophilic cytoplasm to reach the target location (265).

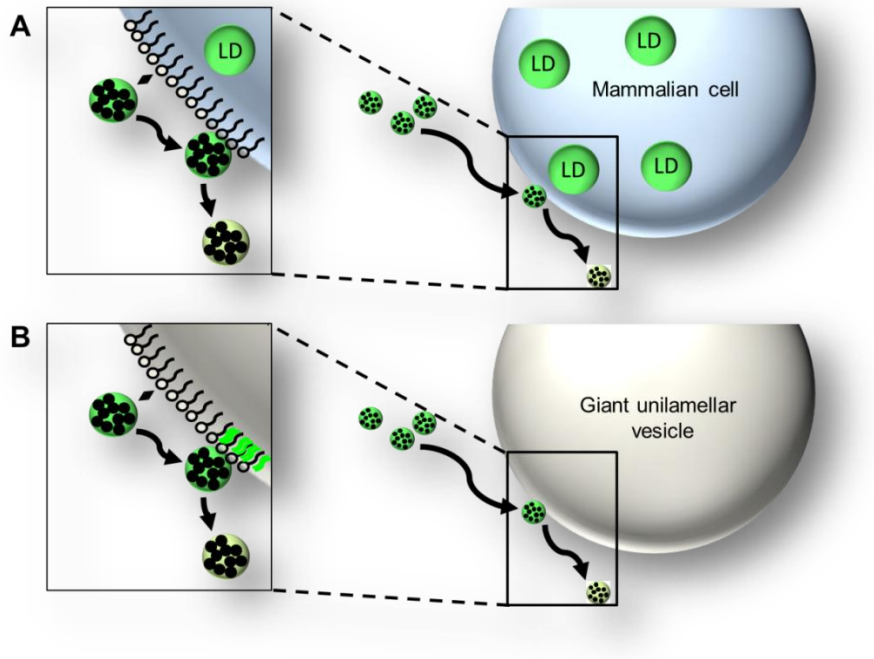

Figure 39: Schematic illustration of the kiss-and-run mechanism. Nanoparticles briefly interact with the lipid bilayer of a cell (A) or a giant unilamellar vesicle (B), thereby releasing its dye that accumulates in lipid droplets (LD) or in the membrane, respectively.

It seems as though PMI fulfills all of these requirements (Figure 9 and Figure 10). Whether this is the case for other molecules was also investigated during this work. We analyzed several other hydrophobic drugs such as etoposide and podophyllotoxin for their release properties out of PLLA nanoparticles (data not shown). We assumed that the drug release of these compounds also occurs via "kiss-and-run". In one of the experiments we compared the effects of free podophyllotoxin (low dosage) with podophyllotoxin that was loaded into PLLA nanoparticles (high dosage). Microtubule (MT) depolymerization was morphologically tracked using U2OS-TagRFP-Tubulin cells (Marinpharm, Germany). In these experiments we could demonstrate that free podophyllotoxin can induce a MT depolymerization within 5 min. In contrary, the treatment of cells with nanoparticle-encapsulated podophyllotoxin (high dosage load) failed to induce a rapid microtubule depolymerization (266). This reveals that an efficient drug release by "kiss-and-run" probably also depends on the chosen drug. But this is certainly only one drawback of nanoparticulate drug delivery systems (267). An additional factor that could influence the release kinetics *in vitro* and *in vivo* is the protein corona of nanoparticles. Interestingly, Paula *et al.* reported that the formation of a protein corona significantly decreases the efficiency of drug release out of mesoporous silica nanoparticles (268). The authors assumed that the dense corona traps the encapsulated drugs hampering its release.

On the interface of membranes and nanoparticles, distinct mechanisms could drive the release of hydrophobic substances out of nanoparticles (55). In general it is known that surfactants have the potential to disrupt the membrane organization by changing the lipid conformation (269). Since nanoparticles are stabilized with surfactants such as sodiumdodecyl sulfate (SDS) it would not be surprising that lipids are reorganized after nanoparticle-membrane interaction (35). Exactly, this interaction could favor the release of the cargo out of the nanoparticle. Other factors that could have an impact on the release mechanism of drugs on the membrane are the hydrophobicity of the nanomaterial and the strength of interaction between nanoparticles and cellular membranes (55). In this study, we analyzed different nanoparticles on their interactions with giant unilamellar vesicles (Figure 10 and Figure 11). As an example, PS-NH_2-BODIPY (NH_2 functionalized) as well as PLLA-Fe-PMI (COOH functionalized) and SPIOPSN-BODIPY (Sulfonate functionalized) displayed two completely different motifs of interaction on the giant unilamellar vesicles. The positively charged PS-NH_2-BODIPY nanoparticles have been observed to permanently interact with the GUVs by dashing around onto the vesicles surface (Figure 11A). Interestingly, after some time of interaction, the nanoparticles disrupted the vesicles implying a strong interaction between both partners. In contrary, the negatively charged nanoparticles PLLA-Fe-PMI and SPIOPSN-BODIPY only temporarily interacted with the GUV without destroying it (Figure 11B).

If the strength of interaction leads to an increased efficiency of cargo release is not clear from our observations since we have used covalently-bound dyes for these experiments. However, we demonstrated that the disruption of the membrane was only induced by strongly interacting and aminofunctionalized nanoparticles (own observation). Lui *et al.* supported this hypothesis (270). They showed that the surface functionalization of silica nanoparticles has an important impact on the membrane integrity of tethered bilayers (270). The authors compared four types of surface functionalizations (COOH, NH_2, bare, PEG). According to their data they observed a distinct order for the surface functionalization regarding their potential to disrupt membranes (amine > carboxyl ~ bare > PEG). In other studies, the mechanism of disruption leads to a hole formation after membrane-nanoparticle interaction (271). Further on, computer simulations calculated that nanoparticle-membrane interactions are also able to induce a thinning of the contacted membrane (272). Over time, this could also result in the collapse of the membrane (55).

To come back to the release mechanism of PMI, one needs also to discuss the effect of hydrophobicity on the interactions of nanoparticles. As previously mentioned, it was demonstrated that PLLA-Fe-PMI nanoparticles release their hydrophobic cargo PMI in hydrophobic media and on hydrophobic surfaces of GUVs (Figure 10). This shows that hydrophobicity might be a crucial factor that can drive the interactions between nanoparticles and lipid membranes. In the past, several simulations calculated the impact of hydrophobic nanoparticles on membranes. Yang and colleagues modeled the simulation of a hydrophobic and a semihydrophobic nanoparticle with a bilayer (273). While the interaction of

hydrophobic nanoparticles with membranes can result in their inclusion into the bilayer, the semihydrophobic nanoparticle is only found to adsorb into the membrane. Also a morphological reorganization of the membrane lipids strongly depends on the hydrophobicity of nanoparticles (51). All of these calculations referring to the impact of hydrophobicity on the nanoparticle-membrane interactions are in compliance with the provided data of this thesis. Based on the release experiments that have been performed, we propose that the release for PMI is mainly triggered by hydrophobic interactions between the membrane and the nanoparticles. This hydrophobic interaction could temporarily provide a more favorable hydrophobic environment for the PMI inside the membrane than inside the nanoparticle.

4.3 Polymeric superparamagnetic nanoparticles are internalized by a macropinocytic-like mechanism

After the long-term exposure of PLLA-FE-PMI nanoparticles, we observed their uptake into cells. Morphologically, the endocytic structures that mediated the nanoparticle uptake resembled macropinocytic ruffles (Figure 12). However, we previously showed that PLLA-Fe-PMI nanoparticles are not suitable to investigate nanoparticle uptake mechanisms (6). To reliably study the entry mechanisms of polymeric nanoparticles, we therefore used well-characterized superparamagnetic iron oxide polystyrene nanoparticles (SPIOPSN) with a fluorescently bound fluorochrome (BODIPY). The SPIOPSN fulfilled all requirements that were necessary to conduct these kinds of studies (6, 37). Since we have shown that SPIOPSN only temporarily interact with cell membranes, we demonstrated an uptake of SPIOPSN via the fluid phase endocytosis (Figure 12).

4.3.1 The entry of SPIOPSN is dependent on several factors of macropinocytosis

To examine the entry routes of SPIOPSN, several endocytic pathways have been investigated by the application of different freely permeable inhibitor molecules (Table 5). The set of inhibitors covered a large number of different endocytic pathways. After intensive research on this project, we mainly focused on inhibitors of macropinocytosis (Figure 12 and Figure 15). Since no standards for the investigation of nanoparticulate macropinocytosis are defined yet, we checked several criteria that have been considered as crucial in viral macropinocytic mechanisms (140). These include the cointernalization of SPIOPSN with fluid-phase tracers. Furthermore, it is necessary to examine the uptake after the modulation of the actin cytoskeleton. Here Rho GTPases as well as Na^+/H^+ exchangers play a major role (94). Last but not least, the influences of several kinases, dynamin, myosin II and microtubule dynamics have to be checked (212). We have summarized some of the major factors that have been tested in this study (Table 20).

Table 20: Factors worth to test in classical macropinocytosis (212).

Factors	Effect
F-actin cytoskeleton	Inhibition influences ruffling and blebbing.
Fluid-phase uptake	Macropinocytic cargoes often colocalize with fluid phase markers (e. g. HRP, Dextran).
Rho GTPases	Rac1 or Cdc42 mediates macropinocytosis.
Na^+/ H^+exchangers	Inhibition by amiloride blocks macropinocytosis by the lowering of submembraneous pH.
Kinases	Inhibition of signaling kinases should suppress macropinocytosis.

Our images show the co-uptake of SPIOPSN with fluorescently-labeled dextran, an important marker of fluid phase endocytosis (Figure 12). As previously demonstrated, dextran is utilized for the tracking of macropinosomes (274). Morphologically, we could show the internalization of nanoparticles via heterogeneously sized vesicles that are also visible by DIC microscopy (Figure 12). Therefore, we concluded from our experiments that SPIOPSN are internalized via a mechanism of fluid-phase endocytosis (212). Further experiments with an inhibitor of F-actin polymerization allowed to assume that actin reorganization plays an important role during the entry of SPIOPSN and dextran (Figure 12). Previous reports for several cargo molecules like peptides, viruses and fluid phase markers already showed a major participation of actin during their cellular entry (275, 276). Also on an ultrastructural level, we partially observe the classical macropinocytic ruffles and protrusions that embraced SPIOPSN and PLLA-Fe-PMI nanoparticles (Figure 12) (277).

4.3.2 SPIOPSN internalization is accompanied by the small GTPases Rac1 and cdc42

As a consequence of this pathway, the entry of SPIOPSN might depend on some small GTPases that are known to induce the reorganization of the actin cytoskeleton (127, 278). To our knowledge, no one has shown the participation of small GTPases during the uptake of nanoparticles. Therefore, we characterized the possible effects of Rac1 as a small GTPase that is known to be located on the inside of macropinocytic ruffles (136, 137). It was demonstrated that the overexpression of the permanently active mutant of Rac1 Q61L induced the formation of roundly-shaped vesicles (Figure 13). These organelles were previously described as nonbudded premacropinosomes (137). The overexpression of this mutant drastically increased the probability to track SPIOPSN during the early stages of uptake since the terminal vesicular budding was not completed yet (137). And indeed, SPIOPSN were found in roundly-shaped premacropinosomes that seemed to be trapped in the early stages of fluid phase uptake (Figure 13). The same phenotype has been observed after the overexpression of constitutively active cdc42 Q61L (Figure 14). In spite of intensive research in the literature, we were not able to find

a comparable confocal close-up image of this cdc42 Q61L-induced phenotype. However, it is generally accepted that the small GTPase cdc42 is tightly associated with Rac1 implying similar effects after overexpression (279, 280). Further on, it is known that both proteins act in the preliminary stages of macropinocytic ruffle formation (280). Based on this argumentation, it was not so surprising that SPIOPSN were found in roundly-shaped cdc42 $Q61L^+$ and Rac1 $Q61L^+$ premacropinosomes.

Moreover, it is also worth to mention that dominant negative cdc42 T17N-GFP colocalized with SPIOPSN. In this particular case, the vesicles were not static as seen after the overexpression of the constitutively active mutants (Figure 14). All cdc42 $T17N^+$ vesicles directly moved through the cell resembling budded $cdc42^+$-macropinocytic vesicle (Figure 14). The colocalization of cdc42 with nanoparticle-containing vesicles is in accordance with the data of the mass spectrometric analysis, where we identified cdc42 as a protein of the SPIOPSN-associated fraction (Supplementary Table S4). However, no quantitative and qualitative reduction of the internalization rate of SPIOPSN was observed after esiRNA-mediated knockdown of cdc42 and the overexpression of cdc42 T17N (Figure 14). The impact of cdc42 knockdown was previously shown for the macropinocytic uptake of the ebola virus (211). In this study the authors reported a reduction of viral uptake after the siRNA-mediated downregulation of cdc42. Taking all of these data into account, we concluded that in spite of the colocalization, cdc42 is not prominent enough to significantly control the uptake rate of SPIOPSN. Consequently, we proposed that the nanoparticles are taken up by an atypical macropinocytic mechanism (150).

4.3.3 SPIOPSN entry is triggered by an atypical type of macropinocytosis

As demonstrated by confocal imaging, SPIOPSN are internalized via macropinocytic structures (Figure 12, Figure 13 and Figure 14). These specific membrane domains are ordered structures (212). Their formation is tightly regulated by several kinases (140, 146). Most of the kinases were shown to modulate the actin cytoskeleton via several routes (281, 282). Thereby, the PI3K signaling is one of the major pathways, which mediate macropinocytosis (283). Combinations of different experiments allow concluding that PI3K signaling acts in a first order followed by the signaling of PLC (144, 284). Stable transfections as well as pharmacological inhibition of PI3K and PLC demonstrated that both enzymes are essential factors in macropinocytic signaling (285). Taking these observations into account, we pharmacologically inhibited PI3K by wortmannin and Ly294002 (Figure 15). Notably, we observed a significant drop of internalized SPIOPSN by analyzing PI3K-inhibited cells.

Subsequently, the PI3K downstream signaling proteins PKC and PLC were inhibited. Both factors are important actin modulators (144, 286). Therefore, it was even more than surprising that even high concentrations of specific inhibitors for PKC and PLC did not alter the internalization rate of SPIOPSN. It is important to mention that this observation is consistent with a case in the field of virology, where a PKC-independent uptake was already reported for HIV-1 (140). This shows that a

uniform picture of macropinocytosis can hardly be shaped. Since the exact mechanisms are still elusive and seem to mainly depend on the investigated cell type and cargo it is challenging to set a standard (140). Also the multiple options of actin reorganization make it hard to draw a clear picture of macropinocytic mechanisms. This also includes the kinase PAK1. PAK1 binds the GTP-bound form of cdc42/Rac1 and modulates the actin cytoskeleton (287). Indeed, we showed that the pharmacological inhibition of PAK1 suppressed the entry of SPIOPSN in the same manner compared to PI3K inhibition (Figure 15).

Cup closure or the scission of macropinosomes

Besides the modulation of the actin cytoskeleton, the closure of the macropinosome depends on PAK1 and requires the phosphorylation of CtBP1/BARS in growth factor triggered macropinocytosis and during echovirus-1 entry (135, 288). This process seems to be independent from dynamin (135). Contrary to this, rare cases of a dynamin-dependent macropinocytosis have been reported (147, 148, 289). This was also observed in our studies. Dynasore treatment as well as the overexpression of dominant negative dynamin II drastically suppressed the number of internalized nanoparticles (Figure 16). On a subcellular level, it is known that dynamin participates in the formation of macropinocytic protrusions (214). Schlunck and colleagues showed that the disruption of dynamin II leads to an altered Rac localization from the cell edges into abnormal dorsal ruffles (214). The consequences of this are inhibited cell spreading and the decrease of lamellipodia formation. Taken together, dynamin is so far mainly seen as a factor of clathrin and caveolae-mediated endocytosis (Figure 18 and Figure 19). However, it is more than important to consider the action of dynamin II in macropinocytic studies.

Stimulation of classical macropinocytosis results in a diminished uptake of nanoparticles

In agreement with the previous results, we concluded that nanoparticles are taken up by an atypical macropinocytic pathway. This was underlined by experiments inducing classical macropinocytic pathways by EGF or PMA (Figure 17). Both types of stimulation had no boosting effect on the rate of internalization. Instead, stimulation of HeLa cells with EGF or PMA resulted in a massive drop of internalized SPIOPSN. We postulated that the uptake of nanoparticles after macropinocytic stimulation could be limited by their own size or owing to the diameter of the pinocytic ruffle (Figure 17). During this process, nanomaterials could be excluded from the macropinocytic ruffle. Normally, EGF and PMA are known to trigger classical signaling cascades of macropinocytosis resulting in an increase of endogenous fluid phase material as we have shown with dextran (Figure 17) (94, 290).

4.2.4 Changes in cholesterol homeostasis suppress the uptake of SPIOPSN

So far we discussed how the internalization of SPIOPSN depends on different kinases and small GTPases. Hitherto, we did not discuss the role of cholesterol during nanoparticle entry. We observed

that the depletion of cholesterol by mβCD suppressed the uptake ratio of SPIOPSN (Figure 21). In general, cholesterol is an important membrane organizer in mammalian cells (291). The disturbance of cholesterol homeostasis can have profound effects on cellular functions resulting in lipid-associated disorders such as Niemann-Pick disease type C or Tangier disease (292). It further causes the deregulation of macropinocytic signaling (138, 293, 294). So far it is known that several membrane proteins prefer to interact with distinct lipids forming highly organized lipid rafts (295). Especially, in macropinocytic signaling, the subcellular localization of important membrane proteins such as Rac1 depends on an intact cholesterol homeostasis. Grimmer and colleagues demonstrated that the depletion of cholesterol prevents the localization of Rac1 to the plasma membrane in A431 cells (138). Further on, the authors showed that the reorganization of the actin cytoskeleton and consequently the membrane ruffling can be influenced by membraneous cholesterol (138, 296). In a particular study with human embryonic kidney cells it has been demonstrated that the reduction of membranous cholesterol decreases the length of actin-dependent protrusions (297).

Disturbance of the endolysosomal cholesterol homeostasis influences the uptake of nanoparticles

During this study, we further demonstrated that not only the depletion of membraneous cholesterol but also the disturbance of endolysosomal cholesterol homeostasis had an effect on the uptake of SPIOPSN (Figure 21). U18666A triggered a Niemann-Pick disease type C by accumulating cholesterol and other lipids in the membrane of the endolysosomal system (Figure 21) (298). Inside these NPC-like HeLa cells, the uptake rate of dextran and SPIOPSN was drastically decreased assuming that NPC proteins might be associated with SPIOPSN-containing vesicles. Indeed, NPC1 and NPC2 were identified by mass spectrometry in the magnetically enriched fraction (Supplementary Table S2). NPC1 and NPC2 are necessary proteins for the efflux of cholesterol and other lipids from late endosomal compartments (298). When these proteins are nonfunctional, lipids accumulate inside the endolysosomal system. Therefore, we investigated whether a siRNA-mediated knockdown of NPC1 could induce such a phenotype. In previous studies, it was observed that siRNA-mediated knockdown of NPC1 is sufficient for a deregulation of cholesterol inside the endolysosomal system (299). Despite of comparable knockdown rates, we did not observe any significant effects on the nanoparticle uptake rate after NPC1 downregulation. Therefore, we concluded that this method is insufficient to study the effect of NPC1 on the uptake of nanoparticles. Notabily, other reports used a more efficient technique to study the impact of NPC1 on the intracellular transport of nanoparticles (83). The authors used NPC1-deficient MEFs and demonstrated that cells with nonfunctional NPC1 have a disturbed rate of exosome formation resulting in an increased retention of the nanomaterial inside the endolysosomal system (83). This study shows the relevance of cholesterol and its transporters in the endocytic mechanisms of nanoparticles.

4.2.5 Flotillin-1 and CD81 knockdown as well as the overexpression of dominant negative ARF1 suppresses SPIOPSN entry

Flotillins are organized as punctuate membrane domains enriched in cholesterol and sphingomyelin (300, 301). The subcellular localization of flotillins depends on cholesterol (131). Furthermore, flotillin microdomains have been implied to modulate the actin cytoskeleton (302). It was shown that flotillin microdomains specifically interact with the cytoskeletal myosin IIa and spectrin (303). Experiments with flotillin-1 knockout mice revealed that flotillin-1 is compromising myosin IIa activity, thereby implicating a role for flotillins in the modulation of the actin cytoskeleton (303). Taking the cholesterol dependence of flotillin and the role in actin modulation into account, one could assume a direct link between flotillins and macropinocytic uptake mechanisms (304). To our knowledge, this has not been observed in detail. However, Glebov *et al.* published a role for flotillin in a clathrin-independent pathway showing that flotillin-1 mediates the transport of the GPI-anchored CD59 and cholera toxin B subunit (88). Considering the investigated cargo molecules, this pathway resembles the CLIC/GEEC pathway, which is also known to mediate the uptake of fluids (90).

In this study we detected a significant drop of internalized nanoparticles in flotillin-1-siRNA-treated cells but observed no colocalization with ctxB (Figure 20; data not shown). Together, this implies an indirect association of flotillin (88) with the uptake mechanism of the investigated nanoparticles. Notably, we identified flotillin-1, flotillin-2 and the GPI-anchored protein CD59 in the magnetic fraction by the mass spectrometry analysis of SPIOPSN-containing vesicles (Supplementary Table S2, Supplementary Table S4). We propose an accumulation of flotillin-1, flotillin-2 and CD59 after the fusion of other endocytic vesicles with SPIOPSN-containing vesicles (305, 306). Furthermore, we assume that the uptake of nanoparticles is indirectly influenced by flotillin-1, since we did not observe a colocalization with ctxB. Altogether, this shows that endocytic proteins and pathways are not strictly separated from each other and could overlap in special cases.

Tetraspanins

Besides flotillin microdomains, tetraspanin-enriched microdomains (TEM) were investigated to study their impact on the uptake of SPIOPSN (Figure 20). In previous works, tetraspanins have been considered as proteins that laterally organize cellular membranes via their interactions with integrins (307). These TEMs consist of the tetraspanins CD9, CD81, CD82 and CD63 which partially interact with each other on the plasma membrane of HeLa cells (307). It has been shown that TEMs/tetraspanins are important receptors for the infection process of HIV-1 and HCV (307, 308). Spoden and colleagues showed that the downregulation or inhibition of several tetraspanins lead to a diminished infection rate of HPV16 (308). We also observed an association of tetraspanins with SPIOPSN-containing vesicles by mass spectrometry (Supplementary Table S2). Therefore, we assumed that TEMs are cointernalized with the nanoparticles or even influence their uptake. To study

this in more detail, we suppressed CD9, CD81, CD82 and CD63 by a siRNA-mediated approach (Figure 20). We observed no influence on SPIOPSN uptake after the knockdown of CD9, CD82 and CD63 but detected a suppressed rate of uptake after CD81 knockdown. Interestingly, CD81 was previously identified as a binding partner for the small macropinocytic GTPase Rac (309). Tejera *et al.* showed that the knockdown of CD81 resulted in significant alterations of focal adhesion and Rac activation (309). In dendritic cells, CD81 influences the formation of lamellipodia indicating an impact on the actin cytoskeleton (310). All of these data highlight a potential association of CD81 with the macropinocytic uptake of SPIOPSN and lays the foundation for further investigations to study the effects of tetraspanins on nanoparticle entry.

The inhibition of ARF1 results in a decreased uptake of nanoparticles

Previously, Kumari *et al.* demonstrated that ARF1 is directly associated with the internalization of ctxB and dextran (90). Consequently, they defined ARF1 as a player of the CLIC/GEEC pathway (90). A second study of Hasegawa and colleagues showed that a mutation of ARF1 causes a significant decrease of internalized dextran during a PDGF-triggered macropinocytosis in NIH3T3 cells (220). The overexpression of dominant negative ARF1 T31N was shown to induce an incomplete closure of the circular dorsal ruffles mediated by actin (220). The authors resumed that the macropinocytic uptake mechanism is blocked by ARF1 (220). Taken together, both groups reported different functions of ARF1 in two distinct pathways.

In this study, we identified four signs indicating a pivotal role of ARF1 in the entry mechanism of SPIOPSN (Figure 22). The first evidence was supplied by the detection of ARF1 in the vesicular fraction of the magnetically purified pellet (Supplementary Table S3). Secondy, we observed a direct interaction between nanoparticles and ARF1 T31N by confocal microscopy (Figure 22). We have demonstrated that the overexpression of ARF1 T31N resulted in a massive decrease of internalized SPIOPSN highlighting the significant effect of ARF1 on nanoparticle endocytosis (Figure 22). We further found that pharmacological inhibiton of ARF1 suppressed the uptake of SPIOPSN (Figure 22). Therefore, we concluded that ARF1 is directly involved in a macropinocytic-like uptake of nanoparticles. By following the definition of Kumari *et al.*, one could describe this entry mechanism as a dynamin-independent CLIC/GEEC pathway (90). However, since we have identified dynamin as an important factor during SPIOPSN entry (Figure 16), we considered this uptake mechanism as a macropinocytic-like one. This was also supported by cryo-TEM images, where we did not identify any tubular endosomal structures that are characteristic for CLIC/GEEC endocytosis (Figure 12). Anyway, the classical structures of the CLIC/GEEC pathway have a diameter of about 40 nm, which are to small for the investigated nanoparticles (126).

Crosstalk between distinct endocytic pathways

It seems that several endocytic mechanisms have significant functional and morphological overlaps hampering the classification of a single pathway. For instance, the CLIC/GEEC pathway is seen as a clathrin-independent pathway (96). However, a crosstalk between both pathways has been observed (85). Disturbance of the CLIC/GEEC pathway triggers a compensation of GPI-linked protein uptake by clathrin-mediated endocytosis (128). Another example of a crosstalk was published by Naslavsky *et al. (311)*. The authors showed that the GPI-linked protein CD59 and MHCI are internalized by a non-CLIC-GEEC pathway. This pathway is clathrin-and dynamin independent and utilizes ARF6-positive endosomes (311). As previously mentioned, also the flotillin-mediated pathway and the CLIC/GEEC pathway was reported to mediate the internalization of CD59 (88). The CLIC/GEEC pathway also resembles macropinocytic-like pathways as shown for adeno-associated virus 2 (AAV2) (95). Internalization of AAV2 depends on factors such as cdc42, ARF1, GRAF1 and EIPA but is insensitive to Rac1 or other macropinocytic inhibitors (95). The resume of the authors was that AAV2 is internalized via a pleiomorphic CLIC/GEEC pathway. Taking all of this into account, it is challenging to identify model cargoes that can be specifically assigned to a single pathway. This shows the close relationship between several entry mechanisms massively depending on cell type and investigated cargo.

4.3 Intracellular trafficking of nanoparticles

So far we discussed the mechanisms how cells internalize superparamagnetic iron oxide polystyrene nanoparticles. We have demonstrated that the entry of SPIOPSN is mediated by an atypical type of macropinocytosis mainly depending on cholesterol, kinases and typical small GTPases of several closely related endocytic mechanisms. To understand the intracellular trafficking of nanoparticles after macropinocytic uptake, we investigated the intracellular trafficking routes of these SPIOPSN (Figure 24-37). This question becomes especially exciting since several endocytic membrane proteins are also located inside the endolysosomal system (307). The reason for this originates in the functionality of the endolysosomal system. Notably, it is responsible for the renewal and recycling of plasma membrane proteins and membrane lipids by internalizing them (312).

As a result, the investigation of intracellular trafficking is a challenging field due to the high turnover rates of the participating proteins (312). Vesicles that bud off from the membrane are consequently able to fuse with other endocytic vesicles afterwards forming a complete novel vesicle with a distinct protein composition (181). Further on, it is well accepted that e. g. the maturation of early endosomes to late endosomes is accompanied by a rapid exchange of important markers (e. g. Rab proteins). This impedes the detection of high rates of colocalization with nanoparticles especially under the asynchronous uptake of nanoparticles (Figure 32) (153).

Early endocytic markers

Since we have proposed an uptake of SPIOPSN via macropinosome-like vesicles, we first checked for the early endocytic marker Rab5 (Figure 24) (142). For epithelial cells and fibroblasts it has been demonstrated that Rab5 and its effector Rabankyrin-5 are important proteins with a cooperative function for the biogenesis of macropinosomes and the endocytic system (142, 230). The authors showed that knockdown of Rab5 and Rabankyrin-5 decreases fluid phase uptake in NIH 3T3 cells. They found that Rab5 and Rabankyrin-5 colocalize with fluid phase-filled macropinosomes that are negative for EEA1 and transferrin (142). In our study, we also observed nanoparticles in fluid phase filled macropinosomes (Figure 25). In spite of extensive studies, no significant association of SPIOPSN with the classical early endosomal marker EEA1 was observed by confocal imaging (data not shown) and by the proteomic analysis of SPIOPSN-containing vesicles. Though, we detected SPIOPSN in $Rab5^+$ vesicles that were detectable by DIC microscopy (Figure 24). Surprisingly, the knockdown of Rab5A (Figure 24) and Rabankyrin-5 (data not shown) did not significantly suppress the uptake of SPIOPSN as contrarily demonstrated by other studies (142). From this, one can infer that other factors might drive the internalization of nanoparticles in HeLa cells. This might also be in accordance with the low rate of colocalization between nanoparticles and Rab5, in spite of the significant detection of Rab5A and Rab5C by mass spectrometry. The low number of colocalization of Rab5 with nanoparticles was also observed by previous studies, where the authors analyzed the colocalization of nanoparticles in the early stages of uptake (151).

Contrary to the low rate of colocalization of Rab5A with SPIOPSN, we found a higher number of SPIOPSN inside $RhoB^+$ vesicles. We detected SPIOPSN inside $RhoB^+$ vesicles that actively moved through the cell (Figure 25). These vesicles were visible by DIC microscopy and resembled fluid phase-filled macropinosomes. Besides the vesicular localization of RhoB-GFP, the protein also localized to the plasma membrane implying that RhoB plays a role in the early stages of endocytosis (313). Indeed, RhoB was detected by mass spectrometry as a protein of the membrane fraction (Supplementary Table S4). From literature it is known that RhoB is a small GTPase acting in the actin-mediated transport of endocytic vesicles (314). Studies using confocal microscopy detected RhoB mainly in early endosomes (315). In this context, RhoB was further shown to influence the entry of virions (223). Overexpression of RhoB significantly increased the endogenous levels of ebola virus glycoprotein and VSVG pseudotyped vector transduction. No effect was observed for GP pseudotyped HIV or adeno-associated virus 2 vector implying a specific role for RhoB during the uptake of viruses (223). However, we concluded that SPIOPSN were internalized by $RhoB^+$ vesicles resembling early macropinosomes.

Late markers of endocytosis

During the life span of an endosome, several fusion and maturation events change the proteomic composition of the vesicle (153). It is well accepted that early endosome to late endosome maturation can be measured by the steady conversion of Rab5 to Rab7 on the surface of endosomes (153). In our experiments, a colocalization of $Rab7^+$ vesicles with SPIOPSN has been recorded (Figure 26; Supplementary Table S2). These late endosomes contained intraluminal vesicles and are probably linked to anterograde and retrograde TGN-transport mechanisms (Figure 28, Figure 29 and Figure 30) (154). TGN-to-LE transport delivers lysosomal hydrolases and membranes to the inside of late endosomes providing proteins for the hydrolytic milieu of the lysosome (156). Lysosome-associated membrane proteins are directly transported by two major pathways. The most prominent pathway is orchestrated by the mannose-6-phosphate-receptor (316). Both types of the M6PR, MPRD and MRPI, were associated with SPIOPSN-containing vesicles (Supplementary Table S2). A so far unknown pathway is M6PR-independent and is mediated by VAMP7 and hVps41 (154). The authors suggest a role for VAMP7 in the transport of lysosome-associated membrane protein carriers showing that VAMP7 is directly involved in cargo transport from TGN-to-LE (154). VAMP7 is also well characterized as an R-SNARE mediating the fusion of late endosomes to lysosomes (192). Notably, we detected the R-SNARE VAMP7 on SPIOPSN-containing vesicles in colocalization experiments and by mass spectrometry (Figure 27; Supplementary Table S2). We proposed that those vesicles, which are SPIOPSN/$VAMP7^+$, were recorded during a heterotypic fusion event between late endosomes and lysosomes. This assumption was based on the observation that several SPIOPSN accumulated inside these organelles. We resumed that such a large number of SPIOPSN was so far only observed in lysosomal organelles.

Another prominent protein on late endosomes is the small GTPase Rab9, which also colocalized with SPIOPSN (Figure 26, Supplementary Table S2) (317). The important role of Rab9 on endosomes becomes apparent after Rab9 downregulation. The knockdown of Rab9 results in a size increase of late endosomes (318). Furthermore, it was demonstrated that Rab9 stimulates the backtransport of M6PR from late endosomes to the TGN in a cell free system (317). This is in compliance with a study that microscopically demonstrated the fusion of $Rab9^+$ late endosomes with the TGN (225). The authors assume that the endocytic system uses a vesicle intermediate to communicate between the endocytic system and the TGN-network, thereby implying the strong interaction between both systems (225).

Pmel17 and tetraspanins in the trafficking pathways of SPIOPSN

We know from previous studies that the endocytic uptake of viruses and nanoparticles can depend on tetraspanin-enriched microdomains (217, 307). Tetraspanins can act as receptors for HPV16 entry or assist in the ESCRT-dependent or independent sorting of other proteins into intraluminal vesicles of

multivesicular bodies (174, 217). In this particular case, the well-studied tetraspanin CD63 facilitates the transport of the melanosomal protein Pmel17 into the ILVs of multivesicular bodies in an ubiquitin-independent manner (174, 226, 227). To study the association of ubiquitin, CD63 and Pmel17 with SPIOPSN-containing vesicles, their colocalization was studied (Figure 28). Interestingly, SPIOPSN-containing vesicles lacked the colocalization with ubiquitin (data not shown). Instead, we detected a colocalization of CD63 with SPIOPSN (Figure 28). Therefore, we asked the question, whether Pmel17 colocalizes with SPIOPSN-containing vesicles. And indeed, we observed a high rate of colocalization of the ILV marker Pmel17 with SPIOPSN inside HeLa cells (Figure 28). This is in accordance with our TEM pictures displaying the close proximity of SPIOPSN to ILVs (Figure 29 and Figure 30). Taking the colocalization of SPIOPSN with CD63 and Pmel17 and the non-colocalization with ubiquitin into account, it is important to raise questions about different MVB subtypes (319). For early endosomes, the existence of subpopulations has already been shown (161). However, if this is also true for multivesicular body has to be investigated in the future.

Multilamellar lysosomes are the terminal organelle for SPIOPSN

The disassembly of nanomaterials is a major prerequisite for the release of encapsulated effector molecules in drug delivery applications (2). Therefore, it is of great interest to identify the terminal subcellular localization of a nanoparticle to gain knowledge about the endolysosomal enzymes that could potentially degrade nanomaterials (Figure 36). In pulse experiments with SPIOPSN using transmission electron microscopy, we found almost all SPIOPSN after 20 h inside multilamellar lysosomes (data not shown). These vesicles contained several multilamellar membranes whorls (Figure 29 and Figure 30) (182). In the past, several groups proposed that multilamellar bodies evolve from the fusion with autophagosomes (182). Indeed, it is well known that lysosomes fuse with $LC3^+$ autophagosomes (320). However, LC3-II is degraded after autolysosomal fusion challenging the detection of a direct interaction between lysosome and autophagosome by LC3-II (321). In our experiments, immunostainings for LC3-II revealed no colocalization with SPIOPSN signals indicating that nanoparticles are not transported via the autophagosomal pathway (Figure 32). However, we found a large number of mitochondrial proteins inside the magnetically enriched fraction (Supplementary Table S5). Further on, TEM images showed multilamellar membrane whorls inside multilamellar lysosomes. Altogether, this implies that SPIOPSN are stored inside lysosomes, which fused with autophagosomes.

4.3.1 Relevance of SPIOPSN trafficking *in vivo* – Studying nanoparticulate biodistribution

Especially, metal containing particles such as SPIOs or gold nanoparticles raise concerns about biodistribution and toxicity while they can be rapidly cleared from the blood stream entering organs such as liver and spleen (322, 323). The distribution of nanoparticles inside *in vivo* systems majorly

depends on their surface modification and size (324, 325). *In vitro*, we tested our SPIOPSN for aggregation in blood and found less morphologically visible aggregation in blood serum. Therefore, we considered this system as stable and injected SPIOPSN into NSG mice (Figure 33). NSG mice are immunodeficient and lack functional immune cells such as dendritic cells or macrophages. Therefore, it is a proper system to study the biodistribution of nanoparticles independently from the immune system. After injection, we magnetically isolated the nanoparticle-containing cells from complete tissues. We observed an endolysosomal like disposition of SPIOPSN after 24 h mainly in spleen and liver cells, while the peripheral blood, kidney and bladder lacked nanoparticles. This is in partial compliance with other studies, mainly detecting nanoparticles in liver and kidney (324). With this experiment, we could show the endolysosomal SPIOPSN uptake *in vivo*. Moreover, SPIOPSN were proven to be sufficient for the magnetic isolation of cells. This magnetic potential of SPIOPSN was subsequently used to study the intracellular trafficking of nanoparticles in more detail (Figure 34).

4.3.2 Reconstruction of intracellular nanoparticle trafficking displays a detailed picture of the proteomic environment of SPIOPSN

So far we have discussed how nanoparticles traffic along the endocytic route. To understand these trafficking pathways in more detail, one has to identify novel factors that are associated with the transport of nanoparticles (Figure 35 and Figure 36). Hitherto, these studies of intracellular nanoparticle trafficking were always based on the manipulation of the cellular systems (132, 151). This could result in drastical changes of the intracellular trafficking machinery. Overexpression or knockdown of membrane proteins may significantly alter the trafficking behavior of cells (153, 318). Moreover, the recent methods are biased by other cargoes such as viruses and can only analyze a low number of proteins at the same time. During this study, we achieved to circumvent such pitfalls by generating an unbiased snapshot of intracellular nanoparticle trafficking using mass spectrometry (Figure 35). Another advantage of this untampered approach is the option to characterize the lysosomal matrix milieu of enzymes (Figure 36). This could provide information for the prospective design of nanocarriers achieving a more specific endolysosomal degradation for an efficient release of the effector molecules.

Identification of proteins heavily depends on the method of subcellular fractionation

Normally, the purification of subcellular compartments is based on the size and the density of the organelle (156). This results in a biased analysis of the isolated vesicles, since only physical parameters are considered. Most of the researchers use differential centrifugation in a sucrose or percoll gradient for these kind of purifications (156, 326, 327). Sometimes, the distribution of distinct organelles (e.g. lysosomes and mitochondria) significantly overlap in hyperosmolar sucrose preventing an appropriate separation of distinct compartments (156). Using our protocol for the magnetic isolation of vesicles, one is only obtaining vesicles, which have engulfed the nanoparticle (Figure 34).

This approach excludes the isolation of endosomes that are not participating in the trafficking of magnetic nanoparticles.

Another great pitfall of all subcellular fractionation methods are unavoidable impurities inside the sample. Especially, in case of sensitive MS methods a large number of unwanted proteins are detectable (156). In conclusion: The more sensitive the method, the more challenging the subcellular fractionation. The proteomic analysis of the endolysosomal system is even more complicated since the cell uses the endocytic pathway for the degradation of non-endolysosomal constituents (328). Especially, the fusion of autophagosomes with lysosomes may insert impurities of defect organelles such as mitochondria or other damaged vesicles (328). To reliably distinguish between positive and false positive results, one has to focus on the enrichment of proteins in the purified fraction in comparison to the remaining fraction (Table 18). However, potentially positive proteins still can be screened by low copy numbers or degradative processes. Here the major drawbacks include the detection of low copy number proteins as well as small proteins (e. g. subunits), hydrophobic insoluble transmembrane proteins, proteins with posttranslational modifications and loosely attached proteins (156). Further on, endogenous fusion events e. g. between different endocytic proteins impedes the clear interpretation and the identification of direct effector proteins in the trafficking of SPIOPSN (156). Altogether, these factors hamper the interpretation of the data. Nevertheless, the analysis of vesicular proteins by MS is a valuable tool to screen for new proteins. However, the relevance of these data has to be confirmed by other methods.

Reconstruction of intracellular trafficking identifies novel promising candidates for prospective studies

The dissection of intracellular nanoparticle trafficking identified a large number of novel proteins that have never been associated with nanoparticles before (Figure 35). These include major markers of different endocytic compartments such as early endocytic compartmens, multivesicular bodies, lysosomes, COP vesicles and lysosomes (Figure 35). Interesting candidates for future applications are primarily represented by proteins of the tetraspanin family. The targeting of tetraspanin-enriched microdomains could be a novel approach for targeted delivery applications towards the endosomal system since these domains are easily accessible to extracellular particles (307).

However, the identification of several nanoparticle associated proteins gives also room for speculations. Especially, the identification of COP proteins raises questions, whether COP vesicles directly interact with the endolysosomal vesicles of a nanoparticle. In this context, it is important to mention that our mass spectrometry data is in compliance with the study of Aniento *et al.*, where the authors identified epsilon COP and beta COP on endosomal membranes (329). Whether this originates from a fusion event of endosomes with COP vesicles needs to be elucidated with other methods, which seems to be challenging. The identification of rare events in SPIOPSN trafficking is a major

problem when using standardized methods such as confocal microscopy. This was also shown by Sandin *et al*. (151). Despite of using spinning disc confocal microscopy, only a low number of colocalization events were detectable between nanoparticles and the early endosomal marker Rab1A, while no colocalization was observed with the COPI coat complex (151). The limitations often originate from the high dynamics of intracellular trafficking. Also low expression levels of the target protein or limitations in the detection by confocal microscopy might play a major role. During this study, we observed that especially the microscopic imaging of magnetic nanoparticles bears limitations. The detection of nanoparticles by PMTs rapidly gives rise to false positive signals on a very low signaling intensity owing to the high light scattering properties of the nanomaterial. This restricts the sensitive detection of markers by immunofluorescence or overexpression of GFP fusion proteins to a minimum. Therefore, our mass spectrometry approach is the more sensitive one, but data interpretation needs to be carefully performed.

Identification of lysosomal matrix proteins and their possible effects on the nanoparticulate protein corona

In the future, it will be necessary to study the degradation of internalized nanomaterial in more detail. Already a large number of studies consider nanomaterials as biodegradable structures but only less provide information about the long-term stability inside the vesicular environment. Even potentially biodegradable nanoparticles remain for a long time inside the endolysosomal system without getting significantly degraded (Lieberwirth, unpublished data) (33). After the deposition of nanoparticles inside lysosomal compartments, the protein corona and the nanomaterial underlies a harsh vesicular milieu of several hydrolases, proteases and other degradative enzymes. It has recently been reported that parts of the nanoparticulate protein corona are cointernalized with the nanoparticle (330). Regularly, ubiquitinylated proteins that are marked for degradation are transported to the lysosome. Therefore, it is possible that proteins on the surface of nanoparticles are marked with ubiquitin considering them for the degradative lysosomal pathway. Since we have not found ubiquitin in nanoparticle containing vesicles at all, we proposed that the transport of nanoparticles to lysosomes is a passively directed process. Anyway, the lysosomal milieu seems to degrade the nanoparticulate protein corona very efficiently shown in an example using a fluorescently labeled albumin (Figure 39).

Especially, for albumin it is known that it is degraded into the lysosome of cells (331). A major candidate for the degradation of albumin is cathepsin D and cathepsin B (332). Since we observed a colocalization of cathepsin D with nanoparticles (Figure 31) and identified cathepsin D/B by mass spectrometry, it was proposed that the protein corona of nanoparticles is degraded inside SPIOPSN containing lysosomes after a short time. This data is in compliance with the data of Wang *et al.*, where protein corona degradation experiments were performed with fluorescently labeled serum showing a degradation of the protein corona inside lysosomal structures (330). Taking this into account, one has to consider that not only the protein corona but also the intravesicular milieu may drastically change

the surface modification and material properties of nanomaterials. We have to keep in mind that this might have a crucial impact on the intracellular drug delivery abilities of nanoparticles.

5 Summary and conclusions

This work investigated the drug delivery abilities, the entry mechanisms and the intracellular trafficking pathways of different polymeric nanoparticles. We learned that the different types of interaction between nanoparticles and cells mainly depend on the used materials. To exploit intelligent drug delivery mechanisms, nanoparticulate systems need to be improved and their interaction with biological components need to be understood.

In the first part of the study, we wanted to know whether we can transport an encapsulated hydrophobic molecule over a membrane barrier. This is particularly important in drug delivery approaches for hardly accessible cells such as B or T lymphocytes. To approach this question, we studied nanoparticle-membrane interaction and a subsequent cargo release of the hydrophobic dye PMI on the membrane of HeLa cells, hMSCs and Jurkat cells. We observed a rapid staining of intracellular lipid droplets and reproduced this delivery mechanism in all three cell lines. We found that the transport of the membrane to the interior of the cell mainly depends on the nanoparticulate carrier but not on free dye molecules. Finally, we hypothesize that PMI release is largely triggered by a temporary nanoparticle-membrane contact. Hydrophobic surfaces of giant vesicles and of plasma membranes can trigger nanoparticle cargo release in a typical “kiss-and-run” dependent manner.

Next, we showed that the uptake of the well-characterized polymeric nanoparticle SPIOPSN is mediated by a macropinocytic-like mechanism. The treatment of cells with typical macropinocytic inhibitors significantly decreased the uptake of SPIOPSN into cells. However, inhibition of classical macropinocytic kinases such as PKC and PLC did not affect the entry of SPIOPSN. Also the stimulation of classical macropinocytosis by PMA and EGF decreased the uptake of SPIOPSN. We further investigated several proteins such as ARF1, Rac1 and cdc42 and showed their important role during the uptake of nanoparticles. Also the knockdown of flotillin-1 as well as the suppression of the tetraspanin CD81 decreased the levels of endogenous nanoparticles. Altogether, this implies an atypical type of macropinocytic uptake the investigated nanoparticles utilized.

Finally, we analyzed the intracellular trafficking pathways of a nanoparticle after a macropinocytic-like entry in HeLa cells. By the proteomic dissection, the intracellular nanoparticle trafficking (INT) was reconstructed based on a simple endocytic model. The analysis of SPIOPSN-containing vesicles resulted in the detection of proteins that have never been linked to INT before. To confirm the data of mass spectrometry, we analyzed several identified key players of intracellular trafficking by confocal live cell imaging. By this approach, SPIOPSN were found to be actively transported via macropinosomes, late endosomes and lysosomes. We were able to reproduce the colocalization of nanoparticles with lysosomal proteins in hMSCs. Strikingly, we identified several lysosomal matrix proteins in the enriched magnetic fraction of the nanoparticle-containing vesicles. It was assumed that the properties of the lysosomal compartment mediate the degradation of the nanoparticulate protein

corona. The degradation of protein corona may give access to the bare surface and the polymeric matrix of nanoparticles opening the way for the degradation of the nanomaterial.

In conclusion, we present a detailed picture of a so far unknown drug delivery mechanism that depends on temporary nanoparticle-membrane interactions. This could remarkably shift the paradigm of drug delivery mechanisms in the field of nano-bio-interactions. Furthermore, we provide evidence that polymeric nanoparticles are mainly internalized via an unspecific atypical macropinocytosis mechanism followed by a subsequent transport of nanoparticles to multilamellar lysosomes. This may set the basis for prospective nanoparticle studies and might help to understand nano-bio-interactions in more detail.

6 Bibliography

1. Nel AE, *et al.* (2009) Understanding biophysicochemical interactions at the nano-bio interface. *Nat Mater* 8(7):543-557.
2. Hofmann D & Mailander V (2013) Pharmacology of nanocarriers on the microscale: importance of uptake mechanisms and intracellular trafficking for efficient drug delivery. *Nanomedicine (Lond)* 8(3):321-323.
3. Yatvin MB, Kreutz W, Horwitz BA, & Shinitzky M (1980) pH-sensitive liposomes: possible clinical implications. *Science* 210(4475):1253-1255.
4. Gilleron J, *et al.* (2013) Image-based analysis of lipid nanoparticle-mediated siRNA delivery, intracellular trafficking and endosomal escape. *Nat Biotechnol* 31(7):638-646.
5. Cecco S, Aliberti M, Baldo P, Giacomin E, & Leone R (2014) Safety and efficacy evaluation of albumin-bound paclitaxel. *Expert Opin Drug Saf* 13(4):511-520.
6. Hofmann D, Messerschmidt C, Bannwarth MB, Landfester K, & Mailander V (2014) Drug delivery without nanoparticle uptake: delivery by a kiss-and-run mechanism on the cell membrane. *Chemical Communications* 50(11):1369-1371.
7. Soppimath KS, Aminabhavi TM, Kulkarni AR, & Rudzinski WE (2001) Biodegradable polymeric nanoparticles as drug delivery devices. *J Control Release* 70(1-2):1-20.
8. Rao JP & Geckeler KE (2011) Polymer nanoparticles: Preparation techniques and size-control parameters. *Prog Polym Sci* 36(7):887-913.
9. Siebert JM, Baier G, Musyanovych A, & Landfester K (2012) Towards copper-free nanocapsules obtained by orthogonal interfacial "click" polymerization in miniemulsion. *Chem Commun (Camb)* 48(44):5470-5472.
10. Tiarks F, Landfester K, & Antonietti M (2001) Preparation of polymeric nanocapsules by miniemulsion polymerization. *Langmuir* 17(3):908-918.
11. Landfester K (2009) Miniemulsion Polymerization and the Structure of Polymer and Hybrid Nanoparticles. *Angew Chem Int Edit* 48(25):4488-4507.
12. Ugelstad J, Elaasser MS, & Vanderho.Jw (1973) Emulsion Polymerization - Initiation of Polymerization in Monomer Droplets. *J Polym Sci Pol Lett* 11(8):503-513.
13. Landfester K & Mailander V (2013) Nanocapsules with specific targeting and release properties using miniemulsion polymerization. *Expert Opin Drug Deliv* 10(5):593-609.
14. Hocherl A, Dass M, Landfester K, Mailander V, & Musyanovych A (2012) Competitive cellular uptake of nanoparticles made from polystyrene, poly(methyl methacrylate), and polylactide. *Macromol Biosci* 12(4):454-464.
15. Baldan A (2002) Review Progress in Ostwald ripening theories and their applications to nickel-base superalloys - Part I: Ostwald ripening theories. *J Mater Sci* 37(11):2171-2202.
16. Bibette J, Morse DC, Witten TA, & Weitz DA (1992) Stability-Criteria for Emulsions. *Phys Rev Lett* 69(16):2439-2442.
17. Thiam AR, Farese RV, & Walther TC (2013) The biophysics and cell biology of lipid droplets. *Nat Rev Mol Cell Bio* 14(12):775-786.
18. Cao Z, Schrade A, Landfester K, & Ziener U (2011) Synthesis of raspberry-like organic–inorganic hybrid nanocapsules via pickering miniemulsion polymerization: Colloidal stability and morphology. *Journal of Polymer Science Part A: Polymer Chemistry* 49(11):2382-2394.
19. Musyanovych A, Rossmanith R, Tontsch C, & Landfester K (2007) Effect of Hydrophilic Comonomer and Surfactant Type on the Colloidal Stability and Size Distribution of Carboxyl- and Amino-Functionalized Polystyrene Particles Prepared by Miniemulsion Polymerization. *Langmuir* 23(10):5367-5376.

20. Gref R, *et al.* (2000) 'Stealth' corona-core nanoparticles surface modified by polyethylene glycol (PEG): influences of the corona (PEG chain length and surface density) and of the core composition on phagocytic uptake and plasma protein adsorption. *Colloids Surf B Biointerfaces* 18(3-4):301-313.
21. Fritz G, Schadler V, Willenbacher N, & Wagner NJ (2002) Electrosteric stabilization of colloidal dispersions. *Langmuir* 18(16):6381-6390.
22. MolinaBolivar JA, GalisteoGonzalez F, & HidalgoAlvarez R (1997) Colloidal stability of protein-polymer systems: A possible explanation by hydration forces. *Phys Rev E* 55(4):4522-4530.
23. Wells MA, Abid A, Kennedy IM, & Barakat AI (2012) Serum proteins prevent aggregation of Fe2O3 and ZnO nanoparticles. *Nanotoxicology* 6:837-846.
24. Tenzer S, *et al.* (2013) Rapid formation of plasma protein corona critically affects nanoparticle pathophysiology. *Nat Nanotechnol* 8(10):772-781.
25. Monopoli MP, Aberg C, Salvati A, & Dawson KA (2012) Biomolecular coronas provide the biological identity of nanosized materials. *Nat Nanotechnol* 7(12):779-786.
26. Salvati A, *et al.* (2013) Transferrin-functionalized nanoparticles lose their targeting capabilities when a biomolecule corona adsorbs on the surface. *Nat Nanotechnol* 8(2):137-143.
27. Natte K, *et al.* (2013) Impact of polymer shell on the formation and time evolution of nanoparticle-protein corona. *Colloids Surf B Biointerfaces* 104:213-220.
28. Murakami H, Kobayashi M, Takeuchi H, & Kawashima Y (1999) Preparation of poly(DL-lactide-co-glycolide) nanoparticles by modified spontaneous emulsification solvent diffusion method. *Int J Pharm* 187(2):143-152.
29. Peracchia MT, *et al.* (1999) Stealth PEGylated polycyanoacrylate nanoparticles for intravenous administration and splenic targeting. *J Control Release* 60(1):121-128.
30. Athanasiou KA, Agrawal CM, Barber FA, & Burkhart SS (1998) Orthopaedic applications for PLA-PGA biodegradable polymers. *Arthroscopy* 14(7):726-737.
31. Höcherl A (2012) Qualitative and absolute quantitative studies of the cell-nanoparticle interaction. (Universitätsbibliothek Mainz).
32. Rezwan K, Chen QZ, Blaker JJ, & Boccaccini AR (2006) Biodegradable and bioactive porous polymer/inorganic composite scaffolds for bone tissue engineering. *Biomaterials* 27(18):3413-3431.
33. Gonzalez MF, Ruseckaite RA, & Cuadrado TR (1999) Structural changes of polylactic-acid (PLA) microspheres under hydrolytic degradation. *J Appl Polym Sci* 71(8):1223-1230.
34. Tartaj P, Morales MD, Veintemillas-Verdaguer S, Gonzalez-Carreno T, & Serna CJ (2003) The preparation of magnetic nanoparticles for applications in biomedicine. *J Phys D Appl Phys* 36(13):R182-R197.
35. Ramirez LP & Landfester K (2003) Magnetic polystyrene nanoparticles with a high magnetite content obtained by miniemulsion processes. *Macromol Chem Physic* 204(1):22-31.
36. Schmidtke-Schrezenmeier G, *et al.* (2011) Labeling of mesenchymal stromal cells with iron oxide-poly(L-lactide) nanoparticles for magnetic resonance imaging: uptake, persistence, effects on cellular function and magnetic resonance imaging properties. *Cytotherapy* 13(8):962-975.
37. Bannwarth MB, *et al.* (2013) Well-defined nanofibers with tunable morphology from spherical colloidal building blocks. *Angew Chem Int Ed Engl* 52(38):10107-10111.
38. Bonnemain B (1998) Superparamagnetic agents in magnetic resonance imaging: Physicochemical characteristics and clinical applications - A review. *J Drug Target* 6(3):167-174.
39. Krishnan KM, *et al.* (2006) Nanomagnetism and spin electronics: materials, microstructure and novel properties. *J Mater Sci* 41(3):793-815.

40. Franko A, *et al.* (2013) Efficient Isolation of Pure and Functional Mitochondria from Mouse Tissues Using Automated Tissue Disruption and Enrichment with Anti-TOM22 Magnetic Beads. *Plos One* 8(12):e82392.
41. Antonelli A, *et al.* (2013) New strategies to prolong the in vivo life span of iron-based contrast agents for MRI. *Plos One* 8(10):e78542.
42. Alexiou C, *et al.* (2011) Cancer therapy with drug loaded magnetic nanoparticles-magnetic drug targeting. *J Magn Magn Mater* 323(10):1404-1407.
43. Bao G, Mitragotri S, & Tong S (2013) Multifunctional nanoparticles for drug delivery and molecular imaging. *Annu Rev Biomed Eng* 15:253-282.
44. Monnard PA & Deamer DW (2002) Membrane self-assembly processes: steps toward the first cellular life. *Anat Rec* 268(3):196-207.
45. Chandler D (2005) Interfaces and the driving force of hydrophobic assembly. *Nature* 437(7059):640-647.
46. Nicolson GL (2013) The Fluid-Mosaic Model of Membrane Structure: Still relevant to understanding the structure, function and dynamics of biological membranes after more than 40years. *Biochim Biophys Acta*.
47. Jaskiewicz K, *et al.* (2012) Probing Bioinspired Transport of Nanoparticles into Polymersomes. *Angew Chem Int Edit* 51(19):4613-4617.
48. Lesniak A, *et al.* (2013) Nanoparticle adhesion to the cell membrane and its effect on nanoparticle uptake efficiency. *J Am Chem Soc* 135(4):1438-1444.
49. Lesniak A, *et al.* (2012) Effects of the presence or absence of a protein corona on silica nanoparticle uptake and impact on cells. *ACS Nano* 6(7):5845-5857.
50. Tatur S, Maccarini M, Barker R, Nelson A, & Fragneto G (2013) Effect of functionalized gold nanoparticles on floating lipid bilayers. *Langmuir* 29(22):6606-6614.
51. Schulz M, Olubummo A, & Binder WH (2012) Beyond the lipid-bilayer: interaction of polymers and nanoparticles with membranes. *Soft Matter* 8(18):4849-4864.
52. Aranda-Espinoza H, Berman A, Dan N, Pincus P, & Safran S (1996) Interaction between inclusions embedded in membranes. *Biophys J* 71(2):648-656.
53. Dan N, Berman A, Pincus P, & Safran SA (1994) Membrane-Induced Interactions between Inclusions. *J Phys Ii* 4(10):1713-1725.
54. Li Y, Chen X, & Gu N (2008) Computational investigation of interaction between nanoparticles and membranes: hydrophobic/hydrophilic effect. *J Phys Chem B* 112(51):16647-16653.
55. Roiter Y, *et al.* (2008) Interaction of nanoparticles with lipid membrane. *Nano Lett* 8(3):941-944.
56. Gopalakrishnan G, *et al.* (2006) Multifunctional lipid/quantum dot hybrid nanocontainers for controlled targeting of live cells. *Angew Chem Int Edit* 45(33):5478-5483.
57. Lipowsky R & Dobereiner HG (1998) Vesicles in contact with nanoparticles and colloids. *Europhys Lett* 43(2):219-225.
58. Welsher K & Yang H (2014) Multi-resolution 3D visualization of the early stages of cellular uptake of peptide-coated nanoparticles. *Nat Nanotechnol* 9(3):198-203.
59. Simon BH, Ando HY, & Gupta PK (1995) Circulation time and body distribution of 14C-labeled amino-modified polystyrene nanoparticles in mice. *J Pharm Sci* 84(10):1249-1253.
60. Ambade AV, Savariar EN, & Thayumanavan S (2005) Dendrimeric micelles for controlled drug release and targeted delivery. *Mol Pharm* 2(4):264-272.
61. Fang J, Nakamura H, & Maeda H (2011) The EPR effect: Unique features of tumor blood vessels for drug delivery, factors involved, and limitations and augmentation of the effect. *Adv Drug Deliv Rev* 63(3):136-151.
62. Maeda H (2013) The link between infection and cancer: tumor vasculature, free radicals, and drug delivery to tumors via the EPR effect. *Cancer Sci* 104(7):779-789.

63. Chari RV (1998) Targeted delivery of chemotherapeutics: tumor-activated prodrug therapy. *Adv Drug Deliv Rev* 31(1-2):89-104.
64. Welte Y, Davies C, Schafer R, & Regenbrecht CR (2013) Patient derived cell culture and isolation of CD133(+) putative cancer stem cells from melanoma. *J Vis Exp* (73):e50200.
65. Brannon-Peppas L & Blanchette JO (2004) Nanoparticle and targeted systems for cancer therapy. *Adv Drug Deliv Rev* 56(11):1649-1659.
66. Dinauer N, *et al.* (2005) Selective targeting of antibody-conjugated nanoparticles to leukemic cells and primary T-lymphocytes. *Biomaterials* 26(29):5898-5906.
67. Cruz LJ, *et al.* (2011) Multimodal imaging of nanovaccine carriers targeted to human dendritic cells. *Mol Pharm* 8(2):520-531.
68. Weissleder R, Kelly K, Sun EY, Shtatland T, & Josephson L (2005) Cell-specific targeting of nanoparticles by multivalent attachment of small molecules. *Nat Biotechnol* 23(11):1418-1423.
69. Dhar S, Gu FX, Langer R, Farokhzad OC, & Lippard SJ (2008) Targeted delivery of cisplatin to prostate cancer cells by aptamer functionalized Pt(IV) prodrug-PLGA-PEG nanoparticles. *Proc Natl Acad Sci U S A* 105(45):17356-17361.
70. Baier G, *et al.* (2012) Suppressing unspecific cell uptake for targeted delivery using hydroxyethyl starch nanocapsules. *Biomacromolecules* 13(9):2704-2715.
71. Mirshafiee V, Mahmoudi M, Lou KY, Cheng JJ, & Kraft ML (2013) Protein corona significantly reduces active targeting yield. *Chemical Communications* 49(25):2557-2559.
72. Aktas Y, *et al.* (2005) Development and brain delivery of chitosan-PEG nanoparticles functionalized with the monoclonal antibody OX26. *Bioconjug Chem* 16(6):1503-1511.
73. Davda J & Labhasetwar V (2002) Characterization of nanoparticle uptake by endothelial cells. *Int J Pharm* 233(1-2):51-59.
74. Win KY & Feng SS (2005) Effects of particle size and surface coating on cellular uptake of polymeric nanoparticles for oral delivery of anticancer drugs. *Biomaterials* 26(15):2713-2722.
75. Sauer AM, *et al.* (2010) Role of endosomal escape for disulfide-based drug delivery from colloidal mesoporous silica evaluated by live-cell imaging. *Nano Lett* 10(9):3684-3691.
76. Cauda V, *et al.* (2010) Colchicine-Loaded Lipid Bilayer-Coated 50 nm Mesoporous Nanoparticles Efficiently Induce Microtubule Depolymerization upon Cell Uptake. *Nano Letters* 10(7):2484-2492.
77. Liu BR, *et al.* (2013) Endocytic Trafficking of Nanoparticles Delivered by Cell-penetrating Peptides Comprised of Nona-arginine and a Penetration Accelerating Sequence. *Plos One* 8(6).
78. Hatakeyama H, *et al.* (2009) A pH-sensitive fusogenic peptide facilitates endosomal escape and greatly enhances the gene silencing of siRNA-containing nanoparticles in vitro and in vivo. *J Control Release* 139(2):127-132.
79. Zhang K, *et al.* (2010) Structure-activity relationships of cationic shell-crosslinked knedel-like nanoparticles: shell composition and transfection efficiency/cytotoxicity. *Biomaterials* 31(7):1805-1813.
80. Zhang K, Fang H, Wang Z, Taylor JS, & Wooley KL (2009) Cationic shell-crosslinked knedel-like nanoparticles for highly efficient gene and oligonucleotide transfection of mammalian cells. *Biomaterials* 30(5):968-977.
81. Elsabahy M & Wooley KL (2012) Design of polymeric nanoparticles for biomedical delivery applications. *Chem Soc Rev* 41(7):2545-2561.
82. Yang Y, Liu F, Liu X, & Xing B (2013) NIR light controlled photorelease of siRNA and its targeted intracellular delivery based on upconversion nanoparticles. *Nanoscale* 5(1):231-238.
83. Sahay G, *et al.* (2013) Efficiency of siRNA delivery by lipid nanoparticles

is limited by endocytic recycling. *Nat Biotechnol* 31(7):653-658.
84. Wang Y & Huang L (2013) A window onto siRNA delivery. *Nat Biotechnol* 31(7):611-612.
85. Doherty GJ & McMahon HT (2009) Mechanisms of endocytosis. *Annu Rev Biochem* 78:857-902.
86. Furthauer M & Smythe E (2014) Systems dynamics in endocytosis. *Traffic* 15(3):338-346.
87. Ford MG, *et al.* (2002) Curvature of clathrin-coated pits driven by epsin. *Nature* 419(6905):361-366.
88. Glebov OO, Bright NA, & Nichols BJ (2006) Flotillin-1 defines a clathrin-independent endocytic pathway in mammalian cells. *Nat Cell Biol* 8(1):46-54.
89. Hayer A, *et al.* (2010) Caveolin-1 is ubiquitinated and targeted to intralumenal vesicles in endolysosomes for degradation. *J Cell Biol* 191(3):615-629.
90. Kumari S & Mayor S (2008) ARF1 is directly involved in dynamin-independent endocytosis. *Nat Cell Biol* 10(1):30-41.
91. Kim JG, *et al.* (2012) Ras-related GTPases Rap1 and RhoA collectively induce the phagocytosis of serum-opsonized zymosan particles in macrophages. *J Biol Chem* 287(7):5145-5155.
92. Donaldson JG (2003) Multiple roles for Arf6: sorting, structuring, and signaling at the plasma membrane. *J Biol Chem* 278(43):41573-41576.
93. Iversen TG, Skotland T, & Sandvig K (2011) Endocytosis and intracellular transport of nanoparticles: Present knowledge and need for future studies. *Nano Today* 6(2):176-185.
94. Koivusalo M, *et al.* (2010) Amiloride inhibits macropinocytosis by lowering submembranous pH and preventing Rac1 and Cdc42 signaling. *J Cell Biol* 188(4):547-563.
95. Nonnenmacher M & Weber T (2011) Adeno-associated virus 2 infection requires endocytosis through the CLIC/GEEC pathway. *Cell Host Microbe* 10(6):563-576.
96. Sahay G, Alakhova DY, & Kabanov AV (2010) Endocytosis of nanomedicines. *J Control Release* 145(3):182-195.
97. Sigismund S, *et al.* (2008) Clathrin-mediated internalization is essential for sustained EGFR signaling but dispensable for degradation. *Dev Cell* 15(2):209-219.
98. Torgersen ML, Skretting G, van Deurs B, & Sandvig K (2001) Internalization of cholera toxin by different endocytic mechanisms. *J Cell Sci* 114(Pt 20):3737-3747.
99. Smith PJ, *et al.* (2012) Cellular entry of nanoparticles via serum sensitive clathrin-mediated endocytosis, and plasma membrane permeabilization. *Int J Nanomed* 7:2045-2055.
100. Ferreira F, *et al.* (2012) Endocytosis of G protein-coupled receptors is regulated by clathrin light chain phosphorylation. *Curr Biol* 22(15):1361-1370.
101. Merrifield CJ, Feldman ME, Wan L, & Almers W (2002) Imaging actin and dynamin recruitment during invagination of single clathrin-coated pits. *Nat Cell Biol* 4(9):691-698.
102. Conner SD & Schmid SL (2003) Differential requirements for AP-2 in clathrin-mediated endocytosis. *J Cell Biol* 162(5):773-779.
103. Zhao X, *et al.* (2001) Expression of auxilin or AP180 inhibits endocytosis by mislocalizing clathrin: evidence for formation of nascent pits containing AP1 or AP2 but not clathrin. *J Cell Sci* 114(Pt 2):353-365.
104. Benmerah A, Bayrou M, Cerf-Bensussan N, & Dautry-Varsat A (1999) Inhibition of clathrin-coated pit assembly by an Eps15 mutant. *J Cell Sci* 112 (Pt 9):1303-1311.
105. Chen H, *et al.* (1998) Epsin is an EH-domain-binding protein implicated in clathrin-mediated endocytosis. *Nature* 394(6695):793-797.
106. Benmerah A, Poupon V, Cerf-Bensussan N, & Dautry-Varsat A (2000) Mapping of Eps15 domains involved in its targeting to clathrin-coated pits. *J Biol Chem* 275(5):3288-3295.
107. Mayor S & Pagano RE (2007) Pathways of clathrin-independent endocytosis. *Nat Rev Mol Cell Biol* 8(8):603-612.

108. Thomsen P, Roepstorff K, Stahlhut M, & van Deurs B (2002) Caveolae are highly immobile plasma membrane microdomains, which are not involved in constitutive endocytic trafficking. *Mol Biol Cell* 13(1):238-250.
109. Simons K & Ikonen E (1997) Functional rafts in cell membranes. *Nature* 387(6633):569-572.
110. Fujimoto T, Kogo H, Nomura R, & Une T (2000) Isoforms of caveolin-1 and caveolar structure. *Journal of Cell Science* 113(19):3509-3517.
111. Parolini I, *et al.* (1999) Expression of caveolin-1 is required for the transport of caveolin-2 to the plasma membrane. Retention of caveolin-2 at the level of the golgi complex. *J Biol Chem* 274(36):25718-25725.
112. Pelkmans L, Kartenbeck J, & Helenius A (2001) Caveolar endocytosis of simian virus 40 reveals a new two-step vesicular-transport pathway to the ER. *Nat Cell Biol* 3(5):473-483.
113. Hao X, *et al.* (2012) Caveolae-mediated endocytosis of biocompatible gold nanoparticles in living Hela cells. *J Phys Condens Matter* 24(16):164207.
114. Wang Z, Tiruppathi C, Minshall RD, & Malik AB (2009) Size and dynamics of caveolae studied using nanoparticles in living endothelial cells. *ACS Nano* 3(12):4110-4116.
115. Oh P, McIntosh DP, & Schnitzer JE (1998) Dynamin at the neck of caveolae mediates their budding to form transport vesicles by GTP-driven fission from the plasma membrane of endothelium. *J Cell Biol* 141(1):101-114.
116. Damke H, Binns DD, Ueda H, Schmid SL, & Baba T (2001) Dynamin GTPase domain mutants block endocytic vesicle formation at morphologically distinct stages. *Mol Biol Cell* 12(9):2578-2589.
117. Taylor MJ, Perrais D, & Merrifield CJ (2011) A high precision survey of the molecular dynamics of mammalian clathrin-mediated endocytosis. *PLoS Biol* 9(3):e1000604.
118. McNiven MA, *et al.* (2000) Regulated interactions between dynamin and the actin-binding protein cortactin modulate cell shape. *J Cell Biol* 151(1):187-198.
119. Macia E, *et al.* (2006) Dynasore, a cell-permeable inhibitor of dynamin. *Dev Cell* 10(6):839-850.
120. Ochoa GC, *et al.* (2000) A functional link between dynamin and the actin cytoskeleton at podosomes. *J Cell Biol* 150(2):377-389.
121. McNiven MA, Baldassarre M, & Buccione R (2004) The role of dynamin in the assembly and function of podosomes and invadopodia. *Front Biosci* 9:1944-1953.
122. Cao H, Chen J, Awoniyi M, Henley JR, & McNiven MA (2007) Dynamin 2 mediates fluid-phase micropinocytosis in epithelial cells. *J Cell Sci* 120(Pt 23):4167-4177.
123. Grassart A, Dujeancourt A, Lazarow PB, Dautry-Varsat A, & Sauvonnet N (2008) Clathrin-independent endocytosis used by the IL-2 receptor is regulated by Rac1, Pak1 and Pak2. *Embo Rep* 9(4):356-362.
124. Lamaze C, *et al.* (2001) Interleukin 2 receptors and detergent-resistant membrane domains define a clathrin-independent endocytic pathway. *Mol Cell* 7(3):661-671.
125. Ory S, Munari-Silem Y, Fort P, & Jurdic P (2000) Rho and Rac exert antagonistic functions on spreading of macrophage-derived multinucleated cells and are not required for actin fiber formation. *J Cell Sci* 113 (Pt 7):1177-1188.
126. Lundmark R, *et al.* (2008) The GTPase-activating protein GRAF1 regulates the CLIC/GEEC endocytic pathway. *Curr Biol* 18(22):1802-1808.
127. Chadda R, *et al.* (2007) Cholesterol-sensitive Cdc42 activation regulates actin polymerization for endocytosis via the GEEC pathway. *Traffic* 8(6):702-717.
128. Sabharanjak S, Sharma P, Parton RG, & Mayor S (2002) GPI-anchored proteins are delivered to recycling endosomes via a distinct cdc42-regulated, clathrin-independent pinocytic pathway. *Dev Cell* 2(4):411-423.
129. Solis GP, *et al.* (2007) Reggie/flotillin proteins are organized into stable

tetramers in membrane microdomains. *Biochem J* 403(2):313-322.
130. Ge L, *et al.* (2011) Flotillins play an essential role in Niemann-Pick C1-like 1-mediated cholesterol uptake. *Proc Natl Acad Sci U S A* 108(2):551-556.
131. Strauss K, *et al.* (2010) Exosome secretion ameliorates lysosomal storage of cholesterol in Niemann-Pick type C disease. *J Biol Chem* 285(34):26279-26288.
132. Vercauteren D, *et al.* (2011) Dynamic colocalization microscopy to characterize intracellular trafficking of nanomedicines. *ACS Nano* 5(10):7874-7884.
133. Kasper J, *et al.* (2013) Flotillin-involved uptake of silica nanoparticles and responses of an alveolar-capillary barrier in vitro. *Eur J Pharm Biopharm* 84(2):275-287.
134. Bryant DM, *et al.* (2007) EGF induces macropinocytosis and SNX1-modulated recycling of E-cadherin. *J Cell Sci* 120(Pt 10):1818-1828.
135. Liberali P, *et al.* (2008) The closure of Pak1-dependent macropinosomes requires the phosphorylation of CtBP1/BARS. *EMBO J* 27(7):970-981.
136. Dharmawardhane S, *et al.* (2000) Regulation of macropinocytosis by p21-activated kinase-1. *Mol Biol Cell* 11(10):3341-3352.
137. Fujii M, Kawai K, Egami Y, & Araki N (2013) Dissecting the roles of Rac1 activation and deactivation in macropinocytosis using microscopic photo-manipulation. *Sci Rep* 3:2385.
138. Grimmer S, van Deurs B, & Sandvig K (2002) Membrane ruffling and macropinocytosis in A431 cells require cholesterol. *J Cell Sci* 115(Pt 14):2953-2962.
139. Mercer J & Helenius A (2008) Vaccinia virus uses macropinocytosis and apoptotic mimicry to enter host cells. *Science* 320(5875):531-535.
140. Mercer J & Helenius A (2012) Gulping rather than sipping: macropinocytosis as a way of virus entry. *Curr Opin Microbiol* 15(4):490-499.
141. Sun P, *et al.* (2003) Small GTPase Rah/Rab34 is associated with membrane ruffles and macropinosomes and promotes macropinosome formation. *J Biol Chem* 278(6):4063-4071.
142. Schnatwinkel C, *et al.* (2004) The Rab5 effector Rabankyrin-5 regulates and coordinates different endocytic mechanisms. *PLoS Biol* 2(9):E261.
143. Veithen A, Cupers P, Baudhuin P, & Courtoy PJ (1996) v-Src induces constitutive macropinocytosis in rat fibroblasts. *J Cell Sci* 109 (Pt 8):2005-2012.
144. Amyere M, *et al.* (2000) Constitutive macropinocytosis in oncogene-transformed fibroblasts depends on sequential permanent activation of phosphoinositide 3-kinase and phospholipase C. *Mol Biol Cell* 11(10):3453-3467.
145. Radhakrishna H, Klausner RD, & Donaldson JG (1996) Aluminum fluoride stimulates surface protrusions in cells overexpressing the ARF6 GTPase. *J Cell Biol* 134(4):935-947.
146. Swanson JA (2008) Shaping cups into phagosomes and macropinosomes. *Nat Rev Mol Cell Biol* 9(8):639-649.
147. Iversen TG, Frerker N, & Sandvig K (2012) Uptake of ricinB-quantum dot nanoparticles by a macropinocytosis-like mechanism. *J Nanobiotechnology* 10:33.
148. Mulherkar N, Raaben M, de la Torre JC, Whelan SP, & Chandran K (2011) The Ebola virus glycoprotein mediates entry via a non-classical dynamin-dependent macropinocytic pathway. *Virology* 419(2):72-83.
149. Haspot F, *et al.* (2012) Human cytomegalovirus entry into dendritic cells occurs via a macropinocytosis-like pathway in a pH-independent and cholesterol-dependent manner. *Plos One* 7(4):e34795.
150. Schelhaas M, *et al.* (2012) Entry of human papillomavirus type 16 by actin-dependent, clathrin- and lipid raft-independent endocytosis. *PLoS Pathog* 8(4):e1002657.
151. Sandin P, Fitzpatrick LW, Simpson JC, & Dawson KA (2012) High-speed imaging of Rab family small GTPases reveals rare events in nanoparticle trafficking in living cells. *ACS Nano* 6(2):1513-1521.

152. Li H, Li Y, Jiao J, & Hu HM (2011) Alpha-alumina nanoparticles induce efficient autophagy-dependent cross-presentation and potent antitumour response. *Nat Nanotechnol* 6(10):645-650.
153. Rink J, Ghigo E, Kalaidzidis Y, & Zerial M (2005) Rab conversion as a mechanism of progression from early to late endosomes. *Cell* 122(5):735-749.
154. Pols MS, *et al.* (2013) hVps41 and VAMP7 function in direct TGN to late endosome transport of lysosomal membrane proteins. *Nat Commun* 4:1361.
155. Minton K (2013) Membrane dynamics: How lysosomes SNARE autophagosomes. *Nat Rev Mol Cell Biol* 14(2):65.
156. Schroder BA, Wrocklage C, Hasilik A, & Saftig P (2010) The proteome of lysosomes. *Proteomics* 10(22):4053-4076.
157. Nonnenmacher M & Weber T (2012) Intracellular transport of recombinant adeno-associated virus vectors. *Gene Ther* 19(6):649-658.
158. Galvez T, Gilleron J, Zerial M, & O'Sullivan GA (2012) SnapShot: Mammalian Rab proteins in endocytic trafficking. *Cell* 151(1):234-234 e232.
159. Spang A (2009) On the fate of early endosomes. *Biol Chem* 390(8):753-759.
160. Mu FT, *et al.* (1995) EEA1, an early endosome-associated protein. EEA1 is a conserved alpha-helical peripheral membrane protein flanked by cysteine "fingers" and contains a calmodulin-binding IQ motif. *J Biol Chem* 270(22):13503-13511.
161. Lakadamyali M, Rust MJ, & Zhuang X (2006) Ligands for clathrin-mediated endocytosis are differentially sorted into distinct populations of early endosomes. *Cell* 124(5):997-1009.
162. Sonnichsen B, De Renzis S, Nielsen E, Rietdorf J, & Zerial M (2000) Distinct membrane domains on endosomes in the recycling pathway visualized by multicolor imaging of Rab4, Rab5, and Rab11. *J Cell Biol* 149(4):901-914.
163. McCaffrey MW, *et al.* (2001) Rab4 affects both recycling and degradative endosomal trafficking. *FEBS Lett* 495(1-2):21-30.
164. Oberbanscheidt P, Balkow S, Kuhnl J, Grabbe S, & Bahler M (2007) SWAP-70 associates transiently with macropinosomes. *Eur J Cell Biol* 86(1):13-24.
165. Kerr MC, *et al.* (2006) Visualisation of macropinosome maturation by the recruitment of sorting nexins. *J Cell Sci* 119(Pt 19):3967-3980.
166. Wang JT, *et al.* (2010) The SNX-PX-BAR family in macropinocytosis: the regulation of macropinosome formation by SNX-PX-BAR proteins. *Plos One* 5(10):e13763.
167. Racoosin EL & Swanson JA (1993) Macropinosome maturation and fusion with tubular lysosomes in macrophages. *J Cell Biol* 121(5):1011-1020.
168. Hanson PI & Cashikar A (2012) Multivesicular body morphogenesis. *Annu Rev Cell Dev Biol* 28:337-362.
169. Murk JL, *et al.* (2003) Influence of aldehyde fixation on the morphology of endosomes and lysosomes: quantitative analysis and electron tomography. *J Microsc* 212(Pt 1):81-90.
170. Ostrowski M, *et al.* (2010) Rab27a and Rab27b control different steps of the exosome secretion pathway. *Nat Cell Biol* 12(1):19-30; sup pp 11-13.
171. Denzer K, Kleijmeer MJ, Heijnen HF, Stoorvogel W, & Geuze HJ (2000) Exosome: from internal vesicle of the multivesicular body to intercellular signaling device. *J Cell Sci* 113 Pt 19:3365-3374.
172. Woodman PG & Futter CE (2008) Multivesicular bodies: co-ordinated progression to maturity. *Curr Opin Cell Biol* 20(4):408-414.
173. Hoorn T, Paul P, Janssen L, Janssen H, & Neefjes J (2012) Dynamics within tetraspanin pairs affect MHC class II expression. *J Cell Sci* 125(Pt 2):328-339.
174. van Niel G, *et al.* (2011) The tetraspanin CD63 regulates ESCRT-independent and -dependent endosomal sorting during melanogenesis. *Dev Cell* 21(4):708-721.

175. Theos AC, *et al.* (2006) A lumenal domain-dependent pathway for sorting to intralumenal vesicles of multivesicular endosomes involved in organelle morphogenesis. *Dev Cell* 10(3):343-354.
176. Wollert T & Hurley JH (2010) Molecular mechanism of multivesicular body biogenesis by ESCRT complexes. *Nature* 464(7290):864-869.
177. Shields SB, *et al.* (2009) ESCRT ubiquitin-binding domains function cooperatively during MVB cargo sorting. *Journal of Cell Biology* 185(2):213-224.
178. Lee JA, Beigneux A, Ahmad ST, Young SG, & Gao FB (2007) ESCRT-III dysfunction causes autophagosome accumulation and neurodegeneration. *Curr Biol* 17(18):1561-1567.
179. Liscum L (2007) A role for NPC1 and NPC2 in intestinal cholesterol absorption--the hypothesis gutted. *Biochem J* 408(1):e1-3.
180. Cruz JC, Sugii S, Yu C, & Chang TY (2000) Role of Niemann-Pick type C1 protein in intracellular trafficking of low density lipoprotein-derived cholesterol. *J Biol Chem* 275(6):4013-4021.
181. Luzio JP, Pryor PR, & Bright NA (2007) Lysosomes: fusion and function. *Nat Rev Mol Cell Biol* 8(8):622-632.
182. Hariri M, *et al.* (2000) Biogenesis of multilamellar bodies via autophagy. *Mol Biol Cell* 11(1):255-268.
183. Mellman I, Fuchs R, & Helenius A (1986) Acidification of the endocytic and exocytic pathways. *Annu Rev Biochem* 55:663-700.
184. Kagedal K, Johansson U, & Ollinger K (2001) The lysosomal protease cathepsin D mediates apoptosis induced by oxidative stress. *FASEB J* 15(9):1592-1594.
185. Coutinho MF, Prata MJ, & Alves S (2012) Mannose-6-phosphate pathway: a review on its role in lysosomal function and dysfunction. *Mol Genet Metab* 105(4):542-550.
186. Eskelinen EL, Tanaka Y, & Saftig P (2003) At the acidic edge: emerging functions for lysosomal membrane proteins. *Trends Cell Biol* 13(3):137-145.
187. Helm CA, Israelachvili JN, & McGuiggan PM (1992) Role of hydrophobic forces in bilayer adhesion and fusion. *Biochemistry* 31(6):1794-1805.
188. Helm CA, Israelachvili JN, & McGuiggan PM (1989) Molecular mechanisms and forces involved in the adhesion and fusion of amphiphilic bilayers. *Science* 246(4932):919-922.
189. Tyauble H, Teubner M, Woolley P, & Eibl H (1976) Electrostatic interactions at charged lipid membranes. I. Effects of pH and univalent cations on membrane structure. *Biophys Chem* 4(4):319-342.
190. Noguchi H & Takasu M (2001) Fusion pathways of vesicles: A Brownian dynamics simulation. *J Chem Phys* 115(20):9547-9551.
191. Jahn R & Grubmuller H (2002) Membrane fusion. *Curr Opin Cell Biol* 14(4):488-495.
192. Balderhaar HJ & Ungermann C (2013) CORVET and HOPS tethering complexes - coordinators of endosome and lysosome fusion. *J Cell Sci* 126(Pt 6):1307-1316.
193. Cypionka A, *et al.* (2009) Discrimination between docking and fusion of liposomes reconstituted with neuronal SNARE-proteins using FCS. *Proc Natl Acad Sci U S A* 106(44):18575-18580.
194. Jahn R & Scheller RH (2006) SNAREs--engines for membrane fusion. *Nat Rev Mol Cell Biol* 7(9):631-643.
195. Bannwarth M (2014) Smart magnetic dispersions-from switchable release to well-defined hybrid nanofibers. (Mainz, Univ., Diss., 2014).
196. Nikiforow I, *et al.* (2010) Self-Stratification During Film Formation from Latex Blends Driven by Differences in Collective Diffusivity. *Langmuir* 26(16):13162-13167.
197. van den Hoff MJ, Moorman AF, & Lamers WH (1992) Electroporation in 'intracellular' buffer increases cell survival. *Nucleic Acids Res* 20(11):2902.
198. Ritz S, *et al.* (2013) Cell-free expression of a mammalian olfactory

receptor and unidirectional insertion into small unilamellar vesicles (SUVs). *Biochimie* 95(10):1909-1916.
199. Candiano G, *et al.* (2004) Blue silver: a very sensitive colloidal Coomassie G-250 staining for proteome analysis. *Electrophoresis* 25(9):1327-1333.
200. Schefe JH, Lehmann KE, Buschmann IR, Unger T, & Funke-Kaiser H (2006) Quantitative real-time RT-PCR data analysis: current concepts and the novel "gene expression's CT difference" formula. *J Mol Med (Berl)* 84(11):901-910.
201. Hofmann D, Messerschmidt C, Bannwarth MB, Landfester K, & Mailander V (2013) Drug delivery without nanoparticle uptake: delivery by a kiss-and-run mechanism on the cell membrane. *Chem Commun (Camb)*.
202. Cauda V, *et al.* (2010) Colchicine-loaded lipid bilayer-coated 50 nm mesoporous nanoparticles efficiently induce microtubule depolymerization upon cell uptake. *Nano Lett* 10(7):2484-2492.
203. Yezhelyev MV, Qi L, O'Regan RM, Nie S, & Gao X (2008) Proton-sponge coated quantum dots for siRNA delivery and intracellular imaging. *J Am Chem Soc* 130(28):9006-9012.
204. Huschka R, *et al.* (2011) Light-induced release of DNA from gold nanoparticles: nanoshells and nanorods. *J Am Chem Soc* 133(31):12247-12255.
205. Baumann D, *et al.* (2013) Complex encounters: nanoparticles in whole blood and their uptake into different types of white blood cells. *Nanomedicine (Lond)* 8(5):699-713.
206. Heiniger HJ, Sodergren A, & Marshall JD (1981) Endocytosis in cytotoxic T-lymphocytes. *Cell Immunol* 59(2):429-434.
207. Farese RV, Jr. & Walther TC (2009) Lipid droplets finally get a little R-E-S-P-E-C-T. *Cell* 139(5):855-860.
208. Thiam AR, Farese RV, Jr., & Walther TC (2013) The biophysics and cell biology of lipid droplets. *Nat Rev Mol Cell Biol* 14(12):775-786.
209. Bulankina AV, *et al.* (2009) TIP47 functions in the biogenesis of lipid droplets. *J Cell Biol* 185(4):641-655.
210. Tauchi-Sato K, Ozeki S, Houjou T, Taguchi R, & Fujimoto T (2002) The surface of lipid droplets is a phospholipid monolayer with a unique Fatty Acid composition. *J Biol Chem* 277(46):44507-44512.
211. Nanbo A, *et al.* (2010) Ebolavirus Is Internalized into Host Cells via Macropinocytosis in a Viral Glycoprotein-Dependent Manner. *Plos Pathogens* 6(9).
212. Mercer J & Helenius A (2009) Virus entry by macropinocytosis. *Nat Cell Biol* 11(5):510-520.
213. Sarkar K, Kruhlak MJ, Erlandsen SL, & Shaw S (2005) Selective inhibition by rottlerin of macropinocytosis in monocyte-derived dendritic cells. *Immunology* 116(4):513-524.
214. Schlunck G, *et al.* (2004) Modulation of Rac localization and function by dynamin. *Mol Biol Cell* 15(1):256-267.
215. Tahara E, Kadara H, Lacroix L, Lotan D, & Lotan R (2009) Activation of protein kinase C by phorbol 12-myristate 13-acetate suppresses the growth of lung cancer cells through KLF6 induction. *Cancer Biol Ther* 8(9):801-807.
216. Haigler HT, McKanna JA, & Cohen S (1979) Rapid stimulation of pinocytosis in human carcinoma cells A-431 by epidermal growth factor. *J Cell Biol* 83(1):82-90.
217. Spoden G, *et al.* (2008) Clathrin- and caveolin-independent entry of human papillomavirus type 16--involvement of tetraspanin-enriched microdomains (TEMs). *Plos One* 3(10):e3313.
218. Silvie O, *et al.* (2006) Cholesterol contributes to the organization of tetraspanin-enriched microdomains and to CD81-dependent infection by malaria sporozoites. *J Cell Sci* 119(Pt 10):1992-2002.
219. Yu X, Breitman M, & Goldberg J (2012) A structure-based mechanism for Arf1-dependent recruitment of coatomer to membranes. *Cell* 148(3):530-542.
220. Hasegawa J, Tsujita K, Takenawa T, & Itoh T (2012) ARAP1 regulates the ring size of circular dorsal ruffles through Arf1 and Arf5. *Mol Biol Cell* 23(13):2481-2489.

221. Donaldson JG, Finazzi D, & Klausner RD (1992) Brefeldin A inhibits Golgi membrane-catalysed exchange of guanine nucleotide onto ARF protein. *Nature* 360(6402):350-352.
222. Gorvel JP, Chavrier P, Zerial M, & Gruenberg J (1991) rab5 controls early endosome fusion in vitro. *Cell* 64(5):915-925.
223. Quinn K, *et al.* (2009) Rho GTPases modulate entry of Ebola virus and vesicular stomatitis virus pseudotyped vectors. *J Virol* 83(19):10176-10186.
224. Meier O, *et al.* (2002) Adenovirus triggers macropinocytosis and endosomal leakage together with its clathrin-mediated uptake. *J Cell Biol* 158(6):1119-1131.
225. Barbero P, Bittova L, & Pfeffer SR (2002) Visualization of Rab9-mediated vesicle transport from endosomes to the trans-Golgi in living cells. *J Cell Biol* 156(3):511-518.
226. Berson JF, Harper DC, Tenza D, Raposo G, & Marks MS (2001) Pmel17 initiates premelanosome morphogenesis within multivesicular bodies. *Mol Biol Cell* 12(11):3451-3464.
227. Pols MS & Klumperman J (2009) Trafficking and function of the tetraspanin CD63. *Exp Cell Res* 315(9):1584-1592.
228. Shultz LD, *et al.* (1995) Multiple defects in innate and adaptive immunologic function in NOD/LtSz-scid mice. *J Immunol* 154(1):180-191.
229. Ashburner M, *et al.* (2000) Gene Ontology: tool for the unification of biology. *Nat Genet* 25(1):25-29.
230. Zeigerer A, *et al.* (2012) Rab5 is necessary for the biogenesis of the endolysosomal system in vivo. *Nature* 485(7399):465-470.
231. Motley A, Bright NA, Seaman MN, & Robinson MS (2003) Clathrin-mediated endocytosis in AP-2-depleted cells. *J Cell Biol* 162(5):909-918.
232. Ren X, Farias GG, Canagarajah BJ, Bonifacino JS, & Hurley JH (2013) Structural basis for recruitment and activation of the AP-1 clathrin adaptor complex by Arf1. *Cell* 152(4):755-767.
233. Sanchez EG, *et al.* (2012) African swine fever virus uses macropinocytosis to enter host cells. *PLoS Pathog* 8(6):e1002754.
234. Vanlandingham PA & Ceresa BP (2009) Rab7 regulates late endocytic trafficking downstream of multivesicular body biogenesis and cargo sequestration. *J Biol Chem* 284(18):12110-12124.
235. Mazurov D, Barbashova L, & Filatov A (2013) Tetraspanin protein CD9 interacts with metalloprotease CD10 and enhances its release via exosomes. *FEBS J*.
236. Fritzsching B, *et al.* (2002) Release and intercellular transfer of cell surface CD81 via microparticles. *J Immunol* 169(10):5531-5537.
237. Kleijmeer MJ, *et al.* (2001) Antigen loading of MHC class I molecules in the endocytic tract. *Traffic* 2(2):124-137.
238. Frolov A, *et al.* (2001) Cholesterol overload promotes morphogenesis of a Niemann-Pick C (NPC)-like compartment independent of inhibition of NPC1 or HE1/NPC2 function. *J Biol Chem* 276(49):46414-46421.
239. Cieutat AM, *et al.* (1998) Azurophilic granules of human neutrophilic leukocytes are deficient in lysosome-associated membrane proteins but retain the mannose 6-phosphate recognition marker. *Blood* 91(3):1044-1058.
240. van Deurs B, Holm PK, Kayser L, Sandvig K, & Hansen SH (1993) Multivesicular bodies in HEp-2 cells are maturing endosomes. *Eur J Cell Biol* 61(2):208-224.
241. Sancak Y, *et al.* (2010) Ragulator-Rag complex targets mTORC1 to the lysosomal surface and is necessary for its activation by amino acids. *Cell* 141(2):290-303.
242. Fader CM & Colombo MI (2009) Autophagy and multivesicular bodies: two closely related partners. *Cell Death Differ* 16(1):70-78.
243. Venditti R, *et al.* (2012) Sedlin controls the ER export of procollagen by regulating the Sar1 cycle. *Science* 337(6102):1668-1672.
244. Hirsh SL, *et al.* (2013) The Vroman effect: competitive protein exchange

with dynamic multilayer protein aggregates. *Colloids Surf B Biointerfaces* 103:395-404.
245. Lux CD, *et al.* (2012) Biocompatible Polymeric Nanoparticles Degrade and Release Cargo in Response to Biologically Relevant Levels of Hydrogen Peroxide. *Journal of the American Chemical Society* 134(38):15758-15764.
246. Kelsch A, *et al.* (2012) HPMA copolymers as surfactants in the preparation of biocompatible nanoparticles for biomedical application. *Biomacromolecules* 13(12):4179-4187.
247. Miaczynska M, *et al.* (2004) APPL proteins link Rab5 to nuclear signal transduction via an endosomal compartment. *Cell* 116(3):445-456.
248. Mitra R, Goodman OB, & Le TT (2014) Enhanced detection of metastatic prostate cancer cells in human plasma with lipid bodies staining. *BMC Cancer* 14:91.
249. Tomcin S (2014) Analyse der intrazellulären Freisetzung von Wirkstoffmodellen via Konfokaler Laser-Raster-Mikroskopie. (Mainz, Univ., Diss., 2014).
250. Khatchadourian A & Maysinger D (2009) Lipid Droplets: Their Role in Nanoparticle-induced Oxidative Stress. *Mol Pharmaceut* 6(4):1125-1137.
251. Przybytkowski E, Behrendt M, Dubois D, & Maysinger D (2009) Nanoparticles can induce changes in the intracellular metabolism of lipids without compromising cellular viability. *FEBS J* 276(21):6204-6217.
252. Mailander V & Landfester K (2009) Interaction of nanoparticles with cells. *Biomacromolecules* 10(9):2379-2400.
253. Tenuta T, *et al.* (2011) Elution of Labile Fluorescent Dye from Nanoparticles during Biological Use. *Plos One* 6(10).
254. Xu P, *et al.* (2009) Intracellular drug delivery by poly(lactic-co-glycolic acid) nanoparticles, revisited. *Mol Pharm* 6(1):190-201.
255. Sun X, Li F, Wang Y, & Liang W (2010) Cellular uptake and elimination of lipophilic drug delivered by nanocarriers. *Pharmazie* 65(10):737-742.
256. Dawson KA (2013) Leave the policing to others. *Nat Nanotechnol* 8(2):73.
257. Savina A & Amigorena S (2007) Phagocytosis and antigen presentation in dendritic cells. *Immunol Rev* 219:143-156.
258. Sharma A, *et al.* (2011) Multivalent niacin nanoconjugates for delivery to cytoplasmic lipid droplets. *Biomaterials* 32(5):1419-1429.
259. Harris CA, *et al.* (2011) DGAT enzymes are required for triacylglycerol synthesis and lipid droplets in adipocytes. *J Lipid Res* 52(4):657-667.
260. Konige M, Wang H, & Sztalryd C (2014) Role of adipose specific lipid droplet proteins in maintaining whole body energy homeostasis. *Biochim Biophys Acta* 1842(3):393-401.
261. Miyanari Y, *et al.* (2007) The lipid droplet is an important organelle for hepatitis C virus production. *Nat Cell Biol* 9(9):1089-1097.
262. Magalhaes LM, *et al.* (2010) High-throughput microplate assay for the determination of drug partition coefficients. *Nat Protoc* 5(11):1823-1830.
263. Burton PS, Goodwin JT, Vidmar TJ, & Amore BM (2002) Predicting drug absorption: How nature made it a difficult problem. *J Pharmacol Exp Ther* 303(3):889-895.
264. Lipinski CA, Lombardo F, Dominy BW, & Feeney PJ (2012) Experimental and computational approaches to estimate solubility and permeability in drug discovery and development settings. *Adv Drug Deliver Rev* 64:4-17.
265. Kubinyi H (1979) Nonlinear dependence of biological activity on hydrophobic character: the bilinear model. *Farmaco Sci* 34(3):248-276.
266. Jordan MA, Thrower D, & Wilson L (1992) Effects of vinblastine, podophyllotoxin and nocodazole on mitotic spindles. Implications for the role of microtubule dynamics in mitosis. *J Cell Sci* 102 (Pt 3):401-416.
267. De Jong WH & Borm PJ (2008) Drug delivery and nanoparticles:applications

and hazards. *Int J Nanomedicine* 3(2):133-149.

268. Paula AJ, *et al.* (2013) Influence of Protein Corona on the Transport of Molecules into Cells by Mesoporous Silica Nanoparticles. *Acs Appl Mater Inter* 5(17):8387-8393.
269. Heerklotz H (2008) Interactions of surfactants with lipid membranes. *Q Rev Biophys* 41(3-4):205-264.
270. Liu Y, Zhang Z, Zhang Q, Baker GL, & Worden RM (2014) Biomembrane disruption by silica-core nanoparticles: effect of surface functional group measured using a tethered bilayer lipid membrane. *Biochim Biophys Acta* 1838(1 Pt B):429-437.
271. Leroueil PR, *et al.* (2007) Nanoparticle interaction with biological membranes: does nanotechnology present a Janus face? *Acc Chem Res* 40(5):335-342.
272. Lin XB, Wang CL, Wang M, Fang K, & Gu N (2012) Computer Simulation of the Effects of Nanoparticles' Adsorption on the Properties of Supported Lipid Bilayer. *J Phys Chem C* 116(33):17960-17968.
273. Li Y, Chen X, & Gu N (2008) Computational Investigation of Interaction between Nanoparticles and Membranes: Hydrophobic/Hydrophilic Effect. *Journal of Physical Chemistry B* 112(51):16647-16653.
274. Krieger SE, Kim C, Zhang L, Marjomaki V, & Bergelson JM (2013) Echovirus 1 entry into polarized Caco-2 cells depends on dynamin, cholesterol, and cellular factors associated with macropinocytosis. *J Virol* 87(16):8884-8895.
275. Saeed MF, Kolokoltsov AA, Albrecht T, & Davey RA (2010) Cellular Entry of Ebola Virus Involves Uptake by a Macropinocytosis-Like Mechanism and Subsequent Trafficking through Early and Late Endosomes. *Plos Pathogens* 6(9).
276. Nakase I, *et al.* (2004) Cellular uptake of arginine-rich peptides: roles for macropinocytosis and actin rearrangement. *Mol Ther* 10(6):1011-1022.
277. Rossman JS, Leser GP, & Lamb RA (2012) Filamentous influenza virus enters cells via macropinocytosis. *J Virol* 86(20):10950-10960.
278. Ridley AJ, Paterson HF, Johnston CL, Diekmann D, & Hall A (1992) The small GTP-binding protein rac regulates growth factor-induced membrane ruffling. *Cell* 70(3):401-410.
279. Allen WE, Jones GE, Pollard JW, & Ridley AJ (1997) Rho, Rac and Cdc42 regulate actin organization and cell adhesion in macrophages. *J Cell Sci* 110 (Pt 6):707-720.
280. Hoppe AD & Swanson JA (2004) Cdc42, Rac1, and Rac2 display distinct patterns of activation during phagocytosis. *Mol Biol Cell* 15(8):3509-3519.
281. Martin SS, *et al.* (1996) Activated phosphatidylinositol 3-kinase is sufficient to mediate actin rearrangement and GLUT4 translocation in 3T3-L1 adipocytes. *Journal of Biological Chemistry* 271(30):17605-17608.
282. Jiménez C, *et al.* (2000) Role of the PI3K regulatory subunit in the control of actin organization and cell migration. *The Journal of cell biology* 151(2):249-262.
283. Araki N, Johnson MT, & Swanson JA (1996) A role for phosphoinositide 3-kinase in the completion of macropinocytosis and phagocytosis by macrophages. *J Cell Biol* 135(5):1249-1260.
284. Koyama N, Kashimata M, Sakashita H, Sakagami H, & Gresik EW (2003) EGF-stimulated signaling by means of PI3K, PLCgamma1, and PKC isozymes regulates branching morphogenesis of the fetal mouse submandibular gland. *Dev Dyn* 227(2):216-226.
285. Amyere M, *et al.* (2002) Origin, originality, functions, subversions and molecular signalling of macropinocytosis. *Int J Med Microbiol* 291(6-7):487-494.
286. Larsson C (2006) Protein kinase C and the regulation of the actin cytoskeleton. *Cell Signal* 18(3):276-284.
287. Shin YJ, Kim EH, Roy A, & Kim JH (2013) Evidence for a novel mechanism of the PAK1 interaction with the Rho-GTPases Cdc42 and Rac. *Plos One* 8(8):e71495.

288. Haga Y, Miwa N, Jahangeer S, Okada T, & Nakamura S (2009) CtBP1/BARS is an activator of phospholipase D1 necessary for agonist-induced macropinocytosis. *EMBO J* 28(9):1197-1207.
289. Gold S, Monaghan P, Mertens P, & Jackson T (2010) A Clathrin Independent Macropinocytosis-Like Entry Mechanism Used by Bluetongue Virus-1 during Infection of BHK Cells. *Plos One* 5(6).
290. Swanson JA (1989) Phorbol esters stimulate macropinocytosis and solute flow through macrophages. *J Cell Sci* 94 (Pt 1):135-142.
291. Kraft ML (2013) Plasma membrane organization and function: moving past lipid rafts. *Mol Biol Cell* 24(18):2765-2768.
292. Maxfield FR & Tabas I (2005) Role of cholesterol and lipid organization in disease. *Nature* 438(7068):612-621.
293. Puntoni M, Sbrana F, Bigazzi F, & Sampietro T (2012) Tangier disease: epidemiology, pathophysiology, and management. *Am J Cardiovasc Drugs* 12(5):303-311.
294. Carstea ED, *et al.* (1997) Niemann-Pick C1 disease gene: homology to mediators of cholesterol homeostasis. *Science* 277(5323):228-231.
295. Lingwood D & Simons K (2010) Lipid Rafts As a Membrane-Organizing Principle. *Science* 327(5961):46-50.
296. Manes S & Martinez C (2004) Cholesterol domains regulate the actin cytoskeleton at the leading edge of moving cells. *Trends in Cell Biology* 14(6):275-278.
297. Khatibzadeh N, Spector AA, Brownell WE, & Anvari B (2013) Effects of Plasma Membrane Cholesterol Level and Cytoskeleton F-Actin on Cell Protrusion Mechanics. *Plos One* 8(2).
298. Subramanian K & Balch WE (2008) NPC1/NPC2 function as a tag team duo to mobilize cholesterol. *P Natl Acad Sci USA* 105(40):15223-15224.
299. Ganley IG & Pfeffer SR (2006) Cholesterol accumulation sequesters Rab9 and disrupts late endosome function in NPC1-deficient cells. *Journal of Biological Chemistry* 281(26):17890-17899.
300. Simons K & Toomre D (2000) Lipid rafts and signal transduction. *Nat Rev Mol Cell Biol* 1(1):31-39.
301. Strauss K (2010) *Exosomes Act as Molecular Vehicles Contributing to Cellular Cholesterol Efflux*.
302. Langhorst MF, Solis GP, Hannbeck S, Plattner H, & Stuermer CA (2007) Linking membrane microdomains to the cytoskeleton: regulation of the lateral mobility of reggie-1/flotillin-2 by interaction with actin. *FEBS Lett* 581(24):4697-4703.
303. Ludwig A, *et al.* (2010) Flotillin microdomains interact with the cortical cytoskeleton to control uropod formation and neutrophil recruitment. *J Cell Biol* 191(4):771-781.
304. Solis GP, *et al.* (2012) Reggies/flotillins regulate E-cadherin-mediated cell contact formation by affecting EGFR trafficking. *Mol Biol Cell* 23(10):1812-1825.
305. Langhorst MF, *et al.* (2008) Trafficking of the microdomain scaffolding protein reggie-1/flotillin-2. *Eur J Cell Biol* 87(4):211-226.
306. Cai B, Katafiasz D, Horejsi V, & Naslavsky N (2011) Pre-sorting endosomal transport of the GPI-anchored protein, CD59, is regulated by EHD1. *Traffic* 12(1):102-120.
307. Nydegger S, Khurana S, Krementsov DN, Foti M, & Thali M (2006) Mapping of tetraspanin-enriched microdomains that can function as gateways for HIV-1. *J Cell Biol* 173(5):795-807.
308. Spoden G, *et al.* (2008) Clathrin- and Caveolin-Independent Entry of Human Papillomavirus Type 16-Involvement of Tetraspanin-Enriched Microdomains (TEMs). *Plos One* 3(10).
309. Tejera E, *et al.* (2013) CD81 regulates cell migration through its association with Rac GTPase. *Molecular Biology of the Cell* 24(3):261-273.
310. Quast T, *et al.* (2011) CD81 is essential for the formation of membrane protrusions and regulates Rac1-activation in adhesion-dependent immune cell migration. *Blood* 118(7):1818-1827.
311. Naslavsky N, Weigert R, & Donaldson JG (2004) Characterization of a

nonclathrin endocytic pathway: membrane cargo and lipid requirements. *Mol Biol Cell* 15(8):3542-3552.
312. Grant BD & Donaldson JG (2009) Pathways and mechanisms of endocytic recycling. *Nat Rev Mol Cell Biol* 10(9):597-608.
313. Prendergast GC (2001) Actin' up: RhoB in cancer and apoptosis. *Nat Rev Cancer* 1(2):162-168.
314. Fernandez-Borja M, Janssen L, Verwoerd D, Hordijk P, & Neefjes J (2005) RhoB regulates endosome transport by promoting actin assembly on endosomal membranes through Dia1. *Journal of Cell Science* 118(12):2661-2670.
315. Rondanino C, *et al.* (2007) RhoB-dependent modulation of postendocytic traffic in polarized Madin-Darby canine kidney cells. *Traffic* 8(7):932-949.
316. Griffiths G, Hoflack B, Simons K, Mellman I, & Kornfeld S (1988) The mannose 6-phosphate receptor and the biogenesis of lysosomes. *Cell* 52(3):329-341.
317. Lombardi D, *et al.* (1993) Rab9 functions in transport between late endosomes and the trans Golgi network. *EMBO J* 12(2):677-682.
318. Ganley IG, Carroll K, Bittova L, & Pfeffer S (2004) Rab9 GTPase regulates late endosome size and requires effector interaction for its stability. *Mol Biol Cell* 15(12):5420-5430.
319. Heijnen HF, *et al.* (1998) Multivesicular bodies are an intermediate stage in the formation of platelet alpha-granules. *Blood* 91(7):2313-2325.
320. Webb JL, Ravikumar B, & Rubinsztein DC (2004) Microtubule disruption inhibits autophagosome-lysosome fusion: implications for studying the roles of aggresomes in polyglutamine diseases. *Int J Biochem Cell Biol* 36(12):2541-2550.
321. Tanida I, Ueno T, & Kominami E (2008) LC3 and Autophagy. *Methods Mol Biol* 445:77-88.
322. Lee PW, *et al.* (2010) The characteristics, biodistribution, magnetic resonance imaging and biodegradability of superparamagnetic core-shell nanoparticles. *Biomaterials* 31(6):1316-1324.
323. Sonavane G, Tomoda K, & Makino K (2008) Biodistribution of colloidal gold nanoparticles after intravenous administration: effect of particle size. *Colloids Surf B Biointerfaces* 66(2):274-280.
324. Shah NB, *et al.* (2012) Blood-nanoparticle interactions and in vivo biodistribution: impact of surface PEG and ligand properties. *Mol Pharm* 9(8):2146-2155.
325. Alexis F, Pridgen E, Molnar LK, & Farokhzad OC (2008) Factors affecting the clearance and biodistribution of polymeric nanoparticles. *Mol Pharm* 5(4):505-515.
326. Taguchi T, *et al.* (2000) Isolation of highly purified rat cerebral lysosomes using percoll gradients with a variety of calcium concentrations. *Environ Health Prev Med* 4(4):217-220.
327. Shibko S & Tappel AL (1965) Rat-Kidney Lysosomes: Isolation and Properties. *Biochem J* 95:731-741.
328. Mizushima N (2007) Autophagy: process and function. *Genes Dev* 21(22):2861-2873.
329. Aniento F, Gu F, Parton RG, & Gruenberg J (1996) An endosomal beta COP is involved in the pH-dependent formation of transport vesicles destined for late endosomes. *Journal of Cell Biology* 133(1):29-41.
330. Wang F, *et al.* (2013) The biomolecular corona is retained during nanoparticle uptake and protects the cells from the damage induced by cationic nanoparticles until degraded in the lysosomes. *Nanomedicine* 9(8):1159-1168.
331. Ohshita T & Hiroi Y (1998) Degradation of serum albumin by rat liver and kidney lysosomes. *J Nutr Sci Vitaminol (Tokyo)* 44(5):641-653.
332. Mego JL (1984) Role of Thiols, Ph and Cathepsin-D in the Lysosomal Catabolism of Serum-Albumin. *Biochemical Journal* 218(3):775-783.

[redacted]

8 Supplementary data

This chapter provides additional data of the lable free quantitative mass spectrometry analysis. The full data set is further on available on www.proteomexhange.org.

Supplementary Table S1: Complete DAVID ontology analysis of proteins. Proteins were enriched > 2-fold in the magnetic fraction compared to the non-magnetic fraction.

18 Cluster(s)		Count
Annotation Cluster 1	**Enrichment Score: 42.07**	
GOTERM_CC_FAT	envelope	145
GOTERM_CC_FAT	organelle envelope	144
GOTERM_CC_FAT	mitochondrial envelope	115
GOTERM_CC_FAT	mitochondrial membrane	111
GOTERM_CC_FAT	mitochondrial inner membrane	96
GOTERM_CC_FAT	organelle inner membrane	99
Annotation Cluster 2	**Enrichment Score: 29.76**	
GOTERM_CC_FAT	lysosome	69
GOTERM_CC_FAT	lytic vacuole	69
GOTERM_CC_FAT	vacuole	75
Annotation Cluster 3	**Enrichment Score: 16.73**	
GOTERM_CC_FAT	vesicle	105
GOTERM_CC_FAT	membrane-bounded vesicle	93
GOTERM_CC_FAT	cytoplasmic membrane-bounded vesicle	91
GOTERM_CC_FAT	cytoplasmic vesicle	100
Annotation Cluster 4	**Enrichment Score: 9.24**	
GOTERM_CC_FAT	membrane fraction	99
GOTERM_CC_FAT	insoluble fraction	101
GOTERM_CC_FAT	cell fraction	120
Annotation Cluster 5	**Enrichment Score: 7.22**	
GOTERM_CC_FAT	outer membrane	26
GOTERM_CC_FAT	organelle outer membrane	24
GOTERM_CC_FAT	mitochondrial outer membrane	22
Annotation Cluster 6	**Enrichment Score: 5.93**	
GOTERM_CC_FAT	respiratory chain complex I	14
GOTERM_CC_FAT	mitochondrial respiratory chain complex I	14
GOTERM_CC_FAT	NADH dehydrogenase complex	14
Annotation Cluster 7	**Enrichment Score: 5.61**	
GOTERM_CC_FAT	membrane-enclosed lumen	171
GOTERM_CC_FAT	organelle lumen	163
GOTERM_CC_FAT	intracellular organelle lumen	156
Annotation Cluster 8	**Enrichment Score: 3.33**	
GOTERM_CC_FAT	actomyosin	9
GOTERM_CC_FAT	stress fiber	8
GOTERM_CC_FAT	actin filament bundle	8
Annotation Cluster 9	**Enrichment Score: 2.51**	
GOTERM_CC_FAT	cell-substrate junction	17
GOTERM_CC_FAT	cell-substrate adherens junction	16
GOTERM_CC_FAT	focal adhesion	15

Annotation Cluster 10	**Enrichment Score: 2.29**	
GOTERM_CC_FAT	clathrin adaptor complex	8
GOTERM_CC_FAT	AP-type membrane coat adaptor complex	8
GOTERM_CC_FAT	clathrin coat	9
GOTERM_CC_FAT	endocytic vesicle membrane	6
Annotation Cluster 11	**Enrichment Score: 2.15**	
GOTERM_CC_FAT	AP-2 adaptor complex	4
GOTERM_CC_FAT	clathrin coat of coated pit	5
GOTERM_CC_FAT	clathrin-coated endocytic vesicle	5
GOTERM_CC_FAT	clathrin coat of endocytic vesicle	4
GOTERM_CC_FAT	clathrin-coated endocytic vesicle membrane	4
GOTERM_CC_FAT	clathrin vesicle coat	4
Annotation Cluster 12	**Enrichment Score: 2.1**	
GOTERM_CC_FAT	microbody part	9
GOTERM_CC_FAT	peroxisomal part	9
GOTERM_CC_FAT	microbody membrane	7
GOTERM_CC_FAT	peroxisomal membrane	7
Annotation Cluster 13	**Enrichment Score: 2.09**	
GOTERM_CC_FAT	protein-lipid complex	8
GOTERM_CC_FAT	plasma lipoprotein particle	8
GOTERM_CC_FAT	triglyceride-rich lipoprotein particle	6
GOTERM_CC_FAT	very-low-density lipoprotein particle	6
GOTERM_CC_FAT	high-density lipoprotein particle	6
Annotation Cluster 14	**Enrichment Score: 1.58**	
GOTERM_CC_FAT	tricarboxylic acid cycle enzyme complex	4
GOTERM_CC_FAT	dihydrolipoyl dehydrogenase complex	3
GOTERM_CC_FAT	mitochondrial alpha-ketoglutarate dehydrogenase complex	3
GOTERM_CC_FAT	mitochondrial tricarboxylic acid cycle enzyme complex	3
Annotation Cluster 15	**Enrichment Score: 1.38**	
GOTERM_CC_FAT	COPI vesicle coat	4
GOTERM_CC_FAT	COPI coated vesicle membrane	4
GOTERM_CC_FAT	COPI-coated vesicle	4
Annotation Cluster 16	**Enrichment Score: 0.97**	
GOTERM_CC_FAT	vesicle lumen	7
GOTERM_CC_FAT	platelet alpha granule lumen	6
GOTERM_CC_FAT	cytoplasmic membrane-bounded vesicle lumen	6
Annotation Cluster 17	**Enrichment Score: 0.58**	
GOTERM_CC_FAT	contractile fiber part	11
GOTERM_CC_FAT	contractile fiber	11
GOTERM_CC_FAT	myofibril	9
Annotation Cluster 18	**Enrichment Score: 0.44**	
GOTERM_CC_FAT	spectrin	3
GOTERM_CC_FAT	cortical actin cytoskeleton	3
GOTERM_CC_FAT	cortical cytoskeleton	3

Supplementary Table S2: Reconstruction of SPIOPSN trafficking is based on the GOTERM: *Lysosome.*

Uniprot_ID	Full protein name
AGAL_HUMAN	galactosidase, alpha
ANAG_HUMAN	N-acetylglucosaminidase, alpha-
AP3M1_HUMAN	adaptor-related protein complex 3, mu 1 subunit
ARL8A_HUMAN	ADP-ribosylation factor-like 8A
ARL8B_HUMAN	ADP-ribosylation factor-like 8B
ARSA_HUMAN	arylsulfatase A
ARSB_HUMAN	arylsulfatase B
ASAH1_HUMAN	N-acylsphingosine amidohydrolase (acid ceramidase) 1
ASM_HUMAN	sphingomyelin phosphodiesterase 1, acid lysosomal
BGAL_HUMAN	galactosidase, beta 1
BGLR_HUMAN	glucuronidase, beta
CATA_HUMAN	catalase
CATB_HUMAN	cathepsin B
CATC_HUMAN	cathepsin C
CATD_HUMAN	cathepsin D
CATL1_HUMAN	cathepsin L1
CATZ_HUMAN	cathepsin Z
CD63_HUMAN	CD63 molecule
CLCN7_HUMAN	chloride channel 7
CLN3_HUMAN	ceroid-lipofuscinosis, neuronal 3
CLN5_HUMAN	ceroid-lipofuscinosis, neuronal 5
DNS2A_HUMAN	deoxyribonuclease II, lysosomal
DPP2_HUMAN	dipeptidyl-peptidase 7
EPDR1_HUMAN	ependymin related protein 1 (zebrafish)
GALNS_HUMAN	galactosamine (N-acetyl)-6-sulfate sulfatase
GGH_HUMAN	gamma-glutamyl hydrolase (conjugase, folylpolygammaglutamyl hydrolase)
GILT_HUMAN	interferon, gamma-inducible protein 30
GLCM_HUMAN	glucosidase, beta; acid (includes glucosylceramidase)
GNS_HUMAN	glucosamine (N-acetyl)-6-sulfatase
HEXA_HUMAN	hexosaminidase A (alpha polypeptide)
HEXB_HUMAN	hexosaminidase B (beta polypeptide)
LAMP1_HUMAN	lysosomal-associated membrane protein 1
LAMP2_HUMAN	lysosomal-associated membrane protein 2
LGMN_HUMAN	legumain
LICH_HUMAN	lipase A, lysosomal acid, cholesterol esterase
LYAG_HUMAN	glucosidase, alpha; acid
MA2B1_HUMAN	mannosidase, alpha, class 2B, member 1
MANBA_HUMAN	mannosidase, beta A, lysosomal
MCLN1_HUMAN	mucolipin 1
MPRD_HUMAN	mannose-6-phosphate receptor (cation dependent)
MPRI_HUMAN	insulin-like growth factor 2 receptor
NAGAB_HUMAN	N-acetylgalactosaminidase, alpha-
NCUG1_HUMAN	chromosome 1 open reading frame 85

NEUR1_HUMAN	sialidase 1 (lysosomal sialidase)
NICA_HUMAN	nicastrin
NPC1_HUMAN	Niemann-Pick disease, type C1
NPC2_HUMAN	Niemann-Pick disease, type C2
PAG15_HUMAN	phospholipase A2, group XV
PCP_HUMAN	prolylcarboxypeptidase (angiotensinase C)
PCYOX_HUMAN	prenylcysteine oxidase 1
PPAL_HUMAN	acid phosphatase 2, lysosomal
PPGB_HUMAN	cathepsin A
PPT1_HUMAN	palmitoyl-protein thioesterase 1
PPT2_HUMAN	palmitoyl-protein thioesterase 2
RAB14_HUMAN	RAB14, member RAS oncogene family
RAB7A_HUMAN	RAB7A, member RAS oncogene family
RAB9A_HUMAN	RAB9A, member RAS oncogene family
RB27A_HUMAN	RAB27A, member RAS oncogene family
S15A4_HUMAN	solute carrier family 15, member 4
SAP_HUMAN	prosaposin
SAP3_HUMAN	GM2 ganglioside activator
SCRB2_HUMAN	scavenger receptor class B, member 2
SPHM_HUMAN	N-sulfoglucosamine sulfohydrolase
STX7_HUMAN	syntaxin 7
STXB2_HUMAN	syntaxin binding protein 2
TM192_HUMAN	transmembrane protein 192
TPP1_HUMAN	tripeptidyl peptidase I
VAMP7_HUMAN	vesicle-associated membrane protein 7
VATG1_HUMAN	ATPase, H+ transporting, lysosomal 13kDa, V1 subunit G1

Supplementary Table S3: Reconstruction of SPIOPSN trafficking is based on the GOTERM: *Vesicle.* **Not considered in GOTERM analysis; manually inserted.*

Uniprot ID	Full protein name
A4_HUMAN	amyloid beta (A4) precursor protein
AAAT_HUMAN	solute carrier family 1 (neutral amino acid transporter), member 5
ADA10_HUMAN	ADAM metallopeptidase domain 10
AMPN_HUMAN	alanyl (membrane) aminopeptidase
AP1B1_HUMAN	adaptor-related protein complex 1, beta 1 subunit
AP2A1_HUMAN	adaptor-related protein complex 2, alpha 1 subunit
AP2A2_HUMAN	adaptor-related protein complex 2, alpha 2 subunit
AP2B1_HUMAN	adaptor-related protein complex 2, beta 1 subunit
AP2M1_HUMAN	adaptor-related protein complex 2, mu 1 subunit
AP2S1_HUMAN	adaptor-related protein complex 2, sigma 1 subunit
APOA1_HUMAN	apolipoprotein A-I
ARSA_HUMAN	arylsulfatase A
ASM_HUMAN	sphingomyelin phosphodiesterase 1, acid lysosomal
AT1A1_HUMAN	ATPase, Na+/K+ transporting, alpha 1 polypeptide
AT1B3_HUMAN	ATPase, Na+/K+ transporting, beta 3 polypeptide

BASI_HUMAN	basigin (Ok blood group)
CATB_HUMAN	cathepsin B
CATD_HUMAN	cathepsin D
CAV1_HUMAN	caveolin 1, caveolae protein, 22kDa
CAV2_HUMAN	caveolin 2
CD9_HUMAN	CD9 molecule
CH60_HUMAN	heat shock 60kDa protein 1 (chaperonin) pseudogene 5
CLIC4_HUMAN	chloride intracellular channel 4
CLN3_HUMAN	ceroid-lipofuscinosis, neuronal 3
CLUS_HUMAN	clusterin
COPB_HUMAN	coatomer protein complex, subunit beta 1
COPB2_HUMAN	coatomer protein complex, subunit beta 2 (beta prime)
COPE_HUMAN	coatomer protein complex, subunit epsilon
COPZ1_HUMAN	coatomer protein complex, subunit zeta 1
DAB2_HUMAN	disabled homolog 2, mitogen-responsive phosphoprotein (Drosophila)
DLDH_HUMAN	dihydrolipoamide dehydrogenase
DNJC5_HUMAN	DnaJ (Hsp40) homolog, subfamily C, member 5
DP13A_HUMAN	adaptor protein, phosphotyrosine interaction, PH domain and leucine zipper containing 1
DPP2_HUMAN	dipeptidyl-peptidase 7
ECE1_HUMAN	endothelin converting enzyme 1
EGFR_HUMAN	epidermal growth factor receptor
EHD1_HUMAN	EH-domain containing 1
FIBA_HUMAN	fibrinogen alpha chain
FIBB_HUMAN	fibrinogen beta chain
FIBG_HUMAN	fibrinogen gamma chain
FLOT1_HUMAN	flotillin 1
GANAB_HUMAN	glucosidase, alpha; neutral AB
GGH_HUMAN	gamma-glutamyl hydrolase (conjugase, folylpolygammaglutamyl hydrolase)
GIPC1_HUMAN	GIPC PDZ domain containing family, member 1
GNAI3_HUMAN	guanine nucleotide binding protein (G protein), alpha inhibiting activity polypeptide 3
GNAS2_HUMAN	GNAS complex locus
GPNMB_HUMAN	glycoprotein (transmembrane) nmb
GTR1_HUMAN	solute carrier family 2 (facilitated glucose transporter), member 1
HEXB_HUMAN	hexosaminidase B (beta polypeptide)
ITA1_HUMAN	integrin, alpha 1
ITB1_HUMAN	integrin, beta 1 (fibronectin receptor, beta polypeptide)
LAMP1_HUMAN	lysosomal-associated membrane protein 1
LAMP2_HUMAN	lysosomal-associated membrane protein 2
MPRI_HUMAN	insulin-like growth factor 2 receptor
MYH11_HUMAN	myosin, heavy chain 11, smooth muscle
MYOF_HUMAN	myoferlin
NEUR1_HUMAN	sialidase 1 (lysosomal sialidase)
NICA_HUMAN	nicastrin
P4K2A_HUMAN	phosphatidylinositol 4-kinase type 2 alpha
PA24A_HUMAN	phospholipase A2, group IVA (cytosolic, calcium-dependent)

PICAL_HUMAN	phosphatidylinositol binding clathrin assembly protein
PLD1_HUMAN	phospholipase D1, phosphatidylcholine-specific
PPT1_HUMAN	palmitoyl-protein thioesterase 1
PTN1_HUMAN	protein tyrosine phosphatase, non-receptor type 1
RAB14_HUMAN	RAB14, member RAS oncogene family
RAB21_HUMAN	RAB21, member RAS oncogene family
RAB2A_HUMAN	RAB2A, member RAS oncogene family
RAB35_HUMAN	similar to hCG1778032; RAB35, member RAS oncogene family
RAB3A_HUMAN	RAB3A, member RAS oncogene family
RAB3D_HUMAN	RAB3D, member RAS oncogene family
RAB5A_HUMAN	RAB5A, member RAS oncogene family
RAB5C_HUMAN	RAB5C, member RAS oncogene family
RAB6B_HUMAN	RAB6B, member RAS oncogene family
RAB7A_HUMAN	RAB7A, member RAS oncogene family
RAI3_HUMAN	G protein-coupled receptor, family C, group 5, member A
RB11A_HUMAN	RAB11A, member RAS oncogene family
RB11B_HUMAN	RAB11B, member RAS oncogene family
RB27A_HUMAN	RAB27A, member RAS oncogene family
RPN1_HUMAN	ribophorin I
SATT_HUMAN	solute carrier family 1 (glutamate/neutral amino acid transporter), member 4
SC23A_HUMAN	Sec23 homolog A (S. cerevisiae)
SCFD1_HUMAN	sec1 family domain containing 1
SDCB1_HUMAN	syndecan binding protein (syntenin)
SH3B4_HUMAN	SH3-domain binding protein 4
SNTB2_HUMAN	syntrophin, beta 2 (dystrophin-associated protein A1, 59kDa, basic component 2)
SPG21_HUMAN	spastic paraplegia 21 (autosomal recessive, Mast syndrome)
STOM_HUMAN	phosphatidylethanolamine binding protein 1
STOM_HUMAN	stomatin
STX12_HUMAN	syntaxin 12
STXB1_HUMAN	syntaxin binding protein 1
STXB2_HUMAN	syntaxin binding protein 2
STXB3_HUMAN	syntaxin binding protein 3
SYPL1_HUMAN	synaptophysin-like 1
TFR1_HUMAN	transferrin receptor (p90, CD71)
TMED2_HUMAN	transmembrane emp24 domain trafficking protein 2
TMEDA_HUMAN	transmembrane emp24-like trafficking protein 10 (yeast)
TPP1_HUMAN	tripeptidyl peptidase I
TSP1_HUMAN	thrombospondin 1
VA0D1_HUMAN	ATPase, H+ transporting, lysosomal 38kDa, V0 subunit d1
VAMP7_HUMAN	vesicle-associated membrane protein 7
VAPA_HUMAN	VAMP (vesicle-associated membrane protein)-associated protein A, 33kDa
VATB2_HUMAN	ATPase, H+ transporting, lysosomal 56/58kDa, V1 subunit B2
VATC1_HUMAN	ATPase, H+ transporting, lysosomal 42kDa, V1 subunit C1
VPP1_HUMAN	ATPase, H+ transporting, lysosomal V0 subunit a1
YKT6_HUMAN	YKT6 v-SNARE homolog (S. cerevisiae)

Manually inserted: Uniprot ID	**Full protein name**
1B55_HUMAN*	HLA class I histocompatibility antigen, B-55 alpha chain
1C06_HUMAN*	HLA class I histocompatibility antigen, Cw-6 alpha chain
ARF1_HUMAN*	ADP-ribosylation factor 1
ARF4_HUMAN*	ADP-ribosylation factor 4
COPG1_HUMAN*	Coatomer subunit gamma-1
LTOR1_HUMAN*	Ragulator complex protein LAMTOR1
LTOR2_HUMAN*	Ragulator complex protein LAMTOR2
LTOR3_HUMAN*	Ragulator complex protein LAMTOR3
RAB1A_HUMAN*	Ras-related protein Rab-1A
RAP1A_HUMAN*	Ras-related protein Rap-1A
RAP1B_HUMAN*	Ras-related protein Rap-1b

Supplementary Table S4: GOTERM: *Membrane fraction.*

Uniprot ID	**Full protein name**
1A68_HUMAN	major histocompatibility complex, class I, A
1B55_HUMAN,	major histocompatibility complex, class I, C; major histocompatibility complex, class I, B
1C06_HUMAN	major histocompatibility complex, class I, C; major histocompatibility complex, class I, B
5NTD_HUMAN	5'-nucleotidase, ecto (CD73)
A4_HUMAN	amyloid beta (A4) precursor protein
AAAT_HUMAN	solute carrier family 1 (neutral amino acid transporter), member 5
ACSL4_HUMAN	acyl-CoA synthetase long-chain family member 4
ADAM9_HUMAN	ADAM metallopeptidase domain 9 (meltrin gamma)
AIP_HUMAN	aryl hydrocarbon receptor interacting protein
ANKH_HUMAN	ankylosis, progressive homolog (mouse)
ANPRC_HUMAN	natriuretic peptide receptor C/guanylate cyclase C (atrionatriuretic peptide receptor C)
APOE_HUMAN	hypothetical LOC100129500; apolipoprotein E
ARF6_HUMAN	ADP-ribosylation factor 6
ARL1_HUMAN	ADP-ribosylation factor-like 1
ARSA_HUMAN	arylsulfatase A
AT12A_HUMAN	ATPase, H+/K+ transporting, nongastric, alpha polypeptide
AT1A1_HUMAN	ATPase, Na+/K+ transporting, alpha 1 polypeptide
AT1A2_HUMAN	ATPase, Na+/K+ transporting, alpha 2 (+) polypeptide
AT1B1_HUMAN	ATPase, Na+/K+ transporting, beta 1 polypeptide
AT2A1_HUMAN	ATPase, Ca++ transporting, cardiac muscle, fast twitch 1
AT2B1_HUMAN	ATPase, Ca++ transporting, plasma membrane 1
AT2B4_HUMAN	ATPase, Ca++ transporting, plasma membrane 4
CADH2_HUMAN	cadherin 2, type 1, N-cadherin (neuronal)
CAV1_HUMAN	caveolin 1, caveolae protein, 22kDa
CAV2_HUMAN	caveolin 2
CD166_HUMAN	hypothetical protein LOC100133690; activated leukocyte cell adhesion molecule

CD276_HUMAN	CD276 molecule
CD59_HUMAN	CD59 molecule, complement regulatory protein
CD81_HUMAN	CD81 molecule
CD82_HUMAN	CD82 molecule
CDC42_HUMAN	cell division cycle 42 (GTP binding protein, 25kDa); cell division cycle 42 pseudogene 2
CERU_HUMAN	ceruloplasmin (ferroxidase)
CKAP4_HUMAN	cytoskeleton-associated protein 4
CLN3_HUMAN	ceroid-lipofuscinosis, neuronal 3
CNN2_HUMAN	calponin 2
COMT_HUMAN	catechol-O-methyltransferase
CPT1A_HUMAN	carnitine palmitoyltransferase 1A (liver)
CTNA1_HUMAN	catenin (cadherin-associated protein), alpha 1, 102kDa
CTNA2_HUMAN	catenin (cadherin-associated protein), alpha 2
CTNB1_HUMAN	catenin (cadherin-associated protein), beta 1, 88kDa
CTND1_HUMAN	catenin (cadherin-associated protein), delta 1
CTR1_HUMAN	solute carrier family 7 (cationic amino acid transporter, y+ system), member 1
CXAR_HUMAN	coxsackie virus and adenovirus receptor
CYB5B_HUMAN	cytochrome b5 type B (outer mitochondrial membrane)
DAF_HUMAN	CD55 molecule, decay accelerating factor for complement (Cromer blood group)
DD19A_HUMAN	DEAD (Asp-Glu-Ala-As) box polypeptide 19A
DIAP1_HUMAN	diaphanous homolog 1 (Drosophila)
DLG1_HUMAN	discs, large homolog 1 (Drosophila)
DP13A_HUMAN	adaptor protein, phosphotyrosine interaction, PH domain and leucine zipper containing 1
DPM1_HUMAN	dolichyl-phosphate mannosyltransferase polypeptide 1, catalytic subunit
DSG2_HUMAN	desmoglein 2
DYN2_HUMAN	dynamin 2
ECE1_HUMAN	endothelin converting enzyme 1
EGLN_HUMAN	endoglin
EHD2_HUMAN	EH-domain containing 2
EPCR_HUMAN	protein C receptor, endothelial (EPCR)
EPHA2_HUMAN	EPH receptor A2
EPHB2_HUMAN	EPH receptor B2
ERG7_HUMAN	lanosterol synthase (2,3-oxidosqualene-lanosterol cyclase)
ERO1A_HUMAN	ERO1-like (S. cerevisiae)
FACE1_HUMAN	zinc metallopeptidase (STE24 homolog, S. cerevisiae)
FERM2_HUMAN	fermitin family homolog 2 (Drosophila)
FLOT1_HUMAN	flotillin 1
FLOT2_HUMAN	flotillin 2
FOLR1_HUMAN	folate receptor 1 (adult)
GBB1_HUMAN	guanine nucleotide binding protein (G protein), beta polypeptide 1
GBG10_HUMAN	DnaJ (Hsp40) homolog, subfamily C
GBG12_HUMAN	guanine nucleotide binding protein (G protein), gamma 12
GIPC1_HUMAN	GIPC PDZ domain containing family, member 1
GNA11_HUMAN	guanine nucleotide binding protein (G protein), alpha 11 (Gq class)
GNAI2_HUMAN	guanine nucleotide binding protein (G protein), alpha inhibiting activity polypeptide 2

GNAI3_HUMAN	guanine nucleotide binding protein (G protein), alpha inhibiting activity polypeptide 3
GNAQ_HUMAN	guanine nucleotide binding protein (G protein), q polypeptide
GNAS2_HUMAN	GNAS complex locus
GPR56_HUMAN	G protein-coupled receptor 56
GTR1_HUMAN	solute carrier family 2 (facilitated glucose transporter), member 1
HGS_HUMAN	hepatocyte growth factor-regulated tyrosine kinase substrate
HMOX1_HUMAN	heme oxygenase (decycling) 1
HMOX2_HUMAN	heme oxygenase (decycling) 2
HYEP_HUMAN	epoxide hydrolase 1, microsomal (xenobiotic)
IGHG2_HUMAN	immunoglobulin heavy constant gamma 2 (G2m marker)
IGHG4_HUMAN	immunoglobulin heavy constant gamma 4 (G4m marker)
IL6RB_HUMAN	interleukin 6 signal transducer (gp130, oncostatin M receptor)
ILK_HUMAN	integrin-linked kinase
ITA1_HUMAN	integrin, alpha 1
ITA2_HUMAN	integrin, alpha 2 (CD49B, alpha 2 subunit of VLA-2 receptor)
ITA3_HUMAN	integrin, alpha 3 (antigen CD49C, alpha 3 subunit of VLA-3 receptor)
ITA5_HUMAN	integrin, alpha 5 (fibronectin receptor, alpha polypeptide)
ITA6_HUMAN	integrin, alpha 6
ITB1_HUMAN	integrin, beta 1 (fibronectin receptor, beta polypeptide=
ITB4_HUMAN	integrin, beta 4
ITB5_HUMAN	integrin, beta 5
KAP2_HUMAN	protein kinase, cAMP-dependent, regulatory, type II, alpha
KPCA_HUMAN	protein kinase C, alpha
L1CAM_HUMAN	L1 cell adhesion molecule
LAMP1_HUMAN	lysosomal-associated membrane protein 1
LAMP2_HUMAN	lysosomal-associated membrane protein 2
LAP2_HUMAN	erbb2 interacting protein
LCAP_HUMAN	leucyl/cystinyl aminopeptidase
LFA3_HUMAN	CD58 molecule
LIMA1_HUMAN	LIM domain and actin binding 1
LIN7C_HUMAN	lin-7 homolog C (C. elegans)
LIS1_HUMAN	platelet-activating factor acetylhydrolase, isoform Ib, subunit 1 (45kDa)
LMAN1_HUMAN	lectin, mannose-binding, 1
MET_HUMAN	met proto-oncogene (hepatocyte growth factor receptor)
MOT1_HUMAN	solute carrier family 16, member 1 (monocarboxylic acid transporter 1)
MPRI_HUMAN	insulin-like growth factor 2 receptor
MPZL1_HUMAN	myelin protein zero-like 1
MRP1_HUMAN	ATP-binding cassette, sub-family C (CFTR/MRP), member 1
MYO1C_HUMAN	myosin IC
NCEH1_HUMAN	arylacetamide deacetylase-like 1
NCPR_HUMAN	P450 (cytochrome) oxidoreductase
NEXN_HUMAN	nexilin (F actin binding protein)
NHRF1_HUMAN	solute carrier family 9 (sodium/hydrogen exchanger), member 3 regulator 1
NHRF2_HUMAN	solute carrier family 9 (sodium/hydrogen exchanger), member 3 regulator 2
NICA_HUMAN	nicastrin

NU155_HUMAN	nucleoporin 155kDa
ODO2_HUMAN	dihydrolipoamide S-succinyltransferase
OST48_HUMAN	dolichyl-diphosphooligosaccharide-protein glycosyltransferase
P4K2A_HUMAN	phosphatidylinositol 4-kinase type 2 alpha
PA24A_HUMAN	phospholipase A2, group IVA (cytosolic, calcium-dependent)
PACN3_HUMAN	protein kinase C and casein kinase substrate in neurons 3
PARVA_HUMAN	parvin, alpha
PARVB_HUMAN	parvin, beta
PGRC1_HUMAN	progesterone receptor membrane component 1
PLAK_HUMAN	junction plakoglobin
PLD1_HUMAN	phospholipase D1, phosphatidylcholine-specific
PODXL_HUMAN	podocalyxin-like
PPAL_HUMAN	acid phosphatase 2, lysosomal
PPIF_HUMAN	peptidylprolyl isomerase F
PPT1_HUMAN	palmitoyl-protein thioesterase 1
PTPRJ_HUMAN	protein tyrosine phosphatase, receptor type, J
PVRL2_HUMAN	poliovirus receptor-related 2 (herpesvirus entry mediator B)
RAB14_HUMAN	RAB14, member RAS oncogene family
RAB18_HUMAN	RAB18, member RAS oncogene family
RAB1B_HUMAN	RAB1B, member RAS oncogene family
RAB31_HUMAN	RAB31, member RAS oncogene family
RAB3A_HUMAN	RAB3A, member RAS oncogene family
RAB5A_HUMAN	RAB5A, member RAS oncogene family
RAGP1_HUMAN	Ran GTPase activating protein 1
RALA_HUMAN	v-ral simian leukemia viral oncogene homolog A (ras related)
RAP2A_HUMAN	RAP2A, member of RAS oncogene family
RAP2B_HUMAN	RAP2B, member of RAS oncogene family
RASN_HUMAN	neuroblastoma RAS viral (v-ras) oncogene homolog
RENR_HUMAN	ATPase, H+ transporting, lysosomal accessory protein 2
RHEB_HUMAN	Ras homolog enriched in brain
RHG17_HUMAN	Rho GTPase activating protein 17
RHOB_HUMAN	ras homolog gene family, member B
RHOG_HUMAN	ras homolog gene family, member G (rho G)
RRAS_HUMAN	related RAS viral (r-ras) oncogene homolog
S12A7_HUMAN	solute carrier family 12 (potassium/chloride transporters), member 7
SCRB1_HUMAN	scavenger receptor class B, member 1
SCRB2_HUMAN	scavenger receptor class B, member 2
SCRIB_HUMAN	scribbled homolog (Drosophila)
SEPT2_HUMAN	septin 2
SNAG_HUMAN	N-ethylmaleimide-sensitive factor attachment protein, gamma
SNTB2_HUMAN	syntrophin, beta 2 (dystrophin-associated protein A1, 59kDa, basic component 2)
SPCS2_HUMAN	signal peptidase complex subunit 2 homolog
SPCS3_HUMAN	signal peptidase complex subunit 3 homolog (S. cerevisiae)
SPTA2_HUMAN	spectrin, alpha, non-erythrocytic 1 (alpha-fodrin)
STAM1_HUMAN	signal transducing adaptor molecule (SH3 domain and ITAM motif) 1

STOM_HUMAN	phosphatidylethanolamine binding protein 1
THY1_HUMAN	Thy-1 cell surface antigen
TMED2_HUMAN	transmembrane emp24 domain trafficking protein 2
TMEDA_HUMAN	transmembrane emp24-like trafficking protein 10 (yeast)
TMX1_HUMAN	thioredoxin-related transmembrane protein 1
TOM22_HUMAN	translocase of outer mitochondrial membrane 22 homolog (yeast)
TOM40_HUMAN	translocase of outer mitochondrial membrane 40 homolog (yeast)
TPBG_HUMAN	trophoblast glycoprotein
TRIP6_HUMAN	thyroid hormone receptor interactor 6
UFO_HUMAN	AXL receptor tyrosine kinase
USO1_HUMAN	USO1 homolog, vesicle docking protein (yeast)
VA0D1_HUMAN	ATPase, H+ transporting, lysosomal 38kDa, V0 subunit d1
VAPA_HUMAN	VAMP (vesicle-associated membrane protein)-associated protein A, 33kDa
VASP_HUMAN	vasodilator-stimulated phosphoprotein
VATB1_HUMAN	ATPase, H+ transporting, lysosomal 56/58kDa, V1 subunit B1
VATF_HUMAN	ATPase, H+ transporting, lysosomal 14kDa, V1 subunit F
VDAC3_HUMAN	voltage-dependent anion channel 3
VPP3_HUMAN	T-cell, immune regulator 1, ATPase, H+ transporting, lysosomal V0 subunit A3
ZO1_HUMAN	tight junction protein 1 (zona occludens 1)
ZYX_HUMAN	zyxin

Supplementary Table S5: GOTERM: *Mitochondrial envelope + mitochondria.*

Uniprot ID	Full protein name
3HIDH_HUMAN	3-hydroxyisobutyrate dehydrogenase
ABCB6_HUMAN	ATP-binding cassette, sub-family B (MDR/TAP), member 6
ABCE1_HUMAN	similar to ATP-binding cassette, sub-family E
ABHDA_HUMAN	abhydrolase domain containing 10
ACADM_HUMAN	acyl-Coenzyme A dehydrogenase, C-4 to C-12 straight chain
ACADV_HUMAN	acyl-Coenzyme A dehydrogenase, very long chain
ACO13_HUMAN	acyl-CoA thioesterase 13
ACON_HUMAN	aconitase 2, mitochondrial
ACOT9_HUMAN	acyl-CoA thioesterase 9
ACOX1_HUMAN	acyl-Coenzyme A oxidase 1, palmitoyl
ACPM_HUMAN	NADH dehydrogenase (ubiquinone) 1, alpha/beta subcomplex, 1, 8kDa
ACSL4_HUMAN	acyl-CoA synthetase long-chain family member 4
ADAS_HUMAN	alkylglycerone phosphate synthase
ADT2_HUMAN	solute carrier family 25 (mitochondrial carrier; adenine nucleotide translocator), member 5; solute carrier family 25 (mitochondrial carrier; adenine nucleotide translocator), member 5 pseudogene 8
ADT3_HUMAN	solute carrier family 25 (mitochondrial carrier; adenine nucleotide translocator), member 6
AIFM2_HUMAN	apoptosis-inducing factor, mitochondrion-associated, 2
AL1B1_HUMAN	aldehyde dehydrogenase 1 family, member B1
AL3A2_HUMAN	aldehyde dehydrogenase 3 family, member A2

ALDH2_HUMAN	aldehyde dehydrogenase 2 family (mitochondrial)
AMPL_HUMAN	leucine aminopeptidase 3
AT5F1_HUMAN	ATP synthase, H+ transporting, mitochondrial F0 complex, subunit B1
ATP5H_HUMAN	ATP synthase, H+ transporting, mitochondrial F0 complex, subunit d
ATP5I_HUMAN	ATP synthase, H+ transporting, mitochondrial F0 complex, subunit E
ATP5J_HUMAN	ATP synthase, H+ transporting, mitochondrial F0 complex, subunit F6
ATP5L_HUMAN	ATP synthase, H+ transporting, mitochondrial F0 complex, subunit G
ATPA_HUMAN	ATP synthase, H+ transporting, mitochondrial F1 complex, alpha subunit 1, cardiac muscle
ATPB_HUMAN	ATP synthase, H+ transporting, mitochondrial F1 complex, beta polypeptide
ATPD_HUMAN	ATP synthase, H+ transporting, mitochondrial F1 complex, delta subunit
ATPG_HUMAN	ATP synthase, H+ transporting, mitochondrial F1 complex, gamma polypeptide 1
ATPK_HUMAN	ATP synthase, H+ transporting, mitochondrial F0 complex, subunit F2
ATPO_HUMAN	ATP synthase, H+ transporting, mitochondrial F1 complex, O subunit
B2L13_HUMAN	BCL2-like 13 (apoptosis facilitator)
BAX_HUMAN	BCL2-associated X protein
BCS1_HUMAN	BCS1-like (yeast)
C1QBP_HUMAN	complement component 1, q subcomponent binding protein
C1TM_HUMAN	methylenetetrahydrofolate dehydrogenase (NADP+ dependent) 1-like
CATA_HUMAN	catalase
CB047_HUMAN	chromosome 2 open reading frame 47
CCHL_HUMAN	holocytochrome c synthase (cytochrome c heme-lyase)
CH60_HUMAN	heat shock 60kDa protein 1 (chaperonin) pseudogene 5; heat shock 60kDa protein 1 (chaperonin) pseudogene 6; heat shock 60kDa protein 1 (chaperonin) pseudogene 1; heat shock 60kDa protein 1 (chaperonin) pseudogene 4; heat shock 60kDa protein 1 (chaperonin)
CHCH3_HUMAN	coiled-coil-helix-coiled-coil-helix domain containing 3
CISD1_HUMAN	CDGSH iron sulfur domain 1
CISY_HUMAN	citrate synthase
CLPP_HUMAN	ClpP caseinolytic peptidase, ATP-dependent, proteolytic subunit homolog (E. coli)
CLPX_HUMAN	ClpX caseinolytic peptidase X homolog (E. coli)
CMC1_HUMAN	solute carrier family 25 (mitochondrial carrier, Aralar), member 12
CMC2_HUMAN	solute carrier family 25, member 13 (citrin)
COX2_HUMAN	Cytochrome c oxidase subunit 2
COX41_HUMAN	cytochrome c oxidase subunit IV isoform 1
COX5A_HUMAN	cytochrome c oxidase subunit Va
CPSM_HUMAN	carbamoyl-phosphate synthetase 1, mitochondrial
CPT1A_HUMAN	carnitine palmitoyltransferase 1A (liver)
CPT2_HUMAN	carnitine palmitoyltransferase 2
CX4NB_HUMAN	COX4 neighbor
CX7A2_HUMAN	cytochrome c oxidase subunit VIIa polypeptide 2 (liver)
CYB5B_HUMAN	cytochrome b5 type B (outer mitochondrial membrane)
DECR_HUMAN	2,4-dienoyl CoA reductase 1, mitochondrial
DHB4_HUMAN	hydroxysteroid (17-beta) dehydrogenase 4
DHE3_HUMAN	glutamate dehydrogenase 1

DHRS1_HUMAN	dehydrogenase/reductase (SDR family) member 1
DHSA_HUMAN	succinate dehydrogenase complex, subunit A, flavoprotein (Fp)
DHSB_HUMAN	succinate dehydrogenase complex, subunit B, iron sulfur (Ip)
DIC_HUMAN	solute carrier family 25 (mitochondrial carrier; dicarboxylate transporter), member 10
DJC11_HUMAN	DnaJ (Hsp40) homolog, subfamily C, member 11
DNJA3_HUMAN	DnaJ (Hsp40) homolog, subfamily A, member 3
DPYL2_HUMAN	dihydropyrimidinase-like 2
ECH1_HUMAN	enoyl Coenzyme A hydratase 1, peroxisomal
ECHA_HUMAN	hydroxyacyl-Coenzyme A dehydrogenase/3-ketoacyl-Coenzyme A thiolase/enoyl-Coenzyme A hydratase (trifunctional protein), alpha subunit
ECHB_HUMAN	hydroxyacyl-Coenzyme A dehydrogenase/3-ketoacyl-Coenzyme A thiolase/enoyl-Coenzyme A hydratase (trifunctional protein), beta subunit
EFGM_HUMAN	G elongation factor, mitochondrial 1
EFTS_HUMAN	Ts translation elongation factor, mitochondrial
EFTU_HUMAN	Tu translation elongation factor, mitochondrial
ES1_HUMAN	chromosome 21 open reading frame 33
ETFA_HUMAN	electron-transfer-flavoprotein, alpha polypeptide
ETFB_HUMAN	electron-transfer-flavoprotein, beta polypeptide
ETHE1_HUMAN	ethylmalonic encephalopathy 1
FAHD1_HUMAN	fumarylacetoacetate hydrolase domain containing 1
FIS1_HUMAN	fission 1 (mitochondrial outer membrane) homolog (S. cerevisiae)
FUMH_HUMAN	fumarate hydratase
GHC1_HUMAN	solute carrier family 25 (mitochondrial carrier: glutamate), member 22
GLSK_HUMAN	glutaminase
GLYM_HUMAN	serine hydroxymethyltransferase 2 (mitochondrial)
GOLP3_HUMAN	golgi phosphoprotein 3 (coat-protein)
GPDM_HUMAN	glycerol-3-phosphate dehydrogenase 2 (mitochondrial)
GRPE1_HUMAN	GrpE-like 1, mitochondrial (E. coli)
GSTK1_HUMAN	glutathione S-transferase kappa 1
HCD2_HUMAN	hydroxysteroid (17-beta) dehydrogenase 10
HCDH_HUMAN	hydroxyacyl-Coenzyme A dehydrogenase
HINT2_HUMAN	histidine triad nucleotide binding protein 2
HMGCL_HUMAN	3-hydroxymethyl-3-methylglutaryl-Coenzyme A lyase
HSDL2_HUMAN	hydroxysteroid dehydrogenase like 2
IDH3A_HUMAN	isocitrate dehydrogenase 3 (NAD+) alpha
IDH3G_HUMAN	isocitrate dehydrogenase 3 (NAD+) gamma
IMMT_HUMAN	inner membrane protein, mitochondrial (mitofilin)
IPYR2_HUMAN	pyrophosphatase (inorganic) 2
ISOC2_HUMAN	isochorismatase domain containing 2
IVD_HUMAN	isovaleryl Coenzyme A dehydrogenase
KAD2_HUMAN	adenylate kinase 2
KAD3_HUMAN	adenylate kinase 3
LETM1_HUMAN	leucine zipper-EF-hand containing transmembrane protein 1
LPPRC_HUMAN	leucine-rich PPR-motif containing
LYPA1_HUMAN	lysophospholipase I

M2OM_HUMAN	solute carrier family 25 (mitochondrial carrier; oxoglutarate carrier), member 11
MCCB_HUMAN	methylcrotonoyl-Coenzyme A carboxylase 2 (beta)
MDHM_HUMAN	malate dehydrogenase 2, NAD (mitochondrial)
MECR_HUMAN	mitochondrial trans-2-enoyl-CoA reductase
MFF_HUMAN	mitochondrial fission factor
MPCP_HUMAN	solute carrier family 25 (mitochondrial carrier; phosphate carrier), member 3
MPPA_HUMAN	peptidase (mitochondrial processing) alpha
MPPB_HUMAN	peptidase (mitochondrial processing) beta
MTCH2_HUMAN	mitochondrial carrier homolog 2 (C. elegans)
MTDC_HUMAN	methylenetetrahydrofolate dehydrogenase (NADP+ dependent) 2, methenyltetrahydrofolate cyclohydrolase
MTX1_HUMAN	metaxin 1
MTX2_HUMAN	metaxin 2
NB5R3_HUMAN	cytochrome b5 reductase 3
NDUA2_HUMAN	NADH dehydrogenase (ubiquinone) 1 alpha subcomplex, 2, 8kDa
NDUA4_HUMAN	NADH dehydrogenase (ubiquinone) 1 alpha subcomplex, 4, 9kDa
NDUA5_HUMAN	NADH dehydrogenase (ubiquinone) 1 alpha subcomplex, 5, 13kDa
NDUAA_HUMAN	NADH dehydrogenase (ubiquinone) 1 alpha subcomplex, 10, 42kDa
NDUAB_HUMAN	NADH dehydrogenase (ubiquinone) 1 alpha subcomplex, 11, 14.7kDa
NDUAD_HUMAN	NADH dehydrogenase (ubiquinone) 1 alpha subcomplex, 13
NDUB3_HUMAN	NADH dehydrogenase (ubiquinone) 1 beta subcomplex, 3, 12kDa
NDUBA_HUMAN	NADH dehydrogenase (ubiquinone) 1 beta subcomplex, 10, 22kDa
NDUF3_HUMAN	NADH dehydrogenase (ubiquinone) 1 alpha subcomplex, assembly factor 3
NDUS1_HUMAN	NADH dehydrogenase (ubiquinone) Fe-S protein 1, 75kDa (NADH-coenzyme Q reductase)
NDUS2_HUMAN	NADH dehydrogenase (ubiquinone) Fe-S protein 2, 49kDa (NADH-coenzyme Q reductase)
NDUS3_HUMAN	NADH dehydrogenase (ubiquinone) Fe-S protein 3, 30kDa (NADH-coenzyme Q reductase)
NDUS8_HUMAN	NADH dehydrogenase (ubiquinone) Fe-S protein 8, 23kDa (NADH-coenzyme Q reductase)
NDUV1_HUMAN	NADH dehydrogenase (ubiquinone) flavoprotein 1, 51kDa
NDUV2_HUMAN	NADH dehydrogenase (ubiquinone) flavoprotein 2, 24kDa
NEUL_HUMAN	neurolysin (metallopeptidase M3 family)
NFU1_HUMAN	NFU1 iron-sulfur cluster scaffold homolog (S. cerevisiae)
NIPS1_HUMAN	nipsnap homolog 1 (C. elegans)
NLTP_HUMAN	sterol carrier protein 2
NNTM_HUMAN	nicotinamide nucleotide transhydrogenase
OAT_HUMAN	ornithine aminotransferase (gyrate atrophy)
ODB2_HUMAN	dihydrolipoamide branched chain transacylase E2
ODBB_HUMAN	branched chain keto acid dehydrogenase E1, beta polypeptide
ODO1_HUMAN	oxoglutarate (alpha-ketoglutarate) dehydrogenase (lipoamide)
ODP2_HUMAN	dihydrolipoamide S-acetyltransferase
ODPA_HUMAN	pyruvate dehydrogenase (lipoamide) alpha 1
ODPB_HUMAN	pyruvate dehydrogenase (lipoamide) beta

OPA1_HUMAN	optic atrophy 1 (autosomal dominant)
P4HA1_HUMAN	prolyl 4-hydroxylase, alpha polypeptide I
P5CR1_HUMAN	pyrroline-5-carboxylate reductase 1
P5CR1_HUMAN	sirtuin (silent mating type information regulation 2 homolog) 7 (S. cerevisiae)
P5CS_HUMAN	aldehyde dehydrogenase 18 family, member A1
PCKGM_HUMAN	phosphoenolpyruvate carboxykinase 2 (mitochondrial)
PDIP2_HUMAN	polymerase (DNA-directed), delta interacting protein 2
PGES2_HUMAN	prostaglandin E synthase 2
PHB_HUMAN	prohibitin
PHB2_HUMAN	prohibitin 2
PNPT1_HUMAN	polyribonucleotide nucleotidyltransferase 1
PP1G_HUMAN	protein phosphatase 1, catalytic subunit, gamma isoform
PPIF_HUMAN	peptidylprolyl isomerase F
PRDX3_HUMAN	peroxiredoxin 3
PRDX4_HUMAN	peroxiredoxin 4
PRS6B_HUMAN	similar to 26S protease regulatory subunit 6B
PTCD3_HUMAN	Pentatricopeptide repeat domain 3
PTH2_HUMAN	peptidyl-tRNA hydrolase 2
PYC_HUMAN	pyruvate carboxylase
QCR1_HUMAN	ubiquinol-cytochrome c reductase core protein I
QCR2_HUMAN	ubiquinol-cytochrome c reductase core protein II
QCR7_HUMAN	similar to ubiquinol-cytochrome c reductase binding protein; ubiquinol-cytochrome c reductase binding protein pseudogene; ubiquinol-cytochrome c reductase binding protein
RAB32_HUMAN	RAB32, member RAS oncogene family
RM12_HUMAN	mitochondrial ribosomal protein L12
RM19_HUMAN	mitochondrial ribosomal protein L19
RM37_HUMAN	mitochondrial ribosomal protein L37
RM39_HUMAN	mitochondrial ribosomal protein L39
RM44_HUMAN	mitochondrial ribosomal protein L44
RM46_HUMAN	mitochondrial ribosomal protein L46
RM49_HUMAN	mitochondrial ribosomal protein L49
RMD3_HUMAN	family with sequence similarity 82, member A2
RRFM_HUMAN	mitochondrial ribosome recycling factor
RT10_HUMAN	mitochondrial ribosomal protein S10
RT22_HUMAN	mitochondrial ribosomal protein S22
RT23_HUMAN	mitochondrial ribosomal protein S23
RT27_HUMAN	mitochondrial ribosomal protein S27
RT28_HUMAN	mitochondrial ribosomal protein S28
RT29_HUMAN	death associated protein 3
SCMC1_HUMAN	solute carrier family 25 (mitochondrial carrier; phosphate carrier), member 24
SCOT1_HUMAN	3-oxoacid CoA transferase 1
SDHF2_HUMAN	chromosome 11 open reading frame 79
SFXN3_HUMAN	sideroflexin 3
SLIRP_HUMAN	chromosome 14 open reading frame 156
SPNS1_HUMAN	spinster homolog 1 (Drosophila)

SSBP_HUMAN	single-stranded DNA binding protein 1
STML2_HUMAN	stomatin (EPB72)-like 2
STOM_HUMAN	phosphatidylethanolamine binding protein 1
SUCB1_HUMAN	succinate-CoA ligase, ADP-forming, beta subunit
SUCB2_HUMAN	similar to sucb; succinate-CoA ligase, GDP-forming, beta subunit
SYDM_HUMAN	aspartyl-tRNA synthetase 2, mitochondrial
SYJ2B_HUMAN	synaptojanin 2 binding protein
SYLM_HUMAN	leucyl-tRNA synthetase 2, mitochondrial
SYTM_HUMAN	threonyl-tRNA synthetase 2, mitochondrial (putative)
THIL_HUMAN	acetyl-Coenzyme A acetyltransferase 1
THIM_HUMAN	hypothetical LOC648603; acetyl-Coenzyme A acyltransferase 2
TIM44_HUMAN	translocase of inner mitochondrial membrane 44 homolog (yeast)
TIM50_HUMAN	translocase of inner mitochondrial membrane 50 homolog (S. cerevisiae)
TOM22_HUMAN	translocase of outer mitochondrial membrane 22 homolog (yeast)
TOM40_HUMAN	translocase of outer mitochondrial membrane 40 homolog (yeast)
TOM70_HUMAN	translocase of outer mitochondrial membrane 70 homolog A (S. cerevisiae)
TRAP1_HUMAN	TNF receptor-associated protein 1
TXTP_HUMAN	solute carrier family 25 (mitochondrial carrier; citrate transporter), member 1
UCRI_HUMAN	ubiquinol-cytochrome c reductase, Rieske iron-sulfur polypeptide-like 1; ubiquinol-cytochrome c reductase, Rieske iron-sulfur polypeptide 1
USMG5_HUMAN	up-regulated during skeletal muscle growth 5 homolog (mouse)
VATA_HUMAN	ATPase, H+ transporting, lysosomal 70kDa, V1 subunit A
VATE1_HUMAN	ATPase, H+ transporting, lysosomal 31kDa, V1 subunit E1
VDAC1_HUMAN	voltage-dependent anion channel 1; similar to voltage-dependent anion channel 1
VDAC2_HUMAN	voltage-dependent anion channel 2
VDAC3_HUMAN	voltage-dependent anion channel 3

Supplementary Table S6: DAVID ontology analysis of the remaining proteins that have been identified.

	Enrichment Score: 3.53	**Count**
Annotation Cluster 1		
GOTERM_CC_FAT	cytoskeletal part	21
GOTERM_CC_FAT	cytoskeleton	26
GOTERM_CC_FAT	actin cytoskeleton	11
GOTERM_CC_FAT	non-membrane-bounded organelle	32
GOTERM_CC_FAT	intracellular non-membrane-bounded organelle	32
Annotation Cluster 2	Enrichment Score: 2.12	
GOTERM_CC_FAT	nuclear pore	6
GOTERM_CC_FAT	pore complex	6
GOTERM_CC_FAT	endomembrane system	16
GOTERM_CC_FAT	nuclear envelope	7
GOTERM_CC_FAT	organelle envelope	7
GOTERM_CC_FAT	envelope	7
Annotation Cluster 3	Enrichment Score: 1.81	
GOTERM_CC_FAT	endomembrane system	16
GOTERM_CC_FAT	endoplasmic reticulum	18

GOTERM_CC_FAT	endoplasmic reticulum membrane	7
GOTERM_CC_FAT	nuclear envelope-endoplasmic reticulum network	7
GOTERM_CC_FAT	endoplasmic reticulum part	7
GOTERM_CC_FAT	organelle membrane	9
Annotation Cluster 4	Enrichment Score: 1.77	
GOTERM_CC_FAT	microtubule cytoskeleton	12
GOTERM_CC_FAT	centrosome	6
GOTERM_CC_FAT	microtubule organizing center	6
Annotation Cluster 5	Enrichment Score: 1.34	
GOTERM_CC_FAT	keratin filament	4
GOTERM_CC_FAT	intermediate filament	5
GOTERM_CC_FAT	intermediate filament cytoskeleton	5
Annotation Cluster 6	Enrichment Score: 1.32	
GOTERM_CC_FAT	ribonucleoprotein complex	10
GOTERM_CC_FAT	cytosolic ribosome	4
GOTERM_CC_FAT	cytosolic part	5
GOTERM_CC_FAT	ribosomal subunit	4
GOTERM_CC_FAT	ribosome	4
Annotation Cluster 7	Enrichment Score: 1.16	
GOTERM_CC_FAT	dynein complex	3
GOTERM_CC_FAT	microtubule	6
GOTERM_CC_FAT	microtubule associated complex	3
Annotation Cluster 8	Enrichment Score: 0.52	
GOTERM_CC_FAT	kinetochore	3
GOTERM_CC_FAT	chromosome, centromeric region	3
GOTERM_CC_FAT	chromosome	5
GOTERM_CC_FAT	chromosomal part	4